Dissertation zur Erlangung des Doktorgrades

der Fakultät für Chemie und Pharmazie

der Ludwigs-Maximilians Universität München

Structural and functional insights into the cytoplasmic RNA exosome and its cofactors

Achim Keidel

aus

Stuttgart, Deutschland

2023

Erklärung:

Diese Dissertation wurde im Sinne von §7 der Promotionsordnung vom 28. November 2011 von Prof. Dr. Elena Conti betreut.

Eidesstattliche Versicherung:

Diese Dissertation wurde eigenständig und ohne unerlaubte Hilfe erarbeitet.

München, 25.07.2023

Achim Keidel

Dissertation eingereicht am 25.07.2023

1. Gutachterin: Prof. Dr. Elena Conti

2. Gutachter: Prof. Dr. Karl-Peter Hopfner

Mündliche Prüfung am 13.09.2023

Table of Contents

Summary ..... *I*

1. Preface *1*

2. Introduction *3*

2.1 Cytoplasmic mRNA decay in eukaryotic cells **3**

2.1.1 Canonical mRNA degradation in eukaryotic cells 4

2.1.2 mRNA surveillance in eukaryotic cells 6

2.2 The RNA Exosome **10**

2.2.1 Functions of the eukaryotic RNA exosome 10

2.2.2 Structure and conservation of the RNA exosome 12

2.3 Exosome adaptors complexes are centered around Ski2-like helicases **14**

2.4 The nuclear RNA exosome **16**

2.5 The cytoplasmic RNA exosome **18**

2.5.1 The Ski2-Ski3-Ski8 complex 18

2.5.2 The adaptor protein Ski7 (yeast) and Hbs1L3 (human) 21

2.5.3 The cytoplasmic Ski238-Ski7-Exo10 assembly: 22

2.5.4 The Ska1 protein in yeast 24

2.6 Scope of this work **25**

3. Materials and Methods *27*

3.1.Purification of full length Ska1 from E.coli **27**

3.2 Purification of Ski238 from Hi5 insect cells and Ski7 from E.coli **28**

3.3 Analytical size exclusion chromatography of Ska1 together with the Ski238 complex **28**

3.4 Pulldown experiments of Ska1 with individual Ski238 complexes **28**

4. Results *29*

4.1 Publication 1: **29**

The human SKI complex regulates channeling of ribosome-bound RNA to the exosome via an intrinsic gatekeeping mechanism **29**

4.2 Publication 2: **71**

Concerted structural rearrangements enable RNA channeling into the cytoplasmic Ski238-Ski7-Exo10 assembly **71**

4.3 Publication 3: **137**

Purification and Reconstitution of the S. cerevisiae TRAMP and Ski Complexes for Biochemical and structural studies **137**

4.4 Biochemical characterization of the Ska1 protein and its interaction with the Ski238 complex **163**

5. Discussion *167*

5.1 Comparison of structure and function of the Ski238 complex in yeast and human 167

5.2 Recruitment of the Ski238 complex to the eukaryotic RNA exosome by Ski7 and Hbs1L3 ... 171

5.3 RNA channeling from Ski2-Cat to the exosome is conserved 174

5.4 Ska1 as a potential regulator of Ski238 helicase activity 176

6. Outlook 179

7. References 181

8. Acknowledgements 189

List of Figures

Figure 1: Schematic overview on canonical mRNA degradation in eukaryotic cells..... 5

Figure 2: Schematic overview on two mRNA surveillance pathways 9

Figure 3: Functions of the RNA exosome in eukaryotic cells..... 11

Figure 4: Structural conservation of the RNA exosome..... 13

Figure 5: Comparison of crystal structures of Mtr4 and Ski2..... 15

Figure 6: Comparison of yeast and human nuclear exosome structures..... 17

Figure 7: Domain organization and structure of the S. cerevisiae Ski238 complex..... 20

Figure 8: Domain organization of S. Cerevisiae Ski7 and its human counterpart the Hbs1L3..... 22

Figure 9: Proposed model for substrate channeling in the cytoplasmic Ski238-Ski7-exosome assembly 23

Figure 10: Purification and biochemical characterization of Ska1 and its interaction with the Ski238 complex 164

Figure 11: Pulldown assays of Ska1 with different domains of Ski238 and different Ski238 complexes..... 166

Figure 12: Atomic models of Ski238 from yeast and human in different conformational states..... 168

Figure 13: Comparison of yeast Ski2ΔArch38 bound to Ski7-N with human Ski238 in the open state..... 173

Figure 14: Conservation analysis of Ski7-N residues that interact with the Ski2 helicase core..... 175

Summary

In eukaryotic cells, the RNA exosome serves as the primary 3' to 5' exonuclease responsible for degrading and processing various RNA substrates. To carry out its diverse functions, the exosome relies on compartment-specific cofactors that provide substrate specificity. In the cytoplasm, the conserved Ski238 complex, centered around the ATP-dependent RNA helicase Ski2, assists the exosome. Additionally, the bridging factor Ski7 in yeast, or its equivalent Hbs1L3 in higher eukaryotes, facilitates the interaction between the Ski238 complex and the RNA-degrading exosome. It is suggested that the Ski238 complex directly associates with the exosome to guide the RNA substrate towards the exosome's nuclease domain. However, molecular structures as proof for the direct channeling are not available and the precise coordination among these cofactors, which ultimately leads to RNA degradation, remains largely unknown.

This thesis presents a collection of structural snapshots that reveal the process of cytoplasmic 3' to 5' RNA degradation by the exosome and its cofactors. This series of complex structures provide unprecedented details regarding the interplay between different modules and reveal significant conformational changes within the Ski238 complex. These conformational rearrangements play a crucial role in coordinating the helicase and the nuclease activity during the degradation process. Based on this knowledge, for the first time, we were able to reconstitute a full Ski238-Ski7-exosome assembly and reveal its cryoEM structure. Remarkably, the interface between the exosome and its cytosolic helicase Ski2 resembles the nuclear complex where the exosome interacts with the helicase Mtr4.

In summary, the presented results offer a holistic understanding of the individual steps involved in 3' to 5' RNA degradation by the exosome in the cytoplasm of eukaryotic cells. These findings reveal both the similarities and differences between yeast and human complexes, serving as a foundation for further elucidation of cytosolic RNA quality control mechanisms.

1. Preface

The degradation and processing of RNA molecules are crucial processes in all kingdoms of life, necessitating the involvement of various factors that recognize specific RNA substrates at the appropriate time, location and developmental stage. Despite extensive research efforts to unravel these pathways at the molecular level, numerous questions remain unanswered. This thesis addresses some of these questions using single particle cryoEM and biochemical approaches to further our understanding of the molecular principles behind RNA degradation in eukaryotic cells.

This thesis is written cumulatively, summarizing the scientific results obtained since 2017 in a concise manner. The second chapter contains an introduction to the scientific background and defines the objectives of this thesis. The third chapter contains a summary of materials and methods important for unpublished work presented in this thesis. The fourth chapter includes three publications that represent the main body of work during my Ph.D. Among these publications, two are original scientific manuscripts, while one is currently under revision. In addition unpublished work on a potential new cofactor for cytoplasmic exosomal RNA degradation is presented. The fifth chapter contains a comprehensive discussion that integrates the findings from the main publications as well as the unpublished work. At last, chapter six provides an outlook on open questions that can be addressed in future studies.

2. Introduction

In the nucleus of eukaryotic cells, large parts of the genome are constantly transcribed in the nucleus leading to a variety of RNA transcripts. The purpose of RNAs is versatile and ranges from information carriers, to structural elements, to regulation functions and RNAs with catalytic activity. The abundance of RNAs within the cell is regulated through an equilibrium between transcription and degradation. Changes in these processes can increase or decrease the amounts of intact transcripts, thereby regulating RNA levels and maintaining cell homeostasis. Most RNA transcripts are targeted by complex protein machineries that are required to ensure the integrity of the RNA molecules through different processing steps. In addition, quality control mechanisms sample the transcriptome for defective and aberrant RNAs to destroy them. These co- and post-transcriptional modifications need to be accurate and mutations in the involved protein machinery often affect the health or viability of the cell or organism. RNA degradation plays a major role in the processing and quality control of transcripts. It is crucial for trimming transcripts to make them functional, or accessible for further maturation steps. RNA degradation can also directly affect gene expression by removing transcripts from the cell. The enzymes that are required in RNA degradation pathways involve helicases, nucleases and RNA-binding proteins (RBPs) that are essentially conserved between all kingdoms of life. While the complexity and number of decay and processing pathways vary substantially, the concept of destructive and constructive RNA degradation pathways can be observed in all living organisms. In *Saccharomyces Cerevisiae* at least 34 different RNases exist that take over the degradation and processing of transcripts. In *Homo sapiens* the estimated minimal number is 60 (Stoecklin and Mühlemann, 2013).

2.1 Cytoplasmic mRNA decay in eukaryotic cells

One important task of RNases is the turnover of mRNAs in the cytoplasm. On the one hand, this comprises the degradation of mRNAs that have been translated and reached their programmed lifetime, known as canonical mRNA degradation. On the other hand, mRNA turnover also entails the destruction of aberrant mRNAs through different mRNA quality control pathways, known as mRNA surveillance. The following paragraphs summarize these processes and also the respective protein machinery involved.

2.1.1 Canonical mRNA degradation in eukaryotic cells

During the transcription of a gene in the nucleus, the produced pre-mRNA is co-transcriptionally modified at both ends. The 5' end is targeted by the capping machinery that involves the sequential action of three enzymes, resulting in the addition of 7-methylguanosin (m7G) resulting in the 5'cap (Shatkin and Manley, 2000). The nascent transcript is also targeted by the splicing machinery, which removes introns and ligates exons to produce the mature mRNA (Rogalska et al., 2023; Vorlaender et al., 2022). Subsequently, a specific sequence in the 3'-UTR of the pre-mRNA is targeted by the polyadenylation machinery and after an endo-nucleolytic cleavage, a poly adenosine (Poly(A)) tail is added with lengths varying between different species (Eckmann et al., 2011). During these maturation steps, the mRNA associates with numerous proteins (e.g. cap-binding complex (CBC), exon junction complexes (EJC's) and poly(A) binding proteins (PABP's)) to form a ribonucleoprotein particle (mRNP) that will be exported from the nucleus.

Once in the cytoplasm, the mRNP will be used as a template for translation and eventually, the mRNA will be destined for degradation. The control of mRNA stability is a key step in gene regulation and depends on the 5'cap and the 3'poly(A)-tail. After export to the cytoplasm, the 5'cap can be bound by the translation initiation factor complex eIF4F, consisting of the cap-binding protein eIF4E (which replaces CBC), the ATP-dependent RNA helicase EIF4A and EIF4G. EIF4G enhances the helicase activity of EIF4A and serves as a binding platform for additional proteins involved in the initiation process, as well as PABP's (R. Jackson et al., 2010; Safaee et al., 2012a). The poly(A)-tail, is coated by PABP's and thereby protects the mRNA from premature degradation (L P Ford et al., 1997). Furthermore, PABP's can interact with the two deadenylase-containing complexes Pan2-Pan3 and Ccr4-Not. It has been shown that Poly(A) length is crucial for the stability of mRNAs and that its shortening to an oligo(A) tail results in degradation of the body of the mRNA (Decker and Parker, 1993; Jalkanen et al., 2014). In terms of RNA degradation, the shortening of the poly(A)-tail by the Pan2-Pan3 deadenylase complex is the first event that initializes the decay of an mRNA (Figure 1).

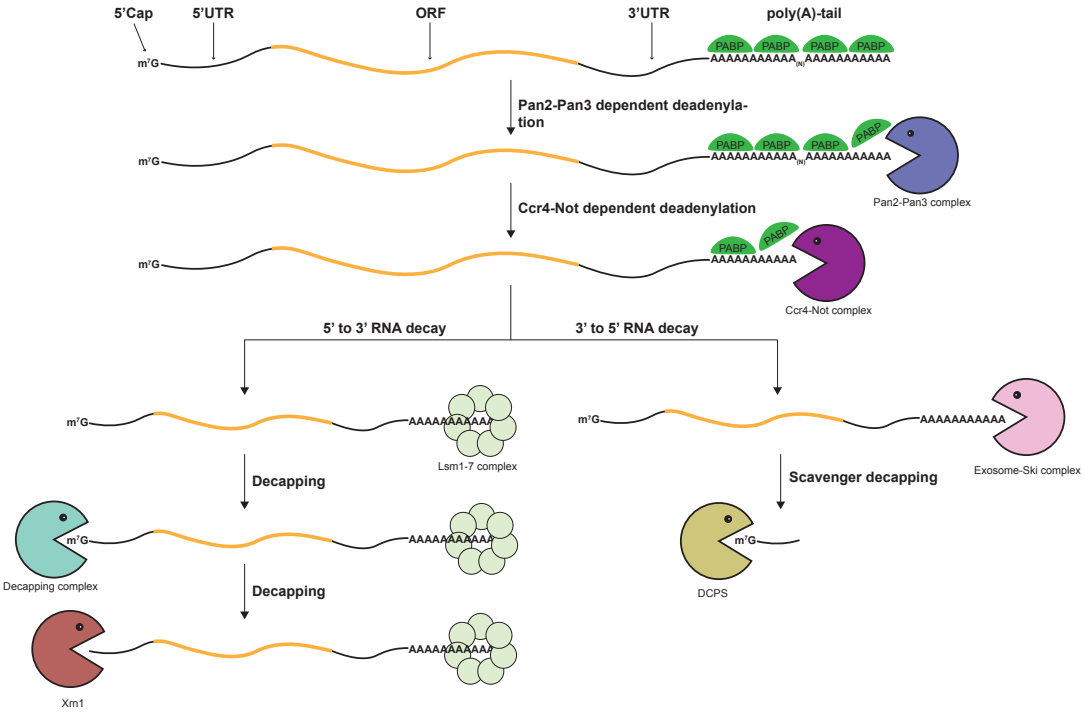

Figure 1: Schematic overview of canonical mRNA degradation in eukaryotic cells. Schematic of an mRNA with a 5' cap followed by a 5'UTR before the protein-encoding open reading frame (ORF) shown in orange, followed by the 3' UTR including the poly(A) tail which is covered by PABPs. Decay of the mRNA is initiated through deadenylation of the poly(A) tail by Pan2-Pan3 and the Ccr4-Not complex. Subsequently, the mRNA is degraded from its 5' end by the exonuclease Xrn1 which requires prior decapping. Alternatively, the mRNA is degraded from its 3' end by the Ski238-Ski7-exosome complex in a decapping-independent manner.

After the initial trimming of the poly(A)-tail by Pan2-Pan3, the Ccr4-Not complex takes over and continues the deadenylation (Tucker et al., 2001a; Wiederhold and Passmore, 2010). From there the mRNA is determined for degradation by the two canonical decay routes (reviewed in Garneau et al., 2007). On the one hand from its 5' end, through association with the Lsm1-7 complex that recruits the decapping complex to remove the 5'cap. This allows the exonuclease Xrn1 to further erode the mRNA from the 5' end (Muhlrad and Parker, 1994). Xrn1 specifically recognizes the 5'-phosphate of decapped mRNAs and couples processive hydrolysis of the substrate with the unwinding of RNA duplexes (Jinek et al., 2011). In addition, Xrn1 can directly interact with the mRNA entry site of ribosomes in yeast indicating that 5' to 3' decay can occur co-translationally (Tesina et al., 2019). On the other hand, the unprotected 3' end of the mRNA can be targeted by the RNA exosome, an ubiquitous 3' to 5' exonuclease

in eukaryotes (reviewed in Chlebowski et al., 2013; Lykke-Andersen et al., 2009). This pathway requires a set of cytoplasmic cofactors that are essential for cytoplasmic 3' to 5' decay (J. S. J. Anderson and Parker, 1998; van Hoof et al., 2002a). This includes the Ski2-Ski3-Ski8 (Ski238) complex that harbors an ATP-dependent RNA helicase and the adaptor protein Ski7 in yeast or Hbs1L3 in mammals (Y. Araki et al., 2001; Halbach et al., 2013a, 2012a; Kalisiak et al., 2017a; Kowalinski et al., 2016a; van Hoof et al., 2000). Similar to Xrn1, the Ski complex can also associate with ribosomes in yeast, but in this case at the mRNA exit site. This suggests that 3' to 5' decay can also occur co-translationally (Schmidt et al., 2016a). In contrast to the 5' to 3' directionality of Xrn1, the 3' to 5' directionality of the RNA Exosome would lead to a collision with the translating ribosome on the mRNA. However, the Ski complex can extract mRNAs from ribosomes *in vitro* which would prevent collision with the RNA Exosome (Zinoviev et al., 2020a).

2.1.2 mRNA surveillance in eukaryotic cells

During translation, the proteins that are encoded on the mRNA are made by the translation machinery which is centered around the ribosome. In the case of faulty or aberrant mRNAs, the ribosome is slowed down or even stalled which triggers one of several quality control pathways which recognize the defective mRNA and eventually target it for degradation. These processes are summarized as mRNA surveillance. This mode of mRNA degradation differs from canonical mRNA degradation pathways since it does not require deadenylation of the poly(A) tail. Currently, there are three major mRNA surveillance pathways described in eukaryotic cells that are specialized for the recognition of specific mRNA defects: no-go mediated decay (NGD), non-stop mediated decay (NSD) and non-sense mediated decay (NMD) (reviewed in Shoemaker and Green, 2012). While NGD and NSD are believed to share protein factors that are involved in the recognition and solvation of stalled ribosomes, NMD requires a different set of factors.

Nonsense mediated decay (NMD) recognizes mRNAs that contains a premature termination codon (PTC) within the ORF and therefore encodes for C-terminally truncated proteins. This can be caused by mutations or aberrant intron splicing. In addition to the removal of faulty mRNAs, NMD has also been described to target ~10 % of unmodified transcripts in mammalian cells to facilitate cellular response to environmental changes (Kurosaki et al., 2019a). During

canonical NMD the main challenge is to discriminate between a PTC and a canonical stop codon. Currently, two hypothesized models explain how these faulty transcripts are recognized and targeted for degradation. In the first, recognition of a PTC is thought to occur through proximity to an EJC, which is deposited near the exon junction during splicing in the nucleus (Le Hir et al., 2001; Maquat, 2001; Shoemaker and Green, 2012). The proximity of an EJC to the PTC is believed to mark transcripts as faulty since canonical stop codons are typically positioned in the 3' exon. In higher eukaryotes, Upf1 recruits translation termination factors eRF1 and eRF3 and senses the proximity to the EJC coordinated by Upf2 and Upf3. This leads to the recruitment of the SMG1-8-9 complex, as well as other downstream factors like the endonuclease SMG6, which ultimately leads to the recycling of ribosomes and degradation of the mRNA (reviewed in Karousis and Mühlemann, 2019; Shoemaker and Green, 2012). Notably, NMD does not always depend on the presence of an EJC. This is especially true in some organisms such as *S. cerevisiae* which on the one side only have a few intron containing genes, but on the other retain robust clearance of NMD transcripts (Wilusz et al., 2001). In these cases, NMD is thought to be regulated by a long 3'UTR that serves as a binding hub for UPF1 which then leads to a discrimination between NMD and canonical termination.

No-go decay (NGD) targets transcripts that have an inhibitory feature within the body of the mRNA that causes translating ribosomes to stall (Figure 2). This includes stem-loops, pseudoknots, GC-rich sequences, or damaged RNA bases (Shoemaker and Green, 2012). In this scenario, ribosomes get stuck on the message and cannot be recycled by canonical termination factors because of the absence of a stop codon in the ribosomal A-site. This can lead to the formation of a 'collided disome' which is the result of a collision between the stalled ribosome and a following, more 5', ribosome that translates along the message. Recent studies have shown, that collided disomes form unique interfaces that recruits further downstream factors. These include the E3 ligase Hel2 (ZNF598 in mammals) which ubiquitinylates ribosomal proteins and the endonuclease Cue2 (NONU-1 in C. elegans) which cleaves the mRNA between the stalled and the collided ribosome (K. D'Orazio et al., 2019; M. Glover et al., 2020). In addition, ribosomes are removed from the transcript by Hbs1 and Dom34 (Pelota in mammals) which are homologs of the canonical termination factors, in tight coordination with Rli1 (ABCE1 in mammals). These factors have been shown to efficiently split ribosomes that are stalled on a transcript independent of the RNA sequence. Notably, *in vitro*

data has shown that the efficiency for ribosome splitting decreases with the increasing length of the RNA extending from the ribosomal A-site.

Non-stop decay (NSD) recognizes transcripts that lack an in-frame stop codon. This includes truncated mRNAs where the ribosomes translate until the end of the mRNA or transcripts that lack a stop codon but with an intact poly(A) tail (Figure 2) (Frischmeyer et al., 2002; Guydosh and Green, 2017; Shoemaker and Green, 2012; van Hoof et al., 2002a). In the first scenario, the translating ribosome encounters the truncated 3' end, and subsequent ribosomes can collide with the first one, triggering a cellular response similar to that of NGD. In the case of a lack of a stop codon before the poly-A tail, the ribosome continues translating into the poly-A tail. This results in the incorporation of multiple consecutive lysine residues into the growing polypeptide chain. The accumulation of lysine residues eventually stalls the ribosome after approximately six lysines due to interactions between the nascent poly-lysine peptide and the ribosomal exit tunnel (Ito-Harashima et al., 2007). This type of stalling near the 3' end of the mRNA is typically resolved by the Ski238-Ski7-exosome machinery. In this case, the Ski238 complex binds to the ribosome, uses its helicase activity to extract the mRNA, and then delivers the mRNA directly to the cytoplasmic exosome for exonucleolytic degradation in the 3' to 5' direction (Halbach et al., 2013a; Kowalinski et al., 2016a; Mitchell et al., 1997a; Schmidt et al., 2016a; Zinoviev et al., 2020a). Overall, both NGD and NSD pathways exhibit a high degree of redundancy, as they are characterized by ribosome collisions following an initial stalling event (Guydosh and Green, 2017). Furthermore, after the endonucleolytic cleavage between the two ribosomes within the collided disome, the resulting product always resembles an NSD stall on a truncated mRNA, where the ribosome sits at the 3’ end of the transcript with an empty ribosomal A-site.

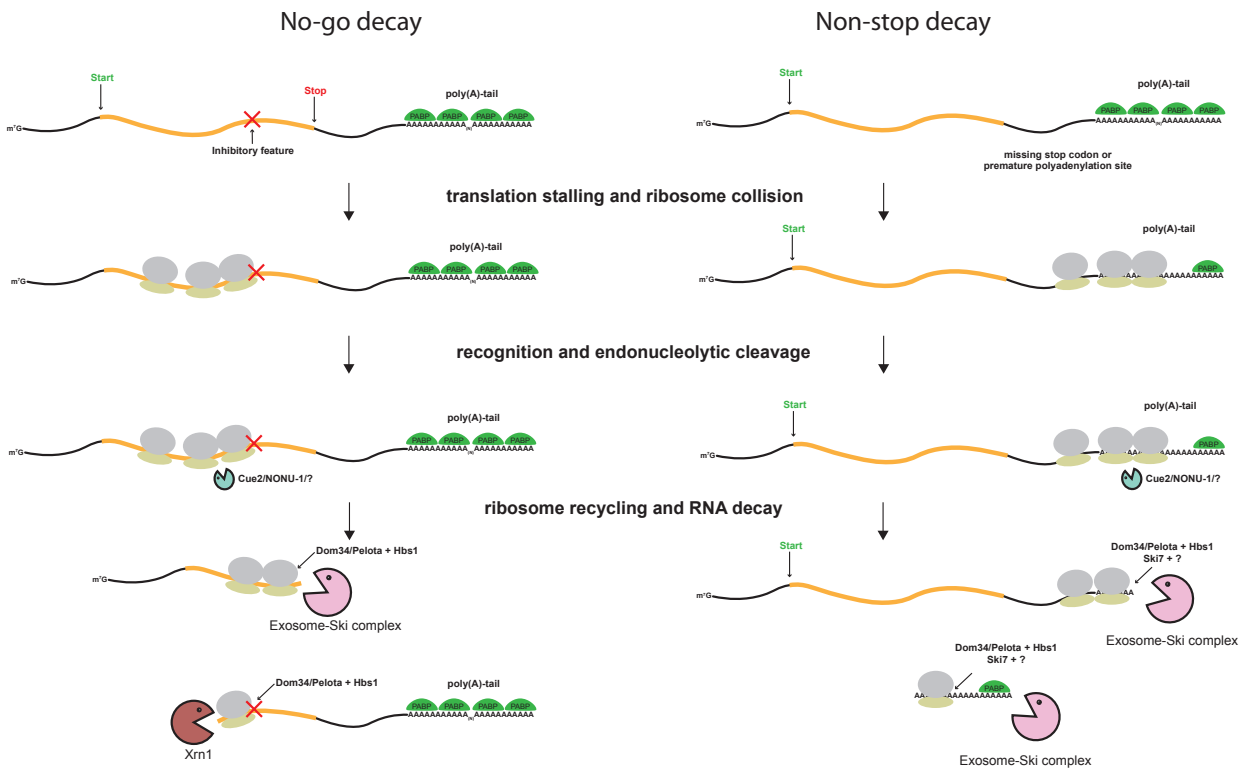

Figure 2: Schematic overview of two mRNA surveillance pathways: No-go decay (Left side) and Non-stop decay (right side). Both pathways are initiated by stalling of ribosomes on the mRNA that leads to a ribosome collision. These collisions are recognized by different factors which eventually lead to the recruitment of an endonuclease that cuts between the first, the stalled ribosome and the second, the collided ribosome. Depending on the nature of the transcript (no-go or non-stop) different 5' and 3' RNA fragments are generated that are either directly targeted for degradation or result in another round of ribosome collision.

2.2 The RNA Exosome

The RNA exosome is a conserved multi-subunit protein complex found in eukaryotic cells. It possesses two distinct enzymatic activities: a processive exonuclease activity, responsible for degrading RNA molecules in a 3' to 5' direction, and an endonuclease activity (Dziembowski et al., 2007a; Liu et al., 2006; Schaeffer et al., 2009). Initially identified as a critical component involved in ribosomal RNA processing in budding yeast (Mitchell et al., 1997a), subsequent studies have revealed its involvement in the degradation and processing of virtually all classes of RNA (Chekanova et al., 2007; R. Gudipati et al., 2012; Pefanis et al., 2014; Schneider and Tollervey, 2013). The RNA exosome is ubiquitously present in both the cytoplasm and nucleus of eukaryotic cells and relies on compartment-specific co-factors to confer substrate specificity. The following discusses the general composition of the eukaryotic exosome, its substrate specificity, as well as its compartment-specific cofactors.

2.2.1 Functions of the eukaryotic RNA exosome

The RNA exosome plays a crucial role in the degradation of various types of RNA molecules. Interestingly, its activity can range from precise trimming of the 3' end during precursor RNA maturation to destruction of an RNA molecule (Figure 3). The processing of RNA molecules by the exosome primarily occurs in the nucleus and is not observed in the cytoplasm. This includes trimming of ribosomal RNA (rRNA) precursors during ribosome biogenesis (C. Allmang et al., 1999; Fromm et al., 2017a; Schuller et al., 2018a), as well as the processing of the 3' end of small nuclear RNAs (snRNAs) and small nucleolar RNAs (snoRNAs) (Kadaba et al., 2006; Kim et al., 2006; Mitchell et al., 1997; Weick et al., 2018; Weick and Lima, 2021). Additionally, besides RNA maturation, the nuclear exosome is involved in the degradation of various transcripts in the nucleus through quality control and surveillance mechanisms. This includes the degradation of snRNAs, snoRNAs, transfer RNAs (tRNAs), and mRNA precursors. Studies in higher eukaryotes have also revealed the involvement of the nuclear exosome in the degradation of enhancer RNAs (eRNAs) and promoter upstream transcripts (PROMPTS) (Lubas et al., 2015, 2011).

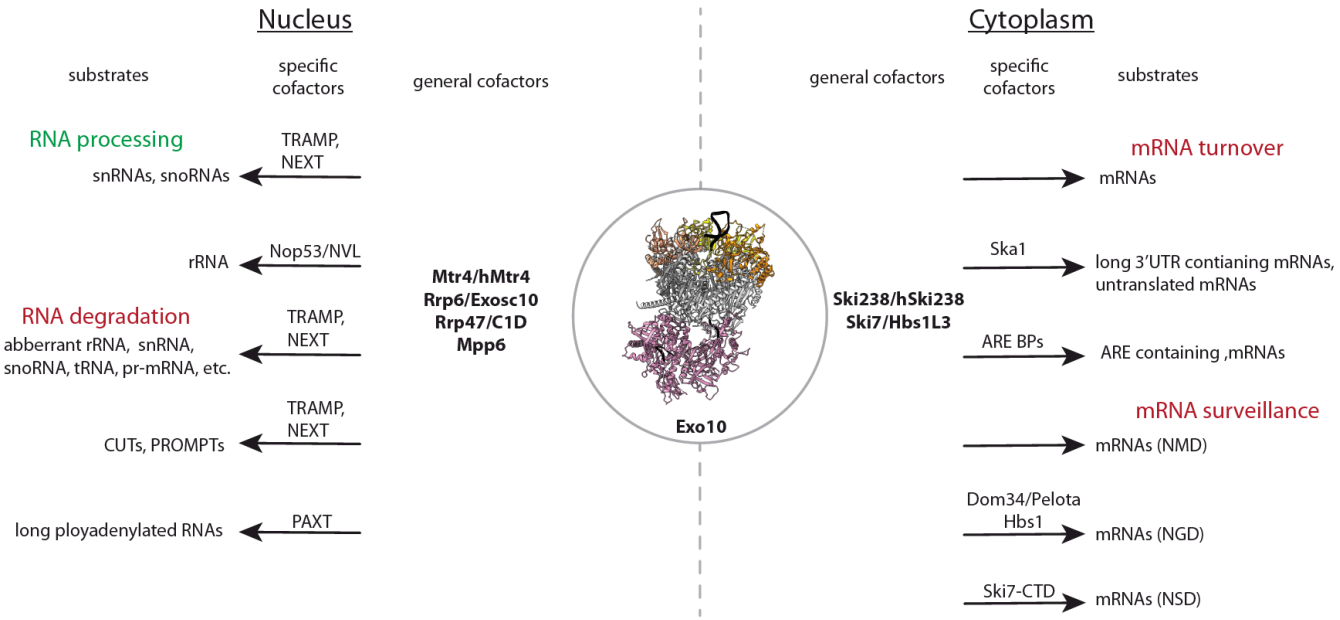

Figure 3: Functions of the RNA exosome in eukaryotic cells. Different degradation and processing pathways feed the RNA substrate into the nuclear exosome (left side) or the cytoplasmic exosome (right side). Specific substrates as well as cofactors and adaptor complexes are indicated (For a more detailed description see Chapter 1.4 and 1.5). Exosome functions are grouped into four categories including constructive (green) RNA processing and destructive (red) nuclear RNA degradation, mRNA surveillance and mRNA turnover (Figure adapted from Lykke-Andersen et al., 2009).

In the cytoplasm, the eukaryotic RNA exosome does not participate in RNA processing but is primarily responsible for the complete degradation of RNA molecules. It serves as an important pathway for general mRNA turnover, ensuring the removal of mRNAs from the cellular pool. Notably, the cytoplasmic 3' to 5' decay machinery is not essential in yeast and has redundancy with the 5' to 3' degradation machinery involving Xrn1 (J. S. J. Anderson and Parker, 1998). Although lacking intrinsic substrate specificity, the cytoplasmic exosome is recruited to AU-rich elements (ARE) in the 3'UTR of specific mRNAs in higher eukaryotes (Chen et al., 2001). Moreover, the exosome has been found to participate in the RNA interference pathway (RNAi) by degrading the 5' fragments generated by the RNAi-induced silencing complex (RISC) (Orban and Izaurralde, 2005). Additionally, apart from mRNA turnover, the exosome contributes to the degradation of mRNA in multiple mRNA surveillance pathways, including NMD, NGD and NSD. In these cases, errors in the mRNA sequence lead to the recruitment of different factors and adaptor complexes, eventually resulting in endonucleolytic cleavage of the mRNA. The resulting 5' fragment (and the 3' fragment in the case of NSD, Figure 2) is subsequently degraded by the cytoplasmic exosome (Doma and Parker, 2006).

2.2.2 Structure and conservation of the RNA exosome

In line with its central function in many aspects of mRNA turnover and degradation, the RNA exosome is structurally conserved in archaea and eukaryotes. Initial structural studies of the archaeal RNA exosome revealed a barrel-like structure composed of the three different subunits Rrp41, Rrp42 and Rrp4 (or Csl4) (Figure 4). The enzymatic subunits Rrp41 and Rrp42 form dimers that assemble a six-subunit barrel consisting of three heterodimers. Both proteins possess phosphorolytic ribonuclease activity and are homologous to the bacterial ribonuclease PH (Büttner et al., 2005; Lorentzen et al., 2007, 2005). On top of the barrel, three copies of the S1/KH RNA-binding domain-containing protein Rrp4 (or Csl4) assemble in a trimeric ring to form the nine subunit archaeal exosome.

Similar to its archaeal counterpart, the yeast RNA exosome is composed of nine subunits that come together to form a barrel-shaped structure with a central pore (Exo9). Within the Exo9, there are two distinct components: a 'cap' consisting of the S1/KH RNA-binding domain-containing proteins Rrp4, Rrp40, and Csl4, and a 'barrel' comprising the RNase PH-like subunits Rrp41, Rrp42, Rrp43, Rrp45, Rrp46, and Mtr3. (Figure 4). While bacterial homologs (PNPase) and archaeal homologs (archaeal Exo9) possess intrinsic phosphorolytic nuclease activity, studies have shown that the subunits of yeast and human Exo9 lack this catalytic activity (Dziembowski et al., 2007a). Consequently, the eukaryotic Exo9 associates with the catalytic subunit Rrp44, which provides the necessary nuclease activity, resulting in the formation of the exosome core (Exo10). Rrp44 is a processive exonuclease that acts in the 3' to 5' direction and relies on Mg^{2+} ions. Furthermore, Rrp44 contains a PIN domain with endonuclease activity (Schaeffer et al., 2009; Schneider et al., 2009). In contrast to yeast, humans possess two compartment-specific homologs of Rrp44: the nuclear DIS3 and the cytoplasmic DIS3L (Tomecki and Dziembowski, 2010). Similar to their yeast counterparts, DIS3 and DIS3L exhibit processive 3' to 5' exonuclease activity, although only DIS3 retains endonuclease activity (reviewed in Zinder and Lima, 2017).

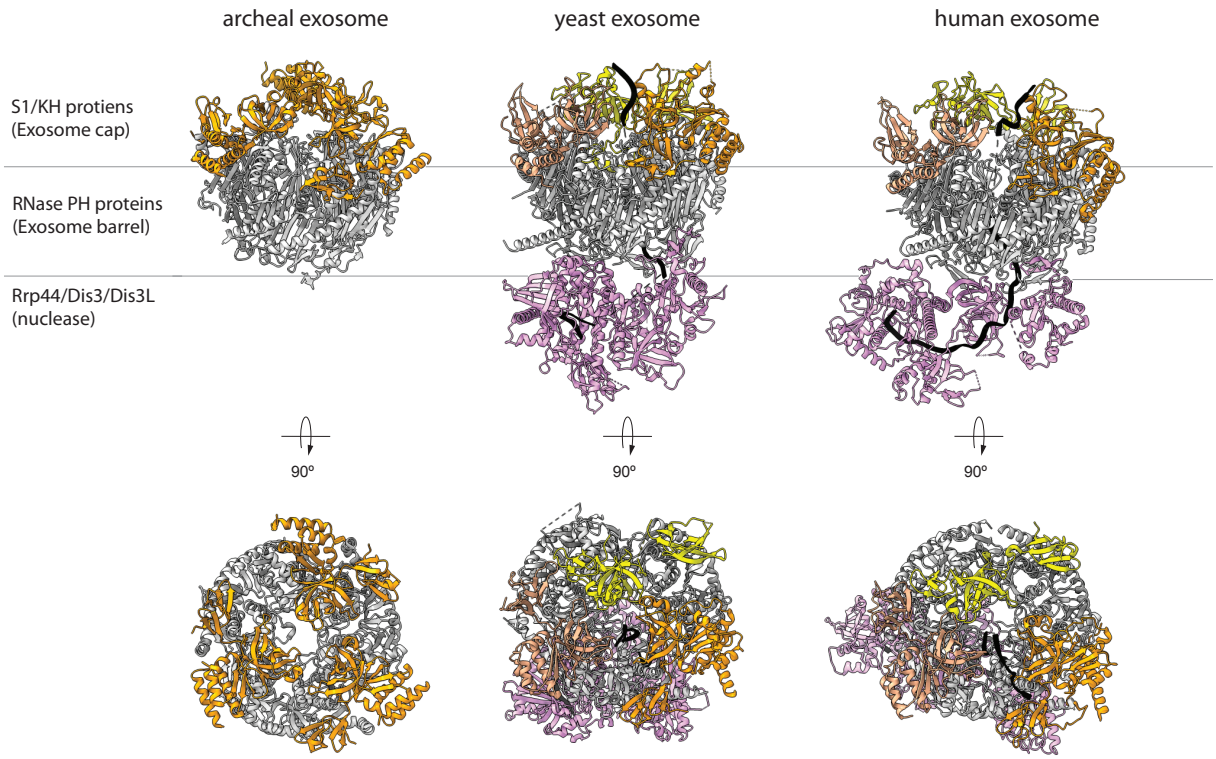

Figure 4: Structural conservation of the archaea (2BA0), yeast (PDB: 5JEA) and human (PDB: 6D6Q) RNA exosome. Individual components including the exosome cap, the RNA (shown in black) channeling exosome barrel and the nuclease domain are indicated on the left. Models are shown in two orientations related by a 90˚ rotation around a horizontal axis. The side view on the complexes shows the structural conservation of the exosome cap and barrel between the species (Upper panels). Yeast and human RNasPH proteins lost catalytic activity and recruit an additional subunit (Rrp44/Dis3/Dis3L) that provides nuclease activity. Top view of the complexes shows the central pore that channels the RNA substrate (lower panels).

2.3 Exosome adaptors complexes are centered around Ski2-like helicases

The multitude of RNA substrates targeted by the eukaryotic RNA exosome requires additional factors that provide substrate specificity. In addition, many substrates have complex secondary and tertiary structures as well as associated protein factors that need to be resolved and/or removed to make the substrates accessible for degradation. The necessary energy to overcome these hurdles is generated by ATP-consuming complexes. These contain compartment-specific Ski2-like helicases that belong to the Superfamily2 (SF2) of helicases (reviewed in Johnson and Jackson, 2013). The nuclear exosome functions together with the helicase Mtr4, while the cytoplasmic exosome requires the Ski238 complex that is centered around the helicase Ski2. The Ski2-like RNA helicases Mtr4 and Ski2 are DExH-box helicases that provide ATP-dependent 3' to 5' RNA unwinding activity. Upon ATP hydrolysis, the helicase can translocate along RNA molecules and unwind double-stranded RNA (Halbach et al., 2012a; M. R. Puno and Lima, 2022; J. Weir et al., 2010). These enzymes share a similar architecture, featuring a 4-domain helicase core composed of two RecombinaseA domains (RecA1 and RecA2), a winged helix domain (WH) and a rachet domain, which is characteristic of Ski2-like helicases (For a more detailed description of the two helicases see Figure 5). The RecA domains contain conserved sequence motifs that are required for nucleotide binding and hydrolysis but also coordinate binding of the RNA substrate. Notably, the domain organization is similar to the DNA helicase Hel308, another member of the Ski2-like helicases. The conservation of the ratchet helix and the winged helix domain, which are proposed to confer unwinding ability in Hel308, suggest that Mtr4 and Ski2 have a similar mode of operation on RNA substrates (Büttner et al., 2007; S. Johnson and Jackson, 2013). In addition to the helicase core, Ski2 and Mtr4 contain another domain that protrudes from the core, the so-called arch or insertion domain (hereafter referred to as arch domain). It consists of a helical stalk followed by a globular beta-barrel domain that possesses RNA binding properties. It is positioned close to the RNA entry side and can adopt different conformations indicating a certain degree of flexibility with respect to the helicase core. The arch domains of Ski2 and Mtr4 are not essential but have been shown to affect helicase activity pointing towards a regulatory function in exosomal RNA degradation (Halbach et al., 2012a; J. Weir et al., 2010). In addition, both Ski2 and Mtr4 have an unstructured N-terminal domain which is involved in interactions with additional cofactors that promote the recruitment of the helicase to the exosome.

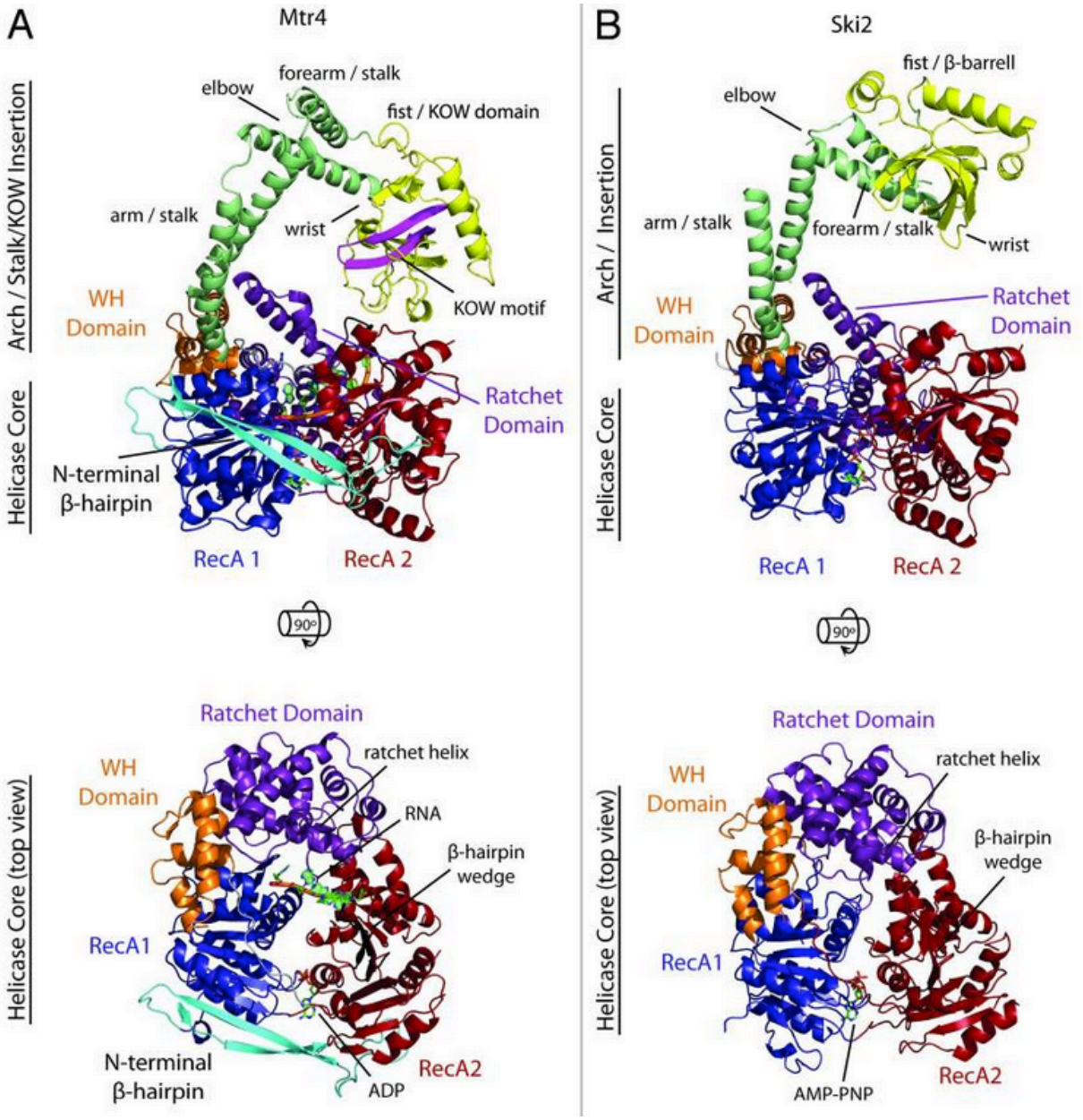

Figure 5: Comparison of crystal structures of Mtr4 (PDB: 2XGJ) and Ski2 (PDB: 4A4Z). Structures are shown in two orientations related by a 90˚ rotation around the horizontal axis. Individual domains are highlighted by different colors and labeled accordingly. In the top view (bottom panels) the arch domain has been removed for better visualization. **A**: Side (upper panel) and top (lower panel) view of Mtr4 bound to RNA and ADP; **B**: Side (upper panel) and top (lower panel) view of Ski2 bound to AMP-PNP. (This Figure was taken from Johnson and Jackson, 2013).

2.4 The nuclear RNA exosome

In the nucleus, the RNA exosome associates with a set of additional factors that are evolutionarily conserved (Makino et al., 2015). The exoribonuclease Rrp6 (EXOSC10 in humans), Rrp47 (C1D in humans), the small protein Mpp6 and the RNA helicase Mtr4. Deletions or mutations of these factors *in vivo* cause RNA degradation effects underpinning their importance in substrate recognition. Rrp6 is a distributive ribonuclease that belongs to the RNase D family (Zuo and Deutscher, 2001). It is a constitutive part of the nuclear RNA exosome and it binds at the RNA entry side of the barrel with high affinity. Rrp6 consists of an N-terminal PMC2NT domain that is followed by the catalytic RNAse D core and two helicases RNase D c-terminal domains (HRDCs). In contrast to Rrp44, Rrp6 does not possess helicase activity and therefore cannot degrade structured RNA sequences. While the majority of Rrp6 is present in the nucleus, studies have suggested that it is also involved in exosome-independent functions in the cytoplasm (Tomecki and Dziembowski, 2010). In addition to its catalytic activity, Rrp6 also interacts with Rrp47 via its PMC2NT domain forming a recruitment platform for Mtr4 (Schuch et al., 2014a). In this interaction, the unstructured N-terminal domain of Mtr4 forms an intertwined interface, that is crucial for the recruitment of Mtr4 to the nuclear exosome. In contrast, Mpp6 is directly recruited to the exosome cap through direct interactions with Rrp40. While it is not required for the association of the nuclear exosome with Mtr4, biochemical and structural studies have shown that it directly interacts with the helicase core of Mtr4 anchoring the helicase near the exosome (Falk et al., 2017a; Gerlach et al., 2018a; Weick et al., 2018a). In addition, it enhances RNA channeling ability of Mtr4 to the nuclear exosome. Due to extensive investigation, multiple structures of Mtr4 bound to the exosome in complex with different substrates, from both yeast and human, are available. These include yeast Mtr4-Rrp6/47-Mpp6-Exo10 bound to 60S pre-ribosome substrate (Schuller et al., 2018a) and human Mtr4-EXOSC10/C1D-Mpp6-Exo10 bound to RNA-DNA hybrid substrate (Weick et al., 2018) (Figure 6). These structures show that the helicase directly binds to the exosome cap and threads the substrate through the exosome barrel until it reaches the nuclease Rrp44 for degradation. The binding sites on the exosome are similar between yeast and human proving a conserved mode of recruitment. Notably, to obtain these structural snapshots, the catalytic activity of the nucleases and/or the chemical properties of the substrate had to be modified. Therefore, these structures reflect a trapped conformation that is possibly transient and low abundant in cells.

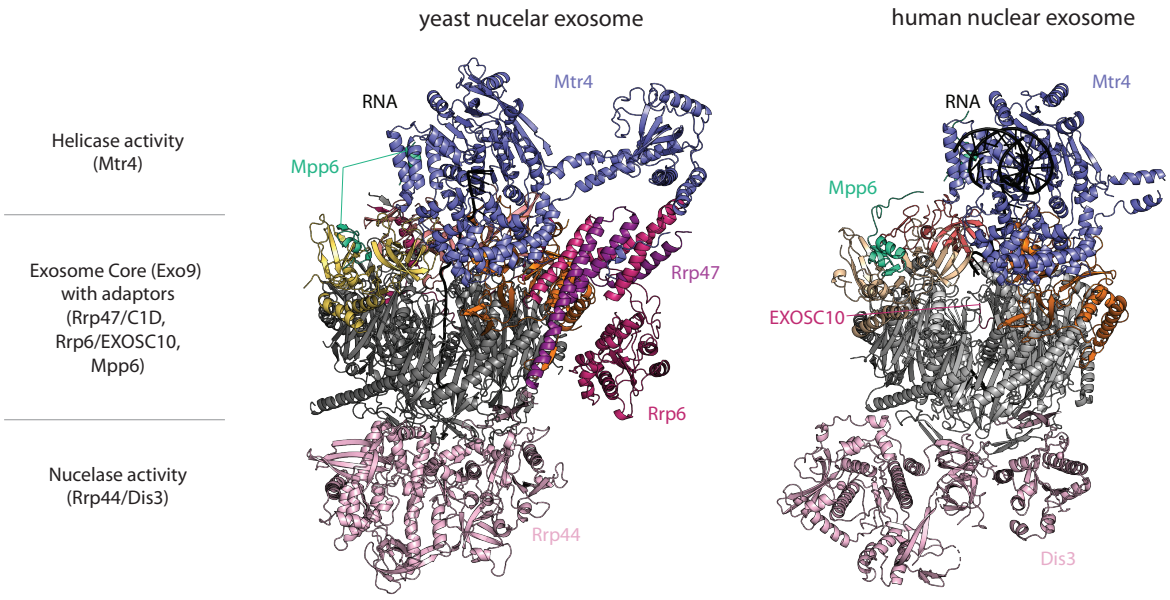

Figure 6: Comparison of yeast (PDB: 6FSZ) and human (PDB: 6D6Q) nuclear exosome structures in complex with Mtr4 and RNA showing the conservation of Mtr4 binding between the species. Individual components including helicase activity, the RNA shielding exosome core and the nuclease activity are indicated on the left. Core subunits are combined as Exo9. Nuclear-specific adaptor proteins are highlighted with labels. In the human structure, the Rrp47 homolog C1D is present in the sample, but not observed in the structure.

Mtr4 has a multitude of other interaction partners to form different complexes that further provide substrate specificity. One of these complexes is the Trf4-Air2-Mtr4 polyadenylation complex (TRAMP). Air2 is a Zinck finger protein implicated in substrate recruitment while Trf4 is a polymerase that adds short polyA stretches to substrate RNA (Schmidt and Butler, 2013b; Zinder and Lima, 2017a). The short polyA triggers unwinding of the substrate by Mtr4 making it accessible for degradation by the exosome. Notably, Air2 and Trf4 can be substituted by the two paralogs Air1 and Trf4. TRAMP has been implicated to target snRNAs, snoRNAs as well as aberrant tRNAs (Figure 3). In addition, it can select for aberrant RNA polymerase II products through a Trf4-mediated interaction with the Nrd1-Nab3-Sen1 complex (Gudipati et al., 2008). In higher eukaryotes including humans, a TRAMP-like complex has also been described consisting of Mtr4 the poly(A) polymerase PAPD5 and the zinc finger protein ZCCHC7. This complex however is poorly characterized and its biochemical properties as well as its structure needs to be further investigated in the future. In humans, a more diverse set of Mtr4-containing complexes has evolved to govern substrate recognition. The most studied example is the nuclear exosome targeting complex (NEXT), only found in metazoan. It is involved in the

recognition of snRNAs, snoRNAs and PROMPTS and targets them for degradation by the exosome. NEXT consist of the RNA-binding protein RBM7 which is linked to Mtr4 by the zinc finger protein ZCCHC8 (Gerlach et al., 2022b; Lubas et al., 2011; R. Puno and Lima, 2022; Schmid and Jensen, 2019a). It is involved in the recognition of PROMPTS and non-coding RNAs like eRNAs, but it also mediates the trimming of 3' extensions in snRNAs, snoRNAs and histone-encoding RNAs (Lubas et al., 2015, 2011; Schmid and Jensen, 2019b). In addition to providing substrate specificity, RBM7 and ZCCHC8 are also involved in the regulation of the helicase activity of Mtr4 (R. Puno and Lima, 2022). More recently, the polyA exosome targeting complex has been described in humans, consisting of Mtr4 and the zinc finger protein ZFC3H1. This complex is believed to target polyadenylated RNAs in the nucleus through direct interaction with the nuclear polyA binding protein (PABPN1) (Beaulieu et al., 2012; Bresson and Conrad, 2013; Meola et al., 2016). The PAXT complex seems to target pre-mRNAs in the nucleus and competes with the export machinery (Meola and Jensen, 2017). However, the molecular mechanisms of how this complex is regulated require further investigation.

2.5 The cytoplasmic RNA exosome

In the cytoplasm, the RNA exosome has two distinct cofactors that are essential for exosomal RNA degradation. First, the Ski238 complex, which is centered around the Mtr4 paralog Ski2 and the Ski7 protein (or HBS1L3 in humans).

2.5.1 The Ski2-Ski3-Ski8 complex

The Ski (superkiller) genes were initially identified through genetic screening in yeast cells infected with a double-stranded RNA virus (Toh-E et al., 1978). Mutations in Ski genes caused the overexpression and secretion of a killer toxin which is lethal to cells not carrying the virus, further described as the superkiller phenotype. Continuous studies over the last decades revealed a set of seven Ski genes which are all part of the cytoplasmic RNA decay machinery including Ski1(Xrn1), Ski2, Ski3, Ski4(Csl4), Ski6 (Rrp41), Ski7 and Ski8 (Benard et al., 1998, 1999; Johnson and Kolodner, 1995a; Larimer and Stevens, 1990a; Matsumoto et al., 1993; Rhee et al., 1989a; van Hoof et al., 2000; Widner and Wickner, 1993). Among the Ski proteins, Ski2, Ski3, and Ski8 combine to form the Ski complex (Ski238) (Figure 7). This heterotetrameric complex exhibits a 1:1:2 stoichiometry and is evolutionarily conserved. In yeast and higher metazoans, Ski238 serves as an essential component in cytoplasmic mRNA turnover and

mRNA surveillance pathways. The yeast Ski238 complex is well characterized on the biochemical and structural level (Halbach et al., 2013a, 2012a). The complex is centered around the Ski2 helicase which provides ATP-dependent RNA helicase activity and is required for exosomal RNA degradation. Besides its helicase core and the Arch domain, Ski2 has a 235 amino acid N-terminal region (Ski2N) that is mainly unstructured. It forms extensive interactions with Ski3, a 168 kDa protein that provides the scaffold of the complex. Ski3 consists of tetratricopeptide repeats (TPR) which form multiple superhelical turns that wrap around Ski2-N and thereby anchor the helicase core (Ski2-Cat) on the complex. Ski3 can be divided into a C-terminal arm (Ski3-C) that comprises binding sites for Ski2-N and a flexible N-terminal arm (Ski3-N) that forms no further contacts within the complex. The superhelical turns of Ski-C form a convex surface that provides the major binding site for Ski2-Cat. In addition to Ski3, the helicase core contacts parts of Ski2-N, which contacts the putative RNA exit site via a conserved RG-loop (Halbach et al., 2013a). Finally, there are two copies of Ski8, a protein with a molecular weight of 44 kDa, which is composed of seven WD40 repeats arranged in a beta-propeller fold. These two copies interact with both Ski3 and Ski2 and further stabilize Ski2-Cat on the complex. One copy is positioned towards the C-terminal end of Ski3 (Ski8-OUT) while the other copy forms more extensive interactions towards the middle of the complex (Ski8-IN). Notably, Ski8 is also involved in meiotic DNA recombination and forms a complex with Spo11, Rec102 and Rec104 (Arora et al., 2004; Bouuaert et al., 2021). This promotes the idea that Ski8 serves as a platform to promote protein-protein interactions. The biochemical studies in yeast have shown that the helicase activity of Ski2 is regulated by an autoinhibitory mechanism between Ski3-N and Ski2-Arch (Halbach et al., 2013a). While it was suggested that the two domains interact with each other to control substrate access to the helicase core, a direct interaction between the two has not been observed. More recently, cryoEM single particle analysis (SPA) of TAP-tagged Ski238 has revealed a direct interaction of the complex with translating ribosomes. Ski238 forms extensive interactions with the small ribosomal subunit (40S) positioning the helicase near the mRNA exit site allowing the mRNA to bind within Ski2-Cat (Schmidt et al., 2016a). Interestingly, this study also revealed that Ski238 favors short 3’ mRNA overhangs on the ribosome consistent with results from *in vitro* helicase assays (Halbach et al., 2013a).

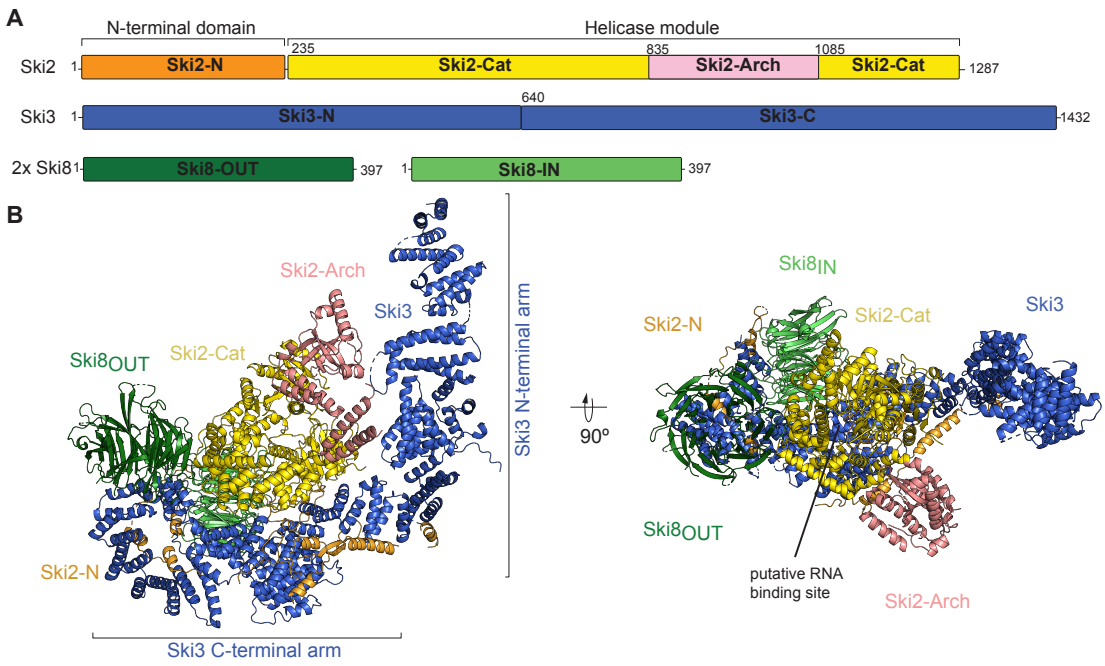

Figure 7: Domain organization and structure of the *S. cerevisiae* Ski238 complex **A**: domain organization of the individual subunits of *S. cerevisiae* Ski238. The N-terminal region of Ski2 (Ski2-N) is shown in orange followed by the helicase core (Ski2-Cat). Within Ski2-Cat, the Ski2-Arch domain is indicated in salmon. Ski3 is divided into its N-terminal (Ski3-N) and C-terminal (Ski3-C) arms, both shown in blue. The two copies of Ski8 (Ski8-OUT and Ski8-IN) are shown in green. **B**: Crystal structure of the *S. cerevisiae* Ski238 complex shown in two different orientations related by a 90˚ rotation around a horizontal axis. Notably, the complex could only be crystallized upon deletion of Ski2-Arch. The structure shown here is a superposition of Ski2-Arch (from PDB: 4A4Z) on Ski2ΔArch38 (PDB:4BUJ). Ski3-N and Ski3-C are indicated with brackets. All labels are colored according to (A). (This Figure was adapted from Halbach et al., 2013).

In higher eukaryotes, including humans, there are homologs of all the components of the Ski238 complex. These homologs include TTC37 (Ski3), WDR61 (Ski8), and Ski2VL (Ski2). Mutations in these genes have been associated with trichohepatoenteric syndrome (THES), a rare disease characterized by diarrhea and immune defects in children (Fabre et al., 2014). This indicates that the Ski238 complex plays an important role in human biology. Based on sequence similarity, it is believed that the human Ski proteins form a complex similar to their yeast counterparts. However, unlike in yeast, human Ski2 primarily participates in exosome-mediated mRNA degradation during mRNA surveillance, while general mRNA turnover relies heavily on the 5' to 3' decay pathways involving Xrn1 (A. Tuck et al., 2020). Recent studies have also demonstrated that human Ski238 can extract mRNA bound to 80S ribosomes *in vitro*, suggesting a direct interaction between human Ski238 and translating ribosomes.

Nevertheless, more research is needed to explore the architecture and biochemical properties of the human Ski238 complex.

2.5.2 The adaptor protein Ski7 (yeast) and Hbs1L3 (human)

In yeast, the second cytoplasmic cofactor, Ski7, plays a crucial role in mediating the interaction between the RNA exosome and the Ski238 complex (Y. Araki et al., 2001; Halbach et al., 2013a). Ski7 is composed of two domains: an N-terminal domain (Ski7-N), essential for all known functions of the cytoplasmic exosome, and a C-terminal domain (Ski7-C), critical for mRNA surveillance in yeast (van Hoof et al., 2002a) (Figure 8). Ski7-N comprises 265 amino acids and is predicted to lack significant tertiary structures. Biochemical studies have revealed that Ski7-N serves as a binding site for both the exosome and the Ski238 complex, acting as a bridging factor between the helicase and the nuclease-containing complex. It is responsible for facilitating the binding of Ski238 to the exosome and facilitating the handover of RNA substrates (Halbach et al., 2013a). The crystal structure of Ski7-N in complex with the exosome from *S. cerevisiae* has demonstrated extensive interactions with Exo10 at the RNA entry site. Surprisingly, Ski7-N occupies a similar interaction surface as Rrp6 does in the case of the nuclear exosome, despite lacking obvious sequence conservation. This mutually exclusive interaction may physically separate the cytoplasmic and nuclear exosome populations within cells. The strong affinity of this interaction (approximately 5 nM) and the co-purification of Ski7 with endogenous exosome subunits suggest that Ski7 is a constitutively associated component of the cytoplasmic exosome (Dziembowski et al., 2007a; Kowalinski et al., 2016a; van Hoof et al., 2002a). The C-terminal domain of Ski7 (Ski7-C) exhibits structural similarities to translational GTPases such as eRF3 and Hbs1, which are involved in translation termination and ribosome recycling. These structural similarities suggest that Ski7-C may directly interact with 80S ribosomes to remove them from defective mRNA during mRNA surveillance. However, unlike its counterparts, Ski7-C cannot hydrolyze GTP, and it remains unclear whether it is involved in the dissociation of 80S ribosomes into individual subunits.

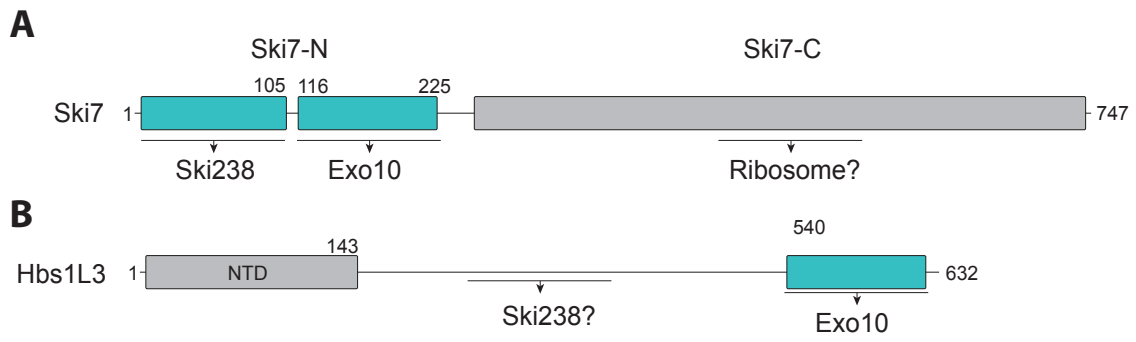

Figure 8: Domain organization of *S. cerevisiae* Ski7 and its human counterpart the Hbs1 splicing isoform 3 (Hbs1L3). **A**: Ski7 is divided in a N-terminal domain (Ski7-N) and a C-terminal domain (Ski7-C). Ski7-N comprises binding sites for the Ski238 complex and the exosome, while Ski7-C is thought to interact with the ribosome during mRNA surveillance.; **B**: Hbs1L3 consists of an N-terminal domain which is shared with other Hbs1 splicing variants. The long C-terminal domain remains mainly uncharacterized, except for a short stretch that interacts with the exosome. The rest of the C-terminal domain is implicated to provide a Ski238 binding site. The known boundaries of the individual domains are highlighted by numbers.

Computational analysis of the Ski7 sequence involved in exosome binding, along with co-immunoprecipitation-mass spectrometry analysis of human exosome complexes, has led to the discovery of a Ski7-like factor in human cells. This factor is a splicing isoform of the Hbs1 protein called Hbs1L3 (Kalisiak et al., 2017a; Kowalinski et al., 2016a). While the N-terminus of Hbs1L3 (residues 1-143) is identical to other splicing variants, it lacks a translational GTPase domain and instead possesses a long C-terminal domain (residues 144-632) (Kowalinski et al., 2016a). Interestingly, a portion of this C-terminal domain (residues 540-632) exhibits sequence conservation with the exosome binding site of Ski7. Pull-down experiments have provided evidence of direct interaction between this region of Hbs1L3 and the human exosome. These findings suggest that Hbs1L3 serves as a link between the cytoplasmic exosome and the Ski238 complex, akin to the role of Ski7 in yeast. However, it remains unclear whether Hbs1L3 can bind to the Ski complex, necessitating further investigation in future studies.

2.5.3 The cytoplasmic Ski238-Ski7-Exo10 assembly:

The Ski238 complex binds and unwinds RNA substrates to make them accessible for the RNA exosome for degradation. RNase protection experiments have shown, that a continuous channel between the two subcomplexes exists *in vitro* spanning from the helicase core of Ski2

through the exosome where it reaches the active site of Rrp44. The formation of this assembly also requires the adaptor protein Ski7 to mediate the interaction of the two subcomplexes. Interestingly, the formation of this channel depends on the activity of the Ski2 helicase which is modulated by two domains within the Ski238 complex (Ski3-N and Ski2-Arch). Given the similarities between Ski2 and Mtr4 in the nucleus, it is postulated that the Ski238 complex can assemble on top of the exosome directly threading the RNA towards the nuclease domain (Figure 8). However, since Ski2 is stably bound within the Ski238 complex, the molecular mechanism of Ski238 recruitment to the exosome has to differ from its nuclear counterpart.

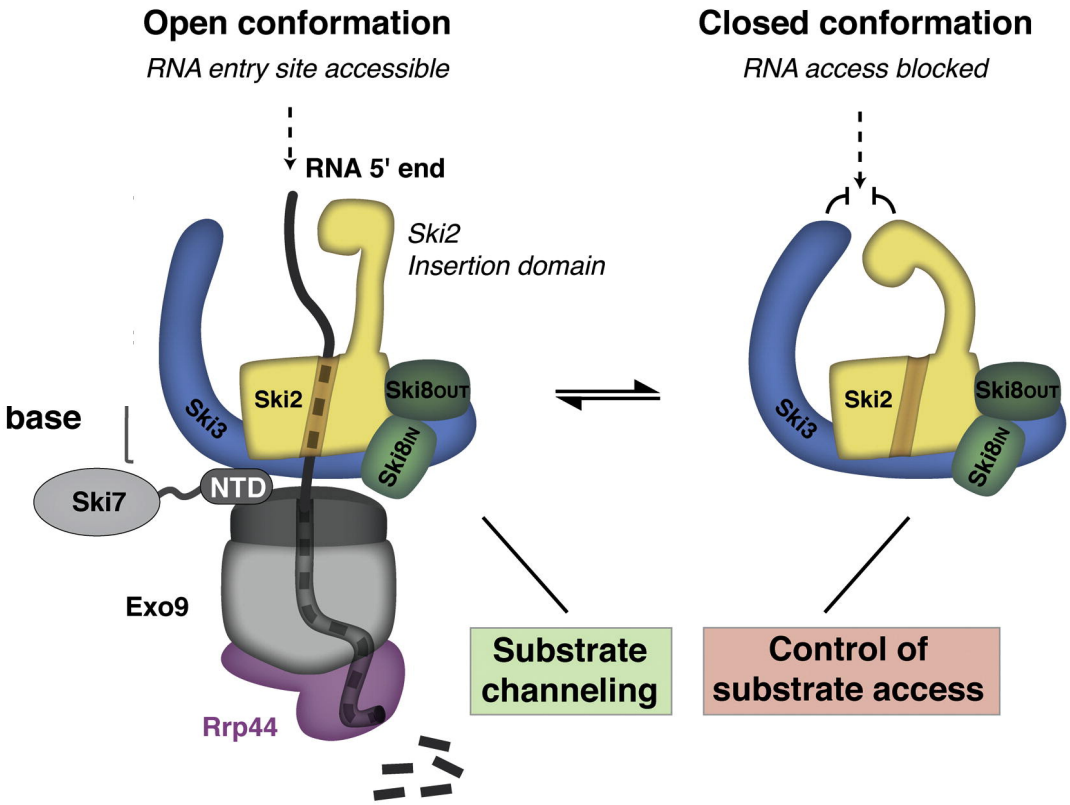

Figure 9: Proposed model for substrate channeling in the cytoplasmic Ski238-Ski7-exosome assembly in yeast. The access of the RNA substrate is regulated by two auxiliary domains Ski2-Arch and Ski3-N. In the inactive state, these two domains prevent the activation of the helicase, possibly through a direct interaction that blocks RNA access. Upon activation, RNA is threaded from the helicase core through the exosome barrel to Rrp44 for degradation. The N-terminal domain of Ski7 mediates the interaction between the two subcomplexes. (This Figure was taken from Halbach et al., 2013).

2.5.4 The Ska1 protein in yeast

Recently a new Ski238-associated factor (Ska1) has been characterized in yeast (Zhang et al., 2019). Affinity purifications followed by mass spectrometry experiments suggest that Ska1 can directly interact with a subpopulation of available Ski238 complex in a given cell. Moreover, the study indicates that Ska1 plays a role in the degradation of various mRNA molecules, including those with long 3' untranslated regions (UTRs) and poorly translated RNAs, among others. Interestingly, Ska1 is not essential for the degradation of non-stop mRNAs, suggesting a more specialized role in recruiting mRNAs that are not associated with ribosomes. According to the proposed model, Ska1 assists the cytoplasmic RNA exosome during RNA degradation in the absence of ribosomes, making it a potential novel cofactor for the cytoplasmic exosome. While homologs of Ska1 have not yet been described in higher eukaryotes, its discovery provides an excellent starting point for further biochemical and structural investigations in yeast.

2.6 Scope of this work

The eukaryotic RNA exosome has been extensively studied in recent decades, providing a comprehensive understanding of how this machinery degrades RNA molecules. While the nuclear cofactors associated with the exosome have been well-characterized both structurally and biochemically, our understanding of how the cytoplasmic RNA exosome interacts with the Ski238 complex during RNA degradation remains limited. Although the crystal structure of the yeast Ski238 complex has offered insights into its architecture, the mechanisms underlying the interaction between the Ski238 complex and Ski7 during recruitment to the exosome remain largely unknown. Moreover, we have only limited knowledge of how the RNA substrate is transferred from the Ski2 helicase to the exosome during degradation. The regulation of this process appears to involve auxiliary domains (Ski2-Arch and Ski3-N) that modulate helicase activity, but it is unclear whether the Ski238 complex and the exosome form a stable assembly during substrate handover, as observed in the nuclear exosome. Additionally, the biochemical and structural properties of the human Ski238 complex are largely unexplored.

This thesis aims to elucidate the architecture and biochemical properties of the human Ski238 complex to confirm its evolutionarily conserved role in exosome-mediated RNA degradation. It is of great interest to determine whether the complex architecture and the regulation of its helicase activity are analogous to those in the yeast system. For the yeast system, this thesis aims to deepen our understanding of the interaction between the Ski238 complex and Ski7. A detailed characterization of this interaction could provide insights into how helicase activity is coordinated with recruitment to the exosome. Additionally, further investigation into the active Ski238-Ski7-Exo10 assembly is crucial, as it remains unclear whether these two subcomplexes form a stable assembly or only transiently interact with each other. Moreover, this thesis explores the potential role of a third cytoplasmic exosome cofactor, Ska1. Considering its involvement in regulating the substrate specificity of the Ski238 complex and its proposed direct association with the complex, Ska1 holds promise as a target for structural studies.

By addressing these research objectives, the thesis aims to advance our understanding of the complex interplay between the cytoplasmic RNA exosome, the Ski238 complex, and associated cofactors, shedding light on the mechanisms of RNA degradation and substrate specificity.

3. Materials and Methods

This chapter includes unpublished protocols for the experiments that are presented in 4.4.

3.1.Purification of full length Ska1 from E.coli

S. cerevisiae Ska1 (Uniprot: P36103) was cloned into a pBR322 vector (EMBL Heidelberg core facility) and recombinantly expressed in BL21(DE)Gold pLysS E. coli (Thermo Fischer Scientific) cells and grown in TB media at 37 ˚C up to OD600 = 1.5 under antibiotic selection. Ska1 was expressed with an N-terminal 6xHis-thioredoxin tag followed by a 3C protease cleavage site and a C-terminal A-G-S-StrepII tag. Expression was induced with 0.1 mM IPTG for approximately 18 hours at 18 ˚C. All of the following harvesting and purification steps were performed on ice or at 4˚C. Bacteria were harvested by centrifugation at 8,500 g and resuspended in 300 ml of 20 mM Tris-HCl pH 8, 200 mM NaCl, 5% (v/v) glycerol, 20 mM imidazole and 1 mM DTT supplemented with 0.1 mM AEBSF protease inhibitor, 0.001 mg/ml DNase, and 0.01 mg/ml lysozyme. Cells were disrupted by a VS-70T sonicator (Bandelin Sonopuls) and lysate was cleared by centrifugation at 75,600 g for 30 min. The filtered lysate was loaded onto two sequential 5 ml HisTrap HP columns (Cytiva). Columns were washed with 10 column volumes (CV) of 20 mM Tris-HCl pH 8, 1000 mM KCl, 5% (v/v) glycerol, 20 mM imidazole and 1 mM DTT. His-tagged proteins were eluted with 20 mM Tris-HCl pH 8, 200 mM NaCl, 5% (v/v) glycerol, 1 mM DTT and 300 mM imidazole on an ÄKTA Prime plus. Peak fractions were pooled and loaded onto two consecutive 5 ml StrepTrap HP columns (Cytiva) followed by washing with 10 CV of 20 mM Tris-HCl pH 8, 200 mM NaCl, and 5% (v/v) glycerol. Strep-tagged proteins were directly eluted into a 5 ml HiTrap Heparin HP column (Cytiva) with 2 CV of 20 mM Tris-HCl pH 8, 200 mM NaCl, 5% (v/v) glycerol, and 2.5 mM Desthiobiotin (DTB) followed by 5 CV of the same buffer, except without DTB. The heparin column was washed with 10 CV of 20 mM Tris-HCl pH 8, 200 mM NaCl, 1% (v/v) glycerol and 1 mM DTT and proteins were eluted by buffer with increasing NaCl gradient (20 mM Tris-HCl pH 8, 1000 mM NaCl, 1% (v/v) glycerol, 1 mM DTT) (up to 100%). Peak fractions were pooled and dialyzed against 20 mM Tris-HCl pH 8, 200 mM NaCl, 1% (v/v) glycerol, and 1 mM DTT overnight at 4˚C. Protein concentration was determined and the samples were mixed with 10% (v/v) glycerol and flash-frozen for storage at -80 ˚C until further

3.2 Purification of Ski238 from Hi5 insect cells and Ski7 from E.coli

Ski238 was purified according to published protocols. A detailed description is presented in chapter 4.4. Ski2-Arch, Ski3-N and Ski7-N were purified after expression in BL21(DE)Gold pLysS *E. coli* according to the previously described protocol (Halbach et al., 2013a, 2012a; Kowalinski et al., 2016a).

3.3 Analytical size exclusion chromatography of Ska1 together with the Ski238 complex

250 pmol of Ski238 was mixed with 100 pmol of HIS-Trx-Ska1-Strep in 20 mM Tris-HCl pH 8, 150 mM NaCl, 2% (v/v) glycerol, and 2 mM DTT and the final volume was adjusted to 250 µl. Analogous, a sample without Ska1 was prepared. Samples were incubated at 4˚ C for 20 min and then concentrated to ~ 50 µl using an Amicon Ultra MWCO 10 kDa. Before injection, samples were centrifuged for 15 min at 16000 g. Size exclusion chromatography was performed on an ÄKTA Micro equipped with a Superose 6 increase 3.2/300 column. Samples were run at 0.025 ml/min and fractionated. The peak fractions were then analyzed via SDS PAGE on 12 % acrylamide gels.

3.4 Pulldown experiments of Ska1 with individual Ski238 complexes

EGFP-pulldowns were performed as previously described (Kowalinski et al., 2016a). In brief, we used 5µg of eGFP-Ski7-N-Strep, 1.1x molar excess of Ski238 and different concentrations of Ska1 (0, 0.5, 1, 2, 4, 6 and 8x molar excess). Proteins were mixed together in Tris-HCl pH 7.5, 150 mM NaCl, 2 mM $MgCl_2$, 2% (v/v) glycerol, 2 mM DTT and 0.05% (v/v) NP40 and adjusted to a final volume of 50µl. 10 µl were taken for the input sample used for SDS PAGE analysis. Then, 20 µl of equilibrated beads and 190 µl of buffer were added. Samples were incubated at 4˚ C for 30 min and then washed 3x with 300 µl buffer. At last, the buffer was completely removed and proteins were eluted with 15 µl of 1x SDS loading buffer.

For Strep-pulldowns, we used M270-Dynabeads coupled to Strep-Tactin (IBA #2-1204-005). In brief, 5 µg of Strep tagged Ska1 was mixed with 1.5x molar excess of the respective proteins (Ski2-Arch, Ski3-N, Ski238, Ski2ΔArch38 and Ski23ΔN8) in Tris-HCl pH 7.5, 150 mM NaCl, 2 mM MgCl2, 2% (v/v) glycerol, and 0.1% (v/v) NP40 and the final volume was adjusted to 50 µl. From here, pulldowns were performed analogously to the eGFP pulldowns described above. Wash steps were done using a magnetic rack.

4. Results

4.1 Publication 1:

The human SKI complex regulates channeling of ribosome-bound RNA to the exosome via an intrinsic gatekeeping mechanism

Alexander Koegel, Achim Keidel, Fabien Bonneau, Ingmar Schaefer and Elena Conti

This research article was published in Molecular Cell, Volume 82, Issue 4, pages 756-769 on the 17th of February 2022. It provides first insights into the architecture and biochemical properties of the human Ski238 complex. The study reveals that the Ski238 complex can adopt different conformations that are linked to the activity of the RNA helicase Ski2. This concept could be observed in yeast and human complexes suggesting a general mode of operation that provides a new binding interface on Ski2 for exosome recruitment. Furthermore, the study reveals a direct interaction of human Ski238 with 80S ribosomes that present a free 3' mRNA overhang similar to previous studies in yeast.

Molecular Cell

Article

The human SKI complex regulates channeling of ribosome-bound RNA to the exosome via an intrinsic gatekeeping mechanism

Graphical abstract

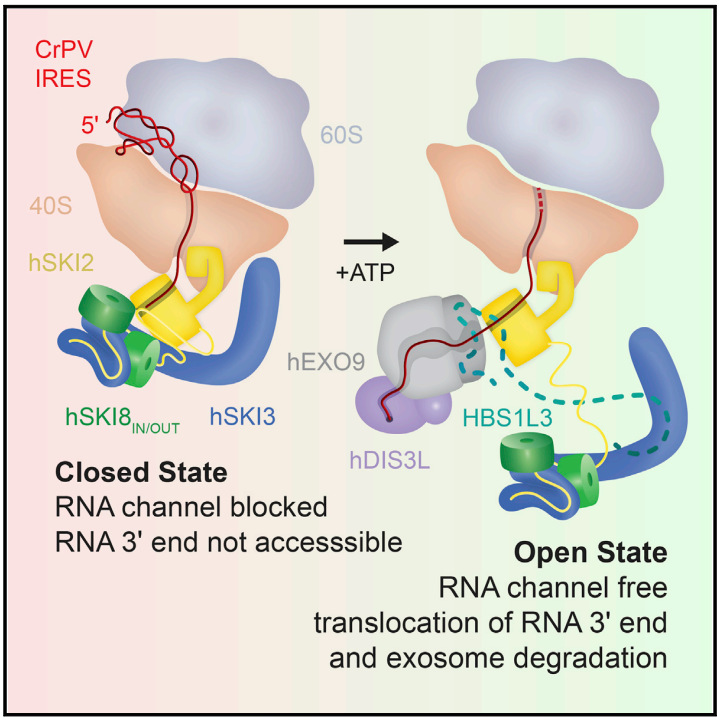

Highlights

- hSKI has closed and open states connected to different helicase conformations
- The intrinsic closed state traps the RNA 3′ end and blocks the RNA exit path
- ATP induces the open state of hSKI, allowing 80S ribosome-bound RNA extraction
- The hSKI open state primes hSKI2 for channeling RNA to the cytosolic exosome

Authors

Alexander Kögel, Achim Keidel, Fabien Bonneau, Ingmar B. Schäfer, Elena Conti

Correspondence

ischaefe@biochem.mpg.de (I.B.S.), conti@biochem.mpg.de (E.C.)

In brief

Kögel et al. show that the human SKI complex adopts distinct conformational states to recognize and extract ribosome-bound RNA in a nucleotide-dependent manner. These functional states regulate access of the RNA 3′ end to the cytoplasmic human exosome for co-translational degradation.

Kögel et al., 2022, Molecular Cell *82*, 756–769
February 17, 2022 © 2022 The Author(s). Published by Elsevier Inc.
https://doi.org/10.1016/j.molcel.2022.01.009

CellPress

CellPress
OPEN ACCESS

Molecular Cell

Article

The human SKI complex regulates channeling of ribosome-bound RNA to the exosome via an intrinsic gatekeeping mechanism

Alexander Kögel,[1] Achim Keidel,[1] Fabien Bonneau,[1] Ingmar B. Schäfer,[1,*] and Elena Conti[1,2,*]
[1]Department of Structural Cell Biology, Max Planck Institute of Biochemistry, Am Klopferspitz 18, 82152 Martinsried, Munich, Germany
[2]Lead Contact
*Correspondence: ischaefe@biochem.mpg.de (I.B.S.), conti@biochem.mpg.de (E.C.)
https://doi.org/10.1016/j.molcel.2022.01.009

SUMMARY

The superkiller (SKI) complex is the cytoplasmic co-factor and regulator of the RNA-degrading exosome. In human cells, the SKI complex functions mainly in co-translational surveillance-decay pathways, and its malfunction is linked to a severe congenital disorder, the trichohepatoenteric syndrome. To obtain insights into the molecular mechanisms regulating the human SKI (hSKI) complex, we structurally characterized several of its functional states in the context of 80S ribosomes and substrate RNA. In a prehydrolytic ATP form, the hSKI complex exhibits a closed conformation with an inherent gating system that effectively traps the 80S-bound RNA into the hSKI2 helicase subunit. When active, hSKI switches to an open conformation in which the gating is released and the RNA 3′ end exits the helicase. The emerging picture is that the gatekeeping mechanism and architectural remodeling of hSKI underpin a regulated RNA channeling system that is mechanistically conserved among the cytoplasmic and nuclear helicase-exosome complexes.

INTRODUCTION

The exosome complex is a conserved RNA-degradation machinery present in both the nucleus and the cytoplasm of all eukaryotes studied to date (Chlebowski et al., 2013; Januszyk and Lima, 2014; Mitchell et al., 1997). In the nucleus, the RNA exosome functions in the processing and decay of a large variety of noncoding transcripts as well as pre-mRNAs (Lingaraju et al., 2019b; Schmid and Jensen, 2019). In the cytoplasm, it primarily targets mRNAs (Schaeffer and van Hoof, 2011; Tuck et al., 2020). The processive ribonuclease module of the RNA-exosome complex is similar in both cellular compartments. Nine subunits form a catalytically inert cage that is traversed by an internal channel (Bonneau et al., 2009; Liu et al., 2006). This channel binds RNA and threads it to the 3′–5′ processive exoribonuclease in the complex: Rrp44 in yeast and the cytoplasmic and nuclear orthologs DIS3 and DIS3L in human (Dziembowski et al., 2007; Gerlach et al., 2018; Liu et al., 2006; Tomecki et al., 2010; Weick et al., 2018). The processive 10-subunit ribonuclease module (Exo-10) has an irreversible degrading action on the RNAs it has accessed. Exo-10 itself, however, lacks substrate specificity and requires different co-factors to target to different RNAs. The exosome co-factors exist in complexes that are compartment-specific and are centered around two RNA helicases, nuclear Mtr4 and cytoplasmic Ski2 (Lingaraju et al., 2019b; Olsen and Johnson, 2021; Weick and Lima, 2021). Together with their adaptors, the helicase co-factors of the exosome appear to control substrate access to the ribonuclease.

Ski2 and Mtr4 harbor similar biochemical properties. Both helicases hydrolyze ATP to power RNA unwinding in a processive manner and with 3′–5′ polarity, melting RNA secondary structures to create a progressively longer single-stranded 3′ end (Khemici and Linder, 2018). Both helicases also share a similar domain organization, with an N-terminal low-complexity region followed by a DExH-unwinding core and an additional domain with RNA-binding and protein-binding properties known as the "arch" (Halbach et al., 2012; Jackson et al., 2010; Weir et al., 2010). However, the two helicases differ in aspects that go beyond the mere presence (in Mtr4) or absence (in Ski2) of a nuclear localization signal. In particular, Mtr4/hMTR4 interacts with a variety of adaptor proteins, forming mutually exclusive complexes that target the different types of RNA substrates in the nucleus (Dobrev et al., 2021; Falk et al., 2014, 2017; Lingaraju et al., 2019a; Schuller et al., 2018; Thoms et al., 2015; Wang et al., 2019). In the cytoplasm, the Ski2/hSKI2 helicase instead mainly targets mRNAs and is part of a single assembly, the Ski complex (Anderson and Parker, 1998; Brown et al., 2000; Tuck et al., 2020).

The Ski proteins were discovered in yeast and named after the superkiller (SKI) phenotype—defined as increased susceptibility to a viral "killer" toxin in strains containing mutations in the *SKI* genes (Toh et al., 1978). The Ski2, Ski3, and Ski8 proteins assemble with a 1:1:2 stoichiometry to form a stable tetrameric

This is an open access article under the CC BY license (http://creativecommons.org/licenses/by/4.0/).

assembly both *in vivo* and *in vitro* (Brown et al., 2000; Halbach et al., 2013; Synowsky and Heck, 2008). The crystal structure of a yeast Ski2-Ski3-Ski8 (Ski) complex has revealed a compact architecture, with the helicase core of Ski2 surrounded by the tetratricopeptide repeat (TPR) protein Ski3 and two WD40-repeat Ski8 subunits (Halbach et al., 2013). In biochemical assays, the RNA-dependent ATPase activity of the yeast Ski2 helicase is downregulated in the context of the Ski complex, but restored upon deletion of the Ski2 arch domain (Halbach et al., 2013). The Ski complex can also associate with translating 80S ribosomes, using the Ski2 arch domain as a major interaction site (Schmidt et al., 2016). The yeast 80S-Ski cryo-EM structure suggested that binding to ribosomes changes the conformation of the Ski2 arch domain, allowing 80S-bound mRNA to enter the helicase core of the Ski complex (Schmidt et al., 2016). The Ski complex also targets ribosome-free regions of mRNAs via the yeast-specific factor Ska1 (Zhang et al., 2019). Finally, the yeast Ski complex can bind Ski7, the adaptor that bridges the interaction to the Exo-10 exosome (Araki et al., 2001).

Orthologs of the yeast Ski2, Ski3, and Ski8 proteins can be identified in higher eukaryotes, such as the corresponding human proteins SKIV2L, TTC37, and WDR61, respectively. Deficiencies in SKIV2L and TTC37 cause trichohepatoenteric syndrome (THES), a congenital disease characterized by very early onset of chronic diarrhea and immune defects in children (Fabre et al., 2013). Several pathogenic mutations have been identified in THES patients, corresponding to either nonsense or missense mutations in SKIV2L or TTC37 (Fabre et al., 2011, 2012; Lee et al., 2016). Furthermore, human SKIV2L has also been linked to viral autoimmunity, as a mediator for the degradation of endogenous immuno-stimulatory RNAs that are produced by a cellular stress response (Eckard et al., 2014). SKIV2L activity has now been shown to act primarily in exosome-mediated degradation during co-translational mRNA surveillance pathways (Tuck et al., 2020) by extracting mRNA from stalled 80S ribosomes (Zinoviev et al., 2020). However, there is currently no structural information that would shed light on the physiological and pathological roles of the hSKI complex. In this work, we used biochemical and cryo-EM analysis to address the molecular mechanisms underlying the functions of the hSKI complex.

RESULTS AND DISCUSSION

The human SKI complex adopts closed and open states

For clarity, we will refer to the human orthologs of the yeast Ski complex subunits as hSKI2 (SKIV2L, ~137.8 kDa), hSKI3 (TTC37, ~175.5 kDa) and hSKI8 (WDR61, ~33.6 kDa) (Figure 1A). The hSKI2 subunit is a multidomain protein. In the text, we designate its individual domains as $hSKI2_N$ for the naturally unstructured N-terminal domain, $hSKI2_{cat}$ for the catalytic DExH core, and $hSKI2_{arch}$ for the arch domain (Figure 1A). In the case of hSKI3, analogous to the yeast ortholog, we refer to its N-terminal and C-terminal arch regions as $hSKI3_N$ and $hSKI3_C$ (Figure 1A; Halbach et al., 2013), respectively.

We co-expressed full-length hSKI2, hSKI3, and hSKI8 in insect cells and co-purified them as a homogeneous complex (Figure S1A). The purified hSKI complex was subjected to cryo-EM structural analysis (Figure S1B). Two-dimensional (2D) classifications of the cryo-EM images revealed the presence of two major subsets of particles (Figure S1C). Each subset was independently processed by three-dimensional (3D) classification followed by 3D refinement (Figure S1D). The subset with fewer particles (~40%) resulted in a reconstruction to a global resolution of ~3.7 Å and showed interpretable density for the majority of the complex (Figures 1B, 1C, and S2A–S2C). We will refer to this reconstruction as the "closed state" of hSKI. The second subset of particles (~60%) was refined to a similar resolution (~3.8 Å) and showed density for a smaller unit (Figures 1D, 1E, and S2D–S2F). We will refer to this reconstruction as the "open state" of hSKI.

The quality of the cryo-EM density map of the closed-state reconstruction enabled us to build most of the atomic model *de novo* (Figures 2A and S2G), with two exceptions. First, there was no ordered density for $hSKI3_N$ (predicted to contain TPRs 1–8); the N-terminal arm of hSKI3 was thus left unmodeled. Second, the density for the $hSKI2_{arch}$ domain displayed a local resolution of 4–12 Å in focused refinement (Figure S2H); therefore, this domain was built by docking a model generated via a structural prediction based on the yeast ortholog (Figure 2A; Halbach et al., 2012; Tunyasuvunakool et al., 2021). In the case of the open-state reconstruction there was no ordered density that would account for the $hSKI2_{cat}$ and $hSKI2_{arch}$ domains, suggesting that they detached from the rest of the complex (Figures 1D and 1E). Based on the structural analysis, we define $hSKI2_{cat}$ and $hSKI2_{arch}$ as the helicase module of hSKI, whereas $hSKI3_C$, $hSKI2_N$, and the two hSKI8 subunits are designated as the gatekeeping module (Figures 1C and 1E).

The gatekeeping module of hSKI forms the epicenter of the complex

We will start by describing the closed-state conformation of hSKI, which is generally similar to that observed in the structure of the *Saccharomyces cerevisiae* ortholog (Halbach et al., 2013; Figures 2A and S3). hSKI is scaffolded around its largest subunit, the TPR-containing protein hSKI3. TPRs are structural repeats consisting of two α-helices that arrange in tandem to form right-handed solenoids, with superhelical turns of approximately 8 TPRs each (Perez-Riba and Itzhaki, 2019). The TPRs 9–40 of the $hSKI3_C$ arm form a crescent-shaped solenoid with four superhelical turns (TPRs 9–16, 17–24, 25–32, 33–40) (Figures 1A and 2A). Most of the fourth superhelical turn is an extension of hSKI3 as compared with the yeast ortholog (Halbach et al., 2013; Figures S3A and S3B). This superhelical turn of hSKI3 is also a hotspot for disease-associated mutations in THES patients (L1485R, R1503C, and L1505S at TPR39—hereby defined as THES-1 hotspot, Figure 2B), suggesting that this region has physiological relevance. Since THES-associated mutations (Fabre et al., 2013) map to many different areas of the complex, we will point to them in the text when describing the corresponding structural features that are affected.

The $hSKI3_C$ arm wraps around the $hSKI2_N$ domain (Figure 2B, left panel). The $hSKI2_N$ domain is an extended region that can be subdivided into individual segments (Figure 2C). The first ("inner") segment (hSKI2 residues 1–121) binds inside the superhelical axis of $hSKI3_C$ with sparse secondary structure elements, spanning almost the entire length of the solenoid and forming

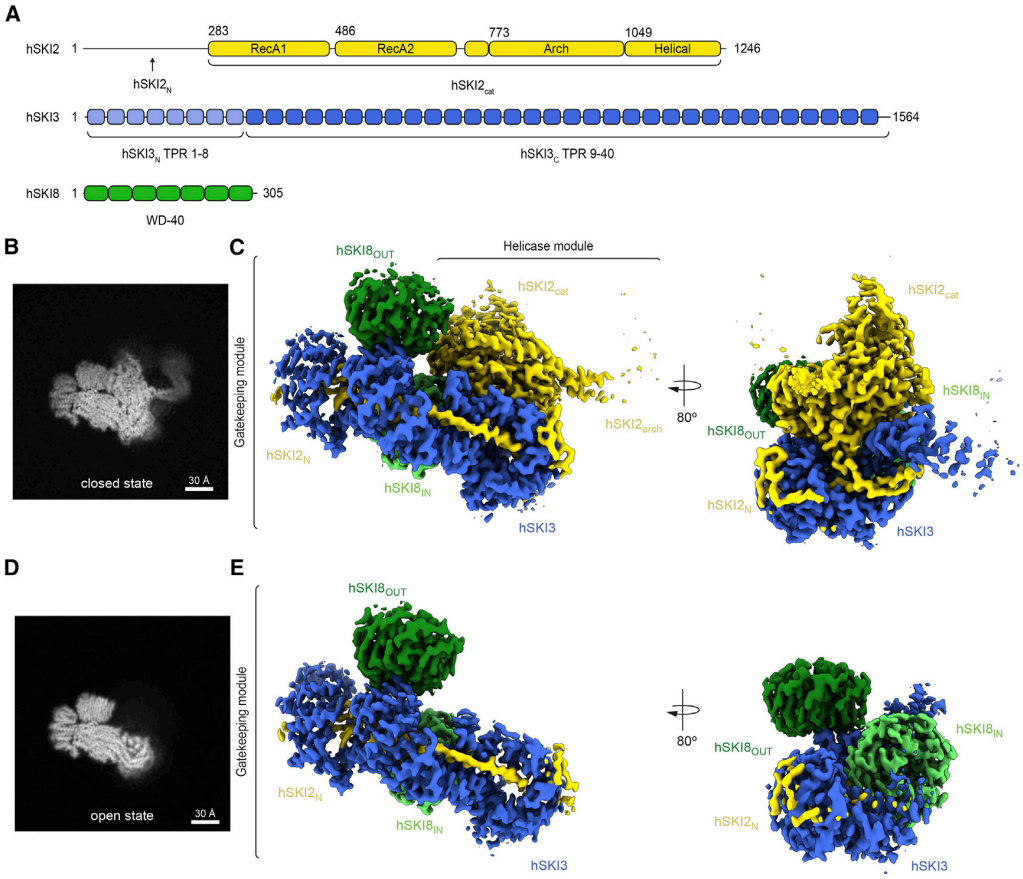

Figure 1. Structural organization and conformational states of hSKI

(A) Domain organization of the human SKI subunits hSKI2 (yellow), hSKI3 (blue), and hSKI8 (green). Predicted folds segments are indicated by rectangles and extended segments by lines. The N-terminal arm of hSKI3 ($hSKI3_N$; TPR 1–8) (light blue) is flexible in all current structural data.

(B and C) Single-particle cryo-EM reconstruction of the closed state of apo hSKI at a global resolution of 3.7 Å. 2D projection of the final reconstruction, showing the density for the $hSKI2_{arch}$ (B). Three-dimensional rendering of the reconstruction with the hSKI subunits in two orientations and colored as in (A). (C) The gatekeeping module ($hSKI2_N$-hSKI3-$hSKI8_{IN}$-$hSKI8_{OUT}$) and the helicase module ($hSKI2_{cat}$-$hSKI2_{arch}$) discussed in the text are indicated.

(D and E) Single-particle cryo-EM reconstruction of the open state of apo hSKI at a global resolution of 3.8 Å. The 2D projection (D) and the 3D reconstruction (E) are in a similar orientation as the closed state in (B) and (C). Only the gatekeeping module is visible in both 2D projection and 3D rendering.

See also Figures S1 and S2; Table S1.

an integral part of its hydrophobic core (Figure 2B, left panel, box 1). This segment ends with a highly conserved "inner ß-hairpin" that is embedded in the second superhelical turn of $hSKI3_C$ (at TPRs 17–19) (Figure 2B; box 2) and connects to an intricate loop structure that we will refer to as the "wedge" segment (hSKI2 residues 122–165) (Figure 2B; box 3). The $hSKI2_N$ wedge segment protrudes from the concave surface of $hSKI3_C$ at the second superhelical turn and, despite lacking secondary structure elements, is well structured by intra- and intermolecular interactions. $hSKI2_N$ continues by binding with an "outer hairpin" ($hSKI2_N$ residues 172–201) along the external convex surface of the solenoid, at the second superhelical turn of $hSKI3_C$ (Figure 2B; box 4). From here, the density of $hSKI2_N$ weakens as it reaches the first superhelical turn of $hSKI3_C$ with an "outer α-helix" (Figures 2C and S3C) and then fades at the linker segment that connects to the RecA1 domain of the well-ordered helicase module.

The $hSKI3_C$ arm also binds the hSKI8 subunits. hSKI8 is a seven-bladed ß-propeller with the wheel-like shape characteristic of WD40-repeat proteins (Stirnimann et al., 2010). The outer hSKI8 subunit ($hSKI8_{OUT}$) adopts an outward position at the third superhelical turn of $hSKI3_C$ (Figure 2A). The internal hSKI8 subunit ($hSKI8_{IN}$) is positioned at the inner concave surface of $hSKI3_C$, interacting with the third superhelical turn (Figure 2A, left panel). THES-associated mutations in hSKI3 map to the $hSKI8_{IN}$-binding site (P1270A and D1283N at TPR 33 and 34). These substitutions (THES-2 hotspot; Figure 2B) are expected to weaken the intermolecular interactions and/or stability of the gatekeeping module. Another cluster of THES-associated mutations in hSKI3 map to the region that wraps around the inner

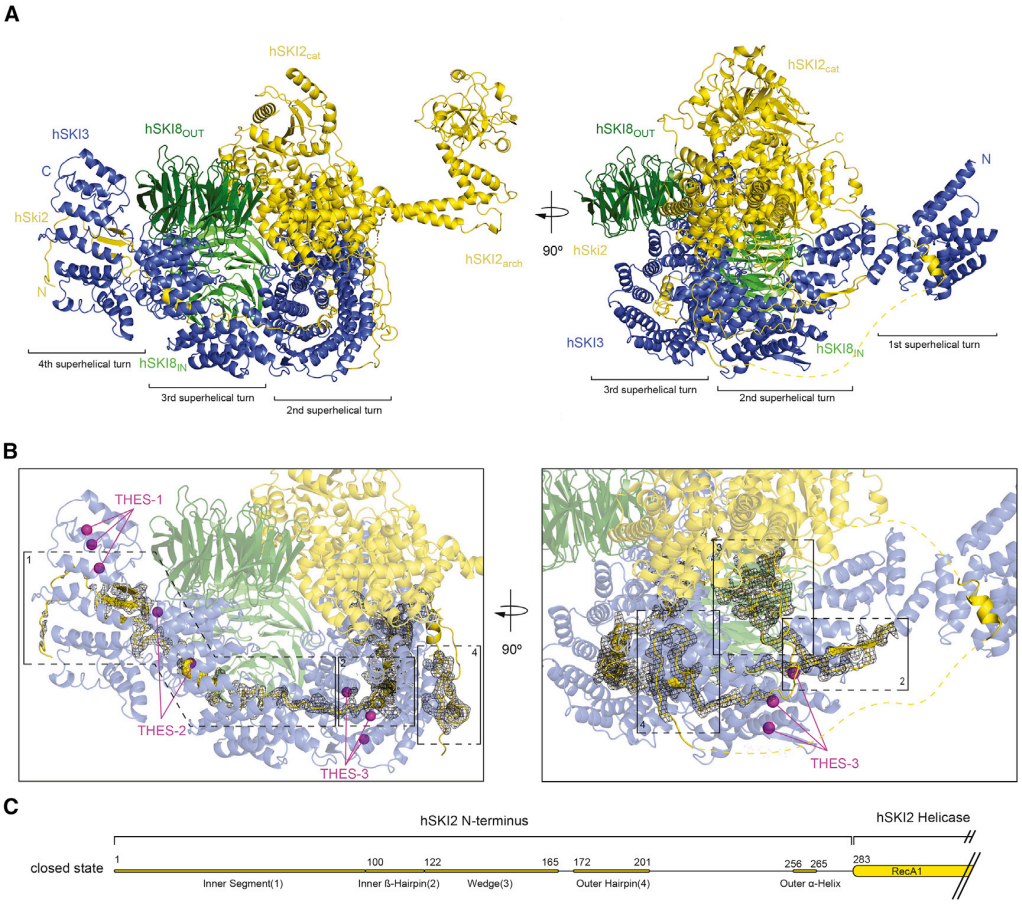

Figure 2. Closed-state conformation of hSKI

(A) Cartoon representations of hSKI in closed state, related by a 90° rotation around a vertical axis (left panel oriented as in Figure 1, same color scheme).

(B) Zoom-in of the gatekeeping module with the difference density for $SKI2_N$ displayed as black mesh. The two representations are oriented as those in (A). Numbering refers to the regions indicated in (B). Highlighted as purple spheres are the positions of THES disease mutants in the core of the gatekeeping module (clustered in the THES-1, THES-2 and THES-3 groups). The numerals 1–4 refer to the regions shown in (C).

(C) Schematic domain organization of $hSKI2_N$ highlighting distinct regions discussed in the text.

See also Figures S1, S2, and S3; Table S1.

segment and are expected to interfere with the proper folding of the superhelix (hSKI3 G673D, G721R, L761P at TPRs 19 and 20, THES-3 hotspot) (Figure 2B).

The helicase module can detach from the gatekeeping module

In the closed-state conformation of SKI, the basal surface of the $hSKI2_{cat}$ domain binds the hSKI3 solenoid at the first and second superhelical turns and hereby interacts with the adjacent $hSKI8_{OUT}$ and $hSKI8_{IN}$ subunits and with the wedge segment of $hSKI2_N$ (Figure 2). The $hSKI2_{arch}$ insertion instead protrudes from the top surface of the $hSKI2_{cat}$ domain, extending into solvent with a curved structure (Figure 2A). In the open-state conformation, not only is there no well-ordered density for the hSKI2 helicase module, but neither is there density for the wedge segment of $hSKI2_N$ or for the first superhelical turn of $hSKI3_C$ including the $hSKI2_N$ outer α-helix (Figures 3A and 3B). In contrast, the internal segment, both the inner ß-hairpin and the outer hairpin of $hSKI2_N$ are bound in the same manner to hSKI3. Thus, in this open-state conformation of hSKI, the hSKI2 helicase module appears to be flexible while it remains linked to the gatekeeping module via the $hSKI2_N$ domain.

The structural analysis suggests that the inner and outer hairpins of $hSKI2_N$ anchor the wedge segment as it undergoes conformational changes connected to the recruitment or detachment of the helicase core from the gatekeeping module. To test the impact of the wedge on the movement of the helicase module, we replaced this segment with a $(Gly\text{-}Ser)_5$ linker and purified the corresponding hSKI-Δwedge mutant complex for cryo-EM analysis (Figures S4A and S4B). The entire dataset of hSKI-Δwedge showed the presence of a complex in the open state (Figure S4B). Thus, the wedge segment of $hSKI2_N$ appears

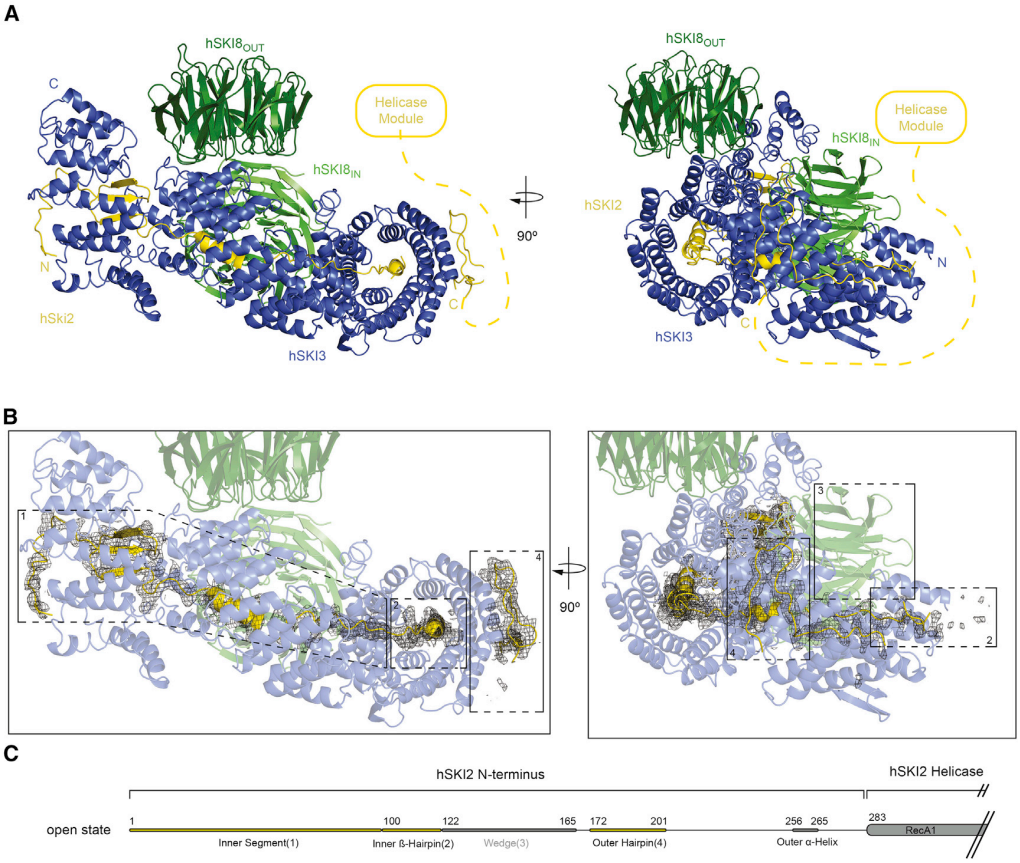

Figure 3. Open-state conformation of hSKI

(A) Cartoon representations of hSKI in open state, oriented as in Figure 2. The connection to the disengaged helicase module is indicated by a dotted yellow line.
(B) Zoom-in of the gatekeeping module with the difference density for $SKI2_N$ displayed as black mesh. The two representations are oriented as in (A). Note that the density for the $hSKI2_N$ wedge (3) is absent and the $hSKI2_N$ inner ß-hairpin (2) is less well-ordered compared with the closed-state reconstruction in Figure 2B.
(C) Schematic domain organization of $hSKI2_N$ highlighting the distinct regions discussed in the text.
See also Figures S1, S2, and S4; Table S1.

to stabilize the closed state. Notably, the structure of the apo *S. cerevisiae* Ski-Δarch complex also showed a similar closed-state architecture with an analogous wedge segment (RG motif, R149-G150) positioned at the bottom of the empty helicase channel (Halbach et al., 2013). However, it is likely that the crystallization procedure selected the most compact conformation for lattice formation, since cryo-EM analysis of the same complex indicates that it is present both in closed and open states (Figures S4C–S4E). Thus, we posit that the presence of the open and closed conformational states is an evolutionarily conserved feature of the Ski complex.

RNA is enclosed in the helicase core in closed-state hSKI

We proceeded to characterize how hSKI binds RNA. In biochemical spectrophotometric enzyme-coupled assays, recombinant hSKI showed RNA-dependent ATPase activity (hSKI-WT) (Figure 4A; Table S2). As control, the ATPase activity of hSKI was abolished in the case of a mutant complex with a glutamic acid to glutamine substitution in the helicase catalytic site (hSKI-DEAD containing the E424Q substitution in hSKI2) (Figure 4A; Table S2). We determined the kinetic parameters for the wild-type complex under steady-state conditions for varying ATP concentrations. Half-maximum velocity was reached at K_m = 149.4 μM ATP with a k_{cat} = 0.685 s^{-1}, which is well under physiological ATP concentrations, similar to *S. cerevisiae* Ski (Halbach et al., 2013).

For the structural analysis, we incubated wild-type recombinant hSKI with a 25-uracil (25U) RNA substrate and the nonhydrolyzable nucleotide analog ADP-BeF (which mimics a prehydrolytic ATP state). Cryo-EM data showed that essentially all particles were in the closed-state conformation, resulting in a 3D reconstruction of RNA-bound hSKI at a global resolution of 3.1 Å (Figures 4B and S5). The cryo-EM reconstruction revealed well-defined density for six ribonucleotides (N1–N6) bound in $hSKI2_{cat}$ in a single-stranded conformation (Figure 4B). $hSKI2_{cat}$

CellPress
OPEN ACCESS

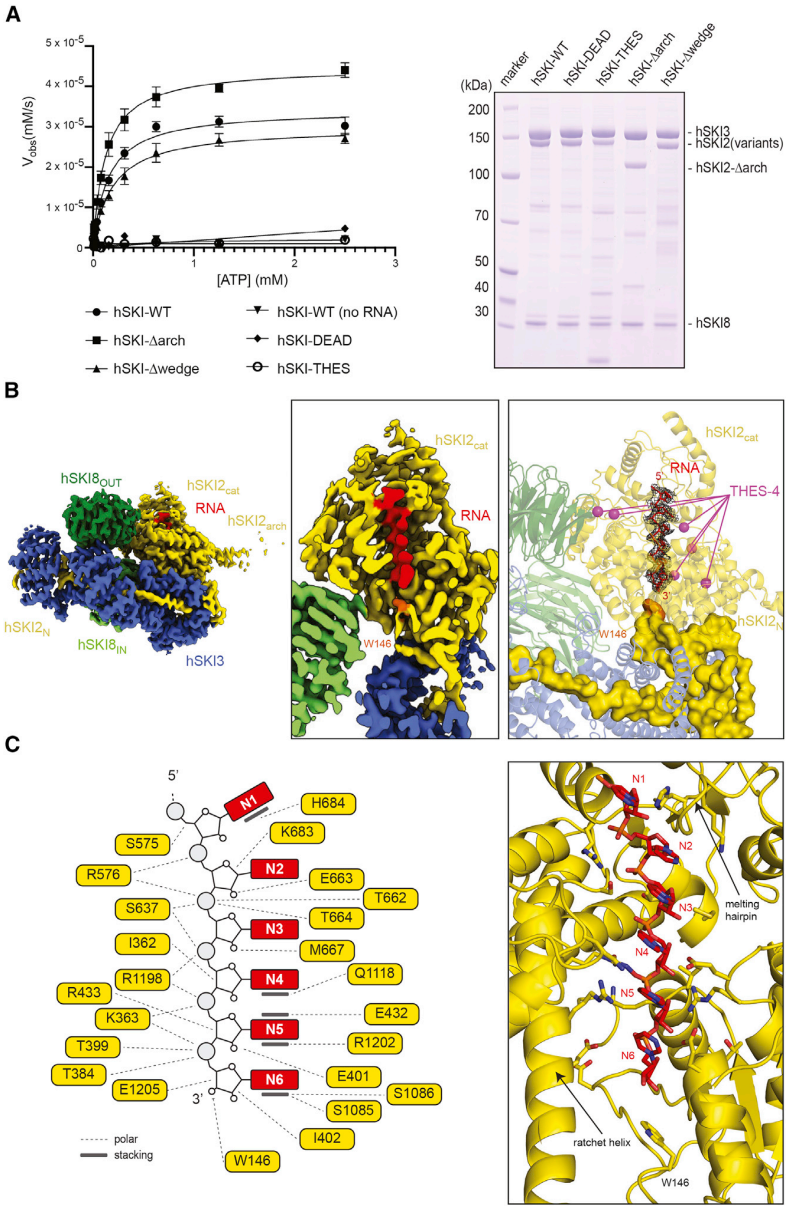

Figure 4. RNA-binding features of hSKI

(A) RNA-dependent ATPase activity of hSKI wild-type and mutants. The mutations Δarch, Δwedge, E424Q (DEAD), and V341G (THES) are in the hSKI2 subunit of the complex. (Left) Enzyme-coupled spectrophotometric assay. Initial ATPase rates are plotted against ATP concentration. Protein and poly(U) RNA concentrations were 50 nM and 10 μg/mL, respectively. Data were fitted according to Michaelis-Menten kinetics (see Table S2 for derived kinetic parameters). Error bar: ±1 standard deviation from three independent experiments. (Right) Coomassie-stained 4%–12% SDS-PAGE of the hSKI samples used in the assay. hSKI2 (variants) refers to all mutants except hSKI2Δarch.

(B) RNA path in the structure of RNA-bound hSKI. The central panel shows a slap view of the 3D reconstruction through the central plane of the RNA channel in $hSKI2_{cat}$. On the right is a zoom-in highlighting the path of the RNA (cartoon representation in red, difference density in black mesh) in hSKI2. The $hSKI2_N$ wedge is indicated in space-fill representation. The position of W146 of the $hSKI2_N$ wedge is indicated in orange. Highlighted as purple spheres are the positions of THES disease mutants in this area of the complex (clustered in the THES-4 group). Note that N1–N6 correspond to uracil nucleotides in the homopolymeric 25U RNA we used in the structural analysis.

(C) Detailed interactions between hSKI2 and the six ordered nucleotides at the RNA 3′ end. (Right) Zoom-in of the structure at the RNA-binding residues. (Left) Corresponding schematic of the interactions (polar and stacking contacts are indicated).

See also Figure S5; Table S1 and S2.

has the characteristic domain organization of DExH helicases: a pair of RecA domains (RecA1 and RecA2) contain the ATPase catalytic site and are juxtaposed to a helical domain, resulting in an overall globular shape with a central channel (Figure S5F) (Ozgur et al., 2015). The 5′ nucleotide (N1) binds at the top surface of $hSKI2_{cat}$, where it engages in base-stacking interactions with the so-called melting hairpin of RecA2 (Figures 4C and S5G). This motif is a conserved structural feature poised to melt RNA duplexes as they enter the DExH core of Ski2-related helicases (Büttner et al., 2007). The ribonucleotide chain then binds along the RNA-binding surface of RecA2 and continues into the helicase channel, threading between the RecA1 domain and the helical domain (at the so-called ratchet helix) (Büttner et al., 2007) (Figure 4C). Several disease-associated mutations in THES patients target the DExH core of hSKI2 in proximity to the ATP-binding site (A332P, V341G, E438K, and R483C substitutions) or adjacent to the RNA-binding surfaces (ΔG1187-Q1193 and ΔS1189-L1195 deletions) and are thus expected to affect the RNA-dependent ATPase properties of the complex (THES-4 hotspot) (Figure 4B, right panel). To test this prediction, we expressed and purified a recombinant hSKI complex mutant with the V341G substitution (hSKI-THES) and indeed found that it is inactive in ATPase assays *in vitro* (Figure 4A; Table S2).

The RNA-binding interactions of the DExH core are evolutionarily conserved not only in hSKI2 orthologs but also in the nuclear helicase Mtr4 (Figure S5F) (Gerlach et al., 2018; Schuller et al., 2018; Weick et al., 2018; Weir et al., 2010). However, the cryo-EM density of hSKI revealed an additional and unexpected feature: the most 3′ end ribonucleotide interacts with the wedge segment of the $hSKI2_N$ domain (Figures 4B and 4C). In particular,

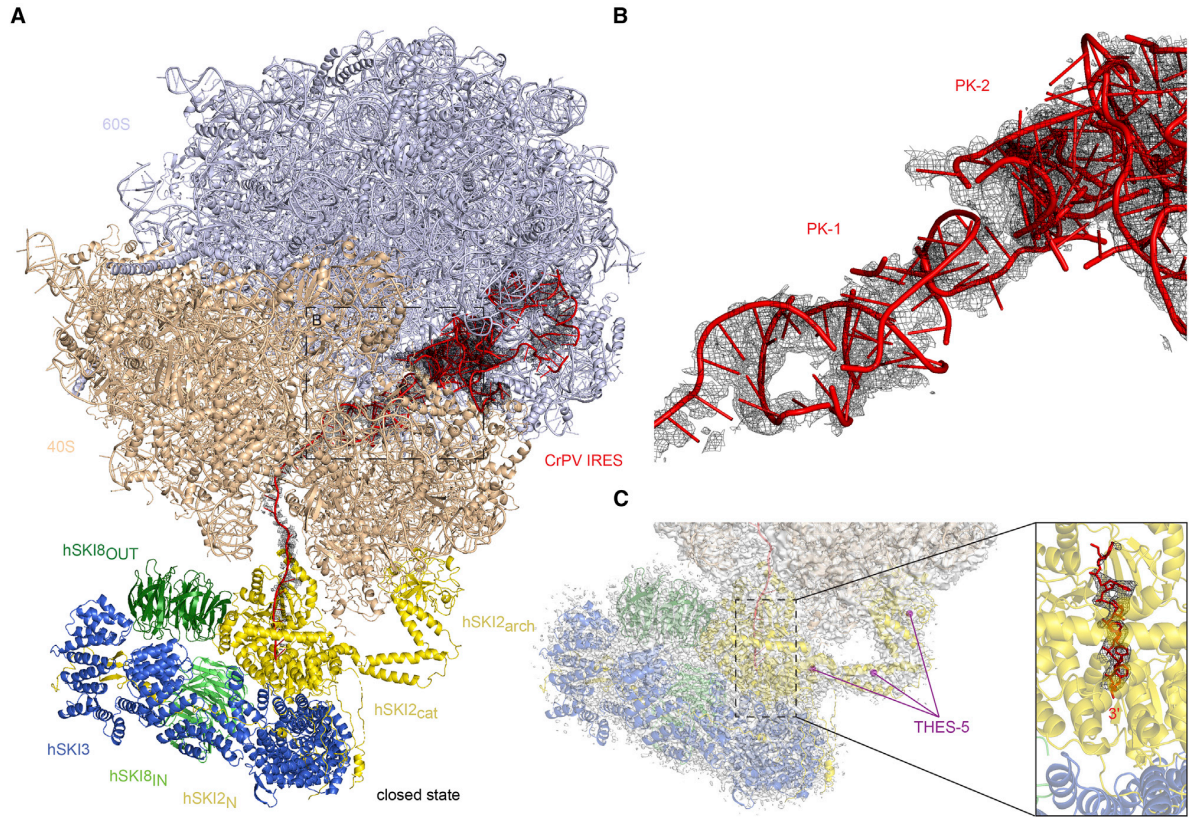

Figure 5. RNA blocked in the hSKI2 helicase in a close-state hSKI-80S complex

(A) Cartoon representation of hSKI bound in a closed state to a human 80S ribosome reconstituted with a CrPV IRES-29 nt RNA. The large and small ribosomal subunits are in light blue and light orange, respectively, and CrPV IRES-29 RNA is in red with corresponding density indicated by black mesh.

(B) Zoom-in view of the 80S-bound RNA at CrPV IRES pseudoknots 1 and 2 (PK-1 and PK-2) with corresponding density.

(C) Zoom-in view of the 80S-bound RNA at the 3′ end. The enlarged photo on the right panel displays the 6 nt that are traceable in hSKI2 in closed-state hSKI. See also Figure S6; Table S1.

a Trp-Gly motif (W146-G147) in the hSKI2$_N$ wedge segment contacts the 3′ hydroxyl group of the N6 ribonucleotide enclosed in the helicase channel. The interactions suggest the presence of a crosstalk between the hSKI2$_N$ wedge loop in the gatekeeping module and the 3′ end of an RNA substrate while in the hSKI2$_{cat}$ core, rationalizing the presence of a single class of particles/states during 3D refinement of the RNA-bound data set as compared with the different subsets of closed and open states in the apo hSKI reconstructions.

80S-bound hSKI is in a closed state in the presence of a prehydrolytic ATP mimic

The observation that the hSKI gatekeeping module obstructs the end of the helicase channel in the closed state raised the hypothesis that in the open state the obstruction in hSKI2 is removed and the exit for the RNA substrate is opened. However, this prediction could not be verified in the context of hSKI complexes in isolation because it was not possible to visualize the detached hSKI2 in open-state hSKI (as the larger gatekeeping module dominates the particle alignment). We proceeded to visualize hSKI bound to a human ribosome (Figure 5).

To reconstitute an appropriate RNA-containing 80S sample, we took advantage of the internal ribosome entry site (IRES) from the cricket-paralysis virus (CrPV) and added a 29-nt sequence at the 3′ end (IRES29 RNA). The CrPV-IRES folds into a stable structure capable of binding directly to the intersubunit space on the ribosomal 40S subunit, which can then join a 60S subunit to form an 80S ribosome (Hellen, 2009). The additional sequence at the 3′ end was included to create a suitable binding platform for hSKI based on previous studies (Schmidt et al., 2016; Zinoviev et al., 2020). In human cells, the SKI complex has been shown to extract 80S-bound mRNAs that contain a 3′ terminal region of at least 19 nt from the P site (Zinoviev et al., 2020).

We incubated the reconstituted 80S-IRES29 with an excess of wild-type hSKI and the nucleotide analog ADP-BeF and purified the assembly by gradient centrifugation for cryo-EM data collection. Data processing yielded a reconstruction with an overall resolution of ~3.1 Å (Figure S6). The density showed significant

CellPress
OPEN ACCESS

flexibility for hSKI, thus requiring an adjustment to the center of mass by subtracting the ribosome signal from the data. The resulting map of 80S-bound hSKI reached a global resolution of 3.6 Å in the core of the helicase complex (Figure S6) and was interpreted by rigid-body fitting the model from the substrate-bound hSKI reconstruction, with no major differences with regard to the position of the four hSKI subunits. The structure of 80S-bound hSKI in the presence of a prehydrolytic ATP mimic thus shows that the hSKI2 helicase module is recruited to the hSKI gatekeeping module in the characteristic closed-state conformation (Figure 5A).

hSKI is flexibly tethered to 80S ribosomes via the hSKI2 helicase module

The hSKI complex binds the 80S ribosome via evolutionarily conserved interactions between hSKI2 and the small ribosomal subunit (Figure 5A). The hSKI2 RecA2 domain binds between the "head" and the "shoulder" of the 40S at ribosomal proteins uS3, uS12, eS10, and rRNA helix 16. The $hSKI2_{arch}$ domain binds the "head" of the 40S at ribosomal protein uS3, uS10, and rRNA helix 41. Several THES-associated disease mutations cluster in positions that would either directly or indirectly affect 40S recognition. For example, the in-frame deletion mutant ΔR888 is in the globular KOW (Kyrpides-Ouzounis-Woese) fold that binds rRNA, while other mutations are within the stalk (the in-frame deletion ΔQ1034) or at the base of the arch (W466G) (THES-5 hotspots; Figure 5C), suggesting the integrity of the arch domain is physiologically important.

Although the positioning of hSKI close to the entry of the ribosome mRNA channel is similar to that of yeast 80S-bound Ski (Schmidt et al., 2016), there are notable differences. First, rRNA helix 16 in the "shoulder" of the 40S is in the classical straight conformation instead of the unusual bent conformation observed in the reconstruction of the yeast complex (Figures S3D and S3E) (Schmidt et al., 2016). Moreover, there is no additional interaction between hSKI and the 40S: the $hSKI8_{OUT}$ subunit is at a distance of 40 Å from the ribosomal proteins uS2, uS5, and eS21 instead of interacting directly with them as was the case for yeast $Ski8_{out}$ (Figure S3E) (Schmidt et al., 2016). Indeed, hSKI is more flexibly tethered to the 40S, rather than packing closely against it as seen in the yeast reconstruction.

In the yeast system, ribosome binding is thought to modulate the conformation of the Ski2 arch domain, thus releasing it from an autoinhibitory state (Schmidt et al., 2016). Although the arch domain of hSKI2 adopts a conformation similar to that observed in the yeast 80S-bound Ski, the same conformation is also observed in the reconstruction of hSKI in isolation (Figure S3D). We therefore conclude that binding to 80S ribosomes does not have a major influence on the hSKI2 arch domain. The differences at the structural level between the two orthologs are consistent with differences at the biochemical level. In yeast, the Ski complex in isolation has only modest ATPase activity that is significantly increased upon removal of the Ski2 arch domain (Halbach et al., 2013). In contrast, removal of the hSKI2 arch domain led only to a minor increase in the ATPase activity of hSKI in isolation (hSKI-Δarch) (Figure 4A; Table S2), suggesting that hSKI is not in a significantly autoinhibited state prior to 80S binding. Whether this reflects physiological differences between the yeast and human complexes is unclear. For example, while hSKI is thought to be exclusively bound to ribosomes (Tuck et al., 2020), yeast Ski is found in mutually exclusive 80S-bound and Ska1-bound complexes (Zhang et al., 2019) and may, accordingly, require additional regulation in this respect.

80S-bound hSKI switches to an open state when in the ATPase active form

The 80S-hSKI (with hSKI in the closed state) shows well-defined density for the ribosome-associated RNA (Figures 5A and 5B). In the structure, the CrPV-IRES RNA has the canonical features expected for the CrPV-IRES alone, with two nested pseudoknots (PK-2 and PK-3) close to the exit of the ribosome mRNA channel and another (PK-1) forming as an independent domain bound in the decoding center of the 40S (Fernández et al., 2014; Schüler et al., 2006). After the A site, the ribonucleotide chain continues until it reaches the surface of the ribosome and then becomes less defined as the RNA reaches solvent. After a distance of about 50 Å from the surface of the 80S, the RNA density becomes well-ordered again as the ribonucleotide chain enters the $hSKI2_{cat}$ core. Here, six nucleotides are bound in the same positions and with the same interactions described for the RNA-bound hSKI structure in isolation, including the interaction of the RNA 3′ end with the wedge segment of the gatekeeping module (Figure 5C). Thus, in the closed state of the 80S-hSKI complex, the RNA 3′ end is trapped in the helicase channel, and the exit site of the RNA substrate is blocked. Consistently, the RNA density also stopped inside the yeast Ski2 helicase core in the reconstruction of the compact RNase-treated yeast 80S-Ski complex (Schmidt et al., 2016).

Previous biochemical experiments have shown that the hSKI complex can extract mRNA from stalled ribosomes (Zinoviev et al., 2020). To recapitulate this scenario in our system, we reconstituted an 80S-CrPV-IRES assembly with wild-type hSKI, incubated with ATP for 15 min and collected cryo-EM data on a Titan Krios microscope (Figure S7). In the corresponding reconstruction, the interaction between 80S and hSKI2 is essentially unchanged with respect to that observed in the presence of a prehydrolytic ATP mimic. Importantly, a fraction of the particles (Figure S7G) showed no ordered density at the base of $hSKI2_{cat}$ for the entire gatekeeping module (Figure 6). Unlike hSKI in isolation, this alignment was dominated by the ribosome-bound hSKI2 in the open state, leaving the separate hSKI gatekeeping module unresolved. Thus, we could now visualize the RNA exiting from the helicase channel of hSKI in the open state (Figure 6C).

The cryo-EM reconstruction of the open state shows that the RNA in the helicase channel extends with well-defined density for three nucleotides more at the 3′ end (N7, N8, and N9) than detected in the closed state (Figure 6C). The base and sugar of ribonucleotide N7 makes polar and stacking interactions with RecA1, resulting in a twist of the ribonucleotide chain of ~180°. The RNA 3′ end exits the helicase core in a bent conformation, with nucleotides N8 and N9 making only minor interactions with the ratchet helix (Figure 6D). Thus, when hSKI is in the open state as observed in the active assembly, the 3′ end of the ribosome-bound RNA traverses the helicase core and occupies the space where the wedge of the gatekeeping module

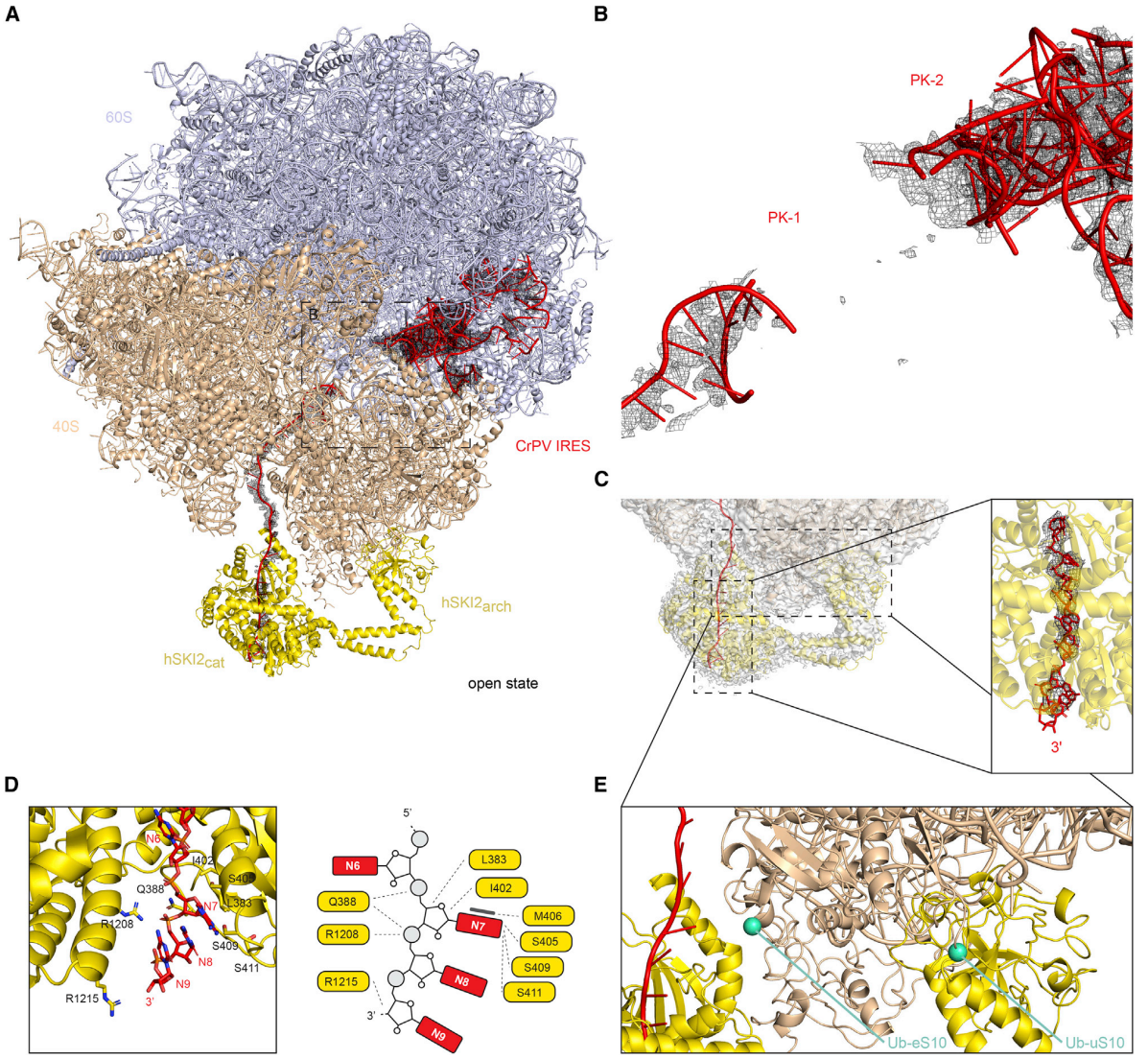

Figure 6. RNA traverses the hSKI2 helicase in an open-state hSKI-80S complex

(A) Cartoon representations of hSKI bound in an open state on a human 80S reconstituted with a CrPV IRES-29 nt RNA. Orientation and coloring as in Figure 5. Note that the gatekeeping module has detached from the helicase module.

(B) Zoom-in view of the 80S-bound RNA at CrPV IRES PK-1 and PK-2. Note that most density for PK-1 has disappeared (compare with Figure 5B), suggesting it has unfolded.

(C) Zoom-in view of the 80S-bound RNA at the 3′ end. The panel on the right shows an enlarged photo of the nine nucleot ides and the RNA 3′ end exiting from hSKI2 in open-state hSKI.

(D) Detailed interactions between hSKI2 and the additional three ordered nucleotides at the RNA 3′ end (downstream of those in Figure 4C). (Right) Zoom-in of the structure at the RNA-binding residues. (Left) Corresponding schematic of the interactions.

(E) N-terminal ubiquitination of eS10 and uS10 ribosomal proteins clashes with binding to the hSKI helicase module. Sites of ubiquitination are indicated as green spheres.

See also Figure S7; Table S1.

was bound in the closed state. Concomitantly, the density for the IRES structure disappears, suggesting that the PKs unfold as the ribosome-bound RNA is extracted and ejected by the hSKI2 helicase (Figure 6B).

The data are consistent with a model whereby the hSKI gatekeeping module detaches when the most 3′ end nucleotide traverses the helicase channel in an ATPase-dependent manner and stays open as the entire ribonucleotide chain is

threaded through, all in an ATPase-dependent manner. The model predicts that the removal of the wedge segment would only impact the initial opening step. Indeed, removal of the wedge segment in the hSKI-Δwedge mutant does not significantly affect the overall ATPase activity of the complex (Figure 4A; Table S2).

Open-state hSKI supports a conserved helicase-exosome RNA channeling mode

The RNA-binding mode observed in the open state of hSKI and, in particular, the bent conformation, with which the ribonucleotide chain traverses the RNA exit channel of hSKI2, are similar in conformation to those observed in the structure of the exosome-bound MTR4 (Weick et al., 2018). These observations suggest that the detached RNA-bound hSKI2 helicase may channel RNA into the cytoplasmic exosome in a manner similar to that observed in the case of MTR4 and the nuclear exosome (Gerlach et al., 2018; Schuller et al., 2018; Weick et al., 2018). To test this prediction, we first biochemically reconstituted the components of the human cytoplasmic exosome (Figure S7A). We purified the inactive 9-subunit core of the human exosome (hEXO9) as previously described for the nuclear complex (Gerlach et al., 2018; Weick et al., 2018). To incorporate the cytoplasmic-specific ribonuclease, we used a human-cell expression system and purified recombinant full-length hDIS3L (with the inactivating D486N mutation). The corresponding 10-subunit cytoplasmic exosome ($hEXO10_c$) binds HBS1L3, a spliced variant of HBS1-like that interacts with $hEXO10_c$ in a similar way as the yeast Ski7 protein interacts with $yExo10_c$ (Kalisiak et al., 2017; Kowalinski et al., 2016). Using size-exclusion chromatography (SEC) experiments, we demonstrated that HBS1L3 also binds hSKI and is required to bridge the interaction between hSKI and $hEXO10_c$ (Figure 7A).

With these purified samples, we performed RNase protection assays (Figure 7B), similar to those we used previously to analyze the RNA-binding properties of exosome complexes (Bonneau et al., 2009; Gerlach et al., 2018). Briefly, a body-labeled, single-stranded RNA was incubated with (catalytically inactive) exosome complexes and treated with benzonase. The footprint (e.g., the size of the RNA fragments that upon protein binding become protected from RNase digestion) was analyzed by denaturing polyacrylamide gel electrophoresis (PAGE) (Figure 7B). The cytoplasmic ribonuclease core complex $hEXO10_c$ gave rise to a characteristic footprint (Figure 7B, lane 1) similar to that previously observed for its nuclear counterpart, $hEXO10_n$ (Gerlach et al., 2018). In the case of the cytoplasmic human exosome, removal of the arch domain was required to observe the increased RNA footprint of the holocomplex with respect to the ribonuclease core (Figure 7B, compare lanes 2 and 4), similarly to its yeast counterpart (Halbach et al., 2013). Remarkably, the difference in footprint between the core and holocomplexes of the cytoplasmic exosome (Figure 7B) is similar to that of the nuclear exosome (Gerlach et al., 2018). Notwithstanding the additional regulatory role of the hSKI2 arch domain, the nuclear and cytoplasmic holoexosomes thus embed a continuous RNA channel of similar length, supporting the notion of a conserved mode of interaction and a conserved channeling mechanism (Figure 7C).

CONCLUSIONS

The hSKI complex undergoes a major remodeling when switching from a closed state to an open state in which the helicase is active and released from the rest of the complex. This large-scale conformational change is underpinned by the structural organization of hSKI into two individual but connected modules: a helicase module and a gatekeeping module. The gatekeeping module can swing open or close toward the helicase module. In the following model, when the hSKI complex is inactive, the gate is closed and binds the helicase module via extensive intermolecular interactions made with the basal surface of the helicase domain. In this closed conformation, the wedge segment in the gate binds and occludes the exit of the helicase channel, enclosing the 3′ end of a bound RNA substrate. Upon activation, that is, in the context of RNA-dependent ATP hydrolysis of 80S-bound hSKI2, the gate opens and detaches from the helicase module, which remains bound to the ribosome. The open state of hSKI is also marked by a movement of the wedge segment, which dissociates from the exit channel of hSKI2, thereby allowing the RNA 3′ end to exit and the ribosome-bound mRNA to be extracted. The efficient interconversion between the large-amplitude conformational changes of the closed and open states is likely due to the covalent tethering of the regulatory and catalytic modules, which can thus remain in proximity even when they are detached from each other.

In contrast to the yeast system, the interaction between hSKI and the 40S ribosomal subunit is exclusively mediated by hSKI2 and is rather flexible in character. The positioning of hSKI2 on the ribosome in the cryo-EM structure explains how it can access a short 3′ overhang of a bound mRNA, a substrate that is expected to arise upon endonucleolytic cleavage after ribosome stalling (Schmidt et al., 2016; Tuck et al., 2020; Zinoviev et al., 2020). The minimal length of the 3′ overhang determined in biochemical assays (Zinoviev et al., 2020) is required to span the distance between the ribosome and the helicase core of hSKI2. However, the SKI complex can also efficiently extract ribosome-bound mRNAs with long overhanging 3′-terminal regions (Zinoviev et al., 2020). The finding that hSKI is flexible when attached to the 80S rationalizes how it can be reached by longer and flexible 3′ overhangs. The position of hSKI in the 80S-bound structure has also interesting repercussions for surveillance mechanisms. The hSKI2 interaction with ribosomal proteins eS10 and uS10 would not be compatible with the ubiquitination of these subunits (Figure 6E), as has been reported to occur on colliding ribosomes (Ikeuchi et al., 2019; Juszkiewicz et al., 2018; Winz et al., 2019).

The gatekeeping mechanism of hSKI does not have a significant inhibitory effect on the ATPase properties of the complex. Once the gate opens, when the most 3′ nucleotide traverses the helicase channel, it stays open until the extraction process is concluded. The arch domain of the helicase also does not have a significant autoinhibitory effect on the ATPase properties of hSKI and, consistently, its conformation is not modulated upon 80S binding, in contrast to what was observed for the yeast ortholog (Schmidt et al., 2016). However, the gatekeeping structure and the arch domain appear to serve an evolutionarily conserved role in regulating RNA channeling to the exosome

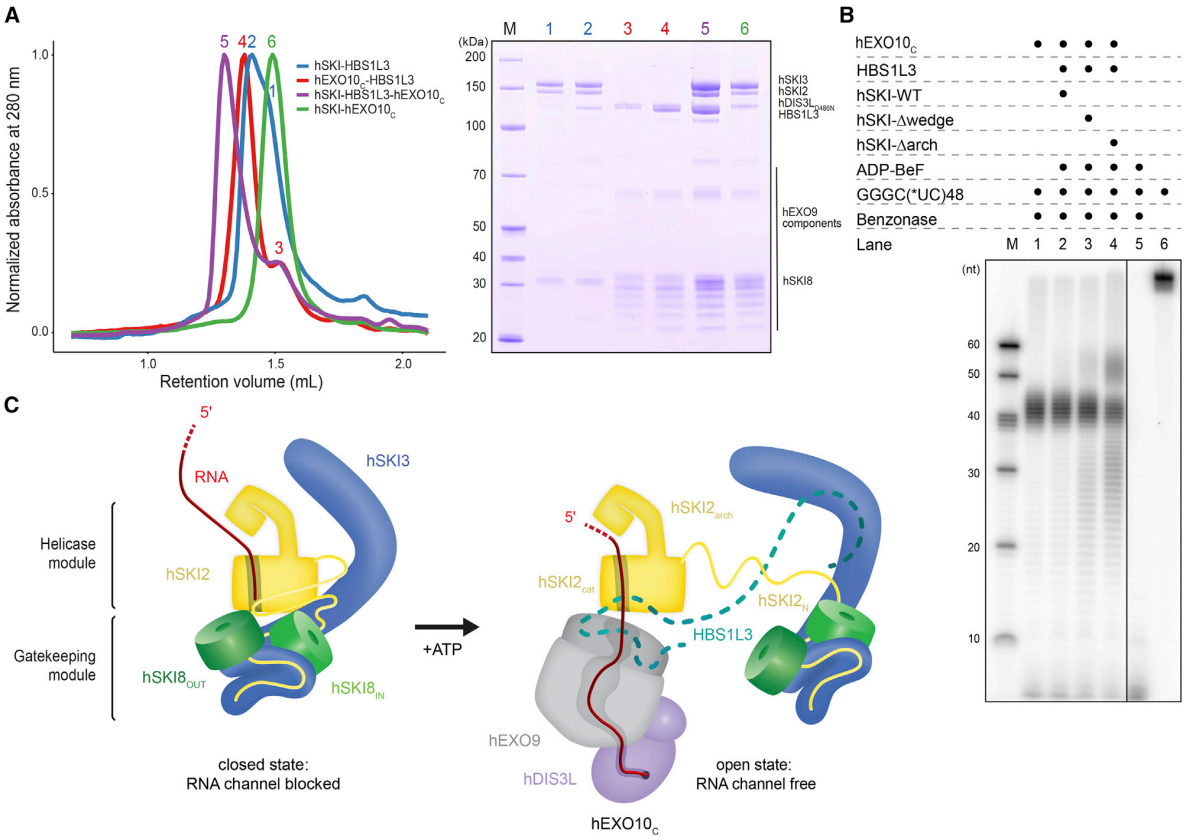

Figure 7. RNA channeling of hSKI to the cytoplasmic exosome

(A) Physical interaction of hSKI and the human cytoplasmic exosome. Size-exclusion chromatography (SEC) assays were carried out with hDIS3L$_{D486N}$ catalytic inactive mutant. The panel on the left is an overlay of the chromatograms, and the panel on the right a Coomassie-stained 4%–12% SDS-PAGE analyzing the peak fractions (as numbered and colored on the left). Note that in the hSKI-HBS1L3 (blue curve) and in the hEXO10$_C$-HBS1L3 (red curve) samples hSKI and hEXO10$_C$ were loaded in excess to control for differences between HBS1L3-bound and -unbound complexes.

(B) RNA path assessed by RNase protection assays of human SKI wild-type and mutants in the context of the human cytoplasmic exosome (human EXO10$_C$ and human HBS1L3). A single-stranded C(*UC)$_{48}$ RNA internally labeled with ^{32}P at the uridine 5′-phosphate was incubated with proteins and nucleotides as indicated and treated with benzonase. The reaction products were analyzed by denaturing urea-PAGE. Note the increase in length of the RNA fragments when the cytoplasmic exosome was incubated with hSKI-Δarch, similar to the increase in length observed in the case of hMTR4 and the nuclear exosome complex (Gerlach et al., 2018). An SDS-PAGE of the proteins and complexes used in this assay is shown in Figure S7A.

(C) Model of the RNA channeling mechanism of the cytoplasmic SKI-exosome holocomplex compatible with the RNA path from (A). In this model, channeling is achieved by hSKI2 in the open-state conformation of hSKI with a similar overall path as observed for the nuclear exosome holocomplex (Gerlach et al., 2018; Schuller et al., 2018; Weick et al., 2018). Note that in context of the wild type, we expect that ATP hydrolysis is required in addition to ATP binding for transition to the hSKI open state and channeling to the exosome.

See also Figure S7.

for degradation (see also Halbach et al., 2013). The current biochemical and structural data suggest that the gatekeeping module dissociates from the hSKI2 helicase module to allow the RNA to progress to the cytoplasmic exosome core with a similar channeling path observed for the nuclear exosome holocomplex. In the context of the nuclear 14-subunit exosome holocomplex, it is likely that a similar gatekeeping mechanism is at play in hMTR4 co-factor complexes. The NEXT (hMTR4-ZCCHC8-RBM7) complex, an assembly that targets noncoding RNAs that are generated upon faulty transcription processes, is a prime candidate for such regulation: the C-terminal domain of hZCCHC8 binds the basal surface of the hMTR4 helicase (Puno and Lima, 2018) and positions Phe673 at the exit of the helicase channel at the equivalent position of hSKI2 W146 (Figure S5H). The similarities suggest parallel evolution of conserved regulatory mechanisms of exosome-associated Ski2-like helicases in different cellular compartments.

Limitations of the study

Conceptual and technical limitations pertain to the ability to further dissect the role of the Trp-containing wedge in a meaningful manner. First, the Trp-RNA interaction is one of the many

CellPress
OPEN ACCESS

RNA-binding interactions in the complex and by itself is unlikely to contribute significant in terms of K_d in biophysical measurements. Second, the wedge segment would only impact the initial opening step and as such it is not possible to measure the impact in bulk ATPase assays. Another limitation is that we cannot assign the exact nucleotides bound in hSKI2 when not using homopolymeric sequences (e.g., in the ribosome-bound structures) nor be sure of the identity of the 3′ end nucleotide. A further limitation is the multiple-days-long time used for the sample preparation in case of the ribosome-bound cryo-EM samples. Over this rather long processing time span, we cannot exclude potential dissociation of hSKI from the ribosome or reversal to the hSKI closed form.

STAR★METHODS

Detailed methods are provided in the online version of this paper and include the following:

- KEY RESOURCES TABLE
- RESOURCE AVAILABILITY
  - Lead contact
  - Materials availability
  - Data and code availability
- EXPERIMENTAL MODEL AND SUBJECT DETAILS
- METHOD DETAILS
  - Cloning, protein expression and purification
  - Ribosome subunit purification
  - *In vitro* transcription of RNA substrates
  - ATPase activity assays
  - Cytoplasmic exosome reconstitution
  - Size exclusion chromatography assays
  - RNase protection assays
  - Cryo-EM sample preparation
  - Cryo-EM data collection and processing
  - Density interpretation and model building
- QUANTIFICATION AND STATISTICAL ANALYSIS

SUPPLEMENTAL INFORMATION

Supplemental information can be found online at https://doi.org/10.1016/j.molcel.2022.01.009.

ACKNOWLEDGMENTS

We are grateful to Daniel Bollschweiler and Tillman Schäfer at the Max Planck Institute of Biochemistry (MPIB) cryo-EM facility for help with EM data collection and the MPIB core facilities for support. We thank Christian Benda and J. Rajan Prabu for maintenance and development of computational infrastructure for EM data processing, Courtney Long for help with the preparation of the manuscript, and members of the lab for discussions. This work was supported by funding from the Max-Planck-Gesellschaft, the European Commission (ERC Advanced Investigator Grant EXORICO), and the Deutsche Forschungsgemeinschaft (DFG SFB1035, GRK1721, SFB/TRR 237) to E.C.

AUTHOR CONTRIBUTIONS

E.C. and A. Kögel initiated the project; A. Kögel, A. Keidel, and F.B. designed and performed experiments; I.B.S. supervised the cryo-EM analyses; E.C., A. Kögel, A. Keidel, and I.B.S. wrote the manuscript.

DECLARATION OF INTERESTS

E.C. is a member of the *Molecular Cell* advisory board.

Received: September 24, 2021
Revised: December 1, 2021
Accepted: January 7, 2022
Published: February 3, 2022

REFERENCES

Afonine, P.V., Klaholz, B.P., Moriarty, N.W., Poon, B.K., Sobolev, O.V., Terwilliger, T.C., Adams, P.D., and Urzhumtsev, A. (2018a). New tools for the analysis and validation of cryo-EM maps and atomic models. Acta Crystallogr. D Struct. Biol. *74*, 814–840. https://doi.org/10.1107/S2059798318009324.

Afonine, P.V., Poon, B.K., Read, R.J., Sobolev, O.V., Terwilliger, T.C., Urzhumtsev, A., and Adams, P.D. (2018b). Real-space refinement in PHENIX for cryo-EM and crystallography. Acta Crystallogr. D Struct. Biol. *74*, 531–544. https://doi.org/10.1107/S2059798318006551.

Anderson, J.S., and Parker, R.P. (1998). The 3′ to 5′ degradation of yeast mRNAs is a general mechanism for mRNA turnover that requires the SKI2 DEVH box protein and 3′ to 5′ exonucleases of the exosome complex. EMBO J *17*, 1497–1506. https://doi.org/10.1093/emboj/17.5.1497.

Araki, Y., Takahashi, S., Kobayashi, T., Kajiho, H., Hoshino, S., and Katada, T. (2001). Ski7p G protein interacts with the exosome and the Ski complex for 3′-to-5′ mRNA decay in yeast. EMBO J *20*, 4684–4693. https://doi.org/10.1093/emboj/20.17.4684.

Bernstein, J., Ballin, J.D., Patterson, D.N., Wilson, G.M., and Toth, E.A. (2010). Unique properties of the Mtr4p-poly(A) complex suggest a role in substrate targeting. Biochemistry *49*, 10357–10370. https://doi.org/10.1021/bi101518x.

Bieniossek, C., Imasaki, T., Takagi, Y., and Berger, I. (2012). MultiBac: expanding the research toolbox for multiprotein complexes. Trends Biochem. Sci. *37*, 49–57. https://doi.org/10.1016/j.tibs.2011.10.005.

Biyani, N., Righetto, R.D., McLeod, R., Caujolle-Bert, D., Castano-Diez, D., Goldie, K.N., and Stahlberg, H. (2017). Focus: the interface between data collection and data processing in cryo-EM. J. Struct. Biol. *198*, 124–133. https://doi.org/10.1016/j.jsb.2017.03.007.

Bonneau, F., Basquin, J., Ebert, J., Lorentzen, E., and Conti, E. (2009). The yeast exosome functions as a macromolecular cage to channel RNA substrates for degradation. Cell *139*, 547–559. https://doi.org/10.1016/j.cell.2009.08.042.

Brown, J.T., Bai, X., and Johnson, A.W. (2000). The yeast antiviral proteins Ski2p, Ski3p, and Ski8p exist as a complex *in vivo*. RNA *6*, 449–457.

Büttner, K., Nehring, S., and Hopfner, K.-P. (2007). Structural basis for DNA duplex separation by a superfamily-2 helicase. Nat. Struct. Mol. Biol. *14*, 647–652. https://doi.org/10.1038/nsmb1246.

Chen, V.B., Arendall, W.B., Headd, J.J., Keedy, D.A., Immormino, R.M., Kapral, G.J., Murray, L.W., Richardson, J.S., and Richardson, D.C. (2010). MolProbity: all-atom structure validation for macromolecular crystallography. Acta Crystallogr. D Biol. Crystallogr. *66*, 12–21. https://doi.org/10.1107/S0907444909042073.

Chlebowski, A., Lubas, M., Jensen, T.H., and Dziembowski, A. (2013). RNA decay machines: the exosome. Biochim. Biophys. Acta *1829*, 552–560. https://doi.org/10.1016/j.bbagrm.2013.01.006.

Dobrev, N., Ahmed, Y.L., Sivadas, A., Soni, K., Fischer, T., and Sinning, I. (2021). The zinc-finger protein Red1 orchestrates MTREC submodules and binds the Mtl1 helicase arch domain. Nat. Commun. *12*, 3456. https://doi.org/10.1038/s41467-021-23565-3.

Dziembowski, A., Lorentzen, E., Conti, E., and Séraphin, B. (2007). A single subunit, Dis3, is essentially responsible for yeast exosome core activity. Nat. Struct. Mol. Biol. *14*, 15–22. https://doi.org/10.1038/nsmb1184.

Eckard, S.C., Rice, G.I., Fabre, A., Badens, C., Gray, E.E., Hartley, J.L., Crow, Y.J., and Stetson, D.B. (2014). The SKIV2L RNA exosome limits activation of

the RIG-I-like receptors. Nat. Immunol. *15*, 839–845. https://doi.org/10.1038/ni.2948.

Emsley, P., Lohkamp, B., Scott, W.G., and Cowtan, K. (2010). Features and development of coot. Acta Crystallogr. D Biol. Crystallogr. *66*, 486–501. https://doi.org/10.1107/S0907444910007493.

Fabre, A., Charroux, B., Martinez-Vinson, C., Roquelaure, B., Odul, E., Sayar, E., Smith, H., Colomb, V., Andre, N., Hugot, J.-P., et al. (2012). SKIV2L mutations cause syndromic diarrhea, or trichohepatoenteric syndrome. Am. J. Hum. Genet. *90*, 689–692. https://doi.org/10.1016/j.ajhg.2012.02.009.

Fabre, A., Martinez-Vinson, C., Roquelaure, B., Missirian, C., Andre, N., Breton, A., Lachaux, A., Odul, E., Colomb, V., Lemale, J., et al. (2011). Novel mutations in TTC37 associated with tricho-hepato-enteric syndrome. Hum. Mutat. *32*, 277–281. https://doi.org/10.1002/humu.21420.

Fabre, A., Martinez-Vinson, C., Goulet, O., and Badens, C. (2013). Syndromic diarrhea/tricho-hepato-enteric syndrome. Orphanet J. Rare Dis. *8*, 5. https://doi.org/10.1186/1750-1172-8-5.

Falk, S., Tants, J.-N., Basquin, J., Thoms, M., Hurt, E., Sattler, M., and Conti, E. (2017). Structural insights into the interaction of the nuclear exosome helicase Mtr4 with the pre-ribosomal protein Nop53. RNA *23*, 1780–1787. https://doi.org/10.1261/rna.062901.117.

Falk, S., Weir, J.R., Hentschel, J., Reichelt, P., Bonneau, F., and Conti, E. (2014). The molecular architecture of the TRAMP complex reveals the organization and interplay of its two catalytic activities. Mol. Cell *55*, 856–867. https://doi.org/10.1016/j.molcel.2014.07.020.

Fernández, I.S., Bai, X.-C., Murshudov, G., Scheres, S.H.W., and Ramakrishnan, V. (2014). Initiation of translation by cricket paralysis virus IRES requires its translocation in the ribosome. Cell *157*, 823–831. https://doi.org/10.1016/j.cell.2014.04.015.

Gerlach, P., Schuller, J.M., Bonneau, F., Basquin, J., Reichelt, P., Falk, S., and Conti, E. (2018). Distinct and evolutionary conserved structural features of the human nuclear exosome complex. Elife *7*, e38686. https://doi.org/10.7554/eLife.38686.

Goddard, T.D., Huang, C.C., Meng, E.C., Pettersen, E.F., Couch, G.S., Morris, J.H., and Ferrin, T.E. (2018). UCSF ChimeraX: meeting modern challenges in visualization and analysis. Protein Sci *27*, 14–25. https://doi.org/10.1002/pro.3235.

Halbach, F., Reichelt, P., Rode, M., and Conti, E. (2013). The yeast ski complex: crystal structure and RNA channeling to the exosome complex. Cell *154*, 814–826. https://doi.org/10.1016/j.cell.2013.07.017.

Halbach, F., Rode, M., and Conti, E. (2012). The crystal structure of *S. cerevisiae* Ski2, a DExH helicase associated with the cytoplasmic functions of the exosome. RNA *18*, 124–134. https://doi.org/10.1261/rna.029553.111.

Hellen, C.U.T. (2009). IRES-induced conformational changes in the ribosome and the mechanism of translation initiation by internal ribosomal entry. Biochim. Biophys. Acta *1789*, 558–570. https://doi.org/10.1016/j.bbagrm.2009.06.001.

Hoh, S.W., Burnley, T., and Cowtan, K. (2020). Current approaches for automated model building into cryo-EM maps using Buccaneer with CCP-EM. Acta Crystallogr. D Struct. Biol. *76*, 531–541. https://doi.org/10.1107/S2059798320005513.

Ikeuchi, K., Tesina, P., Matsuo, Y., Sugiyama, T., Cheng, J., Saeki, Y., Tanaka, K., Becker, T., Beckmann, R., and Inada, T. (2019). Collided ribosomes form a unique structural interface to induce Hel2-driven quality control pathways. EMBO J *38*, e100276. https://doi.org/10.15252/embj.2018100276.

Jackson, R.N., Klauer, A.A., Hintze, B.J., Robinson, H., van Hoof, A., and Johnson, S.J. (2010). The crystal structure of Mtr4 reveals a novel arch domain required for rRNA processing. EMBO J *29*, 2205–2216. https://doi.org/10.1038/emboj.2010.107.

Januszyk, K., and Lima, C.D. (2014). The eukaryotic RNA exosome. Curr. Opin. Struct. Biol. *24*, 132–140. https://doi.org/10.1016/j.sbi.2014.01.011.

Juszkiewicz, S., Chandrasekaran, V., Lin, Z., Kraatz, S., Ramakrishnan, V., and Hegde, R.S. (2018). ZNF598 is a quality control sensor of collided ribosomes. Mol. Cell *72*, 469–481.e7. https://doi.org/10.1016/j.molcel.2018.08.037.

Kalisiak, K., Kuliński, T.M., Tomecki, R., Cysewski, D., Pietras, Z., Chlebowski, A., Kowalska, K., and Dziembowski, A. (2017). A short splicing isoform of HBS1L links the cytoplasmic exosome and SKI complexes in humans. Nucleic Acids Res *45*, 2068–2080. https://doi.org/10.1093/nar/gkw862.

Khatter, H., Myasnikov, A.G., Natchiar, S.K., and Klaholz, B.P. (2015). Structure of the human 80S ribosome. Nature *520*, 640–645. https://doi.org/10.1038/nature14427.

Khemici, V., and Linder, P. (2018). RNA helicases in RNA decay. Biochem. Soc. Trans. *46*, 163–172. https://doi.org/10.1042/BST20170052.

Kowalinski, E., Kögel, A., Ebert, J., Reichelt, P., Stegmann, E., Habermann, B., and Conti, E. (2016). Structure of a cytoplasmic 11-subunit RNA exosome complex. Mol. Cell *63*, 125–134. https://doi.org/10.1016/j.molcel.2016.05.028.

Lee, W.S., Teo, K.M., Ng, R.T., Chong, S.Y., Kee, B.P., and Chua, K.H. (2016). Novel mutations in SKIV2L and TTC37 genes in Malaysian children with tricho-hepatoenteric syndrome. Gene *586*, 1–6. https://doi.org/10.1016/j.gene.2016.03.049.

Li, X., Burnight, E.R., Cooney, A.L., Malani, N., Brady, T., Sander, J.D., Staber, J., Wheelan, S.J., Joung, J.K., McCray, P.B., et al. (2013). piggyBac transposase tools for genome engineering. Proc. Natl. Acad. Sci. USA *110*, E2279–E2287. https://doi.org/10.1073/pnas.1305987110.

Liebschner, D., Afonine, P.V., Baker, M.L., Bunkóczi, G., Chen, V.B., Croll, T.I., Hintze, B., Hung, L.-W., Jain, S., McCoy, A.J., et al. (2019). Macromolecular structure determination using X-rays, neutrons and electrons: recent developments in Phenix. Acta Crystallogr. D Struct. Biol. *75*, 861–877. https://doi.org/10.1107/S2059798319011471.

Lingaraju, M., Johnsen, D., Schlundt, A., Langer, L.M., Basquin, J., Sattler, M., Heick Jensen, T., Falk, S., and Conti, E. (2019a). The MTR4 helicase recruits nuclear adaptors of the human RNA exosome using distinct arch-interacting motifs. Nat. Commun. *10*, 3393. https://doi.org/10.1038/s41467-019-11339-x.

Lingaraju, M., Schuller, J.M., Falk, S., Gerlach, P., Bonneau, F., Basquin, J., Benda, C., and Conti, E. (2019b). To process or to decay: a mechanistic view of the nuclear RNA exosome. Cold Spring Harb. Symp. Quant. Biol. *84*, 155–163. https://doi.org/10.1101/sqb.2019.84.040295.

Liu, Q., Greimann, J.C., and Lima, C.D. (2006). Reconstitution, activities, and structure of the eukaryotic RNA exosome. Cell *127*, 1223–1237. https://doi.org/10.1016/j.cell.2006.10.037.

Mitchell, P., Petfalski, E., Shevchenko, A., Mann, M., and Tollervey, D. (1997). The exosome: a conserved eukaryotic RNA processing complex containing multiple 3′→5′ exoribonucleases. Cell *91*, 457–466.

Olsen, K.J., and Johnson, S.J. (2021). Mtr4 RNA helicase structures and interactions. Biol. Chem. *402*, 605–616. https://doi.org/10.1515/hsz-2020-0329.

Ozgur, S., Buchwald, G., Falk, S., Chakrabarti, S., Prabu, J.R., and Conti, E. (2015). The conformational plasticity of eukaryotic RNA-dependent ATPases. FEBS J *282*, 850–863. https://doi.org/10.1111/febs.13198.

Perez-Riba, A., and Itzhaki, L.S. (2019). The tetratricopeptide-repeat motif is a versatile platform that enables diverse modes of molecular recognition. Curr. Opin. Struct. Biol. *54*, 43–49. https://doi.org/10.1016/j.sbi.2018.12.004.

Petrov, A., Grosely, R., Chen, J., O'Leary, S.E., and Puglisi, J.D. (2016). Multiple parallel pathways of translation initiation on the CrPV IRES. Mol. Cell *62*, 92–103. https://doi.org/10.1016/j.molcel.2016.03.020.

Pettersen, E.F., Goddard, T.D., Huang, C.C., Couch, G.S., Greenblatt, D.M., Meng, E.C., and Ferrin, T.E. (2004). UCSF Chimera—a visualization system for exploratory research and analysis. J. Comput. Chem. *25*, 1605–1612. https://doi.org/10.1002/jcc.20084.

Pisarev, A.V., Unbehaun, A., Hellen, C.U.T., and Pestova, T.V. (2007). Assembly and analysis of eukaryotic translation initiation complexes. Methods Enzymol *430*, 147–177. https://doi.org/10.1016/S0076-6879(07)30007-4.

Puno, M.R., and Lima, C.D. (2018). Structural basis for MTR4-ZCCHC8 interactions that stimulate the MTR4 helicase in the nuclear exosome-targeting

CellPress
OPEN ACCESS

complex. Proc. Natl. Acad. Sci. USA *115*, E5506–E5515. https://doi.org/10.1073/pnas.1803530115.

Rosenthal, P.B., and Henderson, R. (2003). Optimal determination of particle orientation, absolute hand, and contrast loss in single-particle electron cryomicroscopy. J. Mol. Biol. *333*, 721–745. https://doi.org/10.1016/j.jmb.2003.07.013.

Schaeffer, D., and van Hoof, A. (2011). Different nuclease requirements for exosome- mediated degradation of normal and nonstop mRNAs. Proc. Natl. Acad. Sci. USA *108*, 2366–2371. https://doi.org/10.1073/pnas.1013180108.

Schmid, M., and Jensen, T.H. (2019). The nuclear RNA exosome and its cofactors. Adv. Exp. Med. Biol. *1203*, 113–132. https://doi.org/10.1007/978-3-030-31434-7_4.

Schmidt, C., Kowalinski, E., Shanmuganathan, V., Defenouillère, Q., Braunger, K., Heuer, A., Pech, M., Namane, A., Berninghausen, O., Fromont-Racine, M., et al. (2016). The cryo-EM structure of a ribosome-Ski2-Ski3-Ski8 helicase complex. Science *354*, 1431–1433. https://doi.org/10.1126/science.aaf7520.

Schneider, C.A., Rasband, W.S., and Eliceiri, K.W. (2012). NIH Image to ImageJ: 25 years of image analysis. Nat. Methods *9*, 671–675. https://doi.org/10.1038/nmeth.2089.

Schorb, M., Haberbosch, I., Hagen, W.J.H., Schwab, Y., and Mastronarde, D.N. (2019). Software tools for automated transmission electron microscopy. Nat. Methods *16*, 471–477. https://doi.org/10.1038/s41592-019-0396-9.

Schüler, M., Connell, S.R., Lescoute, A., Giesebrecht, J., Dabrowski, M., Schroeer, B., Mielke, T., Penczek, P.A., Westhof, E., and Spahn, C.M.T. (2006). Structure of the ribosome-bound cricket paralysis virus IRES RNA. Nat. Struct. Mol. Biol. *13*, 1092–1096. https://doi.org/10.1038/nsmb1177.

Schuller, J.M., Falk, S., Fromm, L., Hurt, E., and Conti, E. (2018). Structure of the nuclear exosome captured on a maturing preribosome. Science *360*, 219–222. https://doi.org/10.1126/science.aar5428.

Stirnimann, C.U., Petsalaki, E., Russell, R.B., and Müller, C.W. (2010). WD40 proteins propel cellular networks. Trends Biochem. Sci. *35*, 565–574. https://doi.org/10.1016/j.tibs.2010.04.003.

Synowsky, S.A., and Heck, A.J.R. (2008). The yeast Ski complex is a hetero-tetramer. Protein Sci *17*, 119–125. https://doi.org/10.1110/ps.073155908.

Thoms, M., Thomson, E., Baßler, J., Gnädig, M., Griesel, S., and Hurt, E. (2015). The exosome is recruited to RNA substrates through specific adaptor proteins. Cell *162*, 1029–1038. https://doi.org/10.1016/j.cell.2015.07.060.

Toh-E, A., Guerry, P., and Wickner, R.B. (1978). Chromosomal superkiller mutants of *Saccharomyces cerevisiae*. J. Bacteriol. *136*, 1002–1007.

Tomecki, R., Kristiansen, M.S., Lykke-Andersen, S., Chlebowski, A., Larsen, K.M., Szczesny, R.J., Drazkowska, K., Pastula, A., Andersen, J.S., Stepien, P.P., et al. (2010). The human core exosome interacts with differentially localized processive RNaseS: hDIS3 and hDIS3L. EMBO J *29*, 2342–2357. https://doi.org/10.1038/emboj.2010.121.

Tuck, A.C., Rankova, A., Arpat, A.B., Liechti, L.A., Hess, D., Iesmantavicius, V., Castelo-Szekely, V., Gatfield, D., and Bühler, M. (2020). Mammalian RNA decay pathways are highly specialized and widely linked to translation. Mol. Cell *77*, 1222–1236.e13. https://doi.org/10.1016/j.molcel.2020.01.007.

Tunyasuvunakool, K., Adler, J., Wu, Z., Green, T., Zielinski, M., Žídek, A., Bridgland, A., Cowie, A., Meyer, C., Laydon, A., et al. (2021). Highly accurate protein structure prediction for the human proteome. Nature *596*, 590–596. https://doi.org/10.1038/s41586-021-03828-1.

Wang, J., Chen, J., Wu, G., Zhang, H., Du, X., Chen, S., Zhang, L., Wang, K., Fan, J., Gao, S., et al. (2019). NRDE2 negatively regulates exosome functions by inhibiting MTR4 recruitment and exosome interaction. Genes Dev *33*, 536–549. https://doi.org/10.1101/gad.322602.118.

Weick, E.-M., and Lima, C.D. (2021). RNA helicases are hubs that orchestrate exosome-dependent 3′-5′ decay. Curr. Opin. Struct. Biol. *67*, 86–94. https://doi.org/10.1016/j.sbi.2020.09.010.

Weick, E.-M., Puno, M.R., Januszyk, K., Zinder, J.C., DiMattia, M.A., and Lima, C.D. (2018). Helicase-dependent RNA decay illuminated by a cryo-EM structure of a human nuclear RNA exosome-MTR4 complex. Cell *173*, 1663–1677.e21. https://doi.org/10.1016/j.cell.2018.05.041.

Weir, J.R., Bonneau, F., Hentschel, J., and Conti, E. (2010). Structural analysis reveals the characteristic features of Mtr4, a DExH helicase involved in nuclear RNA processing and surveillance. Proc. Natl. Acad. Sci. USA *107*, 12139–12144. https://doi.org/10.1073/pnas.1004953107.

Winz, M.L., Peil, L., Turowski, T.W., Rappsilber, J., and Tollervey, D. (2019). Molecular interactions between Hel2 and RNA supporting ribosome-associated quality control. Nat. Commun. *10*, 563. https://doi.org/10.1038/s41467-019-08382-z.

Zhang, E., Khanna, V., Dacheux, E., Namane, A., Doyen, A., Gomard, M., Turcotte, B., Jacquier, A., and Fromont-Racine, M. (2019). A specialised SKI complex assists the cytoplasmic RNAexosome in the absence of direct association with ribosomes. EMBO J *38*, e100640. https://doi.org/10.15252/embj.2018100640.

Zhang, K. (2016). Gctf: real-time CTF determination and correction. J. Struct. Biol. *193*, 1–12. https://doi.org/10.1016/j.jsb.2015.11.003.

Zheng, S.Q., Palovcak, E., Armache, J.-P., Verba, K.A., Cheng, Y., and Agard, D.A. (2017). MotionCor2: anisotropic correction of beam-induced motion for improved cryo-electron microscopy. Nat. Methods *14*, 331–332. https://doi.org/10.1038/nmeth.4193.

Zinoviev, A., Ayupov, R.K., Abaeva, I.S., Hellen, C.U.T., and Pestova, T.V. (2020). Extraction of mRNA from stalled ribosomes by the ski complex. Mol. Cell *77*, 1340–1349.e6. https://doi.org/10.1016/j.molcel.2020.01.011.

Zivanov, J., Nakane, T., Forsberg, B.O., Kimanius, D., Hagen, W.J., Lindahl, E., and Scheres, S.H. (2018). New tools for automated high-resolution cryo-EM structure determination in RELION-3. Elife *7*, e42166. https://doi.org/10.7554/eLife.42166.

STAR★METHODS

KEY RESOURCES TABLE

REAGENT or RESOURCE	SOURCE	IDENTIFIER
Bacterial and virus strains		
Escherichia coli BL21 (DE3) STAR pRARE	EMBL Heidelberg Core Facility	N/A
Chemicals, peptides, and recombinant proteins		
Sf-900 II SFM medium	Thermo Fisher Scientific	10902096
FreeStyle 293 Expression Medium	Thermo Fisher Scientific	12338018
Polyethylenimine	Polysciences, Inc.	23966
cOmplete protease inhibitor	Roche	5056489001
NuPAGE 4-12% Bis-Tris protein gels	Thermo Fisher Scientific	NP0336BOX
H. sapiens SKI2-SKI3-SKI8 and derivative complexes	This study	N/A
H. sapiens HBS1L3	This study	N/A
H. sapiens hEXO9	Kowalinski et al., 2016	N/A
H. sapiens $DIS3L_{D486N}$	This study	N/A
H. sapiens 40S/60S ribosomal subunits	This study	N/A
T7 RNA Polymerase	MPI Biochemistry Core Facility	N/A
ATP, CTP, GTP, UTP	Jena Bioscience	NU-1010 – 1013
[α^{32}P] UTP	PerkinElmer	NEG007X250UC
DNase I	Roche	4716728001
Benzonase	Merck	71206
ATP	Sigma-Aldrich	A3377
ADP	Sigma-Aldrich	A2754
NADH	Sigma-Aldrich	N4505
Pyruvate kinase/Lactate dehydrogenase	Sigma-Aldrich	P0294
Phosphoenolpyruvate	Sigma-Aldrich	P0564
poly(U) RNA	Sigma-Aldrich	P9528
n-octyl-ß-D-glucoside	Sigma-Aldrich	850511P
BS_3 (bis(sulfosuccinimidyl)suberate)	Thermo Fisher Scientific	A39266
Deposited data		
apo open hSKI cryoEM map and model	This paper	EMD-13925; PDB: 7QDS
apo closed hSKI cryoEM map and model	This paper	EMD-13923; PDB: 7QDR
RNA-bound closed hSKI cryoEM map and model	This paper	EMD-13927; PDB: 7QDY
ribosome-bound closed hSKI complex cryoEM map and model	This paper	EMD-13928; PDB: 7QDZ
ribosome-bound open hSKI complex cryoEM map and model	This paper	EMD-13929; PDB: 7QE0
Raw and analyzed data	This paper	Mendeley doi:10.17632/9w78m35s2v.1
Experimental models: Cell lines		
Spodoptera frugiperda 21 (*Sf21*)	Thermo Fisher Scientific	11497013
Human embryonic kidney 293T (HEK293T)	ATCC	CRL-3216
Oligonucleotides		
$GGGC(*UC)_{48}$_T7_fwd AATTTAATACGACTCACTATA GG	Sigma-Aldrich	N/A
$GGGC(*UC)_{48}$_rev GAGAGAGAGAGAGAGAGAGAGAG AGAGAGAGAGAGAGAGAGAGAGAGAGAGAGAGAGAGAGA GAGAGAGAGAGAGAGAGAGAGAGAGAGA GAGAGCCCTATAGTGAGTCGTATTAAATT	Sigma-Aldrich	N/A

(*Continued on next page*)

Continued		
REAGENT or RESOURCE	SOURCE	IDENTIFIER
IRES29_T7_fwd TAATACGACTCACTATAGGGAAAAA TGTGATCTTGCTTGTAAATAC	Sigma-Aldrich	N/A
IRES29_rev GCGTCTTCCATGGTATCTTG	Sigma-Aldrich	N/A
25U RNA	Sigma-Aldrich	N/A
Recombinant DNA		
pACEBac1-hSKI2-10xHIS-3C-hSKI3-hSKI8 and derivative plasmids	This study	N/A
pEC-6HIS-3C-HBS1L3-$(GS)_3$-eGFP-TS	This study	N/A
pPB-TS-3C-hDIS3L_{D486N}	This study	N/A
pUC-CrPV-IRES-luciferase	This study	N/A
Software and algorithms		
SerialEM	Schorb et al., 2019	https://bio3d.colorado.edu/SerialEM/
Focus	Biyani et al., 2017	https://www.focus-em.org
MotionCor2	Zheng et al., 2017	https://msg.ucsf.edu/software/
Gctf	Zhang, 2016	https://www2.mrc-lmb.cam.ac.uk/kzhang/
Gautomatch	N/A	https://www2.mrc-lmb.cam.ac.uk/kzhang/
RELION 3.0/3.1	Zivanov et al., 2018	https://www3.mrc-lmb.cam.ac.uk/relion/
AlphaFold	Tunyasuvunakool et al., 2021	https://alphafold.ebi.ac.uk/
Buccaneer	Hoh et al., 2020	https://phenix-online.org/
Phenix.real_space_refine	Afonine et al., 2018a	https://phenix-online.org/
Phenix.mtriage	Afonine et al., 2018b	https://phenix-online.org/
Coot	Emsley et al., 2010	https://www2.mrc-lmb.cam.ac.uk/personal/pemsley/coot/
PyMOL2	N/A	https://pymol.org/2/
UCSF Chimera	Pettersen et al., 2004	https://www.cgl.ucsf.edu/chimera/
UCSF ChimeraX	Goddard et al., 2018	https://www.cgl.ucsf.edu/chimerax/
ImageJ	Schneider et al., 2012	https://imagej.nih.gov/ij/
Tidyverse	N/A	https://www.tidyverse.org/
Illustrator	Adobe	https://www.adobe.com
Prism9	GraphPad	https://www.graphpad.com
Other		
HisTrap HP 5ml	Cytiva	17524805
Mono Q 5/50 GL	Cytiva	17516601
Superose 6 Increase 10/300 GL	Cytiva	29091596
StrepTrap HP 5 mL	Cytiva	28907548
Mono S 5/50 GL	Cytiva	17516801
Superdex 200 Increase 10/300 GL	Cytiva	28990944
Superose 6 Increase 3.2/300	Cytiva	29091598
Amicon Ultra MWCO100	Merck	UFC9100
Quantifoil R2/1 Cu 200 mesh	Quantifoil	Q210CR1
Quantifoil R2/1 Cu 200 mesh carbon supported	Quantifoil	Q210CR1-2nm

RESOURCE AVAILABILITY

Lead contact

Further information and requests for resources and reagents should be directed to and will be fulfilled by the lead contact, Elena Conti (conti@biochem.mpg.de).

Materials availability

This study did not generate new unique reagents.

Data and code availability

- Cryo-EM density maps have been deposited in the Electron Microscopy Data Bank (EMDB) and the Protein Data Bank (PDB), respectively, under the accession numbers: EMD-13923 (apo human SKI complex in the closed state, PDB: 7QDR), EMD-13925 (apo human SKI complex in the open state, PDB: 7QDS), EMD-13927 (RNA-bound human SKI complex, PDB: 7QDY), EMD-13928 (80S-bound human SKI complex in the closed state, PDB: 7QDZ) and EMD-13929 (80S-bound human SKI complex in the open state, PDB: 7QE0). Data are available at time of publication.
- Unprocessed and uncompressed imaging data is available at Mendeley Data: https://doi.org/10.17632/9w78m35s2v.1.
- This paper does not report original code.
- Any additional information required to reanalyse the data reported in this work/paper is available from the lead contact upon request.

EXPERIMENTAL MODEL AND SUBJECT DETAILS

All bacterial and eukaryotic cell lines in this study were used for protein production for in vitro experiments, rather than being experimental models in the typical sense. They are listed in the key resources table.

Recombinant proteins were either cloned or synthesized as described in the method details. *Spodoptera frugiperda 21* (*Sf21*) cells were maintained in Sf-900 II SFM medium (Thermo Fisher Scientific) at 27°C. *Escherichia coli* expression strains BL21 STAR pRARE (Thermo Fisher Scientific) were grown in TB medium at 37°C under antibiotic selection to an OD_{600nm} = 2 before inducing protein expression by adding 500 μM IPTG for 16 h at 18°C. HEK 293T cells were adapted to grow in suspension and stable transfected using the piggyBac transposon system (Li et al., 2013). Cells were maintained in FreeStyle 293 Expression medium (Thermo Fisher Scientific) at 37°C and 5% CO_2 and protein expression induced by adding 1 μg/mL doxycycline.

METHOD DETAILS

Cloning, protein expression and purification

The complete open reading frames of *SKIV2L*, *TTC37*, and *WDR61* (UniProt: Q6PGP7, Q15477, Q9GZS3) were cloned from a human cDNA library (MegaMan Human Transcriptome Library, Agilent Technologies) into separate expression cassettes on a single pACEBac1 vector (Bieniossek et al., 2012). A 3C protease cleavable 10xHis-tag on the *TTC37* N-terminus for immobilized metal affinity chromatography (IMAC) was added to all human SKI complex constructs (wild-type, E424Q, V341G, Δwedge, Δarch). The vector was integrated into an engineered baculovirus genome (Bieniossek et al., 2012) and cultured in *Sf21* cells for virus production. *Sf21* cells suspended at 10^6 cells/mL were infected with virus and cultured in Sf-900 II SFM medium at 27°C. Cultures were harvested after 72 h by centrifugation at 2000 g. Cell pellets were resuspended in lysis buffer containing 20 mM Hepes pH7.5, 200 mM NaCl, 25 mM Imidazole and 2mM ß-mercaptoethanol (ß-ME), and supplemented with 200 U/mL benzonase (Merck), 500 μM AEBSF protease inhibitor, and cOmplete EDTA-free protease inhibitor cocktail (Roche). The cells were lysed by ultrasonication (Bandelin, Sonopuls basic). The lysate was cleared by centrifugation at 75,000 g and subjected to a HisTrap HP 5ml column (GE Healthcare) for IMAC. The column was washed with 15 column volumes of 20 mM Hepes pH7.5, 1000 mM NaCl, 200 mM KCl, 10 mM $MgCl_2$, 25 mM Imidazole and 2 mM ß-ME, followed by washing with 5 column volumes of lysis buffer. Protein was eluted in lysis buffer supplemented with 350 mM Imidazole. The eluate was treated with 10 μg/mL His-tagged 3C protease (MPI Biochemistry Core Facility) during overnight dialysis against 20 mM Hepes pH7.5, 100 mM NaCl, 25 mM Imidazole and 2mM ß-ME. 3C protease and His-tags were removed by running the eluate over IMAC. The unbound protein fraction was further purified by ion exchange (Mono Q 5/50 GL, GE Healthcare) and size exclusion chromatography (Superose 6 Increase 10/300 GL, GE Healthcare), and eluted in a final buffer containing 20 mM Hepes pH7.5, 100 mM NaCl, 2 mM Dithiothreitol (DTT).

The complete open reading frame of the HBS1L3 (UniProt: Q9Y450) was commercially synthesized (Eurofins Genomics) and cloned with N-terminal 6xHis-thioredoxin and C-terminal eGFP-TwinStrep tags under a IPTG-inducible promotor for expression in *E. coli*. Transformed *E. coli* BL21 STAR pRARE cells were grown in TB medium at 37°C under antibiotic selection to OD_{600nm} = 2. The temperature was reduced to 18°C and protein expression was induced by addition of 500 μM IPTG. Cells were harvested after 16 h by centrifugation at 8,500 g. Cells were ultrasonicated in the same lysis buffer as above, except it contained 300 mM NaCl. The recombinant protein was kept strictly at 4°C and the purification procedure was processed quickly to avoid degradation. The lysate was cleared by centrifugation and loaded on a HisTrap HP 5 mL column (GE Healthcare) for IMAC. Washing was performed as above, and the protein was eluted and equilibrated with lysis buffer supplemented with 350 mM Imidazole into a StrepTrap HP 5 mL column (GE Healthcare) for a second affinity step. The bound protein was washed with 10 column volumes of buffer containing 20 mM Hepes pH7.5, 300 mM NaCl, 2 mM DTT and addition of 5 mM Desthiobiotin (DTB) eluted the protein. The protein was concentrated in 10 % Glycerol (v/v), flash frozen in liquid nitrogen (LN_2), and stored at -80°C.

The complete open reading frame human DIS3L (UniProt: Q8TF46) with the inactivating D486N mutation (DIS3L$_{D486N}$) was tagged with TwinStrep at the N-terminus and expressed in a HEK 293T stable cell line adapted to grow in suspension. Briefly, HEK 293T cells at 10^6 cells/mL were transfected in FreeStyle 293 Expression Medium (Thermo Fisher Scientific) with hDIS3L cloned into the piggyBac vector with a doxycycline-dependant inducible promoter (Li et al., 2013), the piggyBac transactivator and the hyperactive piggyBac transposase using polyethylenimine (PEI). After a 24 h recovery period, cells were positively selected for 21 days using puromycin and geneticin. 400-800 mL of stably transfected cells (10^6 cells/mL) were induced with 1 μg/mL doxycycline for 48 h and harvested by centrifugation at 800 g. Cells were resuspended in buffer containing 20 mM Hepes pH7.5, 300 mM NaCl, and 2 mM DTT and lysed using a dounce homogeniser. After clearing the lysate by centrifugation, it was loaded on a StrepTrap HP 5 mL column (GE Healthcare) and washed with high salt and lysis buffer (similar to hSKI). The protein was eluted in buffer containing 20 mM Hepes pH7.5, 100 mM NaCl, 5 mM DTB, and 2 mM DTT.

Ribosome subunit purification

Ribosomal 40S and 60S subunits were obtained from untransfected HEK 293T cells (using adapted protocols from Fernández et al. (2014) and Pisarev et al. (2007). 600 x 10^6 cells were pelleted and resuspended on ice for 30 min in lysis buffer containing 20 mM Hepes pH7.5, 300 mM NaCl, 6 mM $MgCl_2$, 0.5 % NP40 (v/v), 2 mM DTT, 500 μM AEBSF. The lysate was cleared by centrifugation at 10,000 g for 15 min and loaded on a 30% sucrose cushion in buffer containing 20 mM Hepes pH7.5, 150 mM KCl, 10 mM $MgCl_2$, 2 mM DTT, followed by ultracentrifugation in a TLA-100.3 rotor (Beckman Coulter) at 86,000 RPM for 90 min. The ribosomal pellets were resuspended in buffer containing 20 mM Hepes pH7.5, 75 mM KCl, 5 mM $MgCl_2$, 2 mM DTT, supplemented with 2 mM puromycin and incubated at 37°C for 15 min. The ribosome solution was then adjusted to 500 mM KCl and subjected to gradient centrifugation in a SW-40 Ti rotor (Beckman Coulter). The sucrose gradients (10-30% w/v) used for centrifugation were diluted in buffer containing 20 mM Hepes pH7.5, 500 mM KCl, 4 mM $MgCl_2$, and 2 mM DTT and mixed using a Gradient Station (Biocomp). After 17 h centrifugation at 22,8000 RPM, the gradients were fractionated from the top (Gradient Station, Biocomp). Fractions corresponding to 40S and 60S ribosomal subunits were pooled separately and concentrated in buffer containing 20 mM Hepes pH7.5, 50 mM KCl, 4 mM $MgCl_2$, and 2 mM DTT.

In vitro transcription of RNA substrates

The sequence of the CrPV IRES construct was taken from the intergenic region of the Cricket paralysis virus genome (NCBI GeneBank: 6025-6232 nt, NC_003924.1). The CrPV IRES was transcribed *in vitro* with T7 RNA polymerase by run-off transcription. The genomic sequence of the CrPV IRES was fused to a portion of the firefly luciferase open reading frame (modified from Petrov et al. [2016]). The CrPV-IRES29 construct was amplified by PCR and then gel purified. *In vitro* transcription of 100 nM CrPV IRES DNA template was carried out in 40 mM Tris-HCl pH8.0, 28 mM $MgCl_2$, 0.01% Triton X-100, 1 mM Spermidine, 5 mM DTT in the presence of 25 mM of each ribonucleotide (ATP, CTP, GTP, UTP, Jena Bioscience) and 100 U/μL T7 RNA Polymerase (MPI Biochemistry Core Facility) at 37°C for 4 h. The DNA template was digested with 1 U/μL DNase I (Roche) and purified by $LiCl_2$ precipitation.

The radioactive body-labelled GGGC(*UC)$_{48}$ RNA was transcribed similarly using an annealed duplex of two DNA oligos (5'-AATT TAATACGACTCACTATAGG-3' and 5'-TTAAATTATGCTGAGTGATATCCCGAGAGAGAGAGAGAGAGAGAGAGAGAGA GAGAGA GAGAGAGAGAGAGAGAGAGAGAGAGAGAGAGAGAGAGAGAGAGAGAGAGAGAGAGAG-3') as a template. Transcription of 0.1 μM template DNA was carried out in the same buffer containing nucleotides as above but with the addition of 1.5 μM radioactive [α^{32}P] UTP (PerkinElmer). After 4 h at 37°C and DNase I treatment, the reaction was phenol extracted, ethanol precipitated and gel purified from an 8% 7M Urea PAGE. The incorporation rate of [α^{32}P] UTP and final transcript concentration were quantified using a liquid scintillation counter (Hidex 300 SL).

ATPase activity assays

ATPase activity of human SKI complex and derivates were measured using a pyruvate kinase/lactate dehydrogenase enzyme-coupled assay (Bernstein et al., 2010). Reactions were prepared as serial two-fold dilutions of 2.5 mM ATP in buffer containing 50 mM Hepes pH7.5, 50 mM KAc, 5 mM $MgAc_2$, 2 mM DTT and 10 μg/mL poly(U) RNA (Sigma). After 20 min equilibration at 37°C, the reactions were started by adding 50 nM hSKI complex. NADH oxidation was monitored at 1 min intervals over the time course of 20 min by measuring absorbance at 340 nm using an infinite M1000PRO 96-well Plate reader (Tecan). All measurements were done in triplicates. A baseline oxidation level of NADH was established by measuring duplicate reactions without the addition of protein (see below for quantification and statistical analysis).

Cytoplasmic exosome reconstitution

Human cytoplasmic exosome (hEXO10$_c$ with the inactivated hDIS3L$_{D486N}$ nuclease) was reconstituted from equal molecular amounts of pre-assembled hEXO9 (purified as previously described) and freshly purified hDIS3L$_{D486N}$. After incubation for 30 min on ice, the salt concentration was adjusted to 50 mM NaCl. The reconstituted hEXO10$_c$ wild-type and mutant complexes were subjected to ion-exchange chromatography (Mono S 5/50 GL, GE Healthcare) and size exclusion chromatography (Superdex 200 Increase 10/300 GL, GE Healthcare) in a final buffer containing 20 mM Hepes pH7.5, 100 mM NaCl, and 2 mM DTT.

Size exclusion chromatography assays

Size exclusion chromatography studies were carried out sequentially over the course of one day using a Superose 6 Increase 3.2/300 (GE Healthcare) column and a buffer containing 20 mM Hepes pH7.5, 150 mM NaCl, and 2 mM DTT. The samples were prepared by mixing substoichiometric amounts of HBS1L3 with either 100 pmol hSKI (blue chromatogram in Figure 7A), or 100 pmol hEXO10$_c$ (red chromatogram in Figure 7A), or 100 pmol hSKI and 100 pmol hEXO10$_c$ (purple chromatogram in Figure 7A). In order to show that HBS1L3 is required to bridge the interaction between hSKI and hEXO10$_c$ and to from a higher order complex, 100 pmol hSKI with 100 pmol hEXO10$_c$ were mixed in absence of HBS1L3 (green chromatogram in Figure 7A). The samples were adjusted to 35 µl with buffer and incubated at 4°C for 15 min before injecting them onto the column. The absorbance at 280 nm was recorded in the chromatograms. For comparison of the retention volumes of the different complexes, the data was normalised and plotted in R using the tidyverse collection of R packages. Peak fractions of the individual gel filtration runs were TCA precipitated and analysed by SDS-PAGE on a NuPAGE 4-12% Bis-Tris gel (Thermo Fisher Scientific).

RNase protection assays

The cytoplasmic exosome complexes (Figure S7A) were concentrated at 500 nM and incubated with 125 nM radioactive body-labelled GGGC(*UC)$_{48}$ substrate in buffer containing 50 mM Hepes pH7.5, 50 mM NaCl, 5 mM $MgCl_2$, 10% Glycerol, 0.1% NP40, 2 mM DTT, and 1 mM ADP-BeF (premixed 1 mM ADP with 1 mM $BeCl_2$ and 5 mM NaF). After 60 min at 4°C to allow for the formation of the ribonucleoprotein complexes, the samples were RNase treated with 37.5 U/µL nM benzonase (Merck) at 25°C for 20 min. The reaction was stopped by adding 10x excess buffer containing 100 mM Tris-HCl pH7.5, 150 mM NaCl, 300 mM NaAc pH.5.2, 10 mM EDTA, and 1% SDS. The RNase protected RNA fragments were purified by phenol extraction and ethanol precipitation, separated on a denaturing 12% polyacrylamide gel containing 7M Urea, and analysed by phosphorimaging (Typhoon FLA7000, Cytiva).

Cryo-EM sample preparation

The substrate-free human SKI complex sample was prepared by concentrating 600 pmol of purified hSKI in buffer containing 20 mM Hepes pH7.5, 100 mM NaCl, and 2 mM DTT to approximately 30 µl. The sample was then crosslinked with 1.5 mM bissulfosuccinimidyl suberate (BS_3) at RT for 20 min and quenched with 5 mM Tris-HCl pH7.5. After centrifugation at 18,000 RCF for 10 min to pellet larger aggregates, the sample was injected onto a Superose 6 Increase 3.2/300 column (GE Healthcare) for size exclusion chromatography by an Aekta micro (GE Healthcare). A single peak fraction (containing approximately 500 nM) was collected and mixed with 0.04 % (v/v) n-octyl-ß-D-glucoside. 4-5 µl of the sample were applied to holey carbon grids (R2/1, 200 mesh, Quantifoil) and glow discharged with negative polarity at 20 mA for 30 sec using an EMS GloQube (MiTeGen). The sample was plunge frozen in a liquid ethane/propane mix using a Vitrobot Mark IV (Thermo Fisher Scientific) operated at 4°C and 95% humidity. Although we only show data from the samples prepared as above, we also prepared the substrate-free human SKI complex without addition of BS3 crosslinking and found similar distributions of closed and open state particles.

Substrate-bound human SKI was prepared in a similar manner as the substrate-free complex above with a few exceptions. Comparable amounts of purified hSKI were concentrated in buffer containing 20 mM Hepes pH7.5, 100 mM NaCl, 2 mM $MgCl_2$, 2 mM DTT, and supplemented with 1.5x molar excess of a 25-uracil RNA (Sigma) and 2 mM ADP-BeF. After incubation at 37°C for 15 min, the reconstituted complex was subjected to size exclusion chromatography and a single peak fraction was processed further without any BS3 crosslinking as described above.

The samples containing the 80S ribosome bound to human SKI complexes were prepared as follows: 100 pmol of purified human 40S was mixed with 150 pmol CrPV IRES carrying a 29 nt 3' overhang in buffer containing 20 mM Hepes pH7.5, 50 mM KCl, 4 mM $MgCl_2$, and 2 mM DTT. After incubation at 37°C for 5 min, 120 pmol human 60S was added and incubation proceeded for another 10 min. 200 pmol of purified substrate-free human SKI complex was added to the 80S-CrPV-IRES-29nt complex. The total volume was adjusted to 200 µl with the above buffer and incubated at 37°C for another 15 min before the sample was placed at 4°C for further treatment. The samples were either incubated with 2 mM ADP-BeF or 1 mM ATP at 37°C for 15 min. ATP treatment was followed by addition of 2 mM ADP-BeF for another 15 min at 37°C to block the ATPase activity of hSKI. The samples were subjected to gradient centrifugation in a SW-40 Ti rotor (Beckman Coulter) at 4°C. 15-40% sucrose gradients (w/v) in buffer containing 20 mM Hepes pH7.5, 50 mM KCl, 4 mM $MgCl_2$, and 2 mM DTT were mixed using the Gradient Master (Biocomb). After 17 h centrifugation at 22,800 RPM, the gradients were fractionated using a Piston Gradient Fractionator (Biocomb). Fractions corresponding to the 80S-CrPV-IRES-SKI complex were concentrated in buffer containing 20 mM Hepes pH7.5, 50 mM KCl, 4 mM $MgCl_2$, and 2 mM DTT by centrifugation at 3,000 RCF using an Amicon Ultra MWCO100 centricon (Millipore). The concentrated samples at an OD_{260} of approximately 8 was supplemented with 0.04 % (v/v) n-octyl-ß-D-glucoside and subsequently used for plunge freezing. The sample was incubated twice for 2 min on carbon supported grids (R2/1, 200 mesh, Quantifoil), previously glow discharged with negative polarity at 20 mA for 20 sec using an EMS GloQube (MiTeGen). Plunge freezing was otherwise carried out as for the substrate-free sample above.

Cryo-EM data collection and processing

The cryo-EM data from substrate-free human SKI were collected on a FEI Titan Krios microscope (Thermo Fisher Scientific) at 300 kV equipped with a Gatan K3 direct electron detector operating in electron counting mode. The microscope is equipped with a post column energy filter set to slit-width of 20 eV. Images were collected by under-focused acquisition (target range

of -0.6 and -2.4 μm) at a nominal magnification of 81,000x set up in SerialEM (Schorb et al., 2019) utilising a beam-tilt based multi-shot acquisition scheme for faster imaging. This resulted in 11,079 micrograph movies (40 movie frames each) acquired at a pixel size of 1.094 Å/pixel with a total exposure of 47.44 e/Å^2 over 4 sec. The collected data were processed in RELION 3.0 and 3.1 (Zivanov et al., 2018). To correct for beam-induced motions and minimize effects of radiation damage, the raw movie frames were aligned using MotionCor2 (Zheng et al., 2017). The aligned micrographs were used to estimate per-micrograph contrast transfer function (CTF) parameters with GCTF (Zhang, 2016). Initial particles (4,400,241) were selected using Gautomatch (http://www.mrc-lmb.cam.ac.uk/kzhang/). Four times down-sampled particles were extracted from the aligned, exposure-weighted micrographs. Reference-free 2D classification and classification in 3D using a 40 Å low-pass filtered starting model based on the crystal structure of the yeast SKI complex (PDB: 4BUJ) resulted in an intermediate subset of 350,147 well-aligning hSKI particles. 3D classification of this particle subset, extracted at the original pixel size, into six classes gave three reconstructions of human SKI complex in the closed state (global resolutions ranging from 8.4 to 10.6 Å), one reconstruction in the open state (9.2 Å), and two at lower resolution. A 40 Å low-pass filtered reconstruction of the closed state complex served as a starting model for the classification. Accuracy and resolution of the reconstructions could be improved by extending to 40 iterations of classification. However, it proved difficult to quantify an equilibrium between open and closed state particles from this classification, in part because a large portion of the particles, e.g. the gatekeeping module, adopts a very similar conformation in the two states. Therefore, we deliberately biased the classification of a particle subset after an initial round of 2D classification using 30 Å low-pass filtered open and closed state starting models (Figure S1). These classifications suggest a particle distribution of roughly 40% in closed and 60% in open state. The classification procedures resulted in two homogenous subsets of particles for open and closed state human SKI complex. Their reconstructions reached a global nominal resolution of 3.7 Å and 3.8 Å after masked 3D auto-refinement and automatic b-factor sharpening (-88.1 and -145.3) in the RELION post-processing routine (Zivanov et al., 2018) according to the Fourier shell correlation (FSC) cut-off criterion for the independent half maps of 0.143 (Rosenthal and Henderson, 2003). Peripheral regions of the reconstructions, particularly for the closed state, could be improved by focused refinements with local searches. Masks were applied to TPRs 34-40 of hSKI3$_C$, hSKI2$_{cat}$, hSKI2$_{arch}$ and the hSKI2$_N$ outer segments to improve local resolutions and volume connectivity.

Substrate-bound human SKI data were collected similar to the substrate-free complex above, but at 105,000x nominal magnification. A total of 11,413 micrograph movies were acquired at a pixel size 0.8512 Å/pixel with a total exposure of 68.31 e/Å^2 over 3 sec and spread over 30 movie frames. Beam-induced motion correction, CTF estimation, particle picking, and processing were done in a similar way as for the substrate-free data. 6,036,405 down-scaled particles were initially extracted from the aligned, exposure-weighted micrographs and particles that appeared to be non-hSKI discarded by 2D and 3D classification. A resulting subset of 534,613 human SKI particles were found and extracted at the original pixel size of 0.8512 Å/pixel. Further 3D classification into 6 classes, using a starting model based on these data, lead to the selection of a final subset of 144,441 particles. Initial 3D refinement estimated an overall nominal resolution of 3.5 Å. The quality of the reconstruction and the level of resolved detail was further improved by Bayesian polishing to correct for per-particle motion and by stepwise refinement of the per-particle CTF (taking into account the beam-tilted data acquisition scheme). This resulted in a final reconstruction with an overall global resolution estimated as 3.1 Å according to the gold-standard Fourier shell correlation (0.143) criterion. Masking and map sharpening using an automatically determined global b-factor of -52.3 was carried out in the RELION post-processing routine (Zivanov et al., 2018).

ADP-BeF-treated hSKI-ribosome data were measured on a FEI Titan Krios microscope at 105,000x nominal magnification. The K3 detector was used in correlated-double sampling mode (CDS) and the energy filter set to slit width of 10 eV. 15,073 micrographs movies were acquired with a total exposure of 55.8 e/Å ^{2} equally spread over 35 frames during 5 sec. On-the-fly micrograph movie processing was assisted by Focus (Biyani et al., 2017), which ran Motioncor2 (Zheng et al., 2017), GCTF (Zhang, 2016), and Gautomatch (https://www2.mrc-lmb.cam.ac.uk/research/locally-developed-software/zhang-software/#gauto) on individual images while the data were being collected. Subsequent particle processing was carried out in RELION 3.1 (Zivanov et al., 2018). Down-scaled particles were extracted from the aligned, exposure-weighted micrographs and classified in 2D and 3D to discard non-ribosomal and low-resolution particles from the data. The cleaned ribosomal particles (1,601,273) were extracted at the original pixel size of 0.8512 Å/pixel and aligned in a 3D auto-refinement with a spherical mask using a 40 Å down-filtered starting model based on PDB: 4UG0 (Khatter et al., 2015). The refined particles were then used to subtract a large portion of the 80S ribosome signal from the corresponding particle images. To improve alignment precision and the quality of the reconstructions in the subsequent steps, the particle images were then recentred on the remaining hSKI signal and re-extracted in a smaller box in RELION 3.1 (Zivanov et al., 2018). The subtracted particle images were 3D classified with local search into 7 classes using a wide mask. The final subset of consisted of 51,048 particles. The ribosome-signal-subtracted particles were aligned by 3D auto-refinement, which resulted in a reconstruction of hSKI in the closed state at an overall nominal resolution of 3.6 Å according to the FSC cut-off criterion of 0.143. For masking and map sharpening in the RELION 3.1 post-processing procedure (Zivanov et al., 2018), an ad-hoc b-factor of -20 was applied. The automatically determined b-factor of -122.6 resulted in an over-sharpened map with loss of connectivity. This discrepancy might be due to successive subtraction of a large portion of the total signal in the particle stacks. Next, the signal subtraction was reverted and the corresponding 80S-IRES-hSKI particles refined to 3.1 Å global resolution according to the FSC cut-off criterion of 0.143. A b-factor of -70.7 was automatically estimated in the RELION post-processing routine (Zivanov et al., 2018). The quality of the map in areas of the

CrPV IRES and hSKI complex, however, was not satisfactory. Therefore, we subtracted the signal of the 60S ribosomal subunit from the reconstruction and aligned the remaining 40S-IRES-hSKI particles by 3D auto-refinement, which yielded a reconstruction at 3.1 Å global resolution according to the FSC cut-off criterion of 0.143. Masking and map sharpening in RELION post-processing (Zivanov et al., 2018) was performed using an ad-hoc b-factor of -10 (automatically determined b-factor -73.6). While the map quality for hSKI in this reconstruction improved only marginally, the resolution and volume connectivity for the CrPV IRES in the intersubunit space improved significantly.

ATP-treated hSKI-ribosome data were collected on a FEI Titan Krios microscope at 105,000x nominal magnification. 21,212 micrograph movies were acquired with a total dose of 67.6 e/Å^2 equally spread over 40 movie frames during 6 sec exposure time. On-the-fly data processing was assisted by Focus (Biyani et al., 2017) as described above and continued in RELION 3.1 (Zivanov et al., 2018). 2D and 3D classification resulted in 1,089,263 clean ribosomal particles, which were aligned in 3D auto-refinement for subsequent subtraction of a large portion of the 80S ribosome signal. The subtracted particle images of the ATP-treated hSKI-ribosome data were 3D classified with local searches into 6 classes using a wide mask. The classification resulted in one class that shows well-aligning density for the hSKI complex. In a second round of 3D classification using a 30 Å low-pass filtered starting model of the open state, separation of open and closed particles was possible and resulted in selection of a final subset of 76,838 open state particles. 3D auto-refinement of the subset was exclusively possible with local searches and resulted in a reconstruction at 6.5 Å global resolution according to the FSC cut-off criterion of 0.143. A b-factor of -210.6 was estimated automatically using a tight mask in the RELION post-processing procedure (Zivanov et al., 2018). For the corresponding ribosome-bound reconstructions, signal reversion and subtraction procedures similar to the ADP-BeF-treated hSKI-ribosome data above were applied. This led to an open 80S-IRES-hSKI reconstruction at 3.0 Å global resolution using a -76.3 b-factor and an open 40S-IRES-hSKI reconstruction at 3.0 Å global resolution using an ad-hoc b-factor of -10 (automatically determined b-factor -79.2).

Data processing on both hSKI-ribosome data sets required signal subtraction of the ribosome to yield reconstructions of comparable interpretability and quality as those described in the manuscript. Classical focused classification and refinement procedures did not yield results of comparable quality and interpretability.

Density interpretation and model building

Resolution and quality of the substrate-free hSKI reconstruction in closed state enabled us to build its structure de novo. Structure building was guided by a Buccaneer initial model within the CCP-EM suite (Hoh et al., 2020) based on published high-resolution yeast Ski structures (Halbach et al., 2012, 2013). The structure was then further completed and refined in Coot (Emsley et al., 2010) and iteratively finalised using real-space refinement in the Phenix suite (Liebschner et al., 2019). Rigid-body fitting using UCSF Chimera (Pettersen et al., 2004) into focussed refined maps enabled us to build peripheral regions of the complex: TPRs 34-40 in the C-terminus of hSKI3$_C$; TPRs 10-14 in the N-terminal region of hSKI3$_C$ (α-helices without sequence); parts of the solvent exposed areas of hSKI2$_N$ (with register defined by AlphaFold prediction); the globular part of hSKI2$_{arch}$ (which was interpreted with an AlphaFold prediction) (Figure S2H**)**. The reconstruction of substrate-free hSKI in open state was interpreted by rigid-body fitting (UCSF Chimera) a hSKI2$_{cat/arch}$ depleted version of substrate-free hSKI structure in closed state followed by modulating and refinement of the open state hSKI structure in Coot (Emsley et al., 2010) and real-space refinement (Phenix). Both closed and open state substrate-free human SKI reconstructions were validated using MolProbity (Chen et al., 2010) within the cryo-EM validation tool in the phenix suite (Liebschner et al., 2019).

The substrate-bound hSKI reconstruction was interpreted by rigid-body fitting (UCSF Chimera) of the substrate-free hSKI structure in the closed state described above. The six ribonucleotides of the 25-uracil RNA substrate were built into the structure of substrate-bound hSKI using Coot, and then refined and finalised by real-space refinement (Phenix). The final substrate-bound human SKI complex reconstruction was validated using MolProbity (within the cryo-EM validation tool in the phenix suite).

The reconstruction of closed state hSKI bound to ribosome was interpreted by rigid-body fitting (UCSF Chimera) the structure of substrate-bound hSKI. Small variations in hSKI2$_{cat}$ and the six ribonucleotides within hSKI2$_{cat}$ were adjusted and refined using Coot and real-space refinement (Phenix). This model along with the structure of the 40S ribosomal subunit taken from PDB: 4UG0 (Khatter et al., 2015) and the structure of the CrPV IRES mimicking a pre-translocated ribosomal state (PDB: 4V92 [Fernández et al., 2014]) were all used to interpret the corresponding 40S-IRES-hSKI reconstruction in closed state by rigid-body fitting (UCSF Chimera). The corresponding 80S-IRES-hSKI reconstruction in closed state was subsequently interpreted by rigid-body fitting the above mentioned 40S-IRES-hSKI structure in closed state together with the structure of the 60S ribosomal subunit from the structure of the human 80S ribosome (PDB: 4UG0).

The reconstruction of open state hSKI bound to ribosome was interpreted by rigid-body fitting (UCSF Chimera) the structure of the helicase module from the structure of substrate-bound hSKI detailed above. The structure was further completed in Coot by building additional downstream ribonucleotides traversing hSKI2$_{cat}$. Small variations with respect to hSKI2$_{cat}$ and the ribonucleotides inside hSKI2$_{cat}$ were adjusted and refined in Coot and real-space refinement. The corresponding 40S-IRES-hSKI reconstruction in open state was interpreted similar to the closed state above by rigid-body fitting the ribosome-bound structure of hSKI in open state and the structures of human 40S ribosomal subunit (PDB: 4UG0) and CrPV IRES (PDB: 4V92). The PK-1 nucleotides of the CrPV IRES in the intersubunit space of the ribosome were omitted from the structure where there was no apparent density. The corresponding full 80S-IRES-hSKI reconstruction in open state was interpreted similarly as the one in the closed state above by rigid-body

fitting the 40S-IRES-hSKI structure in the open state together with the structure of the 60S ribosomal subunit (PDB: 4UG0). In the closed and open state 40S-IRES-hSKI reconstructions the same volume level was applied to compare the PK-1 CrPV IRES densities in the intersubunit space without bias.

QUANTIFICATION AND STATISTICAL ANALYSIS

The kinetic parameters of ATP hydrolysis by human SKI were calculated according to Michaelis-Menten theory at various ATP substrate concentrations under steady-state conditions. The baseline corrected initial velocities (v_0) as a function of substrate concentration were used to approximate the Michaelis-Menten equation ($v_0 = (v_{max} \cdot [S]) / (K_m + [S])$). The kinetic parameters v_{max}, K_m and k_{cat} were derived from the approximation using a total enzyme concentration $[E_{tot}] = 0.05\ \mu M$. The approximation of the Michaelis-Menten equation was done using a non-linear regression model in the Prism9 (GraphPad) software.

Molecular Cell, Volume *82*

Supplemental information

The human SKI complex regulates channeling of ribosome-bound RNA to the exosome via an intrinsic gatekeeping mechanism

Alexander Kögel, Achim Keidel, Fabien Bonneau, Ingmar B. Schäfer, and Elena Conti

Supplementary Figure S1. Cryo-EM data analysis of recombinant apo hSKI (related to Figures 1, 2 and 3)

Characteristics of the apo hSKI single particle cryo-EM sample and data. **(A) On the left,** analytical size exclusion chromatography profile on a S6 increase column (Cytiva) of a representative hSKI preparation, and on the right is a 4-12 % Coomassie stained SDS-PAGE of a peak fraction of the SEC run (labelled with *, M is Marker). In **(B)** a representative cryo-EM micrograph of the apo hSKI sample (A) is shown. This image was recorded at 300 kV with a pixel size of 1.024 Å/pix using a post-GIF K3 direct detector. **(C)** 2D class averages of the apo hSKI sample in the closed (left hand panel, red frame) and open (right hand panel, blue frame) state conformations. **(D)** Processing scheme of the single particle cryo-EM dataset of the apo hSKI sample resulting in 3D reconstructions for the closed (red frame) and open (blue frame) states.

Supplementary Figure S2. Cryo-EM reconstruction analysis of apo hSKI (related to Figures 1, 2 and 3)

Quality indicators of the apo hSKI closed and open 3D reconstructions. Local resolution estimates and Fourier Shell Correlations (FSC) of the closed **((A)** and **(B))** and the open **((D)** and **(E))** reconstructions of the apo hSKI cryo-EM SPA data. The FSC of the masked independent half maps were calculated in the RELION 3.1 postprocessing routine and the map vs model FSC using phenix.mtriage. The FSC cut-off criteria of 0.5 and 0.143 are indicated by dotted lines. Angular sampling distributions of the closed **(C)** and open **(F)** reconstructions of the apo hSKI data. Sampling angle data were plotted in 3º by 3º bins and sampling bins coloured according to particle number with red indicating more and blue fewer particles. **(G)** Selected model and map regions of the closed state reconstructions showing the quality of the structural data. **(H)** Local resolution estimate of a focused 3D reconstruction of the $hSKI2_{arch}$ (panel on the left) used for rigid fitting of a homology model of this domain (panel on the right) and completion of the closed state model.

Supplementary Figure S3. Structural conservation between human SKI and yeast Ski (related to Figures 2, 3, 5 and 6)

Comparisons of the hSKI apo and the *S. cerevisiae* Ski structures. In **(A)** the model of hSKI closed apo state is juxtaposed to the yeast Ski model. SKI2 is coloured in yellow,

SKI3 in blue, $SKI8_{IN}$ in green and $SKI8_{OUT}$ in dark green. The SKI3 C-terminal module is absent in the yeast structure (box (B)). **(B)** Detailed view of the C-terminal module of hSKI3 in complex with the N-terminus of the hSKI2. **(C)** The hSKI2 N-terminal outer a-helix is sandwiched between hSKI3 TPR13 and TPR14. Note that the residue numbering of the $Ski2_N$ a-helix (see also Figure 2C) is based on prediction from AlphaFold (Tunyasuvunakool et al., 2021). A focused 3D reconstruction on the first superhelical turn of hSKI3 in the hSKI apo closed state is coloured according to local resolution on the left and displayed together with the respective part of the model on the right. **(D)** hSKI2 helicase modules of the apo hSKI closed state, the RNA-bound hSKI closed state and the *S.c.* Ski structure in comparison. Note the similar orientation and conformation of the $SKI2_{arch}$ with respect to the $SKI2_{cat}$ in all three structures. **(E)** Comparison of the human and the yeast 80S bound by human and yeast SKI complex respectively (*S. cerevisiae* 80S-Ski complex from PDB:5MC6). SKI2 is coloured in yellow, SKI3 in blue, $SKI8_{IN}$ in green, $SKI8_{OUT}$ in dark green, the CrPV IRES in the human case and the mRNA and tRNA in the yeast case in red, the 60S ribosomal subunit is in light blue and the 40S ribosomal subunit in light orange. The yeast and human SKI complexes sit in different orientations on the respective 80S and the RNAs appear differently bound to the helicase modules. In the yeast case this leaves 2-3 nucleotide positions to ySki2 R149 unoccupied (ySki2 R149 is structurally in the equivalent position as hSKI2 W146).

Supplementary Figure S4. SKI2 elements impacting the open/closed state (related to Figure 2, 3 and 4)

Details of selected elements in the $hSKI2_N$. In **(A)** a multiple sequence alignment (MSA) of eukaryotic SKI2 homologs focussed on the N-terminal wedge and a schematic representation of this region in the hSKI2 construct used for the hSKI-Δwedge complex is plotted. Degrees of conservation are indicated by shades of yellow in the MSA with darker shades highlighting stronger conservation. The organisation of the different motives of interest in proximity to the hSKI2 wedge is indicated in the cartoon atop the MSA by thicker yellow lines. A Coomassie stained SDS-PAGE of this sample is shown in Fig. 7B. These samples were vitrified on holey-carbon Cu grids and imaged at 200kV using a K2 direct detector in counting model at a pixel size of 1.885 Å/pix. In the top panel in **(B)** reference-free 2D class averages of these cryo-EM SPA data of the

hSKIΔwedge complex are displayed. These 2D class averages are overall similar to those of the apo open hSKI particles in Fig. S1C. The apo open hSKI complex was fitted into the low-resolution 3D reconstruction of the hSKIΔwedge complex in the panel at the bottom. The unmodelled density on the right with corkscrew-like appearance corresponds to the unmodelled hSKI3 N-terminal TPRs. Note the absence of any interpretable density for the hSKI2 helicase module. hSKI2 is coloured in yellow, hSKI3 in blue, $hSKI8_{IN}$ in green and $hSKI8_{OUT}$ in dark green. In single particle cryo-EM, a *S. cerevisiae* Ski-Δarch complex adopts an open and closed conformation. **(C)** Coomassie stained 4-12 % SDS-PAGE of the yeast SkiΔarch complex. These samples were vitrified on holey-carbon Cu grids and imaged at 200kV using a K2 direct detector operated as above. Reference-free 2D class averages and the final 3D reconstruction of the closed state of the yeast Ski-Δarch complex are in **(D)**. **(E)** shows reference-free 2D class averages and the final 3D reconstruction of the open state of the yeast Ski-Δarch complex. Ski2 is coloured in yellow, Ski3 in blue, $Ski8_{IN}$ in green and $Ski8_{OUT}$ in dark green. **(F)** Fourier shell correlation of the masked independent half-maps for the 3D reconstructions of hSKIΔwedge (shown in **(B)**, forest green) as well as the closed and open states of the yeast Ski-Δarch complex (shown in **(D)** and **(E),** coloured in salmon and olive, respectively)**.**

Supplementary Figure S5. Characteristics of the RNA-bound closed hSKI single particle cryo-EM data (related to Figure 4)

(A) shows a representative cryo-EM micrograph and reference-free 2D class averages of the RNA-bound closed hSKI sample recorded at 300 kV with a pixel size of 0.8512 Å/pix using a Gatan K3 camera. In **(B)** the processing scheme of the single particle cryo-EM dataset of the hSKI sample is outlined. This resulted in the final 3D reconstruction with a global resolution estimate of 3.1 Å for the closed RNA-bound state (red frame). The local resolution estimates are plotted on the final reconstruction in **(C)**, the FSC of the masked independent half-maps of the final reconstruction and the model vs map FSC in **(D)**. Here the FSC cut-off criteria of 0.5 and 0.143 are indicated by dotted lines. The angular sampling distribution for the final reconstruction is in **(E).** Angular sampling data were plotted in 3º by 3º bins in this panel. Note the absence of any noticeable fraction of open state particles in these SPA data (see 3D classification in **(B)**). Comparisons of the closed RNA-bound hSKI2 helicase with

hMTR4. In **(F)** RNA-bound human MTR4 in grey is superposed onto the closed RNA-bound hSKI2 helicase in yellow (human MTR4 from PDB:6D6Q). The RNA is coloured in red. Note the very similar path of the RNA in both structures. **(G)** Details of the RNA channel in the helicase module of the RNA-bound hSKI apo closed state similar to Fig. 4C. Residues interacting with the RNA are shown in stick representation. Colour scheme as in **(F)**. **(H)** Superposition of the RNA bound hSKI2 with human MTR4 bound to ZCCHC8$_{CTD}$. Residues W146 of the hSKI2$_{wedge}$ and F673 of the ZCCHC8$_{CTD}$ occupy very similar positions at one end of the RNA channel in the two structures (MTR4: ZCCHC8$_{CTD}$ from PDB:6C90). In the RNA-bound closed hSKI structures this residue closes off the RNA channel of the hSKI2 helicase at the 3' end prohibiting the RNA from further threading through.

Supplementary Figure S6. Characteristics of the closed ribosome-bound hSKI single particle cryo-EM sample and data (related to Figure 6)

(A) Typical 15-40 % (w/v) Sucrose gradient profile used for reconstitution of the closed state ADP-BeF-treated human 80S-IRES-hSKI complex on the left (80S-IRES-hSKI black curve; 80S-IRES grey curve). Peak fractions (indicated by *) were run out on a 4-12 % SDS-PAGE and the Coomassie stained gel is in the right panel. hSKI8 is not clearly identifiable on the gel most likely due to the prevalence of human 80S ribosomal proteins between 30 and 40 kDa. These peak fractions were vitrified and imaged at 300 kV using a post-GIF K3 camera with a pixel size of 0.8512 Å/pix **(B)**. Reference-free 2D class averages of the closed state 80S-IRES-hSKI sample are shown in **(C)**. Density for the hSKI complex is discernible atop the 40S ribosomal subunit in most of these 2D class averages. **(D)** displays the processing workflow for the closed ribosome-bound hSKI single particle cryo-EM data resulting, after subtraction of the 80S density, in a reconstruction of the hSKI complex at 3.6 Å resolution. The red masks indicate the regions of the map not subtracted from the data. The angular sampling distribution, the FSC of the independent masked half-maps and the map vs model FSC as well as the local resolution estimates plotted on the final closed ribosome-bound hSKI structure are shown in **(E)**, **(F)** and **(G)** respectively. In **(F)** dotted lines indicate the FSC cut-off criteria of 0.5 and 0.143.

Supplementary Figure S7. Characteristics of the open ribosome-bound hSKI single particle cryo-EM data (related to Figure 7)

(A) The purified protein samples used in the RNase protection assays in Figure 7B are shown on a Coomassie-stained 4-12 % SDS-PAGE. The samples are peak fractions from size-exclusion chromatography purifications. In **(B)** a representative micrograph (at a pixel size of 0.8512 Å/pix) and in **(C)** reference-free 2D class averages of the ATP-treated 80S-IRES-hSKI complex in open state are shown. In most 2D class averages density for the hSKI2 helicase at the top of the 40S ribosomal subunit is identifiable. Note the distinct structure of the $hSKI2_{arch}$ in these 2D class averages. **(D)** shows the local resolution estimates for the open ribosome bound hSKI structure from which the density of the 80S has been subtracted. In **(E)** angular sampling distribution for the reconstruction in **(D)** is plotted and in **(F)** the FSC for the masked independent half-maps and the model vs map for said reconstruction with dotted lines indicate the FSC cut-off criteria of 0.5 and 0.143. **(G)** shows the processing scheme with the red masks indicating the region of the map not subtracted from the data. After subtraction both 3D classifications with either apo closed hSKI or open ribosome-bound hSKI as reference model identify sub-populations of both the open and the closed hSKI state in these data. Of the ~110 000 particles identified initially as hSKI-bound, approximately 65% appear clearly in the open state in the second round of focused 3D classification using the open state as start model. The hSKI2 helicase is well ordered in these data since the 80S serves as an anchor for its substrate engagement. This is in contrast and somewhat paradoxical to the apo open hSKI state, where the helicase domain appears flexible in relation to the rest of the complex.

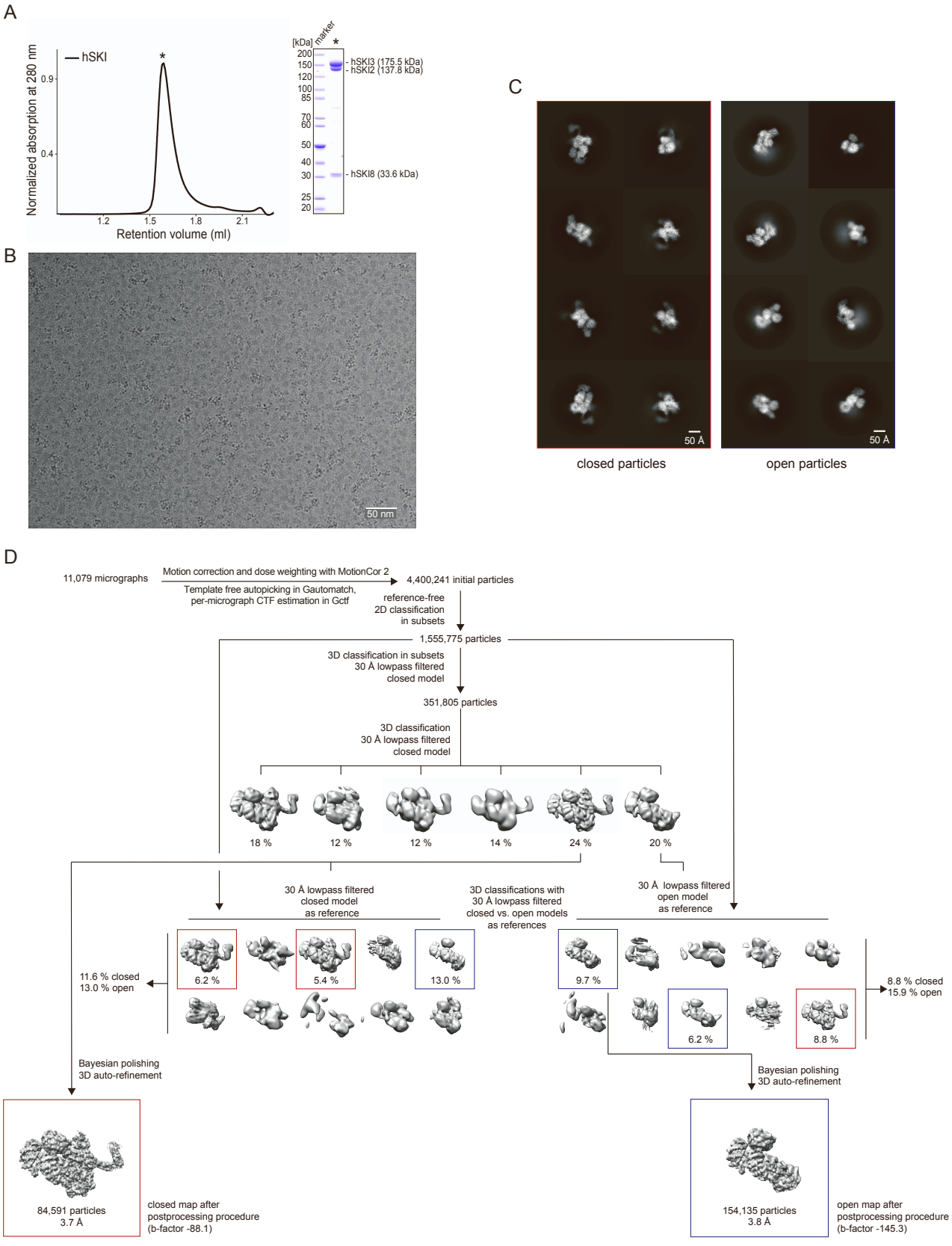
A
hSKI
Normalized absorption at 280 nm
0.9
0.4
1.2
1.5
1.8
2.1
Retention volume (ml)
[kDa]
marker
200
150
120
100
85
70
60
50
40
30
25
20
- hSKI3 (175.5 kDa)
- hSKI2 (137.8 kDa)
- hSKI8 (33.6 kDa)
B
50 nm
C
50 Å
50 Å
closed particles
open particles
D
11,079 micrographs
Motion correction and dose weighting with MotionCor 2
Template free autopicking in Gautomatch,
per-micrograph CTF estimation in Gctf
4,400,241 initial particles
reference-free
2D classification
in subsets
1,555,775 particles
3D classification in subsets
30 Å lowpass filtered
closed model
351,805 particles
3D classification
30 Å lowpass filtered
closed model
18 %
12 %
12 %
14 %
24 %
20 %
30 Å lowpass filtered
closed model
as reference
3D classifications with
30 Å lowpass filtered
closed vs. open models
as references
30 Å lowpass filtered
open model
as reference
6.2 %
5.4 %
13.0 %
11.6 % closed
13.0 % open
9.7 %
6.2 %
8.8 %
8.8 % closed
15.9 % open
Bayesian polishing
3D auto-refinement
Bayesian polishing
3D auto-refinement
84,591 particles
3.7 Å
closed map after
postprocessing procedure
(b-factor -88.1)
154,135 particles
3.8 Å
open map after
postprocessing procedure
(b-factor -145.3)

Figure S1

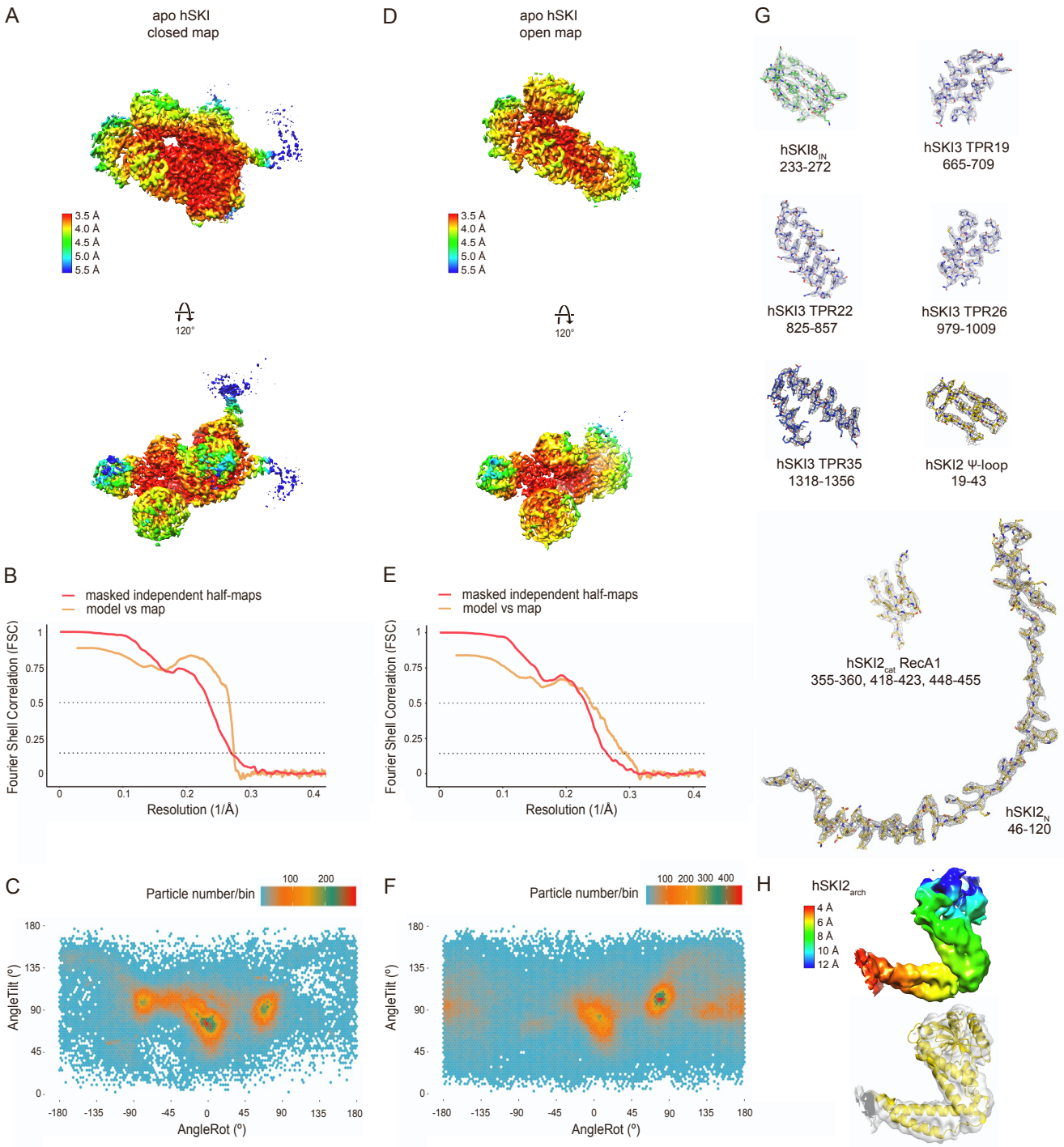
A
apo hSKI
closed map
3.5 Å
4.0 Å
4.5 Å
5.0 Å
5.5 Å
120°
D
apo hSKI
open map
3.5 Å
4.0 Å
4.5 Å
5.0 Å
5.5 Å
120°
G
hSKI8IN
233-272
hSKI3 TPR19
665-709
hSKI3 TPR22
825-857
hSKI3 TPR26
979-1009
hSKI3 TPR35
1318-1356
hSKI2 Ψ-loop
19-43
hSKI2cat RecA1
355-360, 418-423, 448-455
hSKI2N
46-120
B
masked independent half-maps
model vs map
Fourier Shell Correlation (FSC)
Resolution (1/Å)
E
masked independent half-maps
model vs map
Fourier Shell Correlation (FSC)
Resolution (1/Å)
C
Particle number/bin
AngleTilt (°)
AngleRot (°)
F
Particle number/bin
AngleTilt (°)
AngleRot (°)
H
hSKI2arch
4 Å
6 Å
8 Å
10 Å
12 Å

Figure S2

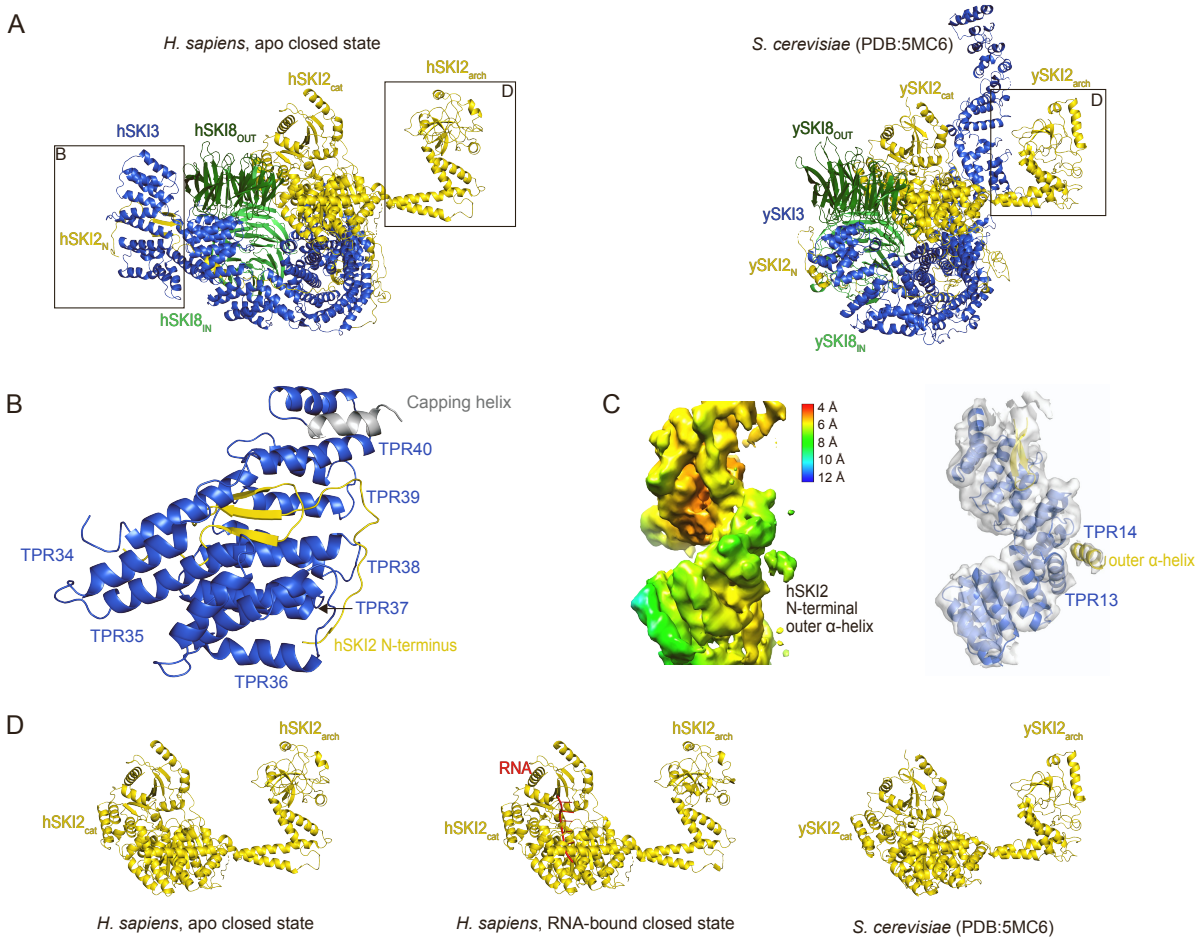
A
H. sapiens, apo closed state
hSKI2cat
hSKI2arch
D
hSKI3
hSKI8OUT
B
hSKI2N
hSKI8IN
S. cerevisiae (PDB:5MC6)
ySKI2cat
ySKI2arch
D
ySKI8OUT
ySKI3
ySKI2N
ySKI8IN
B
Capping helix
TPR40
TPR39
TPR34
TPR38
TPR37
TPR35
hSKI2 N-terminus
TPR36
C
4 Å
6 Å
8 Å
10 Å
12 Å
hSKI2
N-terminal
outer α-helix
TPR14
outer α-helix
TPR13
D
hSKI2arch
hSKI2cat
H. sapiens, apo closed state
RNA
hSKI2arch
hSKI2cat
H. sapiens, RNA-bound closed state
ySKI2arch
ySKI2cat
S. cerevisiae (PDB:5MC6)
E
IRES
H. sapiens
tRNA
mRNA
S. cerevisiae
60S
40S
SKI

Figure S3

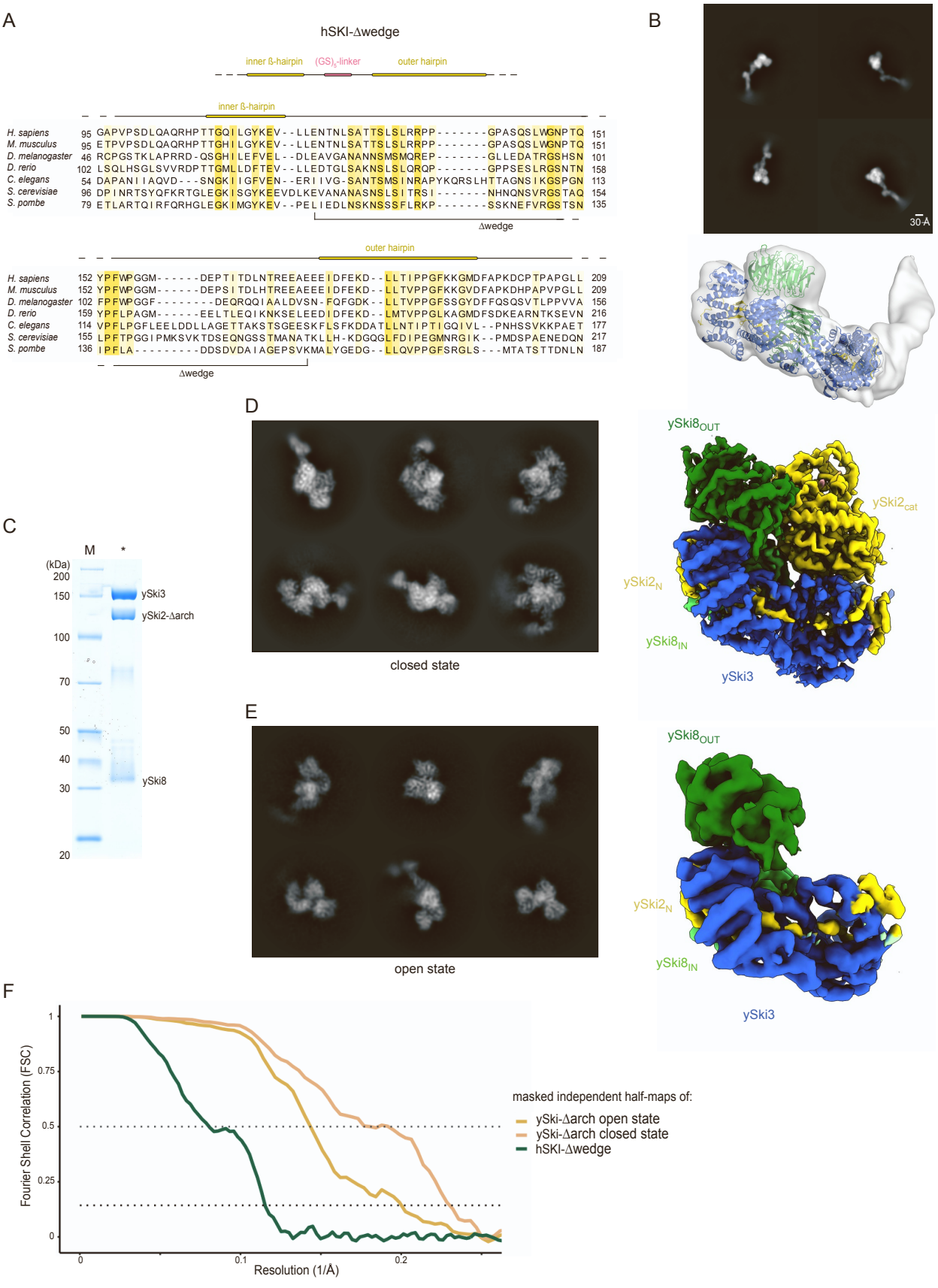
A
hSKI-Δwedge
inner ß-hairpin
(GS)n-linker
outer hairpin
H. sapiens
M. musculus
D. melanogaster
D. rerio
C. elegans
S. cerevisiae
S. pombe
Δwedge
B
30 Å
C
M
*
(kDa)
200
150
100
70
50
40
30
20
ySki3
ySki2-Δarch
ySki8
D
closed state
E
open state
yski8OUT
yski2cat
yski2N
yski8IN
yski3
F
Fourier Shell Correlation (FSC)
Resolution (1/Å)
masked independent half-maps of:
ySki-Δarch open state
ySki-Δarch closed state
hSKI-Δwedge

Figure S4

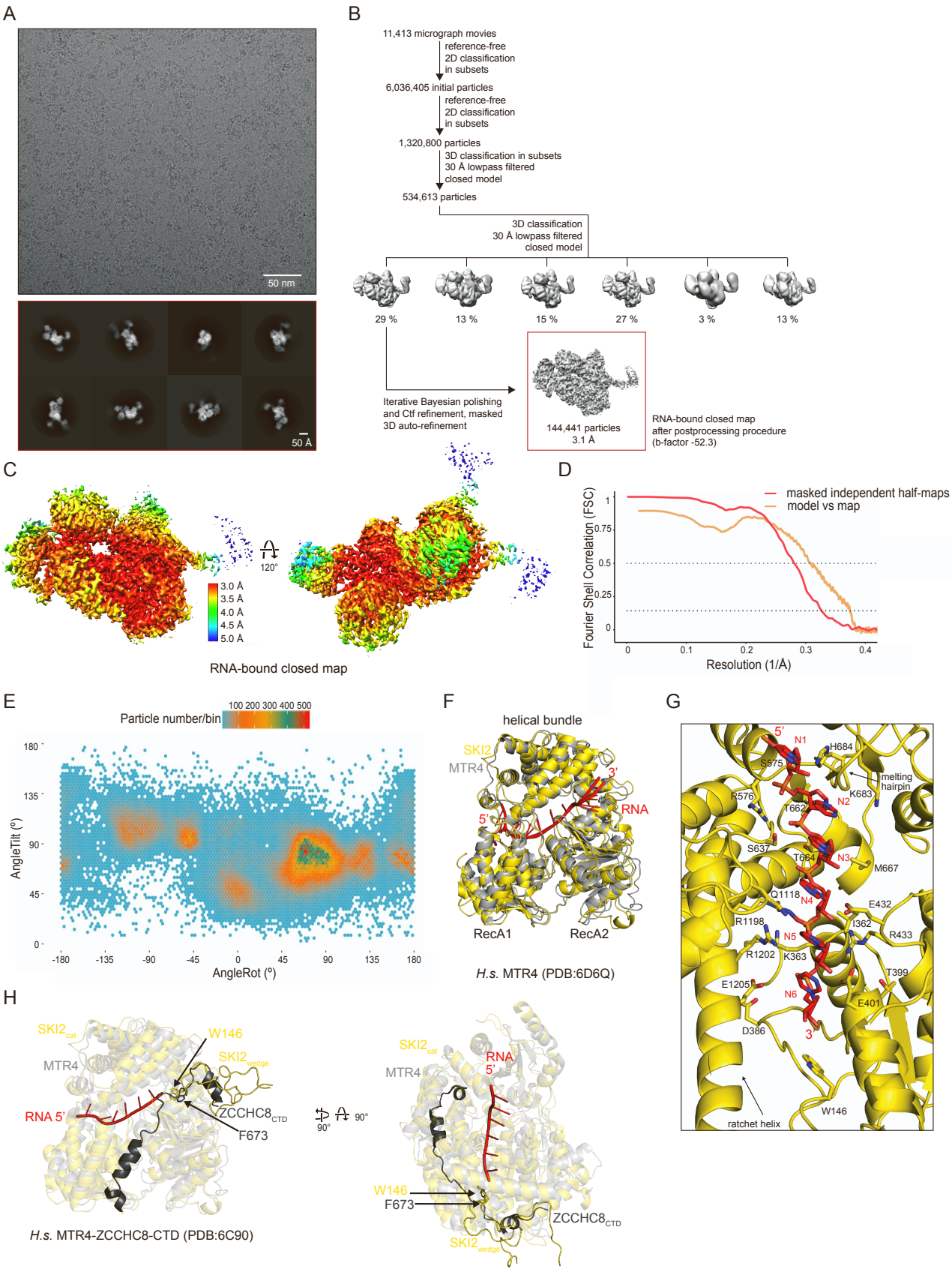
A
50 nm
50 Å
B
11,413 micrograph movies
reference-free
2D classification
in subsets
6,036,405 initial particles
reference-free
2D classification
in subsets
1,320,800 particles
3D classification in subsets
30 Å lowpass filtered
closed model
534,613 particles
3D classification
30 Å lowpass filtered
closed model
29 %
13 %
15 %
27 %
3 %
13 %
Iterative Bayesian polishing
and Ctf refinement, masked
3D auto-refinement
144,441 particles
3.1 Å
RNA-bound closed map
after postprocessing procedure
(b-factor -52.3)
C
120°
3.0 Å
3.5 Å
4.0 Å
4.5 Å
5.0 Å
RNA-bound closed map
D
masked independent half-maps
model vs map
Fourier Shell Correlation (FSC)
Resolution (1/Å)
E
Particle number/bin
100 200 300 400 500
AngleTilt (°)
AngleRot (°)
F
helical bundle
SKI2
MTR4
RNA
RecA1
RecA2
H.s. MTR4 (PDB:6D6Q)
G
melting
hairpin
ratchet helix
H
SKI2cat
SKI2wedge
W146
MTR4
RNA 5'
ZCCHC8CTD
F673
90°
H.s. MTR4-ZCCHC8-CTD (PDB:6C90)

Figure S5

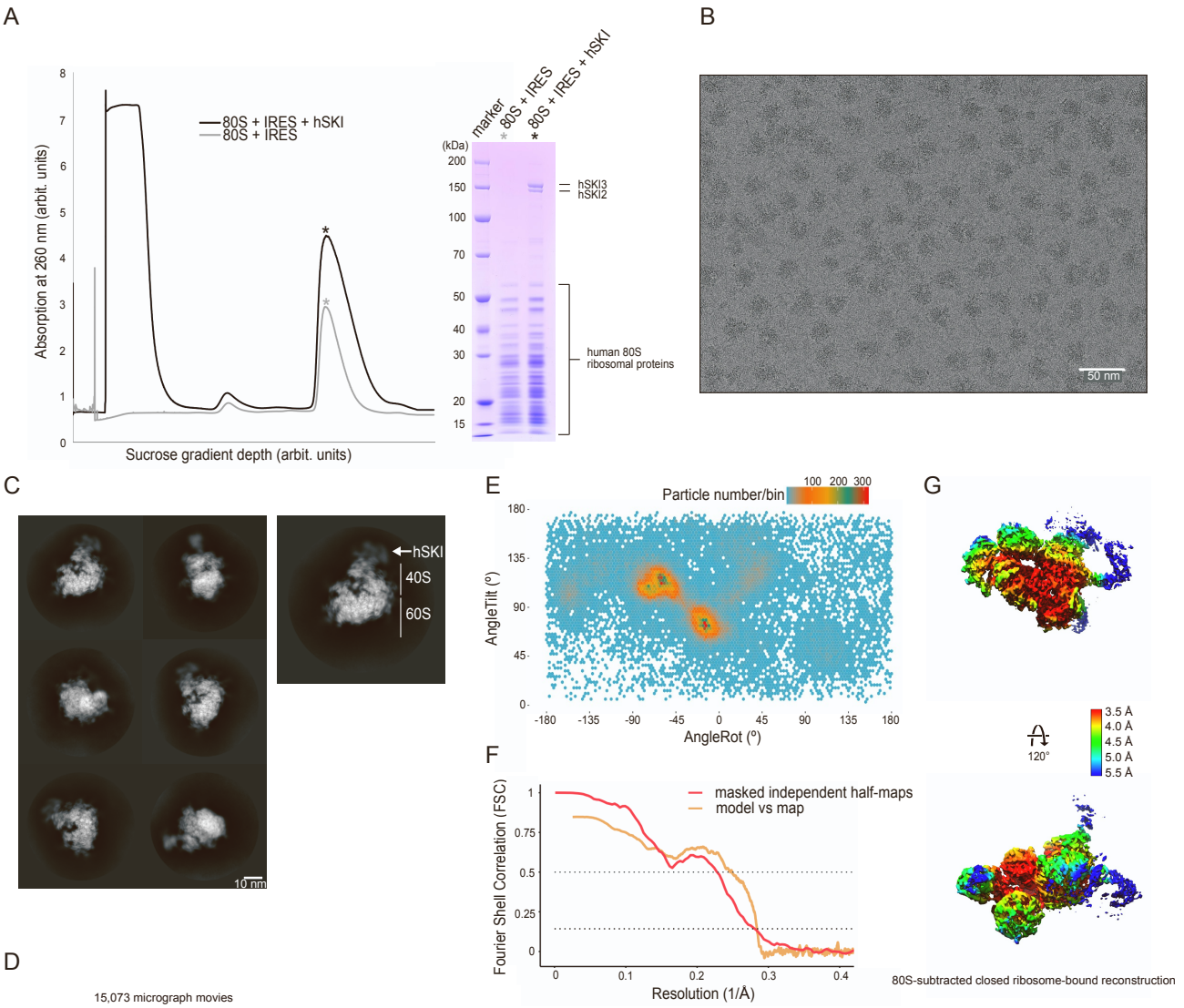
A
80S + IRES + hSKI
80S + IRES
Absorption at 260 nm (arbit. units)
Sucrose gradient depth (arbit. units)
marker
80S + IRES
80S + IRES + hSKI
(kDa)
hSKI3
hSKI2
human 80S ribosomal proteins
B
50 nm
C
hSKI
40S
60S
10 nm
E
Particle number/bin
AngleTilt (°)
AngleRot (°)
F
masked independent half-maps
model vs map
Fourier Shell Correlation (FSC)
Resolution (1/Å)
G
120°
3.5 Å
4.0 Å
4.5 Å
5.0 Å
5.5 Å
80S-subtracted closed ribosome-bound reconstruction
D
15,073 micrograph movies
Motioncor2
Gctf
Gautomatch
1,601,273 initial particles
reference-free 2D classification in subsets
558,449 particles
3D classification in subsets 30 Å lowpass filtered reference model (PDB 4UG0)
490,011 particles
3D auto-refinement 30 Å lowpass filtered reference model (PDB 4UG0)
mask for 80S signal subtraction
masked 3D classification of subtracted, recentered particles, local searches, 30 Å lowpass filtered apo closed hSKI model
10 %
10 %
17 %
26 %
15 %
8 %
14 %
masked 3D auto-refinement
51,048 particles 3.6 Å
80S-subtracted closed ribosome-bound reconstruction after postprocessing procedure (b-factor -25)
51,048 particles 3.1 Å
60S-subtracted closed ribosome-bound reconstruction after postprocessing procedure (b-factor -10)
mask for 60S signal subtraction
51,048 particles 3.1 Å
full closed ribosome-bound reconstruction after postprocessing procedure (b-factor -70.7)
60S ribosome signal subtraction, masked 3D auto-refinement
revert signal subtraction, masked 3D auto-refinement

Figure S6

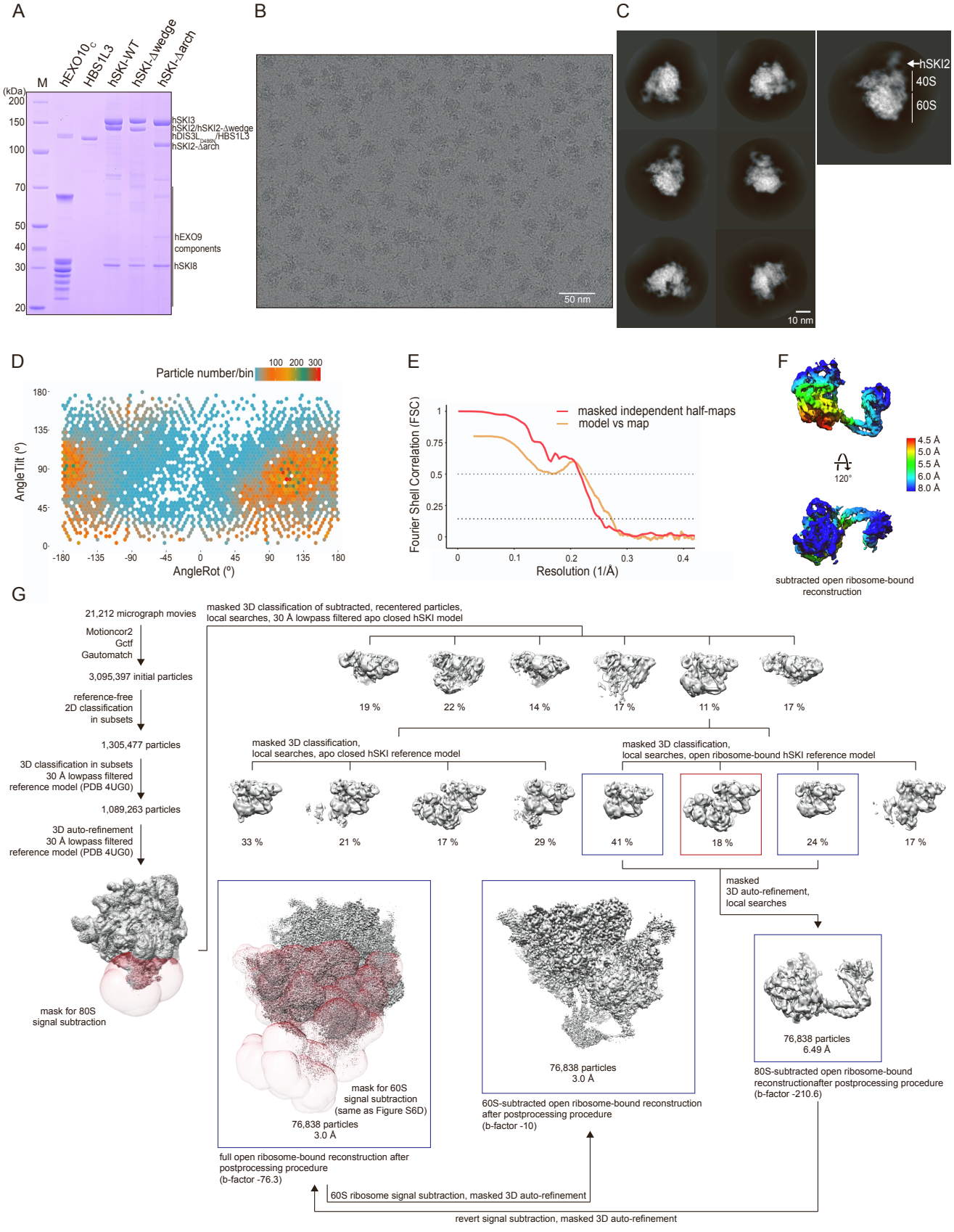
A
M
hEXO10c
HBS1L3
hSKI-WT
hSKI-Δwedge
hSKI-Δarch
(kDa)
200
150
100
70
50
40
30
20
hSKI3
hSKI2/hSKI2-Δwedge
hDIS3L2-D480N/HBS1L3
hSKI2-Δarch
hEXO9 components
hSKI8
B
50 nm
C
hSKI2
40S
60S
10 nm
D
Particle number/bin
100 200 300
AngleTilt (°)
AngleRot (°)
E
masked independent half-maps
model vs map
Fourier Shell Correlation (FSC)
Resolution (1/Å)
F
120°
4.5 Å
5.0 Å
5.5 Å
6.0 Å
8.0 Å
subtracted open ribosome-bound reconstruction
G
21,212 micrograph movies
Motioncor2
Gctf
Gautomatch
3,095,397 initial particles
reference-free 2D classification in subsets
1,305,477 particles
3D classification in subsets 30 Å lowpass filtered reference model (PDB 4UG0)
1,089,263 particles
3D auto-refinement 30 Å lowpass filtered reference model (PDB 4UG0)
mask for 80S signal subtraction
masked 3D classification of subtracted, recentered particles, local searches, 30 Å lowpass filtered apo closed hSKI model
19 %
22 %
14 %
17 %
11 %
17 %
masked 3D classification, local searches, apo closed hSKI reference model
33 %
21 %
17 %
29 %
masked 3D classification, local searches, open ribosome-bound hSKI reference model
41 %
18 %
24 %
17 %
masked 3D auto-refinement, local searches
mask for 60S signal subtraction (same as Figure S6D)
76,838 particles
3.0 Å
full open ribosome-bound reconstruction after postprocessing procedure (b-factor -76.3)
76,838 particles
3.0 Å
60S-subtracted open ribosome-bound reconstruction after postprocessing procedure (b-factor -10)
76,838 particles
6.49 Å
80S-subtracted open ribosome-bound reconstructionafter postprocessing procedure (b-factor -210.6)
60S ribosome signal subtraction, masked 3D auto-refinement
revert signal subtraction, masked 3D auto-refinement

Figure S7

Table S1. Cryo electron microscopy data collection summary, processing statistics and model quality indicators (related to Figures 1, 4, 5 and 6)

Cryo electron microscopy data collection					
Microscope	FEI Titan Krios GII				
Voltage (kV)	300				
Camera	Gatan K3-Summit				
Energy Filter	Gatan Quantum-LS (GIF)				
Pixel size (Å/pix)	1.094		0.851		
Preset target global defocus range (µm)	0.6 - 2.4				
3D reconstruction	**apo closed *H.s.* SKI**	**apo open *H.s.* SKI**	**RNA bound closed *H.s.* SKI**	**ribosome bound closed *H.s.* SKI**	**ribosome bound open *H.s.* SKI**
Number of movies	11,079		11,413	15,073	21,212
Exposure per sec (e^-/Å^2/s) /total exposure (e^-/Å^2)	11.86/47.44		22.77/68.31	11.16/55.8	11.27/67.62
Number of frames/movie	40		30	35	40
Initially selected particle candidates	4,400,241		6,036,405	1,601,273	3,095,397
Final number of particles	84,591	154,135	144,441	51,048	76,838
Resolution FSC independent halfmaps (Å)[a]	3.7	3.8	3.1	3.6	6.5
Local resolution range (Å)	3.3-15.8	3.4-13.1	2.8-12.6	3.1-15.6	4.6-10.7
Sharpening B-factor determined/applied (Å^2)	-88.1/-88.1	-145.3/-145.3	-52.3/-52.3	-73.6/-25	-210.6/-210.6
EMDB accession number	EMD-13923	EMD-13925	EMD-13927	EMD-13928	EMD-13929

Table S1 - continued.

Refinement	**apo closed *H.s.* SKI**	**apo open *H.s.* SKI**	**RNA bound closed *H.s.* SKI**	**ribosome bound closed *H.s.* SKI**	**ribosome bound open *H.s.* SKI**
PDB code	7QDR	7QDS	7QDY	7QDZ	7QE0
No atoms	22,827	13,798	22,933	22,598	7,619
Residues (protein)	2,991	1,771	2,991	2,924	949
Residues (RNA)	-	-	6	6	9
CC_{box}, CC_{mask}, CC_{volume}[b]	0.81, 0.86, 0.85	0.80, 0.82, 0.81	0.77, 0.80, 0.77	0.86, 0.81, 0.79	0.87, 0.74, 0.73
Resolution $_{FSC\ map\ vs.\ model@0.143}$ (Å)[b]	3.6	3.3	2.7	3.0	4.0
r.m.s. deviations					
Bond lengths (Å)	0.006	0.005	0.009	0.007	0.004
Bond angles (°)	0.819	0.852	1.101	0.969	0.998
Ramachandran favored (%)	94.25	94.32	94.39	95.05	96.19
Ramachandran allowed (%)	5.75	5.68	5.61	4.95	3.81
Ramachandran disallowed (%)	0.00	0.00	0.00	0.00	0.00
MolProbity score	1.99	2.04	1.96	2.09	2.07
Clash score	12.26	14.02	11.49	17.6	20.94

[a]according to the Fourier Shell Correlation (FSC) cut-off criterion of 0.143 defined in (Rosenthal and Henderson, 2003)
[b]according to the map-vs.-model Correlation Coefficient definitions in (Afonine et al., 2018)

Table S2. Kinetic parameters of hSKI ATP hydrolysis derived according to Michaelis-Menten (related to Figure 4A)

	hSKI-WT	hSKI-Δarch	hSKI-Δwedge	hSKI-WT (no RNA)	hSKI-DEAD*	hSKI-THES
V_{max} (μM/s)	0.03427	0.04478	0.02990	0.002387	N/A	0.0009766
K_m (μM)	149.4	121.5	190.5	582.2	N/A	-2.574
k_{cat} (s^{-1})	0.6853	0.8957	0.5981	0.04775	N/A	0.01953
R^2	0.9817	0.9871	0.9822	0.2016	N/A	0.1477

*The hSKI-DEAD data could not be reconciled with the Michaelis-Menten equation. No kinetic parameters were derived (N/A, not applicable).

4.2 Publication 2:

Concerted structural rearrangements enable RNA channeling into the cytoplasmic Ski238-Ski7-Exo10 assembly

Achim Keidel, Alexander Kögel, Peter Reichelt, Eva Kowalinski, Ingmar Schäfer and Elena Conti

This research article is currently under review with Molecular Cell. It provides structural insight into how the Ski238 complex interacts with Ski7 during cytoplasmic RNA degradation. In addition, we could show that the different conformational states of the Ski238 complex affect the recruitment of Ski7, providing an additional layer of regulation during substrate handover from the helicase to the exosome. At last, we could visualize a cytoplasmic exosome in association with the Ski2 helicase that actively degrades RNA. The striking similarities of this assembly with the nuclear exosome in complex with Mtr4 from both, yeast and human, suggest that this mode of recruitment is also conserved in the human Ski238 exosome assembly.

Concerted structural rearrangements enable RNA channeling into the cytoplasmic Ski238-Ski7-exosome assembly

Achim Keidel[1], Alexander Kögel[1], Peter Reichelt[1], Eva Kowalinski[2], Ingmar B. Schäfer[1] and Elena Conti[1,*]

1 Department of Structural Cell Biology, Max Planck Institute of Biochemistry, Am Klopferspitz 18, 82152 Martinsried, Munich, Germany.

2 EMBL Grenoble, 71 Avenue des Martyrs, 38000 Grenoble, France.

* corresponding author (conti@biochem.mpg.de)

Summary

The Ski2-Ski3-Ski8 (Ski238) helicase complex directs cytoplasmic mRNAs towards the nucleolytic exosome complex for degradation. In yeast, the interaction between Ski238 and exosome requires the adaptor protein Ski7. We determined different cryo-EM structures of the Ski238 complex depicting the transition from a rigid autoinhibited closed conformation to a flexible active open conformation, in which the Ski2 helicase module has detached from the rest of Ski238. The open conformation favors the interaction of the Ski3 subunit with exosome-bound Ski7, leading to the recruitment of the exosome. In the Ski238-Ski7-exosome holocomplex, the Ski2 helicase module binds the exosome cap, enabling the RNA to traverse from the helicase through the internal channel to the Rrp44 exoribonuclease. Our study pinpoints how conformational changes within the Ski238 complex regulate exosome recruitment for RNA degradation. We also reveal the remarkable conservation of helicase-exosome RNA channeling mechanisms throughout eukaryotic nuclear and cytoplasmic exosome complexes.

Highlights

- Structures of sequential steps in cytoplasmic exosome-mediated RNA degradation
- Concerted binding and detachment events in Ski238 lead to exosome recruitment
- RNA is threaded from the Ski2 helicase to the exosome ribonuclease
- Conserved RNA channeling mechanisms between cytoplasmic and nuclear exosomes

Introduction

RNA decay is critical for regulating eukaryotic gene expression and maintaining cellular homeostasis. Many RNA decay pathways involve the actions of the RNA exosome (Mitchell et al., 1997a), a multi-subunit molecular machinery that progressively shortens transcripts from their 3' end, in a nucleotide-by-nucleotide manner, until they are destroyed (reviewed in Chlebowski et al., 2013; Makino et al., 2013; Zinder and Lima, 2017). Notably, this *modus operandi* serves a dichotomous purpose, namely in the productive trimming of structured RNA precursors into their mature nuclear forms (reviewed in Lingaraju et al., 2019). The versatility and important functions of the evolutionary conserved RNA exosome complexes are reflected not only in the many regulatory checkpoints put in place to limit excessive or uncontrolled degradation, but also in the association with disease-causing mutations (reviewed in Fasken et al., 2020).

Substrate selection poses a significant challenge to the exosome. The processive core of the exosome, the ten-subunit exosome complex (Exo10), lacks inherent selectivity, and must instead rely on an intricate set of cofactors (reviewed in Chlebowski et al., 2013; Makino et al., 2013; Zinder and Lima, 2017). The 3'-5' RNA helicases Ski2 (in the cytoplasm) and Mtr4 (in the nucleus) are central components in the exosome cofactors networks for their roles in unwinding RNAs and/or remodeling ribonucleoprotein complexes (RNPs), making the transcripts accessible to the Exo10 exoribonuclease site (reviewed in Olsen and Johnson, 2021; Weick and Lima, 2021). These helicases do not function in isolation. Rather, Ski2 constitutively binds Ski3 and Ski8 to comprise the cytoplasmic Ski2-Ski3-Ski8 complex (Ski238) while Mtr4 can interact with different and mutually exclusive binding factors in the nuclear compartment. Furthermore, these cofactor complexes require adaptors to bind the Exo10, namely Ski7/HBS1L3 in the cytoplasm (Kalisiak et al., 2017a; Kowalinski et al., 2016a) and Rrp6,

Rrp47 and Mpp6 in the nucleus (reviewed in Schmid and Jensen, 2019). Currently, we have a fairly comprehensive understanding of the molecular mechanisms with which Mtr4 is recruited by the nuclear cofactors to Exo10 (Falk et al., 2017a; Schuch et al., 2014a; Wasmuth et al., 2017), either in the context of synthetic RNA oligos (Gerlach et al., 2018a; Weick et al., 2018a) or in the context of an endogenous pre-ribosomal RNP substrate (Schuller et al., 2018a). In contrast, we only have a partial understanding of the mechanisms with which the Ski238 complex is recruited to the cytoplasmic exosome core (Ski7-Exo10).

Ski238 was originally identified in budding yeast from a 'Superkiller' phenotype (Toh-E et al., 1978; Vodkin et al., 1974) and then shown to facilitate 3'-5' mRNA degradation by the Ski7-Exo10 in both mRNA turnover (J. S. J. Anderson and Parker, 1998) and mRNA surveillance pathways (Mitchell and Tollervey, 2003a; Takahashi et al., 2003; van Hoof et al., 2002a). Yeast Ski238 can bind directly to translating ribosomes (Schmidt et al., 2016a). The corresponding Ski238-ribosome interaction is conserved in humans, where it acts primarily in co-translational mRNA surveillance pathways (A. Tuck et al., 2020; Zinoviev et al., 2020a). Cryogenic electron microscopy (cryo-EM) structural studies of yeast and human Ski238 complexes have revealed conserved architectural features (Koegel et al., 2022). The Ski238 complex is constitutively in a 'closed' state, with the helicase module of Ski2 (consisting of the catalytic domain and the so-called arch domain) docked onto the gatekeeping module (formed by the C-terminal arm of Ski3, the N-terminal domain of Ski2 and two Ski8 proteins) (Halbach et al., 2013a; Koegel et al., 2022). In the closed state, the exit of the Ski2 RNA helicase channel is blocked by the gatekeeping module, effectively inhibiting the helicase properties of the complex. When active, the Ski238 switches to an 'open' state, whereby the Ski2 helicase module detaches from the gatekeeping module, allowing the unwound RNA 3' end to exit the helicase channel. Last but not least, biochemical data have shown that the arch domain of Ski2 negatively

regulates the helicase activity of Ski238 as well as its ability to channel RNA to the Exo10. The molecular mechanisms of this arch domain-mediated regulation remain unknown.

Studies in yeast first identified the protein Ski7 as the adaptor required to bridge the interaction between the Ski238 and Exo10 complexes (Y. Araki et al., 2001). Although this bridging factor was originally thought to be unique to *S. cerevisiae*, Ski7-like proteins have recently been identified in alternative splicing products of a gene encoding a co-translational quality control factor, *HBS1L*, as reported in the case of other fungi (Marshall et al., 2013), human (HBS1 isoform 3, HBS1L3) (Kalisiak et al., 2017a; Kowalinski et al., 2016a) and zebrafish (Cabrera-Quio et al., 2021). These Ski7 orthologues have been shown to have important functions *in vivo* in modulating RNA levels in early embryogenesis both in vertebrates (Cabrera-Quio et al., 2021) and invertebrates (Blatt et al., 2021). *S. cerevisiae* Ski7, however, remains the best characterized adaptor at the molecular level, and thus the best entry point to understand how the RNA-unwinding Ski238 and the RNA-degrading Exo10 are physically brought together.

Yeast Ski7 is a multidomain protein with an N-terminal extended region (required for all Exo10 functions) followed by a C-terminal domain with the typical fold of translational GTPases (whose function is restricted to the non-stop mRNA quality control pathway) (Y. Araki et al., 2001; Kowalinski et al., 2015; van Hoof et al., 2002a). The Ski7 N-terminal region is known to contain distinct Exo10-binding and Ski238-binding segments (Y. Araki et al., 2001). The interaction between Ski7 and the Exo10 is stable *in vivo* (Dziembowski et al., 2007a), and it is characterized by nanomolar binding affinity *in vitro* and by extensive contacts at the structural level (Kowalinski et al., 2016a). Conversely, little is known about how Ski7 recruits Ski238. In this work, we first elucidated the recognition mechanism between the yeast Ski238 and Ski7. By uncovering unexpected layers of regulation that link the Ski238-binding and the

Exo10-binding events of Ski7, we were then able to visualize the direct connection between the RNA unwinding and RNA degradation activities of the yeast cytoplasmic exosome holocomplex (Ski238-Ski7-Exo10).

Results and Discussion

Mechanism of arch-mediated autoinhibition in yeast Ski238

Ski7 is the necessary adaptor between Ski238 and the Exo10, but how it binds to Ski238 is unclear. To address this, we reconstituted the complex between recombinant *S. cerevisiae* Ski238 and Ski7. Full-length Ski2, Ski3 and Ski8 were co-expressed in insect cells and co-purified as a homogenous complex ($Ski238_{FL}$) (Halbach et al., 2013a; Keidel et al., 2020). The Ski7 N-terminal region ($Ski7_N$, residues 1-235, encompassing both the expected Ski238-binding and Exo10-binding segments (Y. Araki et al., 2001)) was obtained from bacterial cell expression. A complex of $Ski238_{FL}$, $Ski7_N$, a 30-mer polyU RNA and AMP-PNP was purified to homogeneity (Figure S1A) and subjected to single particle cryo-EM analysis (Figures S1B, S1C and S1D), yielding a final reconstruction at a nominal resolution of ~2.8 Å (Figures S1D and S1E). In this reconstruction, the overall architecture of the central core of Ski238 exhibited a closed conformation as observed previously (Halbach et al., 2013a; Koegel et al., 2022), with the helicase domain of Ski2 (the catalytic $Ski2_{cat}$) interacting with the gatekeeping module of the complex (Figures 1 and S1F). Briefly, the gatekeeping module consists of the C-terminal portion of Ski3 ($Ski3_C$) and two copies of Ski8 (Figures 1 and S1F). $Ski3_C$ forms a superhelical structure of tetratricopeptide repeats (TPRs). The N-terminal domain of Ski2 ($Ski2_N$, Figure 1A) threads inside the concave surface of the TPR superhelix (formed by the so-called A helices of

TPR motifs) (Figure 1B). The convex surface of the superhelix (formed by the so-called TPR B helices) binds two copies of the WD40-repeat protein Ski8 (known as $Ski8_{IN}$ and $Ski8_{OUT}$ in accordance to their more inward and outward positions in the complex (Halbach et al., 2013a)). The reconstruction also showed well defined density for four ribonucleotides in $Ski2_{cat}$ (Figures 1B and 1C), with the 5' end at the entry of the helicase channel and the 3' end reaching the first half of the so-called 'ratchet' helix (Büttner et al., 2007).

Although $Ski7_N$ was present in the sample, the density did not exhibit features corresponding to Ski7. However, it showed an unexpected conformation of the arch domain of Ski2 ($Ski2_{arch}$) and the N-terminal arm of Ski3 ($Ski3_N$), with the two corresponding densities protruding separately from the core and approaching each other (Figures 1B and 1C). Since the resolution of the map at these two protrusions was lower than in the core (Figure S1C), we performed signal subtraction followed by local refinement to focus on the interface of $Ski2_{arch}$ and $Ski3_N$, yielding a reconstruction at a nominal resolution of 2.9 Å in this area (Figures S1D and S1E). The density allowed us to position previous models of $Ski2_{arch}$ (Halbach et al., 2012a) and the portion of $Ski3_N$ encompassing residues 402-639 (Halbach et al., 2013a) as rigid bodies, revealing their direct interaction. The conformation of $Ski2_{arch}$ and $Ski3_N$ we observed in this reconstruction differs from that in the 80S-bound Ski238 complex (Schmidt et al., 2016a), and rationalizes previous biochemical data showing that removal of either $Ski2_{arch}$ or $Ski3_N$ is required to increase the RNA-dependent enzymatic activities of Ski238 (Halbach et al., 2013). The autoinhibition mechanism of $Ski2_{arch}$ and $Ski3_N$ does not stem from preventing the access of RNA to the helicase core: in the reconstruction, these domains do not physically block access to the helicase channel, which indeed contains RNA (Figures 1B and C). Rather, the structural and biochemical analyses suggest that $Ski2_{arch}$ and $Ski3_N$ together rigidify the

closed conformation of an RNA-bound Ski238, disfavoring the switch to the open, active conformation.

Release of Ski238 autoinhibition orchestrates the concerted recognition of Ski7

The absence of $Ski7_N$ in the reconstruction of the $Ski238_{FL}$-RNA complex prompted us to explore whether $Ski2_{arch}$ would also negatively impact Ski7 binding. We therefore compared the Ski7 binding properties of the $Ski238_{FL}$ with Ski238 lacking the Ski2 arch domain ($Ski2_{\Delta arch}38$). In microscale thermophoresis measurements, the Ski7-binding affinities of $Ski2_{\Delta arch}38$ or $Ski238_{FL}$ were similar, with dissociation constants registering in the low micromolar range in both cases (~ 0.12 μM Kd) (Figure S2A). Such comparatively weak binding properties were distinct from the stronger interaction between $Ski7_N$ and the Exo10 (dissociation constants in the low nanomolar range (Kowalinski et al., 2016)). Consistently, the interaction of $Ski7_N$ with Ski238 did not withstand high salt concentration, in contrast to the $Ski7_N$-Exo10 interaction (Figure S2B).

To assess this interaction at the structural level, we reconstituted a complex of $Ski2_{\Delta arch}38$, $Ski7_N$, a 30-mer polyU RNA and AMPPNP (Figure S2C) and subjected it to the same cryo-EM pipeline as for the full-length complex described above (Figures S2C-G). We obtained 3D reconstructions in different conformations generally corresponding to closed and open states (Figures 2A and 2B, respectively). In addition, we obtained a reconstruction of an intermediate state that we interpreted as a snapshot of the transition from the closed to the open conformations of the complex (Figures S3A). The three reconstructions reached nominal resolutions of 2.8 Å to 3.1 Å (Figure S2G), but with progressively increasing flexibility from the closed to the intermediate to the open state.

The 3D reconstruction of Ski2$_{\Delta arch}$38 in the closed state (Figure 2A) showed two significant differences when compared to the corresponding closed conformation of Ski238$_{FL}$ (Figure 1B). First, the density of Ski3$_N$ was not well resolved in the Ski2$_{\Delta arch}$38 reconstruction, suggesting enhanced flexibility of Ski3$_N$ in the absence of Ski2$_{arch}$. Second, on the outer surface of Ski3$_C$ we found additional density that, albeit poorly defined, pointed to the presence of two α-helices (with hindsight corresponding to Ski7$_N$ helices 1 (Ski7$_N$-H1) and 3 (Ski7$_N$-H3), Figures 2A and 2C). In an intermediate state where the helicase domain was partially detached from the gatekeeping module, the additional density was more pronounced showing the presence of a third helix (with hindsight corresponding to Ski7$_N$ helix 2 (Ski7$_N$-H2), Figure S3A). Last, in the open state of Ski2$_{\Delta arch}$38, density for Ski2$_{cat}$ was absent, implying its detachment from the complex. Similar to the human orthologue, Ski2$_{cat}$ is presumably flexible in solvent and tethered to the gatekeeping module by Ski2$_N$ (Koegel et al., 2022). The additional density on the outer surface of the Ski3$_C$ TPR motifs became well ordered in the open state (Figures 2B, 2C, S2F and S2G), allowing us to build an atomic model for the interacting regions of Ski7$_N$.

We concluded that Ski7 binding to the gatekeeping module of Ski238 responds to the detachment of the helicase module as it transitions to the fully active state. From a biophysical standpoint, the weak binding properties and conformational heterogeneity in the sample would prevent obtaining exact Ski7-binding affinity measurements for each conformation. From a structural perspective, however, the release of Ski2$_{cat}$ from the gatekeeping module appears to subtly modulate the spacing between the helices of neighboring TPR's of Ski3$_C$, creating a better Ski7-binding environment.

Ski7 interaction sites on the surface of Ski3 are important *in vitro* and *in vivo*

In the atomic model based on the locally refined reconstruction of the open state Ski2$_{\Delta arch}$38, we observe that Ski7$_N$ binds the convex surface of Ski3$_C$ between TPRs 20-29 with well-ordered density for three helices that we defined as H1, H2 and H3 (residues 1-12, 29-34 and 76-87, respectively) (Figures 3A and 3B). The rest of Ski7$_N$ was either partially or completely disordered. Ski7$_N$-H1 interacts with the central region of Ski3$_C$ at the inter-repeat space formed by the B helices of TPR 26 and 27. Here, the side chains of Ski7 Leu4 and Ile12 project into a pocket of Ski3 lined by hydrophobic residues, including Leu1179 and Phe1182 (Figure 3B lower right panel). Lowering the threshold of the unsharpened 3D reconstruction showed that the density continues towards Ski7$_N$-H2 (Figure S3B), a shorter helix that docks into the inter-repeat space formed by the B helices of TPR 28 and 29 (Figure 3B lower left panel). From here, Ski7 threads back in a U-shaped topology and binds with Ski7$_N$-H3 at an unusually large intra-repeat insertion formed between the A and B helices of TPR 20. Ski7$_N$-H3 inserts hydrophobic residues (Ski7 Leu78 and Leu82) into a hydrophobic pocket formed around Ski3 Val878 (Figure 3B upper right panel). The binding mode and peculiar U-shaped topology is further supported by targeted predictions by AlphaFold (Jumper et al., 2021) (i.e., narrowing down the putative interacting areas of Ski7$_N$ and Ski238 in the predictions based on the experimental information) (Figure S3C and S3D).

To test the atomic model experimentally, we designed structure-based point mutations and assessed their effect *in vitro* and *in vivo*. We engineered mutations in the two binding pockets of Ski3 that appeared to contribute the more stable interactions with Ski7$_N$: the binding pocket for the Ski7$_N$-H1 at Ski3 TPR26 (L1179K, F1882K = Mut1) and the binding pocket for Ski7$_N$-H3 at Ski3 TPR 20 (V878K = Mut2). Recombinant Ski238 complexes either wild type (wt) or with the Ski238 Mut1 and Mut2 substitutions were expressed and purified, and served as prey in GFP pull-down assays using purified recombinant GFP-tagged Ski7$_N$ as bait.

In these assays, the interaction of $Ski7_N$ with Ski238 Mut1 or Mut2 complexes was severely impaired compared to Ski238 wt (Figure 3C). Next, we introduced these mutations *in vivo* using variations of the *SKI3-egfp* and *xrn1*Δ strains we previously described (Halbach et al., 2013). The *XRN1* gene encodes the exoribonuclease active in 5'-3' mRNA degradation pathways and is synthetically lethal with a deletion of genes encoding proteins in the 3'-5' degradation pathway, including *SKI3 (ski3*Δ/*xrn1*Δ, Figure 3D) (Johnson and Kolodner, 1995; Larimer and Stevens, 1990). The *ski3-Mut2*/*xrn1*Δ strain showed growth defects of increasing severity by shifting the temperature from 30˚C and 37˚C (Figure 3D). For the *ski3-Mut1*/*xrn1*Δ strain, we observed a synthetic lethal effect at either temperature (Figure 3D). We concluded that the Ski7-binding pockets of Ski3 we identified in the cryo-EM structural analysis are important for function.

Reconstitution of a stable Ski238-Ski7-Exo10 holocomplex for structural analysis

We proceeded to try and visualize the structure of an RNA-bound Ski238-Ski7-Exo10 holocomplex. We reconstituted an active Exo10 complex (comprised of the exoribonuclease Rrp44 and the Exo9 barrel) in presence of $Ski7_N$. For the helicase complex, after unsuccessful attempts with $Ski238_{FL}$, we focused on a Ski238 complex lacking $Ski2_{arch}$ and $Ski3_N$ ($Ski2_{\Delta arch}3_{\Delta N}8$), with the rationale of removing the autoinhibitory regulatory layers and facilitating the concerted Ski7 recognition by Ski238, as described above (Figure 2). Upon incubating $Ski2_{\Delta arch}3_{\Delta N}8$, Exo10 and $Ski7_N$ and testing the formation of the corresponding holocomplex by size-exclusion chromatography, we noticed a biochemical behavior consistent with a rather unstable assembly (namely the presence of two overlapping peaks in the

chromatogram, one of which corresponded to individual and thus unbound Ski2$_{\Delta arch}$3$_{\Delta N}$8 and Ski7$_N$-Exo10 complexes) (Figures 4A and S4A).

Reasoning that the instability of the holocomplex may be due to the low affinity of the Ski238-Ski7$_N$ interaction (Figures S2A and S2B), we introduced a protein engineering strategy known as the SpyTag-SpyCatcher system. This system is a protein ligation method that takes advantage of a covalent bond forming naturally between a bacterial surface protein (SpyCatcher) and the peptide it binds to (SpyTag) (Zakeri et al., 2012). We genetically fused the 13-amino acid SpyTag peptide sequence at the C-terminus of Ski3$_{\Delta N}$ and purified the corresponding recombinant Ski2$_{\Delta arch}$3$_{\Delta N}$8-SpyTag complex. The SpyCatcher domain was fused to Ski7$_N$, initially by testing two tethering positions (either the N-terminus or the C-terminus of Ski7$_N$) to evaluate the suitability of different ligation geometries (Figures 4B and S4B). Incubation of individually purified Ski2$_{\Delta arch}$3$_{\Delta N}$8-SpyTag and N-terminally fused SpyCatcher$_N$-Ski7$_N$ samples resulted in a covalently linked complex, as judged by the appearance of a 150kDa band in denaturing polyacrylamide gels corresponding to the covalently-bound Ski3-SpyTag- SpyCatcher-Ski7 polypeptide (Figures S4C). A similar protocol was used to alternatively fuse the SpyCatcher domain to the C-terminus of Ski7$_N$ (Figures 4B, S4B and S4C). The biochemical properties of the two covalently linked complexes were compared to the wild-type in RNase protections assays in order to assess the suitability of the ligation geometry (Figure 4C).

The RNase protection assays were carried out as previously described (Bonneau et al., 2009), incubating a single-stranded body-labeled (CU)$_{28}$C RNA with different versions of Ski238-Ski7$_N$ complexes and with a catalytically-inactive 10-subunit exosome core (Exo10$_{in}$) containing an inactive version of the Rrp44 ribonuclease (Rrp44$_{in}$) (Bonneau et al. 2009). In the case of Exo10$_{in}$, addition of RNase A/T1 is known to result in the accumulation of 30-33

ribonucleotide fragments, corresponding to the footprint of a ribonucleotide chain inside this complex (Makino et al., 2013). Incubation of $Exo10_{in}$ with $Ski2_{\Delta arch}38$ and $Ski7_N$ has been shown to also accumulate protected fragments of about 43-44 nucleotides that are believed to represent the RNA footprint of the cytoplasmic exosome holocomplex (Halbach et al., 2013). Adding the covalent Ski238-$Ski7_N$ complex formed with the C-terminally tagged SpyCatcher (Ski238-$SpyCatch_C$-$Ski7_N$) resulted in weaker RNase protection patterns while the N-terminally tagged SpyCatcher (Ski238-$SpyCatch_N$-$Ski7_N$) behaved as the wild-type complex (Figure 4C), and we therefore focused on the latter. Mixing the covalently Ski238-$SpyCatch_N$-$Ski7_N$ complex with a slight (1.3x) excess of catalytically active Exo10 allowed purifying a Ski238-Ski7-Exo10 holocomplex by size-exclusion chromatography, as judged by the presence of a well-separated peak at low retention volumes in the chromatogram (Figures 4A and S4A). We concluded that using a SpyTag-SpyCatcher covalent fusion strategy allowed us to reconstitute an active and stable Ski238-Ski7-Exo10 holocomplex.

Structure of an active Ski238-Ski7-Exo10 holocomplex

We proceeded to structurally characterize the stabilized Ski238-Ski7-Exo10 holocomplex by single-particle cryo-EM. The purified, active assembly (Figure S4D) was incubated with ATP and a 55-nucleotide single-stranded RNA containing a 3' hairpin for 25 minutes before grid application and vitrification (Figure S5A). Cryo-EM data were collected on a FEI Titan Krios microscope (Figure S5B). After initial particle picking, the particles were subjected to multiple rounds of 2D classification (Figure S5C). Selected 2D class averages were used for *ab initio* 3D reconstruction and heterogeneous refinement to derive 3D reconstructions. Of the 3D classes we obtained, several corresponded to individual Ski238 and $Ski7_N$-Exo10 complexes, while one

showed more extensive density features (Figure S5D). Systematic cleaning of the particle stack resulted in a final 3D reconstruction with local resolutions ranging from 2.5 Å and 3.5 Å resolution (Figures 4D, S5D and S5E). The reconstruction revealed density for the two enzymatic subunits (the helicase domain of Ski2 and the Exo10 ribonuclease Rrp44), the Exo9 barrel and the Exo10-binding segment of $Ski7_N$ (residues 119-225). The best-defined region of the map was at $Ski7_N$-Exo9 and the least defined at the more peripheral parts of Rrp44 (Figures 4D and S5E). The other protein elements in the sample (including the gatekeeping module of $Ski2_{\Delta arch}3_{\Delta N}8$ and the Ski238-binding segment of Ski7) showed no ordered density in this 3D reconstruction, albeit connected and covalently linked to the Ski7 Exo10-binding segment (Figures 4B and 4D).

The overall structure of the helicase-ribonuclease core of the Ski238-Ski7-Exo10 holocomplex (Figure 4E) showed the characteristic barrel-like structure of Exo9, with a ring of six RNase PH-like subunits (Rrp41, Rrp45, Rrp56, Rrp43, Mtr3, and Rrp42) capped by a ring of three S1/KH proteins (the so-called 'cap' proteins Rrp4, Rrp40 and Csl4). Rrp44 binds at the bottom of the RNase PH ring while Ski7 binds the cap and the top of the RNase PH rings with similar features as observed in a previous crystal structure (Kowalinski et al., 2016), namely with three α-helices that we can now redefine in the context of the rest of Ski7 as helix 4 ($Ski7_N$-H4) (docking on Csl4 N-terminal domain, NTD), helix 5 ($Ski7_N$-H5) (docking on Mtr3 and Rrp43) and helix 6 ($Ski7_N$-H6) (docking on Rrp43 and Csl4 C-terminal domain, CTD) (Figures 4D, 4E and S5F). Interestingly, an additional helix projecting out of the cap ring ($Ski7_N$-H7, Ski7 residues 212-225) contacts the Ski2 helicase domain (Figures 4D, 4E and S5F).

The reconstruction also allowed us to visualize density for RNA as it is threaded from the Ski2 helicase to the Rrp44 exoribonuclease (Figure 5A and S5G). The ribonucleotide chain could be traced in an unsharpened 3D reconstruction, although it was not possible to assign the

nucleotide sequence, possibly due to the inherent flexibility of RNA captured during the degradation process (Figure S5G). The ribonucleotide chain exits the Ski2 helicase core, extending towards Exo10. Here, RNA approaches the cap proteins at conserved residues of Rrp4 (Phe123 and Phe127) and Rrp40 (Phe80) with similar contacts as observed for the human nuclear exosome Mtr4 assembly (Weick et al., 2018). The ribonucleotide chain then continues inside the Exo9 core. Here, the path observed in the cryo-EM reconstruction is consistent with a previous crystal structure of $Ski7_N$-Exo10 (Kowalinski et al., 2016), with the ribonucleotide chain traversing through Exo9 until reaching the active site of the Rrp44 nuclease (Figure S5G).

RNA channeling is conserved between cytoplasmic and nuclear exosome holocomplexes

With the structure of this Ski238-Ski7-Exo10 holocomplex at hand, we wondered how the association of the Ski2 helicase with $Ski7_N$-Exo10 would relate to the nuclear exosome that uses the helicase Mtr4. By superposing the structure of the yeast Ski238-Ski7-Exo10 with the nuclear exosome Mtr4 structures from both yeast or human, we observed remarkable similarities in the interactions of cytoplasmic Ski2 and nuclear Mtr4 with the Exo10 (Figure 5B, S6A and S6B).

As in the case of Mtr4 (Gerlach, Schuller et al., 2018; Weick et al., 2018), the helicase domain of Ski2 binds the top of the Exo9 barrel at an angle, with the helical bundle and RecA1 domains contacting in particular the cap protein Rrp4 and with the RecA2 domain being exposed to solvent (Figures 5A and 5B). Rrp4 contains an N-terminal domain (NTD, bound to Rrp41) and an S1-KH module (with the KH domain bound to Rrp42 and the S1 domain positioned near the RNA-entry channel of Exo9). The Rrp4 NTD domain projects a set of hydrophobic residues (Met68, Val91 and Leu94) towards a conserved hydrophobic patch at the outer surface of the

Ski2$_{cat}$ helical-bundle domain (Leu1112, Leu1133, Ile1258 and Arg1115) (Figures 5C, S6A and S6C). An analogous interaction has been observed in the nuclear exosome (with the corresponding hydrophobic patch of MTR4 Met872, Phe893 and Ile1014, human numbering, Figures S6A and S6B). The Rrp4 S1 domain also contacts the Ski2$_{cat}$ helical bundle (with Rrp4 Glu107 and Gly109 inserting into a pocket lined by the conserved Ski2 Arg1115) (Figures 5C, S6A and S6C). A similar interaction has also been observed in the nuclear exosome (with the corresponding MTR4 Arg875, human numbering, Figures S6A and S6B).

The RecA1 domain of Ski2 is further recognized at the S1 domain of Rrp4, at a site known to be essential *in vivo* in yeast (Malet et al., 2010). Here, a positively-charged loop in the Rrp4 S1 domain (centered at Arg150) interacts with a conserved negatively-charged patch of the Ski2 RecA1 domain (Asp433 and Asp437) (Figures 5D, S6A and S6C). A similar interaction also takes place in the nuclear exosome (with the corresponding MTR4 Asp231). However, in the Ski238-Ski7-Exo10, the RecA1 domain of the helicase makes additional contacts with the same negatively-charged patch interacting with the CTD domain of Csl4 (via Arg215) (Figures 5D, S6A and S6C). This interaction appears to be promoted by Ski7$_N$-H7, which extends from the CTD of Csl4 and latches onto to a shallow pocket in RecA1 with Ski7 Ala 223 and Phe224 further engaging this aromatic residue in a cation-π interaction with the guanidinium group of Rrp4 Arg150 (Figures 5D, S6A and S6C). Although there is no direct equivalent of this interaction in the nuclear exosome, there is a conceptual similarity with Mpp6 (as it extends from a cap protein, Rrp40, to latch onto the Mtr4 helicase at RecA2) (Figure S6A). Notably, the site of Ski2 RecA1 where Ski7 latches on would only be accessible upon detachment of the gatekeeping module, as this occupies the same site of Ski2$_{cat}$ in the closed state of Ski238. Furthermore, the superposition of Ski2$_{cat}$ in the Ski238-Ski7-Exo10 holocomplex with the closed state of Ski238 shows that binding of the gatekeeping module and binding of the cap proteins to the

helicase domain are mutually exclusive, further supporting the concept of a concerted, sequential mechanism of conformational regulation that is required to channel RNA from the Ski2 helicase to Ski7$_N$-Exo10 (Figure S6D).

Conclusions

The formation of the yeast Ski238-Ski7-Exo10 holocomplex is controlled at the molecular level by a multilayered regulatory mechanism that coordinates the structural rearrangements driving activation of the helicase complex with the recruitment of the ribonuclease complex (Figure 6). In a resting state, Ski238 is stabilized in an autoinhibited closed-state conformation by the interactions of the Ski2 arch domain and the Ski3 N-terminal arm. Dissolution of this interaction (e.g., by the displacement of the Ski2 arch domain) is required to facilitate transition into the active open state, which is characterized by the release of the Ski2 helicase module from the gatekeeping module of the complex. Such conformational change has a dual function in the recruitment of the Ski238-Ski7-Exo10 holocomplex: it facilitates the recruitment of Ski7 to the gatekeeping module of Ski238 and it facilitates the positioning of the helicase module of Ski238 on Exo10, near the entry of the Ski7$_N$-Exo10 RNA-binding channel. Altogether, this allows for formation of a single continuous RNA-binding channel between the helicase and ribonuclease sites of the holocomplex. We speculate that this multi-layered regulatory mechanism is likely to be beneficial to ensuring correct substrate selection in light of the transient nature of holocomplex formation.

Displacement of the helicase arch domain appears to be a pivot point in the orchestrated series of events described above. In the biochemical and structural studies we report here we mimicked this step by using truncation mutants, but *in vivo* such displacement is likely to occur

upon binding to the ribosomes both in yeast (Schmidt et al., 2016) and human (Koegel et al., 2022). Although the specific Ski3-binding segments of yeast Ski7 (i.e., helices H1, H2, H3) do not share obvious conservation at the sequence level with the human counterpart HBS1L3, we note that the unexpected Ski2-binding segment of Ski7 (i.e., helix H7) is conserved in HBS1L3 (Kowalinski et al., 2016). It is therefore plausible that the regulatory mechanisms we discovered in the yeast system translate into other eukaryotes. More generally, while the exosome helicases and adaptor proteins differ in the nucleus and cytoplasm, they converged on using similar interaction topologies and RNA channeling mechanisms in the two subcellular compartments.

ACKNOWLEDGEMENTS

We thank Petra Bierle and Tatjana Krywcun for technical assistance; Marc Baumgaertner and Elisabeth Stegmann for assistance in insect-cell protein expression and purification; Fabien Bonneau for help with RNase protection assays; Nicole Eisele for help with yeast experiments; Andrè Ferdigg for assistance with MST experiments. We are grateful to Tilman Schäfer and Daniel Bollschweiler at the MPIB cryo-EM facility and Stephan Uebel at the MPIB core facility for outstanding support on cryo-EM and MST measurements; J. Rajan Prabu and Christian Benda for excellent maintenance of computational infrastructure. Finally, we thank Courtney Long for invaluable help in preparing the manuscript and all members of our group for thoughtful suggestions and inspiring discussions throughout the project. This work was supported by funding from the Max Planck Gesellschaft, the ERC Advanced Investigator Grants EXORICO (740329) and GOVERNA (101054447), and the German Research Foundation (DFG SFB1035).

AUTHOR CONTRIBUTIONS

E.C., A.Ke. and E.K. initiated the project; A.Ke. purified proteins and performed all biochemical experiments with input from A.Kö. P.R. generated yeast strains and performed viability assays; A. Ke. and I.B.S. conducted cryo-EM structure determinations; E.C. and A.Ke. wrote the manuscript with input from all authors.

DECLARATION OF INTERESTS

E.C. is a member of the *Molecular Cell* advisory board

Main text figures:

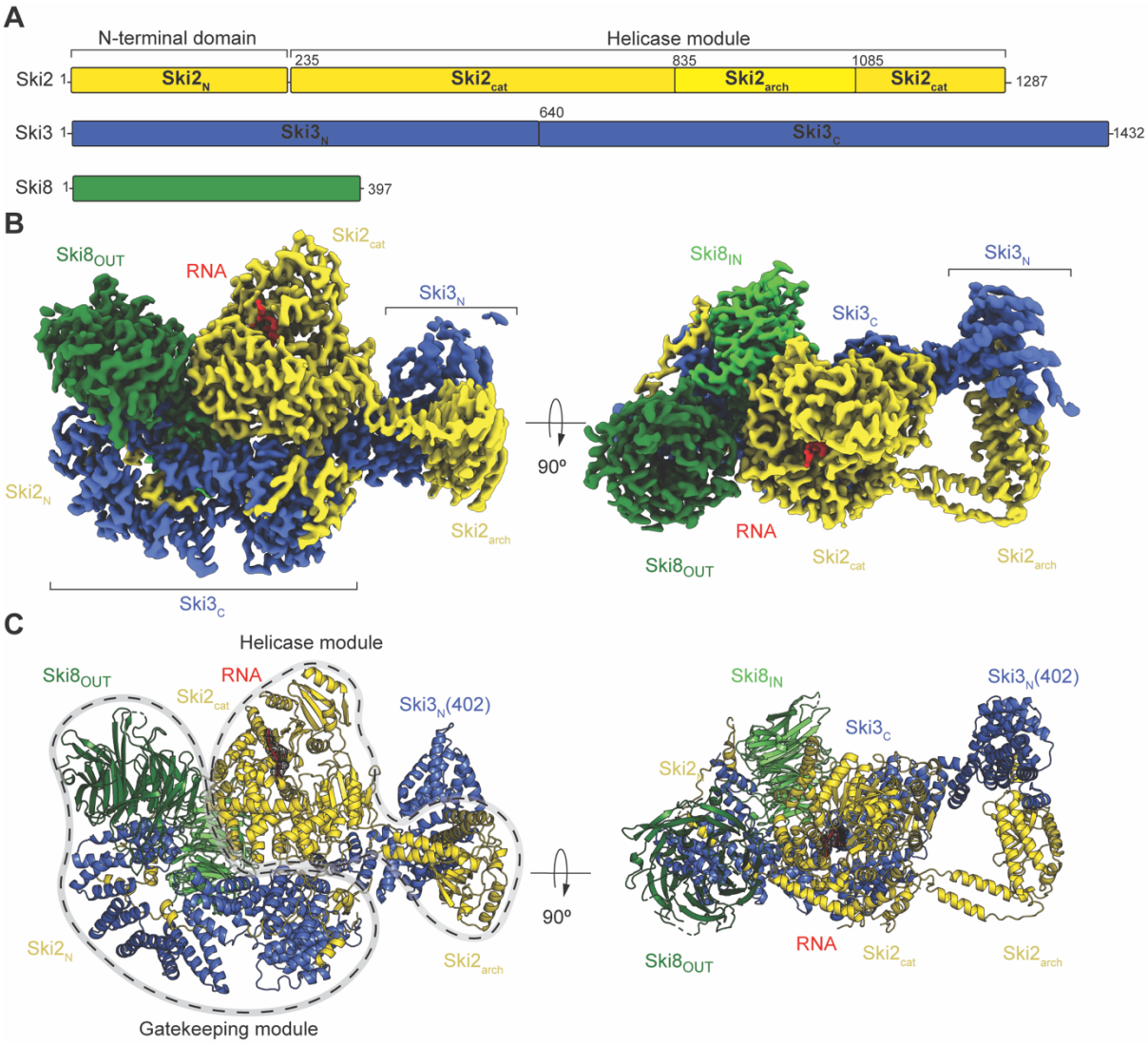

Figure 1. Autoinhibited conformation of yeast Ski238 bound to RNA

(A) Domain organization of the yeast Ski238 subunits Ski2 (yellow), Ski3 (blue), and Ski8 (green).

(B) Single-particle cryo-EM reconstruction of $Ski238_{FL}$ bound to RNA at a global resolution of ~2.8 Å, shown in two different orientations related by a 90˚ rotation around a horizontal axis. Density colored as in (A) and RNA colored in red. $Ski3_N$ and $Ski3_C$ indicated by brackets

(C) Composite structural model of the $Ski238_{FL}$ obtained from interpreting cryo-EM reconstructions. Structure of $Ski3_N$ (1-401) is not modelled due to lack of experimental density. Position of $Ski3_N$ 402 is labeled. Gatekeeping module ($Ski2_N$, $Ski3_C$, $Ski8_{IN}$, $Ski8_{OUT}$) and Helicase module ($Ski2_{cat}$, $Ski2_{arch}$) are highlighted by dotted lines (Also see Figure S1F).

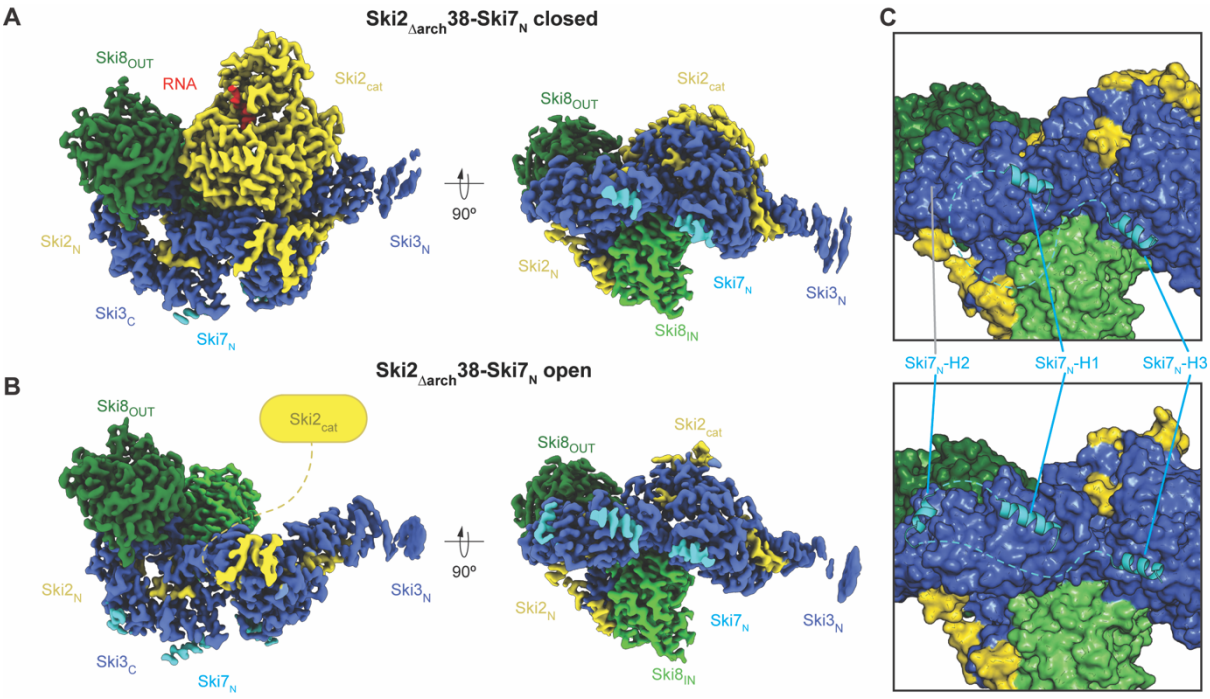

Figure 2. Conformational states of yeast Ski238 affect binding to Ski7

(A and B) Single-particle cryo-EM reconstruction of Ski2$_{\Delta arch}$38 in the closed state conformation (A) and open state conformation (B) bound with Ski7$_N$-(1-235) at a global resolution of ~2.8 Å. Maps are shown in two different orientations related by a 90˚ rotation around a horizontal axis (left panel oriented as in Figure 1, same color scheme). Ski7$_N$ is shown in cyan. In (B) the detached Ski2$_{cat}$ is indicated with a solid yellow line.

(C) Zoom-in of the model at the Ski2$_{\Delta arch}$38-Ski7$_N$ binding interface showing the density of the three Ski7 alpha-helices are only visible on open-state Ski2$_{\Delta arch}$ 38 (lower panel). Note only two alpha-helices are visible on closed-state Ski2$_{\Delta arch}$ 38 (upper panel). Ski2$_{\Delta arch}$38 is shown in surface representation, Ski7 is shown in cartoon representation.

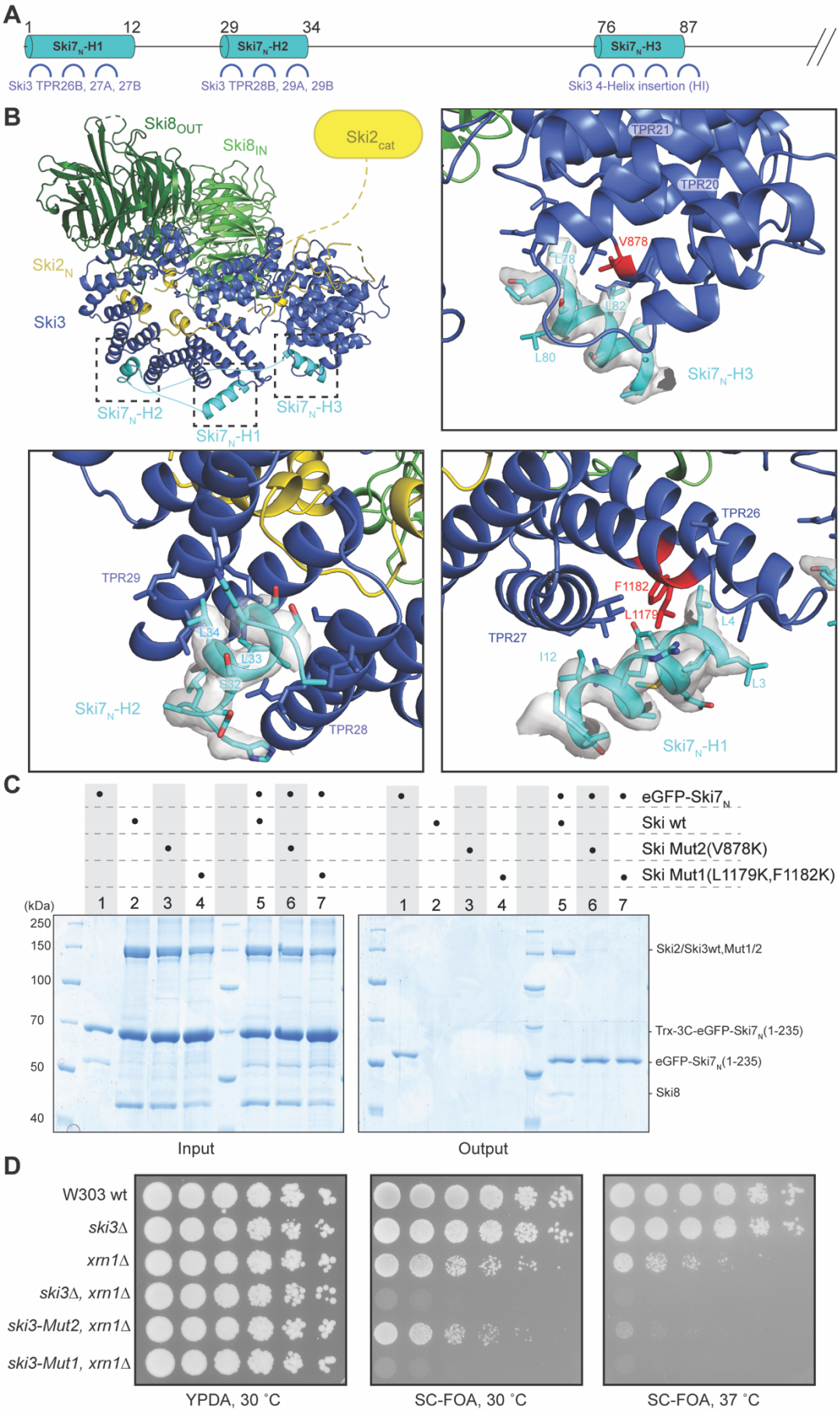
A
1
12
29
34
76
87
Ski7N-H1
Ski7N-H2
Ski7N-H3
Ski3 TPR26B, 27A, 27B
Ski3 TPR28B, 29A, 29B
Ski3 4-Helix insertion (HI)
B
Ski8OUT
Ski8IN
Ski2cat
Ski2N
Ski3
Ski7N-H2
Ski7N-H3
Ski7N-H1
TPR21
TPR20
V878
L78
I82
L80
Ski7N-H3
TPR29
L34
L33
S32
Ski7N-H2
TPR28
TPR26
F1182
L1179
L4
TPR27
I12
L3
Ski7N-H1
C
eGFP-Ski7N
Ski wt
Ski Mut2(V878K)
Ski Mut1(L1179K,F1182K)
(kDa)
1 2 3 4 5 6 7
1 2 3 4 5 6 7
250
150
100
70
50
40
Ski2/Ski3wt,Mut1/2
Trx-3C-eGFP-Ski7N(1-235)
eGFP-Ski7N(1-235)
Ski8
Input
Output
D
W303 wt
ski3Δ
xrn1Δ
ski3Δ, xrn1Δ
ski3-Mut2, xrn1Δ
ski3-Mut1, xrn1Δ
YPDA, 30 °C
SC-FOA, 30 °C
SC-FOA, 37 °C

Figure 3. Ski7 binds Ski3 C-terminal arm at functionally important sites

(A) Topology-based domain organization of the Ski7 N-terminal arm (residues 1-116). Secondary structure elements are indicated by cylinders. Interactions between $Ski7_N$ helices and $Ski3_C$ secondary structures are highlighted by labels.

(B) Overview of yeast $Ski2_{\Delta arch}38$ in open state bound by $Ski7_N$, with black boxes indicating Ski7 interactions with Ski3. Corresponding zoom-in views of the three Ski7 alpha-helices and their interaction with $Ski3_C$ TPRs are shown (color scheme and orientations same as in Figure 2B). Cryo-EM density for $Ski7_N$ shown as transparent surface in grey. Point mutations in $Ski3_C$ TPRs that disrupt binding with $Ski7_N$ are labeled in red.

(C) Coomassie-stained SDS gel analysis of GFP pull-down assays. Coprecipitation with $Ski7_N$ (TRX-3C-eGFP-$Ski7_N$(1-235)-Strep) was disrupted in Ski238 complexes harboring single or double mutations in Ski3 (compare lane 5 to lanes 6 and 7 in right panel). Pulldowns were done in the presence of 3C protease cleaving of the TRX-tag during the experiment which leads to a shift of the $Ski7_N$ band.

(D) Growth assay of wild-type (wt) and mutant yeast strains. Endogenous *SKI3* was replaced by wt or mutant *SKI3* (same as C) in strains where endogenous *XRN1*

was deleted. All strains (except wt, ski3Δ, and xrn1Δ) also carried an *XRN1-URA3* rescue plasmid. For the growth assay, cells were grown to early exponential phase and spotted in serial dilutions onto synthetic complete-fluoroorotic acid (SC-FOA) medium or control plates and grown at 30 ˚C or 37 ˚C. Medium containing SC-FOA selects for cells that have lost the *XRN1-URA3* plasmid.

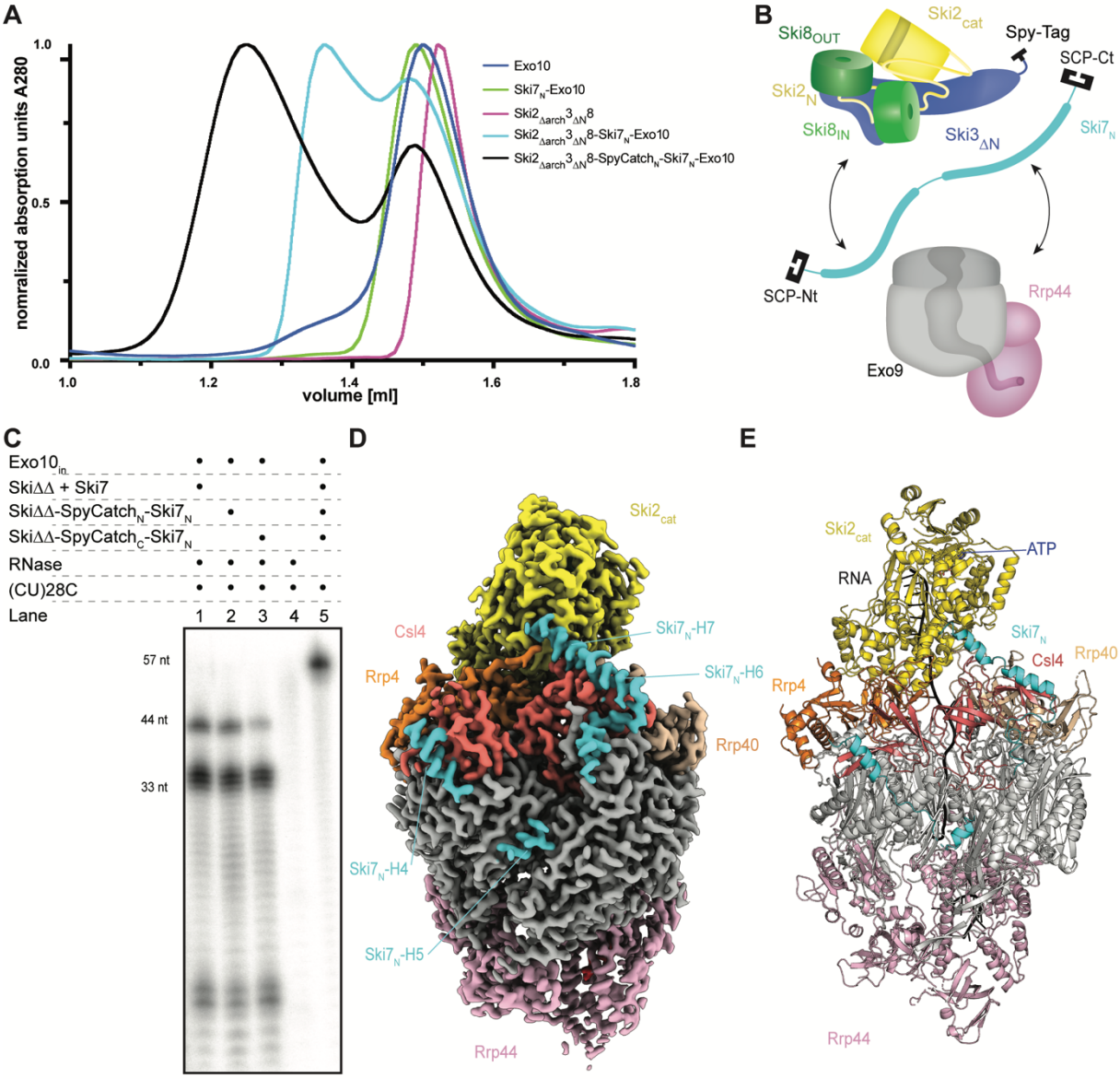

Figure 4. Cryo-EM reconstruction of an active RNA-bound Ski238-Ski7-Exo10 holocomplex

(A) Biochemical analysis to determine stability of a recombinant Ski2$_{\Delta arch}$3$_{\Delta N}$8-Ski7$_N$-Exo10 holocomplex. Pre-mixed complexes were subjected to size-exclusion chromatography experiments (S6i 3.2/300 column). An overlay of the chromatograms is shown and fractions were analyzed on SDS-PAGE gels (see Fig. S4A). Note that a 1.3x molar excess of the respective exosome complex was used in sample preparation for Ski2$_{\Delta arch}$3$_{\Delta N}$8-Ski7$_N$-Exo10 (light blue) and Ski2$_{\Delta arch}$3$_{\Delta N}$8-SpyCatch$_N$-Ski7$_N$-Exo10 (black) to ensure complete complex formation.

(B) Schematic depicting the SpyTag-SpyCatcher engineering strategy used to stabilize an active Ski238-Ski7-Exo10 holocomplex. The Spy-Tag was positioned on the N-terminus of Ski3$_{\Delta N}$ and the Spy-Catcher (SCP) was positioned

either at the C- or at the N-terminus arm of $Ski7_N$. Cartoon representation of the Exo9 core (gray) in association with Rrp44 (pink).

(C) Functional efficiency of covalently linked Ski238-Ski7-Exo10 holocomplex shown by RNase protection assay. A ^{32}P body-labeled RNA substrate $(*CU)_{28}C$ was incubated with the respective proteins and treated with RNase A/T1 mix. The samples were analyzed on a 12% denaturing UREA-PAGE gel. RNA fragments of 43-44 nucleotides accumulated in samples from control and covalently linked Ski238-Ski7-Exo10 holocomplexes. $Ski2_{\Delta arch}3_{\Delta N}8$ is labeled as SkiΔΔ.

(D) Overview of the covalently-bound Ski238-Ski7-Exo10 holocomplex shown in surface representation. Colors are as in (B), except for the cap proteins Csl4 (dark salmon), Rrp4 (orange), and Rrp40 (wheat) are now highlighted. Note that Ski238 is in the open state and therefore only the detached Ski2 helicase module ($Ski2_{cat}$) is visible, while the Ski7 helices that contact the Ski238 gatekeeping module are not visible.

(E) Atomic model of *S. cerevisiae* Ski238-Ski7-Exo10 holocomplex. Colors and orientation are the same as in (D).

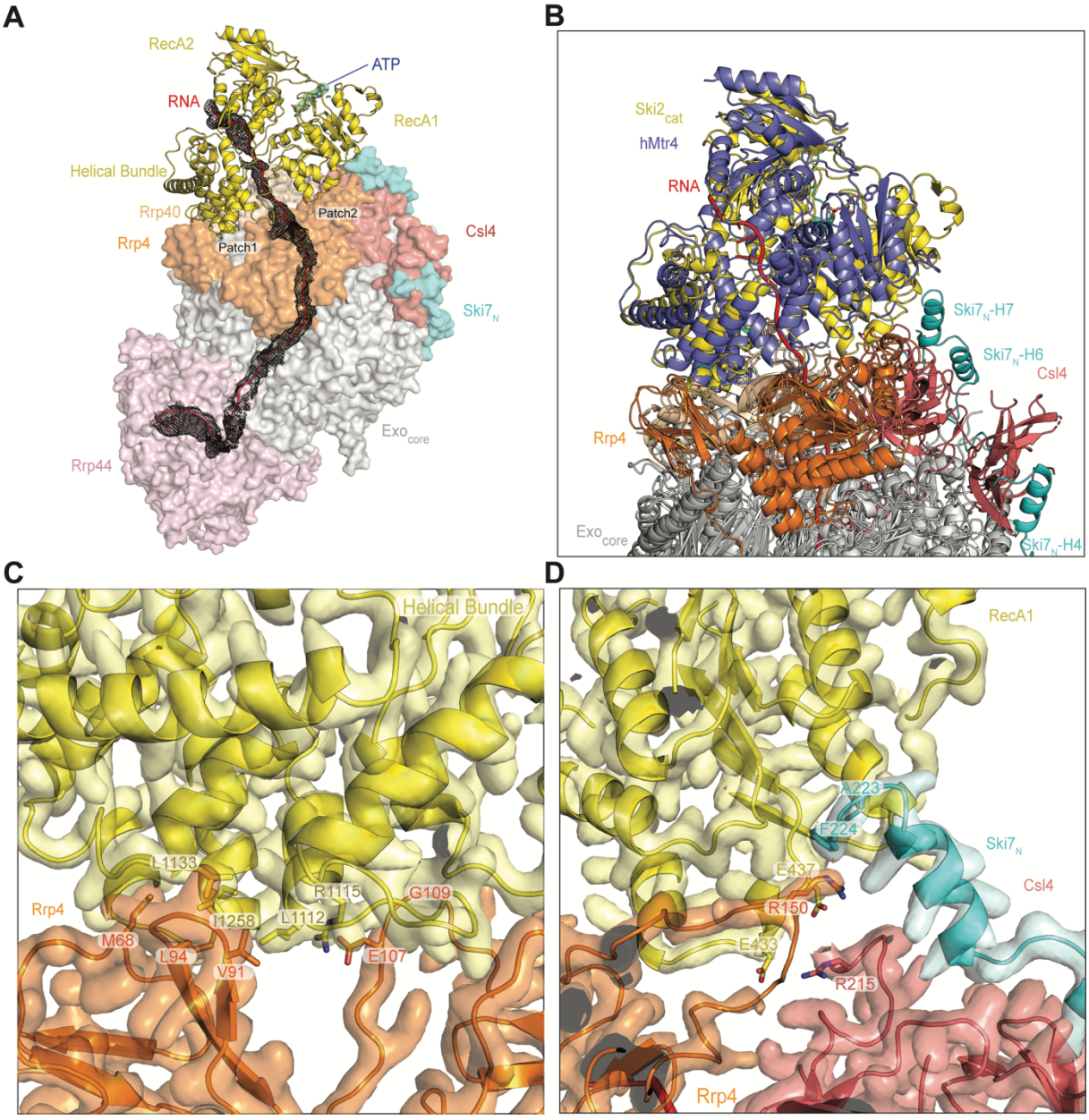

Figure 5. Helicase recruitment to the Exo10 is conserved between nucleus and cytoplasm

(A) Overview of the Ski238-Ski7-Exo10 holocomplex bound to a 55-nucleotide single-stranded RNA with a 3' hairpin and ATP. The $Ski7_N$-Exo10 is in surface representation and $Ski2_{cat}$ is in cartoon representation. Ski238 is in the open state and the individual domains of $Ski2_{cat}$ module are indicated. RNA is in red with corresponding density shown in black mesh. ATP (green) shown in stick representation with EM density. Two interaction patches shown in C and D are labeled (Patch 1 and 2).

(B) Comparison of *S. cerevisiae* Ski2 and human Mtr4 binding to Exo10. Front view on the superposition of the cytoplasmic Ski2 and nuclear Mtr4 (PDB: 6D6Q) helicase cofactors. The structure is shown in cartoon ribbon with colors as in Figure 4D, Mtr4 is colored in slate, RNA in red.

(C and D) Zoom-in views of the interaction patches between Ski2 and the $Ski7_N$-Exo10 in cartoon representation. Patches are indicated in the overall structure in (B). The Ski2 helical bundle contacts the Exo10 protein Rrp4 (C) while the Ski2 RecA1 domain contacts the Exo10 proteins Rrp4 and Csl4 as well as $Ski7_N$-H7 (D). Interacting residues are shown in stick representation. EM density is shown transparent in the same color as the respective subunits.

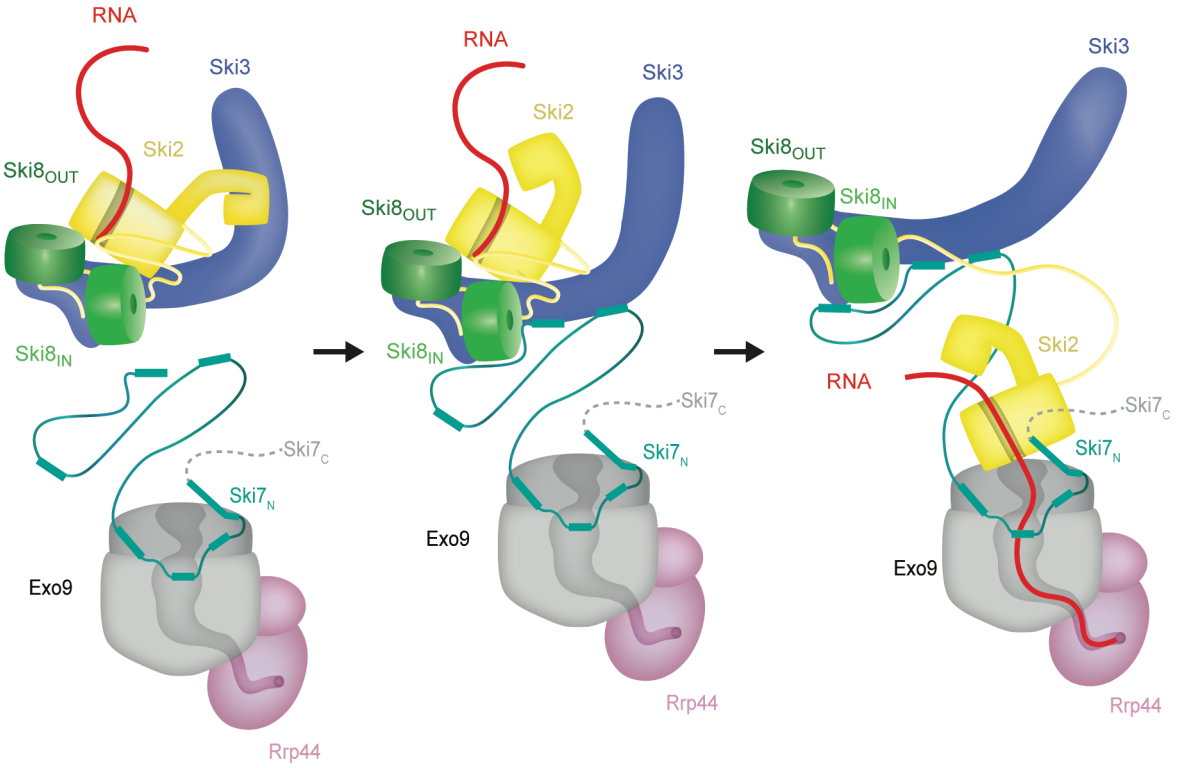

Figure 6. Model of the Ski238-Ski7-Exo10-mediated 3' – 5' RNA decay in eukaryotes

The proposed model shows that closed-state Ski238 can bind the 3' end of RNA, but must undergo conformational changes to the open state to interact with Ski7-Exo10 in order to form a continuous channel that may be traversed by RNA. This mode of recruitment and RNA pathway is in keeping with the human Ski238-Exo10 model (Koegel et al., 2022) and the nuclear exosome holocomplex (Gerlach et al., 2018, Schuller et al., 2018, Weick et al., 2018). Note that ATP is not shown for simplicity but we expect ATP binding and subsequent hydrolysis is necessary for architectural rearrangement of Ski.

STAR Methods

RESOURCE AVAILABILITY

Lead Contact

Further Information and requests for resources and reagents should be directed to and will be fulfilled by the Lead Contact, Elena Conti (conti@biochem.mpg.de)

Materials availability

This study did not generate new unique reagents

Data and code availability

- Cryo-EM density maps have been deposited in the Electron Microscopy Data Bank (EMDB) and the Protein Data Bank (PDB), respectively, under the accession numbers: EMDB: xxxx, PDB: XXX (Ski238$_{FL}$), EMDB: xxxx, PDB: XX (Ski2$_{\Delta arch}$38-Ski7$_{N}$ closed), EMDB: xxxx, (Ski2$_{\Delta arch}$38-Ski7$_{N}$ intermediate), EMDB: xxxx, PDB: XX (Ski2$_{\Delta arch}$38-Ski7$_{N}$ open), EMDB: xxxx, PDB: XXX (Ski238-Ski7$_{N}$-Exo10)
- All cryo-EM reconstructions and atomic models can be downloaded here:
- This paper does not report original code.
- Any additional information required to reanalyse the data reported in this work/paper is available from the lead contact upon request.

EXPERIMENTAL MODEL AND SUBJECT DETAILS

Bacterial and insect cells used in this study were for protein production to conduct *in vitro* experiments and structural analysis. Yeast strains were used for *in vivo* viability assays. All cell types are listed in the Key Resources Table and handling information pertinent to each cell type are described in method details.

METHOD DETAILS

Protein expression and purification of Ski7 constructs from *E. coli*

S. cerevisiae Ski7 (Uniprot: Q08491) was cloned into a pBR322 vector (EMBL Heidelberg core facility) and recombinantly expressed in BL21(DE)Gold pLysS *E. coli* (Thermo Fischer Scientific) cells and grown in TB media at 37 ˚C up to OD_{600} = 1.5 under antibiotic selection. Ski7 constructs were expressed with an N-terminal 6xHis-thioredoxin tag followed by a 3C protease cleavage site and a C-terminal A-G-S-StrepII tag. For the $Ski7_N$-$SpyCatch_N$ construct, the SpyCatcher domain (Zakeri et al.) was fused to the N-terminus of $Ski7_N$, behind the 3C cleavage site followed by a 4x(GS) linker. For the $Ski7_N$-$SpyCatch_C$ construct a 4x(GS) linker followed by the SpyCatcher domain with a C-terminal Strep tag, was fused to the C-terminus of $Ski7_N$. Expression was induced with 0.1 mM IPTG for approximately 18 hours at 18 ˚C. All of the following harvesting and purification steps were performed on ice or at 4˚C. Bacteria were harvested by centrifugation at 8,500 g and resuspended in 300 ml of 20 mM Tris-HCl pH 7.4, 250 mM NaCl, 1% (v/v) glycerol, and 20 mM imidazole supplemented with 0.1 mM AEBSF protease inhibitor, 0.001 mg/ml DNase, and 0.01 mg/ml lysozyme. Cells were disrupted by a VS-70T sonicator (Bandelin Sonopuls) and lysate was cleared by centrifugation at 75,600 g for 30 min. Filtered lysate was loaded onto two sequential 5 ml HisTrap HP columns (Cytiva).

Columns were washed with 10 column volumes (CV) of 20 mM Tris-HCl pH 7.4, 250 mM NaCl, 1% (v/v) glycerol, 20 mM imidazole, 2.5 mM $MgSO_4$, 50 mM KCl and 2 mM ATP followed by another 10 CV of 20 mM Tris-HCl pH 7.4, 1000 mM KCl, 1% (v/v) glycerol and 20 mM imidazole. His-tagged proteins were eluted with 20 mM Tris-HCl pH 7.4, 250 mM NaCl, 1% (v/v) glycerol and 300 mM imidazole on an ÄKTA Prime plus. Peak fractions were pooled and loaded onto two consecutive 5 ml StrepTrap HP columns (Cytiva) followed by washing with 10 CV of 20 mM Tris-HCl pH 7.4, 250 mM NaCl, and 1% (v/v) glycerol. Strep-tagged proteins were directly eluted into a 5 ml HiTrap Heparin HP column (Cytiva) with 2 CV of 20 mM Tris-HCl pH 7.4, 250 mM NaCl, 1% (v/v) glycerol, and 2.5 mM Desthiobiotin (DTB) followed by 5 CV of the same buffer, except without DTB. The heparin column was washed as above and proteins were eluted by buffer with increasing NaCl gradient (20 mM Tris-HCl pH 7.4, 1000 mM NaCl, 1% (v/v) glycerol, 1 mM DTT) (up to 60% salt). Peak fractions were pooled and dialyzed against 20 mM Tris-HCl pH 7.4, 200 mM NaCl, 1% (v/v) glycerol, and 1 mM DTT overnight at 4˚C. Protein concentration was determined and the samples were mixed with 10% (v/v) glycerol and flash frozen for storage at -80 ˚C until further use.

Ski7 proteins (His_6-TRX-3C-$Ski7_N$(1-105)-AGC-Strep) used in microscale thermophoresis experiments underwent an additional SEC step. Samples were supplemented with 20 mM imidazole before purification over a 5 ml HisTrap HP column followed by 2 CV of the above dialysis buffer. Subsequently, the flow through was concentrated using a Amicon Ultra MWCO 10 kDa and injected onto a Superdex 75 Increase 10/300 GL column (GE Healthcare) equilibrated in 20 mM HEPES pH 7.4, 150 mM NaCl, 1% (v/v) glycerol and 1 mM DTT. Peak fractions were pooled and directly used in microscale thermophoresis experiments.

Protein expression and purification of Ski238 constructs from *Sf21* insect cells

The complete open reading frames for recombinant *S. cerevisiae* Ski2, Ski3, and Ski8 (Uniprot: P35207, P17883, and Q02793) were cloned into separate expression cassettes simultaneously or individually on pAECBac1 vectors (Bieniossek et al., 2012) using the Multibac™ system (Geneva Biotech) per the manufacturer's instructions. In the constructs containing $Ski2_{\Delta arch}$, residues 835-1085 were replaced with a GSRG linker. In the constructs containing $Ski3_{\Delta N}$, residues 1-521 were removed. In the SpyTag-$Ski2_{\Delta arch}3_{\Delta N}8$ construct, the SpyTag was fused to the N-terminus of $Ski3_N$ followed by an AGS linker. Vectors were incorporated into a baculovirus genome and virus amplified in *Sf*21 cells grown in Sf-900 II SFM medium (Thermo Fisher Scientific) at 26 ˚C. Hi5™ cells at 1 x 10^6 cells/ml were infected with 1% (v/v) virus solution, or in case of co-infection a 1:1 mixture of virus was used. After incubation for 3 days at 26 ˚C, cells were harvested by centrifugation for 10 min at 800 g. Purification of Ski238 complexes was performed as previously described (Halbach et al., Keidel et al.). Briefly, cells were sonicated in lysis buffer (300 ml of 20 mM Tris-HCl pH 7.4, 150 mM NaCl, 2 mM $MgCl_2$, 25 mM imidazole and 1 mM 2-mercaptoethanol (ß-ME)) supplemented with 0.1 mM AEBSF protease inhibitor, 0.001 mg/ml DNase and 75 U of benzonase (Merck). Lysate was cleared by centrifugation at 75,600 g for 60 min at 4 ˚C. Filtered lysate was supplemented with one cOmplete EDTA-free protease inhibitor tablet (Roche) and then loaded onto two interconnected 5 ml HisTrap HP columns on a loop overnight. The columns were washed with 10 CV of lysis buffer followed by 10 CV of 20 mM Tris-HCl pH 7.4, 1000 mM NaCl, 2 mM $MgCl_2$, 25 mM imidazole and 1 mM ß-ME. His-tagged proteins were eluted with 20 mM Tris-HCl pH 7.4, 150 mM NaCl 300 mM imidazole and 1 mM ß-ME. Peak fractions were pooled and loaded onto a 5 ml HiTrap Q HP column and washed with 20 mM Tris-HCl pH 7.4, 150 mM NaCl and 1 mM ß-ME until the absorption at 280 nm reached baseline level. Proteins were eluted with

buffer containing increasing NaCl concentrations (20 mM Tris-HCl pH 7.4, 1000 mM NaCl and 1 mM ß-ME) (up to 50% salt). The peak fractions were pooled, supplemented with 5 µg of 3C protease and dialyzed against 20 mM Tris-HCl pH 7.4, 100 mM NaCl, 2 mM $MgCl_2$, and 1 mM ß-ME overnight. Protein was concentrated using Amicon Ultra MWCO 100 000 kDa and injected onto a HiLoad Superdex 200 16/600 GL column (Cytiva) equilibrated in 20 mM HEPES pH 7.4, 100 mM NaCl, 2 mM $MgCl_2$, and 1 mM ß-ME. Peak fractions were pooled, supplemented with 10% (v/v) glycerol, flash frozen in liquid nitrogen and stored at -80 ˚C until further use.

The *S. cerevisiae* $Ski7_N$-Exo10 complex was prepared as previously described (Makino et al., Kowalinski et al.)

Spy reaction to introduce covalent link between $Ski7_N$-$SpyCatch_{C/N}$ and SpyTag-$Ski2_{\Delta arch}3_{\Delta N}8$

For initial spy reactions, 150 pmol of $SpySki2_{\Delta arch}3_{\Delta N}8$ was mixed with 500 pmol of either $Ski7_N$-$SpyCatch_C$ or $Ski7_N$-$SpyCatch_N$. Mixtures were supplemented with 1 µl of 3C protease solution (2 mg/ml) and adjusted to a final volume of 100 µl with 20 mM Tris HCl pH 7.5, 350 mM NaCl, 2 mM $MgCl_2$, 2 % (v/v) glycerol, and 2 mM ß-ME. The reaction was incubated at 4 ˚C overnight and success of a spontaneous covalent link forming between Ski7 and Ski3 was analysed by SDS PAGE on a 12% acrylamide gel. For large scale spy reactions, 3 nmol of Spy-tagged $Ski2_{\Delta arch}3_{\Delta N}8$ was mixed with 5 nmol of $Ski7_N$-$SpyCatch_N$ in 20 mM Tris HCl pH 7.5, 350 mM NaCl, 2 mM $MgCl_2$, 2 % (v/v) glycerol, and 2 mM ß-ME and incubated overnight at 4 ˚C. Concentrated samples were injected onto a Superdex 200 increase 10/300 GL column equilibrated in 20 mM HEPES pH 7.4, 350 mM NaCl, 2 mM $MgCl_2$, 2 % (v/v) glycerol and 2 mM

ß-ME. Peak fractions were collected and subjected with 10 % glycerol, flash frozen liquid nitrogen, and stored at -80 ˚C.

Pulldown with recombinant proteins

Pulldown experiments were performed as previously described with minor differences (Kowalinski et al.) Briefly, 5 µg of tagged bait protein (eGFP-AGS-Ski7$_N$(1-235)-Strep) was mixed with 1.2x molar excess of the untagged interaction partner (Exo9 or Ski238). Mixtures were diluted in 20 mM HEPES pH 7.4, 150 mM NaCl, 2 mM $MgCl_2$, 2 mM DTT, 0.1 % (v/v) NP40 and adjusted to a final volume of 50 µl. 10 µl were taken as the input sample for SDS PAGE analysis. The remaining 40 µl were mixed with 20 µl of equilibrated GFP-Binder resin, 190 µl of buffer from above and 0.25 µl of 3C protease (2 mg/ml). After incubation for 45 min at 4 ˚C, beads were spun for 1 min at 1,000 g and supernatant was removed. Subsequently, beads were washed 4 times with 200 µl of buffer containing increasing NaCl concentrations (up to 1M). Beads were dried using 20 µl gel loading tips and proteins were eluted by adding 1x SDS sample buffer and directly analyzed by SDS-PAGE on a 12 % acrylamide gel.

Microscale thermophoresis experiments

Affinity measurements were performed with a Nanotemper monolith NT.115 according to the manufacturer's protocol. Prior to the affinity measurements, we labeled Ski7$_N$(1-105)-AGC-Strep at the cysteine using the Monolith Protein Labeling Kit RED-Malemide 2nd Generation (Nanotemper Technologies) per the instructions. All proteins were dialyzed against a buffer containing 20 mM HEPES pH 7.5, 100 mM NaCl, 2 mM $MgCl_2$, 10 % (v/v) glycerol, and 2 mM

DTT). Ski238 and Ski2$_{\Delta arch}$38 complexes were serially diluted to 20 nM and mixed with equal amounts of Ski7$_N$(1-105)-AGC-Strep-RED. Thermophoresis was measured with MST power of 40%, LED power of 80%, and with standard parameters pre-set on the NanoTemper monolith NT.115 machine. Data were analysed using the MO software (Nanotemper Technologies). Samples were run in triplicate to establish standard deviations.

Size exclusion chromatography

SEC (size exclusion chromatography) experiments were performed at 4 ˚C on an ÄKTA Micro using a Superose 6 increase 3.2/300 column (GE Healthcare) in SEC buffer (20 mM HEPES pH 7.4, 100 mM NaCl, 2 mM $MgCl_2$, and 2 mM TCEP). For Exo10, Exo11 and Ski2$_{\Delta arch}$3$_{\Delta N}$8 samples, 120 pmol of the respective complex was adjusted to a volume of 30 µl using the SEC buffer. The sample was supplemented with 1 µl of 3C protease (0.2 mg/ml), incubated on ice for 1 h and centrifuged for 15 min at 21, 130 g and then 25 µl were injected onto the column. For the Exo10 + Ski2$_{\Delta arch}$3$_{\Delta N}$8, Ski7$_N$Exo10 + Ski2$_{\Delta arch}$3$_{\Delta N}$8 and Exo10 Ski7-SpyCatch$_N$-Ski2$_{\Delta arch}$3$_{\Delta N}$8 samples, 120 pmol of the respective Ski238 complex was mixed with 170 pmol of the respective exosome complex prior to injection. Absorption readings were overlayed using GraphPad Prism9 (Dotmatics) to compare stability and retention times. Peak fractions from SEC were analyzed via SDS PAGE on 15 % acrylamide gels.

Complex Reconstitution and grid preparation for cryo-EM

To reconstitute Ski238$_{FL}$ bound with Ski7$_N$ and RNA, 3,500 pmol of Ski238 was mixed with 7,000 pmol of Trx-3C-Ski7$_N$-(1-235) in a total volume of 1 ml in 20 mM HEPES pH 7.4, 150 mM

NaCl, 2 mM $MgCl_2$, and 2 mM ß-ME supplemented with 1 µl of 3C protease (2 mg/ml) for 2 h at 4 ˚C. Then, 10 µM of RNA-U_{30} was added to the mixture and incubated for another 30 min at 4 ˚C. The sample was concentrated to 500 µl using a Amicon Ultra MWCO 30 kDa and injected onto a Superdex 200 increase 10/300 GL column equilibrated in the same buffer, with the exception of a lower NaCl concentration (75 mM). Peak fractions were analyzed by SDS PAGE on a 12 % acrylamide gel. The pooled peak fractions were centrifuged for 15 min at 21,130 g and A280 absorption was measured using UV-vis spectroscopy before adjusting to 2 mg/ml with the SEC buffer. The sample was treated with 0.05% n-octyl- β-D-glucoside (v/v) before cryo-EM grid preparation.

To prepare the Ski2$_{\Delta arch}$38-Ski7$_N$-(1-235) complex bound to RNA, 7,000 pmol of Ski2$_{\Delta arch}$3$_{\Delta N}$8 was mixed with 14,000 pmol of Trx-3C-Ski7$_N$-(1-235) in a total volume of 1.5 ml in 20 mM HEPES pH 7.4, 150 mM NaCl, 2 mM $MgCl_2$, and 2 mM ß-ME supplemented with 1 µl of 3C protease (2 mg/ml) for 2 h at 4 ˚C. Addition of RNA and chromatography purification were the same as above. Peak fractions were analyzed by SDS PAGE on a 10 % acrylamide gel. The pooled peak fractions were centrifuged for 15 min at 21,130 g and A280 absorption was measured using UV-vis spectroscopy and adjusted to 2 mg/ml using the SEC buffer. The sample was treated with 0.05% n-octyl- β-D-glucoside (v/v) prior to cryo-EM grid preparation.

To prepare the SpyTag-SpyCatcher Ski238-Ski7$_N$-Exo10 holocomplex, 3,800 pmol of inactive Ski7-SpyCatch$_N$Ski2$_{\Delta arch}$3$_{\Delta N}$8 was mixed with 5,000 pmol of active Exo10 in 20 mM HEPES pH 7.4, 350 mM NaCl, 2 mM $MgCl_2$, and 2 mM ß-ME supplemented with 1 µl of 3C protease (2 mg/ml) to a total volume of 500 µl. The mixture was incubated at 4 ˚C for 1 h and loaded onto a Superdex 200 increase 10/300 GL column. For analysis, 1/10 of the sample was loaded onto a Superose 6 increase 3.2/300 GL column and fractions were analyzed by SDS PAGE on a 12 % acrylamide gel. The peak fractions containing the assembled Ski2$_{\Delta arch}$3$_{\Delta N}$8-SpyCatch$_N$-Ski7$_N$-

Exo10 were pooled, supplemented with glycerol 10 % (v/v), flash frozen in liquid nitrogen and stored at -80 ˚C. To assemble an active complex bound to RNA, 600 pmol of purified $Ski2_{\Delta arch}3_{\Delta N}8$-$SpyCatch_N$-$Ski7_N$-Exo10 was mixed with 10000 pmol of RNA 5'-hairpin-U_{60} in 50 mM HEPES pH 7.4, 50 mM NaCl, 5 mM $MgCl_2$, and 2 mM TCEP to a total volume of 100 µl. The sample was incubated at room temperature for 45 min before addition of ATP at a 2 mM final concentration and the reaction mixture was incubated for another 25 min at 25 ˚C. The mixture was centrifuged for 20 min at 21,130 g and supplemented with 0.05% n-octyl- β-D-glucoside (v/v) before immediate use in cryo-EM grid preparation.

In all cases, 4 µl of sample was applied to R2/1, Cu200 Quantifoil grids that were glow discharged for 20 sec with negative polarity at 20 mA using an EMS GloQube (MiTeGen). Samples were incubated on the grid for 1 min and then plunged into liquid ethane/propane using a Vitrobot Mark IV at 4˚C and 100 % humidity. Grids were then directly clipped and stored in liquid nitrogen. All grids were prescreened for good ice quality on a ThermoFischer GlaciosTEM operated at 200 kV prior to final data acquisition.

Cryo-EM data acquisition and processing

High resolution cryo-EM movies of different datasets were collected on a FEI Titan Krios G2 microscope (Thermo Fisher Scientific) operated at 300 kV, equipped with a K3 Summit direct detector operated in counting mode, and a post-column Gatan energy filter set to slit-width of 20 eV. The target defocus range for all three datasets was set from 0.6 µm to 2.2 µm in 0.2 µm steps. FOCUS software was used to pre-select recorded movies during acquisition, using a CTF max resolution cutoff at < 5 Å (Biyani et al., 2017). All three datasets were preprocessed with MotionCor2, to correct for radiation damage and beam induced motion of the sample

(Zheng et al., 2017). The summed exposure weighted micrographs were imported to cryoSPARC (versions 3.3.2 and 4.2.1) for further processing. CTF parameters were determined using Patch-CTF estimation. For all datasets, 1,000 micrographs underwent particle picking using the blob picker tool in cryoSPARC, extracted and subjected to 2D classification. The resulting 2D classes were used to either train a model for the Topaz (Bepler et al., 2019) picker (Ski238$_{FL}$-Ski7 Ski7 box size = 288 Å, Ski2$_{\Delta arch}$38-Ski7 box size = 352 Å) or as input for the template picker (Ski2$_{\Delta arch}$3$_{\Delta N}$8-SpyCatch$_N$-Ski7$_N$-Exo10 box size = 360 Å) for picking on all micrographs. A resolution cut-off value of 0.143 gold standard Fourier shell correlation (GSFSC) was applied overall.

For Ski238$_{FL}$-Ski7$_N$(1-235), a total of 9,416 micrograph movies were collected at a nominal magnification of 105,000x (0.8512 Å pixel size). Data was collected using serialEM with a multi-shoot script that acquires images from a 5x5 hole pattern without stage shift, taking 4 images per hole leading to 100 exposure groups in the dataset. During imaging, a total exposure of 67.5 e/Å^2 was evenly distributed over 30 frames in 4 sec. Initially, a total of 2,023,469 particles were extracted. After multiple rounds of 2D classification, a stack of 1,476,216 particles was used for *ab initio* 3D reconstruction into 3 models, followed by heterogenous refinement into three classes. Closer inspection of the resulting reconstructions allowed us to identify three different particles sets: closed with Ski2$_{arch}$, closed without Ski2$_{arch}$ and open without Ski2$_{cat/arch}$. The closed with Ski2$_{arch}$ particles were used for two subsequent rounds of heterogenous refinement to systematically remove damaged and badly aligned particles. The resulting cleaned stack of 538,530 particles was used for non-uniform refinement and reached a global nominal resolution of 2.84 Å. Subsequent, heterogenous refinement into 3 classes allowed us to further sort the particles. The resulting particle stack of 385,414 particles was

used for non-uniform refinement and after automated negative b-factor weighting (b-factor=121.9) reached a global nominal resolution of 2.84 Å. To further improve the resolution of the 3D reconstruction, we performed signal subtraction of the Ski238$_{core}$ or the Ski2$_{arch}$-Ski3$_{N}$ interface followed by local refinements. After post-processing and automated negative b-factor weighting (b-factor=135.4, 117.8), the subtracted particle stacks reached a nominal resolution of 2.96 Å and 2.92 Å, respectively. Although the resolution of Ski238$_{core}$ did not improve, the Ski2$_{arch}$-Ski3$_{N}$ interface was better resolved and used to assist model building (Figure S1A and B).

For Ski2$_{\Delta arch}$38-Ski7$_{N}$-(1-235), a total of 7,127 micrograph movies were collected at a nominal magnification of 105,000x (0.8512 Å pixel size). Data was collected using serialEM with a multi-shoot script that acquires images from a 5x5 hole pattern without stage shift, taking 3 images per hole leading to 75 exposure groups in the dataset. During imaging, a total exposure of 77.7 e/Å^2 was evenly distributed over 35 frames in 4 sec. Multiple rounds of 2D classification on 1,017,173 extracted particles produced a stack of 956,268 particles that were then used for *ab initio* 3D reconstruction into 3 models, followed by heterogenous refinement into six classes. Closer inspection of the resulting reconstructions allowed us to identify three different particles sets: closed, intermediate and open. The closed particles underwent another round of heterogenous refinement into four classes to remove damaged and badly aligned particles. The resulting cleaned stack of 371,916 particles was used for non-uniform refinement and after automated negative b-factor weighting (b-factor=123.6) reached a global nominal resolution of 2.84 Å. The same procedure was done for the intermediate and open particles. The cleaned intermediate stack of 104,956 particles after non-uniform refinement and subsequent automated negative b-factor weighting (b-factor=113.5) resulted in 3D reconstructions reaching a global nominal resolution of 3.12 Å. The cleaned open stack

of 357,690 particles (b-factor=125.7) resulted in 3D reconstructions reaching a global nominal resolution of 2.85 Å. To further improve the resolution of the open 3D reconstruction, we performed signal subtraction of the flexible $Ski3_N$ interface followed by local refinement. The subtracted particle stacks reached a nominal resolution of 2.80 Å (b-factor=117.4).

For $Ski2_{\Delta arch}3_{\Delta N}8$-$SpyCatch_N$-$Ski7_N$-Exo10, a total of 18,608 micrograph movies were collected at a nominal magnification of 105,000x (0.8512 Å pixel size). Data was collected using serialEM with a multi-shoot script that acquires images from a 5x5 hole pattern without stage shift, taking 5 images per hole leading to 125 exposure groups in the dataset. During imaging a total exposure of 63.36 e/$Å^2$ was evenly distributed over 38 frames in 3 sec, and a total of 10,437,666 particles were extracted. After multiple rounds of 2D classification, a stack of 2,491,222 particles was used for *ab initio* 3D reconstruction into three models, followed by heterogenous refinement into eight classes. Due to the number of particles, heterogenous refinements were done in five subsets using ~500,000 particles. Closer inspection of the resulting 3D reconstructions allowed us to identify six different particles within each subset ($Ski7_N$-Exo10 RNA, $Ski7_N$-Exo10, Ski238-$Ski7_N$-Exo10, Ski238 closed and Ski238 open). This classification was similar for all five subsets. Each Ski238-$Ski7_N$-Exo10 particle stack was used for another round of heterogenous refinement into three classes to remove damaged and badly aligned particles and then combined. The resulting cleaned stack of 338,757 particles was used for non-uniform refinement and after automated negative b-factor weighting (b-factor=99.6) reached a global nominal resolution of 2.48 Å.

For all final particle stacks, we included the different optics group using the exposure group utilities tool. For post-processing, we accounted for per-group CTF parameters and higher

order abbreviations, as well as per-particle defocus. To assist map interpretation, model building and for figure displays, the final refined maps were sharpened with DeepEMhancer (Sanchez-Garcia et al., 2021).

Model building and refinement

For all models, rigid-body fitting was performed with available structures using USCF Chimera (Pettersen et al. 2004). The models were manually adjusted in Coot (Emsley et al., 2010)and real space refined in phenix.refine (Afonine et al., 2018). Progress in modeling was monitored via the map-to-model correlation coefficients and map versus model FSCs (Table S1). Structures were created in PyMOL2 and ChimeraX (Goddard et al., 2018).

The Ski238$_{FL}$ model was interpreted by rigid body fitting with available crystal structures (Ski2$_{\Delta arch}$38 PDB: 4BUJ, Ski2$_{arch}$ PDB: 4A4K) into a final map obtained from non-uniform refinement. Then the individual chains were adjusted with real space refinements. The local refined map was used to improve the Ski2$_{arch}$-Ski3$_{N}$ interface reconstruction. Ski2$_{arch}$ was individually placed in the map by real space refinement. The helices of Ski3$_{N}$ (residues 402-658) were individually rigid body fitted into the map. Additionally, a short helix of Ski2$_{N}$ was rigid body fitted into extra density next to Ski3$_{N}$ (606-656). The local resolution did not allow us to identify the register of this helix and therefore it was assigned based on the previous crystal structure (Ski2$_{\Delta arch}$38 PDB: 4BUJ). In the helicase core, we could observe additional density that we interpreted to be RNA based on similarities with RNA bound human Ski2 (PDB: 7QDY) and yeast Mtr4 (PDB: 6FSZ). The 4 nucleotides of the RNA-U$_{30}$ observed in the helicase core were built *de novo* using RCrane in Coot.

To interpret Ski2$_{\Delta arch}$38-Ski7 in the open state, we rigid-body fitted the Ski238$_{FL}$ structure into the map obtained from non-uniform refinement. Ski2$_{cat}$ was removed and all chains were assigned individually by real space refinement. Due to flexibility, residues 643-701 of Ski3$_N$ were rigid body fitted into the map. The rest of Ski3$_N$ was removed from the model. Density bound to Ski3 could be assigned to three helices of Ski7$_N$ and were built *de novo*. To assist map interpretation, we used a map sharpened with DeepEMhancer and we further generated Alphafold2 predictions of a minimal Ski23-Ski7 complex (Figure S3C and D) that are in accordance with our model. Building of Ski2$_{\Delta arch}$38-Ski7 in the closed state was initially done as described for the open state. Ski2$_{cat}$ was rigid-body fitted and then individually adjusted by real space refinement. The additional signal in the core of Ski2$_{cat}$ was interpreted as RNA based on the Ski238$_{FL}$ model. The RNA was then rigid-body fitted into the map. Ski2$_{arch}$ (832-1087) and Ski3$_N$ (until 402-661) were removed.

The Ski2$_{\Delta arch}$3$_{\Delta N}$8-SpyCatch$_N$-Ski7$_N$-Exo10 was interpreted by rigid-body fitting the available crystal structure of the Exo10 bound to Ski7 (PDB: 5JEA) and the RNA bound Ski2$_{cat}$ from our Ski238$_{FL}$ model. Each side chain and the individual domains (RecA1, RecA2 and helical bundle) of Ski2$_{cat}$ were individually corrected by rigid-body fitting. Likewise, due to flexibility in the nuclease, certain parts of Rrp44 (Residues 9-237, 252-493, 494-910 and 911-1001) were also build by rigid-body fitting. Afterwards all side chains were corrected by real space refinement, except for Rrp44 (Residues 494-1001). For interpretation of the continuous RNA density that extends from Ski2$_{cat}$ to Rrp44, we used the unsharpened map from non-uniform refinement of the Ski238-Ski7-Exo10 assembly. For building the poly-U RNA, we superposed available exosome structures bound to RNA and Mtr4 (PDB: 5JEA, 6FSZ and 4IFD). All nucleotides were converted to U and then individual RNA chains were rigid body fitted to the map. The best fitting RNA segments were selected by visual inspection and combined into a continuous RNA

chain consisting of 34 nucleotides. RNA bases were removed, except for nucleotides bound to $Ski2_{cat}$ (0-3), within Exo10 (8-10) and bound to Rrp44 (28-33). Additional density between the two RecA domains of $Ski2_{cat}$ was interpreted and built as ATP based on the overlap with the crystal structure of the nucleotide-bound Ski2 (4A4Z).

RNase protection assays

Body-labeled 57-mer of (CU)28C RNA was prepared by *in vitro* transcription of a template (oFB27-T7 annealed with oFB47-T7-60-cuc-R, see key resource table) with radioactively labeled [alpha 32-P] UTP (Perkin-Elmer) using T7 RNA polymerase. The reaction mix was processed with Turbo DNase and RNaseT1, then purified by gel electrophoresis (8% acrylamide (19:1) 7M Urea in 1x TBE) and the RNA was retrieved by gel extraction. The transcription estimate was estimated using a liquid scintillation counter. The purified transcript was dissolved in RNase free water at 10 µM. Protein complexes were incubated with 5 pmol of body-labeled RNA in 50 mM HEPES-NaOH (pH 7.5), 50 mM NaCl, 5 mM magnesium diacetate, 10% (w/v) glycerol, 0.1% (w/v) NP40, 1 mM DTT and 1 mM of ADP for 1h at 4 ˚C. Final protein concentrations were 0.5 µM for Exo10 or alternatively 0.75 µM for $Ski7_N$-(1-235), $Ski2_{\Delta arch}3_{\Delta N}8$, $Ski7_N$-$SpyCatch_C$-$Ski2_{\Delta arch}3_{\Delta N}8$ and $Ski7_N$-$SpyCatch_N$-$Ski2_{\Delta arch}3\Delta 8$. The reaction mixtures were then supplemented with 0.5 µl of RNase A/T1 mix (5000 U/ml) and incubated for 20 min at 20 ˚C. The reaction was stopped by adding 11x of buffer containing 300 mM NaCl, 60 mM NaOAc and 0.2% SDS. The protected RNA fragments were recovered by two consecutive phenol extractions with phenol/chloroform/isoamyl alcohol (25:24:1). The RNA was precipitated with 540 µl of 100% ethanol for 1.5 h at -20 ˚C. The precipitate was pelleted at 16,100 g for 15 min and the pellets were washed twice with 300 µl of 80% ethanol

solution. Then the pellets were dried using a speed-vac for 10 min at 45 ˚C and resuspended in 8 µl of 70% BFE. 3.5 µl of protein sample was boiled for 3 min and separated at 10 W for 1.75 h on a denaturing 15% acrylamide (19:1) 7M Urea gel. Afterwards the gel was exposed to a phosphor screen at -80 ˚C overnight. Bands were visualized using a Typhoon FLA 7000 (GE Healthcare).

Yeast experiments

The strains in this study are based on the haploid *S. cerevisi*ae W303 mat strain with the following additional genetic background: ski3Δ::kanMX4, xrn1Δ::natNT1 | Ycplac33-XRN::URA3, except for the control strains, wildtype and the individual single deletions of ski3 and xrn1. The mutant strains were obtained by gene replacement of the double deletion strain. The construct for gene replacement was generated by the Gibson assembly method. The individual amino acid changes were introduced via oligonucleotides where wildtype genomic yeast DNA or previously used bacterial protein expression plasmids served as a template and amplified by PCR. Two fragments carrying the respective amino acid change were joined with a third fragment carrying the selection marker and inserted into the construct. The assembly was flanked by 50 homologous base pairs on both the 5' and 3' end to facilitate and target gene replacement in the correct ski3 genomic locus. Transformation was done as previously described (Dietz et al. 2007) using approximately 1 µg of DNA. Cells were rescued overnight in 1 ml YPAD at 26°C and subsequently plated on YPAD/hygromycin media incubated at 30°C for 3 days. Replica plating was done on YPAD/hygromycin and YPAD/G418 to obtain a $G418^{s}$ $hygromycin^{r}$-$nourseothricin^{r}$-strain. Genomic DNA was prepared from these strains, ski3 genomic locus was PCR amplified and subsequently

sequenced to confirm the introduction of anticipated amino acid exchanges. Initially the strains were constructed without C-terminal tags on Ski3 to avoid interference of additionally introduced amino acids in viability studies. In a second step, a 6xHA tag was introduced at the C-terminus as previously reported (Knop et al. 2004) in the previously generated strains to determine protein expression.

QUANTIFICATION AND STATISTICAL ANALYSIS

All statistical analyses are indicated in the figure legends to the relevant data and in the corresponding STAR Methods section.

SUPPLEMENTARY INFORMATION

Table S1. Cryo electron microscopy data collection summary, processing statistics and model quality indicators

Data collection parameters and processing					
Dataset	**Ski238$_{FL}$**	**Ski2$_{\Delta Arch}$387-Ski7$_{N}$**			**Ski238-Ski7$_{N}$-Exo10**
Microscope	FEI Titan Krios G2				
Voltage [kV]	300				
Camera	Gatan K3				
Energy Filter	Gatan Quantum-LS (GIF)				
Magnification	105000x	105000x			105000x
Pixel Size [e^-/A^2]	0.8512	0.8512			0.8512
Electron exposure ($e^-/Å^2$)	67.5	77.7			63.36
Target defocus range [µm]	0.6 – 2.2	0.6 – 2.2			0.6 – 2.2
Number of movies	9416	7127			18608
Initally selected particles	2 023 469	1 017 173			10 437 666
		‘closed’	‘intermediate’	‘open’ Ski3N subtracted	
Final number of particles	385414	371 916	104 956	357690	338 757
Resolution [Å]	2.84	2.84	3.12	2.80	2.55
Local resolution range [Å]	2.84-10				

Sharpening B-factor [Å^2]	-121.9	-123.6	-113.5	-117.4	-166.05
Refinement					
No. of atoms	20903	17675	-	11574	30792
Residues (protein/nucleotide)	2786/4	2361/4	-	1530/0	3919/34
Ligands	-		-		ATP
CC_{box}, CC_{mask}, CC_{volume}	0.70, 0.85, 0.83	0.67, 0.79, 0.77	-	0.61, 0.76, 0.75	0.76, 0.90, 0.86
CC for individual chains (Ski2=A, Ski3=B, Ski8=C,D, Ski7=E, RNA=X	A = 0.785, B = 0.784, C = 0.835, D = 0.777, X = 0.588	A = 0.748, B = 0.706, C = 0.782, D = 0.658, E = 0.616, X = 0.656	-	A = 0.620, B = 0.685, C = 0.771, D = 0.702, E = 0.666	-
Resolution $_{FSC\ map\ vs.\ model\ (0/0.143/0.5)}$ [Å]	2.8/2.8/3.0	2.7/2.8/3.1	-	2.7/2.8/3.0	2.4/2.5/2.6
r.m.s. deviations					
Bond legths [Å]	0.002	0.004	-	0.003	0.005
Bond angles [°]	0.526	0.570	-	0.508	0.630
Ramachandran favored [%]	97.89	96.37	-	97.86	96.44
Ramachandran allowed [%]	2.11	3.63	-	2.14	3.48
Ramachandran outliers [%]	0.00	0.00	-	0.00	0.08
MolProbity score	1.51	1.53	-	1.78	1.68
Clash score	5.24	5.37	-	4.62	3.75

Rotamere outliers [%]	4.21	0.41	-	4.76	2.36

Supplementary figures:

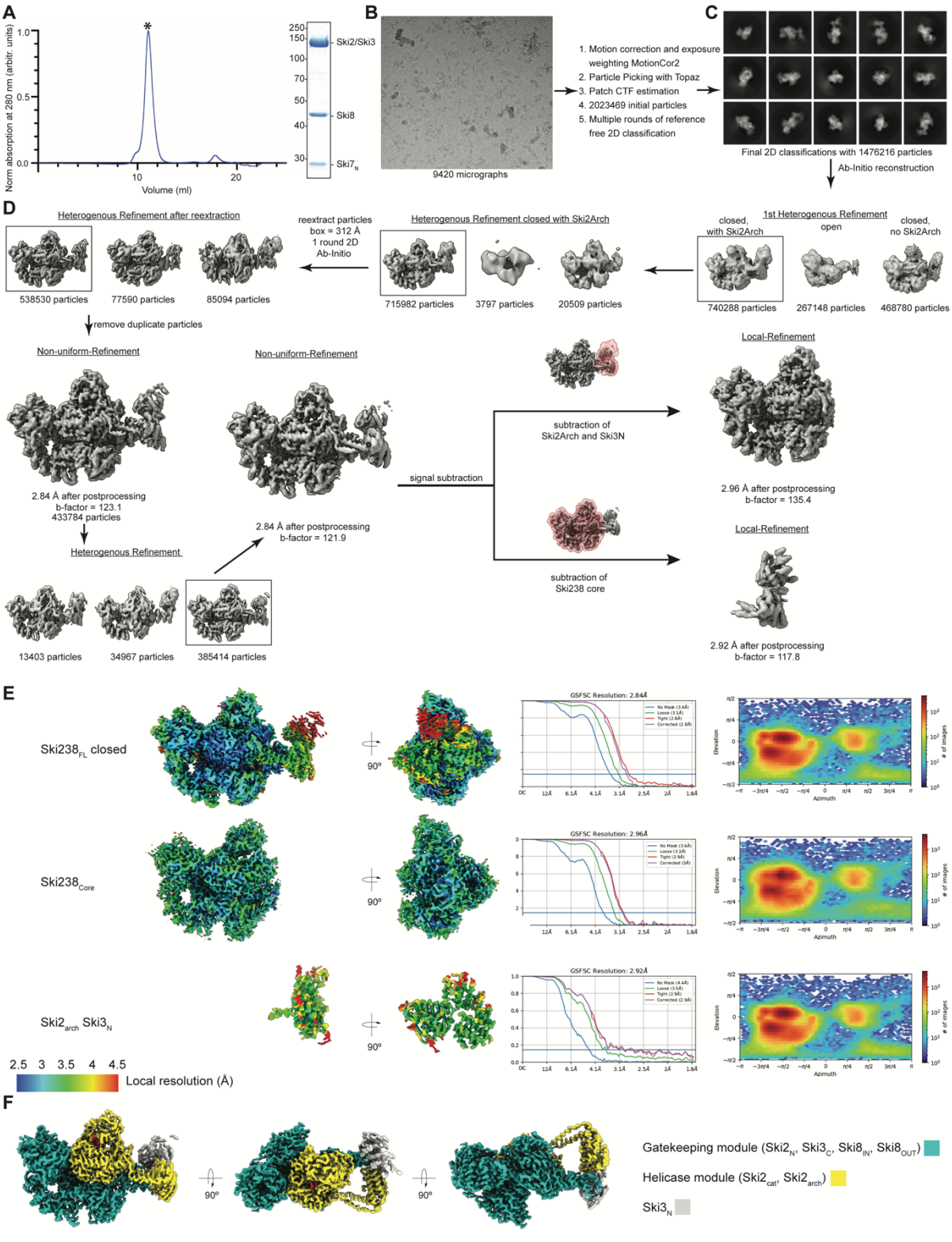

Figure S1. Cryo-EM analysis of recombinant full-length Ski238 ($Ski238_{FL}$) with $Ski7_N$ and RNA (related to Figure 1)

(A) Size exclusion chromatography (SEC) analytical profile of $Ski238_{FL}$ reconstituted with $Ski7_N$ over a S200i 10/300 GL column (left) with corresponding 12% Coomassie stained SDS-PAGE of the peak fractions (right).

(B) Representative cryo-EM micrograph collected on a Titan Krios G2 at 300 kV with a pixel size of 0.8512 Å/pix using a K3 direct electron detector.

(C) Representative 2D class averages of the initial selection of $Ski238_{FL}$ complexed with $Ski7_N$.

(D) Cryo-EM data processing scheme. Pre-processing steps and heterogeneous refinement resulted in two particle stacks of $Ski238_{FL}$ in the closed and the open conformation, respectively. For the closed state, a 20 Å low-pass filtered map was used for mask generation (transparent red) focusing either on the Ski238 core or $Ski2_{arch}$:$Ski3_N$. Subsequent signal subtraction and local refinement yielded a map of Ski238 core at a resolution of 3.0 Å and Ski2-Arch:Ski3-N at 2.9 Å. All maps shown are unsharpened maps obtained after refinements.

(E) Local resolution estimates of the final non-uniform and local refinements for the cryo-EM SPA datasets in (D), shown in two different orientations related by a 90˚ rotation around a vertical axis (left panel). Corresponding Fourier shell correlation (FSC) curves of respective maps, as well as angular distribution plot obtained from cryoSPARC (right panel).

(F) Single-particle cryo-EM reconstruction of $Ski238_{FL}$ bound to RNA (Figure 1B) shown in three different orientations related by a 90˚ rotation around a horizontal axis. Gatekeeping module consisting of $Ski2_N$, $Ski3_C$, $Ski8_{IN}$ and $Ski8_{OUT}$ colored in sea green. Helicase module consisting of $Ski2_{cat}$ and $Ski2_{arch}$ colored in yellow. $Ski3_N$ colored in grey RNA colored in red.

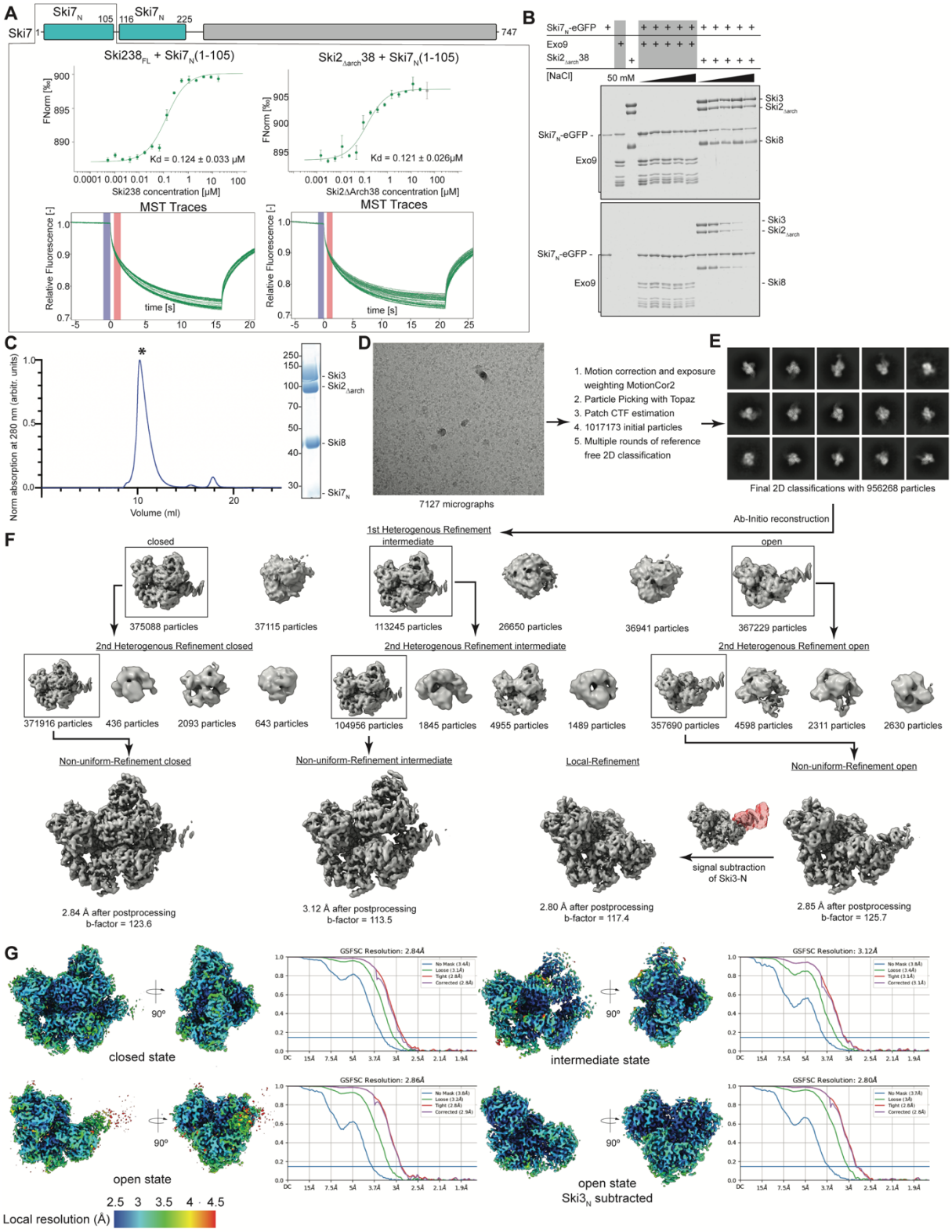

Figure S2. Biochemical and structural analysis of Ski2$_{\Delta arch}$38 in complex with Ski7$_N$ (related to Figure 2)

(A) Domain organization of *S. cerevisiae* Ski7 is shown on top, with Ski7$_N$ terminus colored cyan and Ski7-C terminus in gray. The bottom panel shows a biophysical analysis using microscale thermophoresis to quantify

the $Ski7_N$ affinity ($Ski7_N$-(1-105)-NHS-Red) for $Ski238_{FL}$ and $Ski2_{\Delta arch}38$. Dissociation constant (K_D) was calculated from triplicate measurements with standard deviation indicated by error bars. The respective MST-traces are shown.

(B) Protein coprecipitations with GFP pull-down assays. with recombinant $Ski2_{\Delta arch}38$, Exo9 and $Ski7_N$-(eGFP-Ski7(1-235)-Strep). Increasing salt concentration (50 mM up to 1M NaCl, indicated by black triangles) disrupts $Ski7_N$ binding to $Ski2_{\Delta arch}38$, but not between $Ski7_N$ and Exo9.

(C) SEC analytical profile of recombinant $Ski2_{\Delta arch}38$-$Ski7_N$ reconstituted over a S200i 10/300 GL column (left panel) with corresponding 12% Coomassie stained SDS-PAGE gel of the peak fraction (right panel).

(D) Representative cryo-EM micrograph of $Ski2_{\Delta arch}38$-$Ski7_N$ collected on a Titan Krios G2 at 300 kV with a pixel size of 0.8512 Å/pix using a K3 direct electron detector.

(E) Representative 2D class averages of $Ski2_{\Delta arch}38$-$Ski7_N$.

(F) Cryo-EM data processing scheme. Heterogeneous refinement of 2D class averages resulted in three major particle stacks representing $Ski2_{\Delta arch}38$-$Ski7_N$ in a closed, intermediate and open conformation. Respective particle stacks (black boxes) were used for another round of heterogenous refinement followed by non-uniform refinement of the best resulting class. For the open conformation, a 20 Å low-pass filtered map was used for mask generation (transparent red) focusing on the flexible $Ski3_N$. Subsequent signal subtractions and local refinement yielded a map of open $Ski2_{\Delta arch}38$-$Ski7_N$ at a resolution of 2.8 Å. All maps shown are unsharpened maps obtained after refinements.

(G) Local resolution estimation of the final non-uniform and local refinements for $Ski2_{\Delta arch}38$-$Ski7_N$ cryo-EM SPA datasets, with orientations and color scheme same as Figure S1E. Corresponding FSC curves obtained from cryoSPARC.

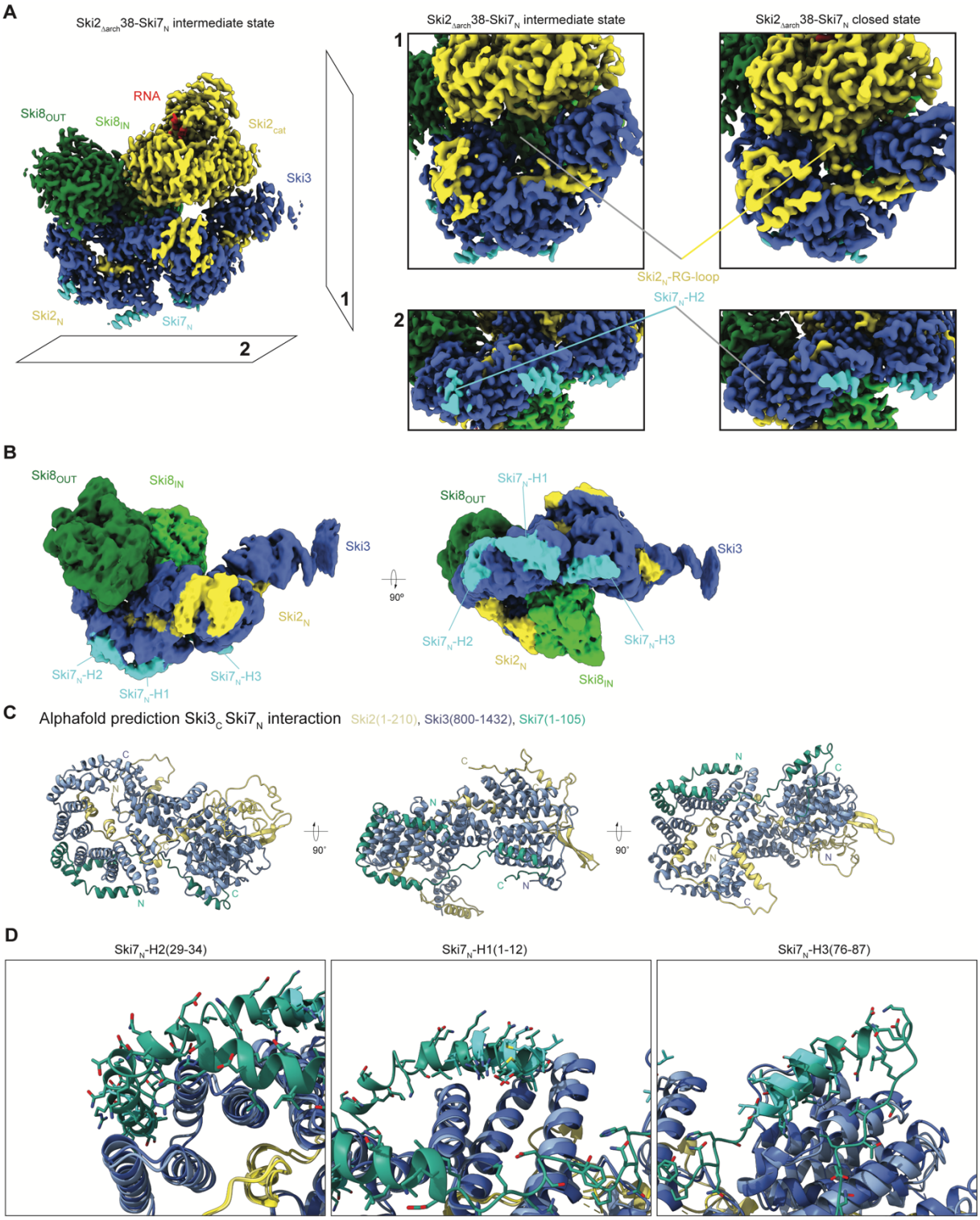

Figure S3. Map interpretation and model validation of Ski7$_N$ on Ski2$_{\Delta arch}$38 by Alphafold2 predictions (related to Figure 3)

(A) 3D reconstruction of Ski2$_{\Delta arch38}$-Ski7$_N$ in the intermediate conformation (left panel). Colors and orientation are identical to Figure 2A. (1-2) Planes indicate a front view (1) and a bottom view (2) of the complex. Comparison

of Ski2$_{\Delta arch}$38-Ski7$_N$ intermediate and closed conformation (right panel). (1) Zoom-in view showing the position of Ski2$_{cat}$ and Ski2$_N$-RG-loop/Wedge (129-164) (Halbach et al., 2013a; Koegel et al., 2022). Note that the RG-loop/Wedge does not adopt a defined structural conformation and that Ski2$_{cat}$ is shifted upwards compared to the closed conformation. (2) Zoom-in view of the Ski7$_N$ binding site on Ski3$_C$ showing that Ski7-H2 is not recruited in the closed state.

(B) Unsharpened 3D reconstructions of Ski2$_{\Delta arch}$38-Ski7$_N$ in open state at low threshold (ChimeraX, level ~ 0.1), shown in two orientations related by a 90˚ rotation around a horizontal axis. Ski2 colored in yellow, Ski3 in blue, Ski8$_{IN}$ in green and Ski8$_{OUT}$ in dark green, and RNA in red. Additional signal in the open state was observed at Ski3$_C$ and assigned to Ski7$_N$ (cyan). (C) Alphafold2 multimer prediction of the Ski23 in the open conformation and Ski7 binding sites showed overall structural similarity to the cryo-EM map analysis. Ski2-N(1-210) (pale yellow) Ski3$_C$(800-1432) (light blue) and Ski7$_N$ (1-105) (sea green) shown in three different orientations related by a 90˚ rotation around a vertical axis. N and C termini are indicated by N and C and colored according to the corresponding protein.

(D) Superposition of Alphafold2 prediction (C) and the Ski2$_{\Delta arch}$38-Ski7$_N$ model reconstructed in this study. Zoom-in views at Ski7$_N$-H2 (left panel), Ski7$_N$-H1 (middle panel) and Ski7$_N$-H3 (right panel). Colors for the predicted model are identical to (C) and colors for Ski2$_{\Delta arch}$38-Ski7$_N$ are identical to Figure 3B. Ski7$_N$ is in stick representation.

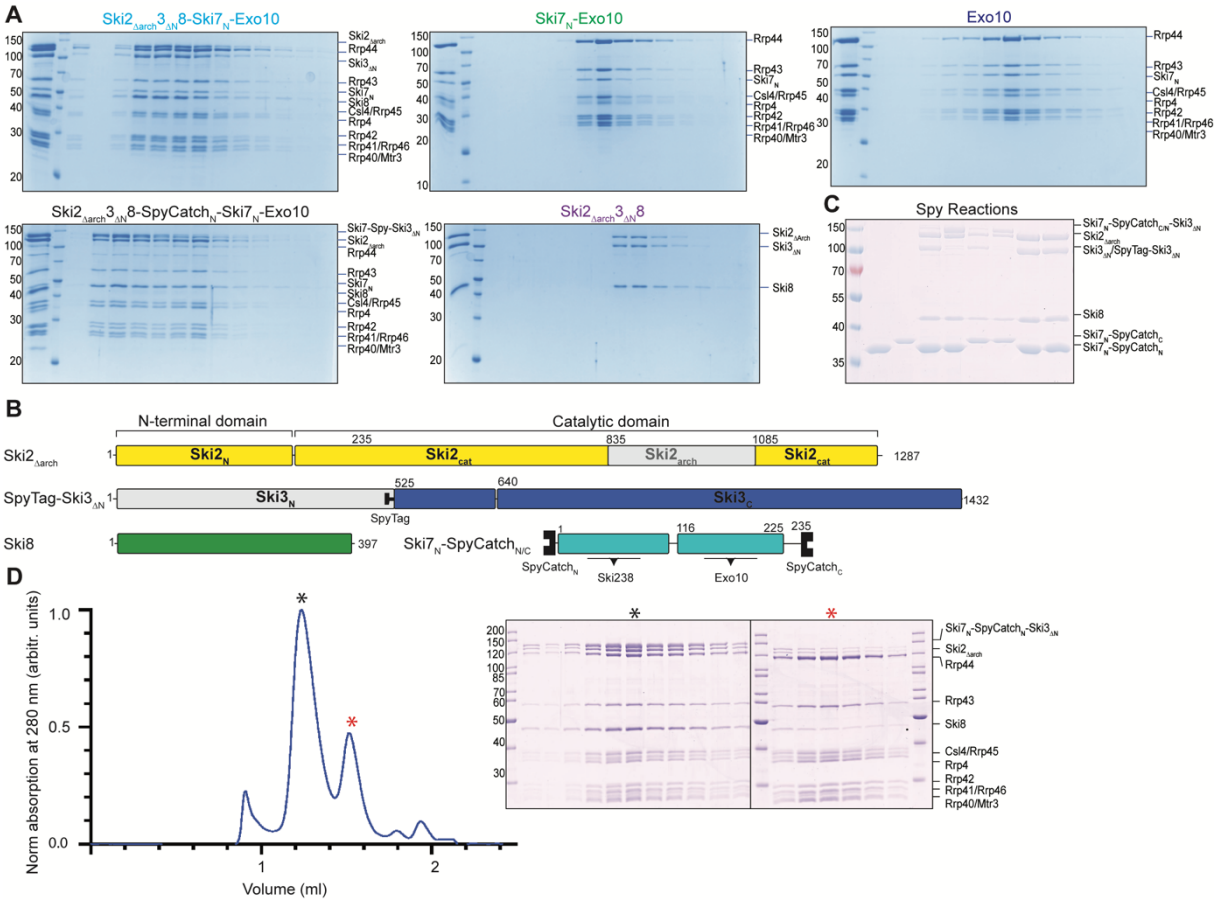

Figure S4. Biochemical characterization of recombinant Ski238 with Ski7$_N$ and Exo10 (related to Figure 4)

(A) Coomassie-stained 12% SDS-PAGE gels showing protein components from SEC peak fractions after runs with different Exo10, Ski7 and Ski238 combinations. Color of the labels correspond to color of the corresponding curves in Figure 4A.

(B) Domain organization of the yeast Ski2$_{\Delta arch}$3$_{\Delta N}$8 and Ski7$_N$ showing placement of the SpyTag and SpyCatcher (SpyCatch). Constructs were used for stabilization of Ski238- Ski7$_N$-Exo10 (also see Figure 4B). Ski238 subunits Ski2 (yellow) Ski3 (blue) Ski8 (green) and SpyTag (black). Ski7$_N$ (cyan/grey) and SpyCatch$_{N/C}$ (black). Grey areas represent deleted portions.

(C) SDS-PAGE gel confirming covalent linking between Spy-Ski2$_{\Delta arch}$3$_{\Delta N}$8 and SpyCatch$_{N/C}$-Ski7$_N$.

(D) Reconstitution of Ski238-SpyCatch$_N$-Ski7 with Exo10 over S6i 3.2/300GL SEC column used for cryo-EM SPA. SEC profile (left panel) with corresponding 12% Coomassie stained SDS-PAGE of the individual fractions (right panel).

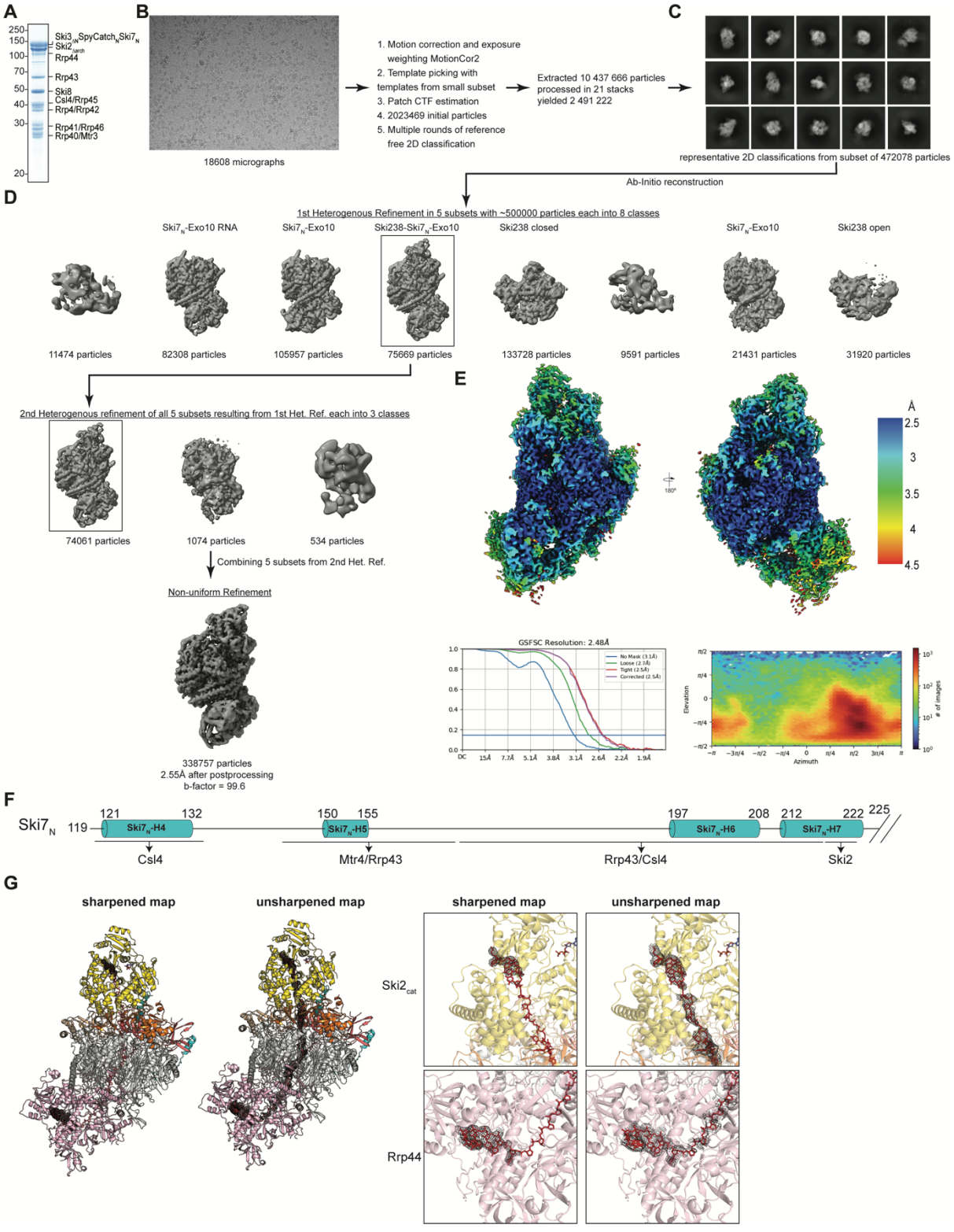

Figure S5. Cryo-EM analysis of recombinant active Ski238-Ski7-Exo10 holocomplex (related to Figure 4)

(A) Coomassie-stained 12% SDS-PAGE gel of the SEC peak fraction of Ski238-SpyCatch$_N$-Ski7 with Exo10 after incubation with ATP and RNA (see also Figure S4D).

(B) Representative cryo-EM micrograph collected on a Titan Krios G2 collected at 300 kV with a pixel size of 0.8512 Å/pix using a K3 direct electron.

(C) Representative 2D class averages.

(D) Cryo-EM data processing scheme. After pre-processing steps and 2D classification, selected particles were classified by heterogeneous refinement and 3D classification into five subclasses representing various subcomplexes. The sub-population of particles clearly representing the $Ski7_N$-Exo10 bound to open state Ski238 was subjected to a second round of heterogenous refinement. Afterwards, the obtained particles stacks were merged and subjected to a final non-uniform refinement.

(E) Local resolution estimates of the final non-uniform and local refinements for the cryo-EM SPA datasets in (D), shown in two different orientations related by a 90˚ rotation around a vertical axis (top panel). Corresponding FSC curves of respective map, as well as angular distribution plot obtained from cryoSPARC (bottom panel).

(F) Topology-based domain organization of the Ski7 N-terminal arm (residues 119-225). Secondary structure elements are indicated by cylinders. Interactions between $Ski7_N$ helices with Exo10 subunits and Ski2 are indicated below.

(G) Model of Ski238-$Ski7_N$-Exo10 with RNA density from sharpened (left) and unsharpened (middle) cryo-EM reconstruction shown in black. Orientation and coloring are analog to Figure 5A. Comparison of RNA signal in $Ski2_{cat}$ (upper right) and Rrp44 (lower left). The unsharpened map shows continuous density for the RNA substrate while the sharpened map only shows density within $Ski2_{cat}$ or Rrp44.

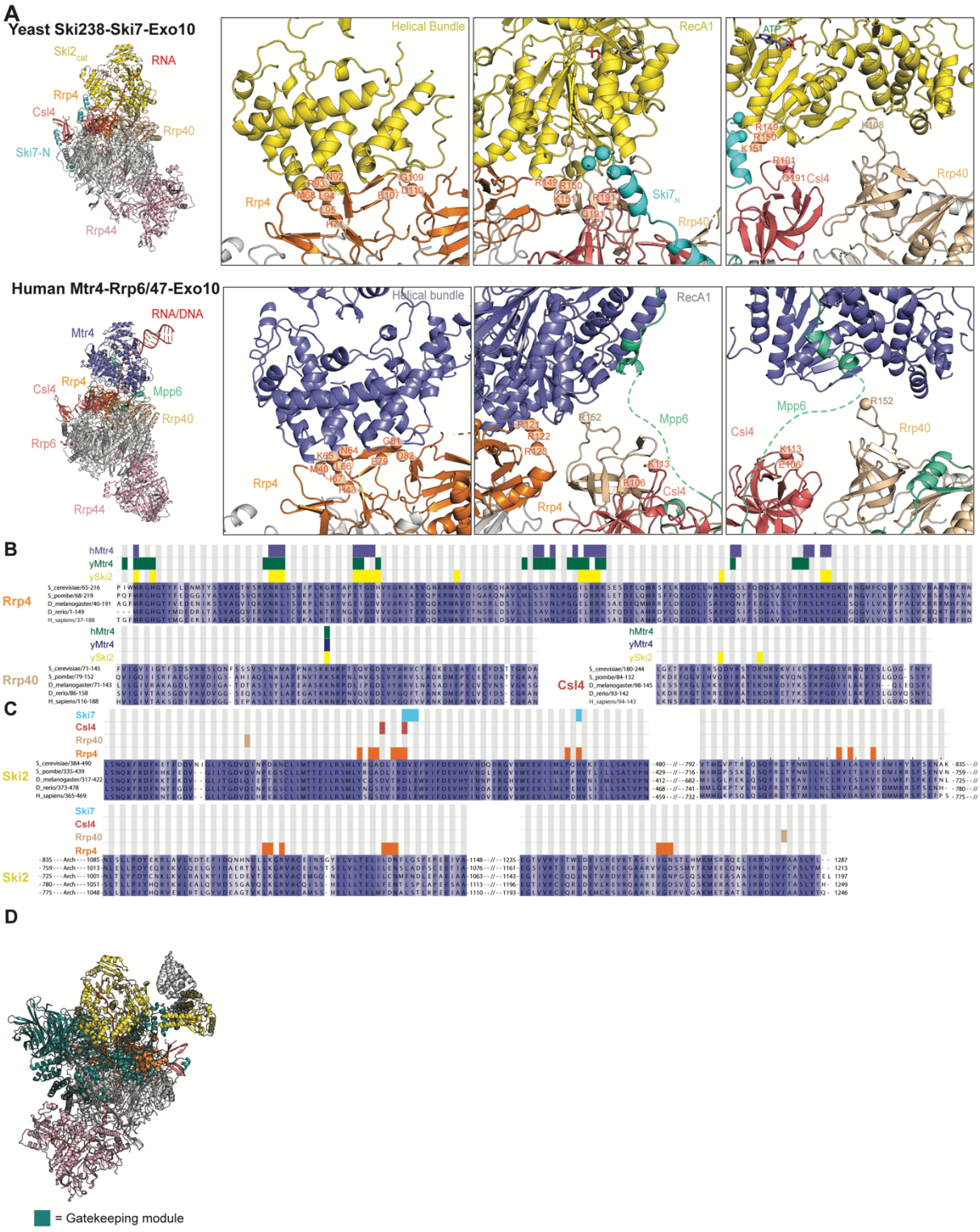

Figure S6. Comparison of ySki2 and hMtr4 binding sites on Exo10 with sequence alignments (related to Figure 5)

(A) Comparison of Ski238-Ski7-Exo10 and nuclear exosome helicase assemblies from *S. cerevisiae* (top) and *H. sapiens* (bottom), respectively. For both complexes, a model is shown in cartoon representation in the same

orientation (left panel). Zoom-in views on the individual binding sites between helicase and the Exo10 cap proteins are shown, similar to Figure 5C and 5D. Conserved residues in cap proteins Csl4, Rrp4 and Rrp40 are shown as spheres and labeled with residue numbers.

(B) Multiple sequence alignments of Exo10 cap proteins from different organisms show conservation of cap proteins and overlap of helicase interaction sites based on available models. (Organism with uniport identifier; *S. cerevisiae*: P17883, *S. pombe*: O94474, *D. melanogaster*: Q6NNB2, *D. rerio*: A0A8M1RLS7, and *H. sapiens*: Q6PGP7). Alignments were performed using Clustal Omega and visualized with Jalview. Sequence conservation is shown by color from variable (white) to conserved (blue). Colored bars above the alignments indicate residues involved in protein-protein interactions with ySki2 (this study), yMtr4 (6FSZ) and hMtr4 (6D6Q).

(C) Amino acid sequence alignments of Ski2 from different organisms. Alignments were performed as above (Figure S6B). Sequence conservation is shown by color from variable (white) to conserved (blue). Residues involved in protein-protein interactions with Rrp4, Rrp40, Csl4 and Ski7 are indicated above the alignment by colored bars.

(D) Superposition of Ski238$_{FL}$ and Ski238-Ski7$_{N}$-Exo10 showing the clash of the Gatekeeping module (Ski2$_{N}$, Ski3$_{C}$, Ski8$_{IN}$, Ski8$_{OUT}$) with the Exo10. Models were superposed on Ski2$_{cat}$. Colors for Ski238-Ski7$_{N}$-Exo10 are identical to Figure 4D. For Ski238$_{FL}$, the Gatekeeping module is colored in sea green. Ski2$_{arch}$ is colored in yellow, Ski3$_{N}$ in grey.

REFERENCES:

Afonine, P.V., Poon, B.K., Read, R.J., Sobolev, O.V., Terwilliger, T.C., Urzhumtsev, A., Adams, P.D., 2018. Real-space refinement in PHENIX for cryo-EM and crystallography. Acta Crystallogr. Sect. D 74, 531–544. https://doi.org/10.1107/S2059798318006551

Anderson, J.S.J., Parker, R., 1998. The 3′ to 5′ degradation of yeast mRNAs is a general mechanism for mRNA turnover that requires the SKI2 DEVH box protein and 3′ to 5′ exonucleases of the exosome complex. EMBO J. 17, 1497–1506. https://doi.org/10.1093/emboj/17.5.1497

Araki, Y., Takahashi, S., Kobayashi, T., Kajiho, H., Hoshino, S., Katada, T., 2001. Ski7p G protein interacts with the exosome and the Ski complex for 3′-to-5′ mRNA decay in yeast. EMBO J. 20, 4684–4693. https://doi.org/10.1093/emboj/20.17.4684

Bepler, T., Morin, A., Rapp, M., Brasch, J., Shapiro, L., Noble, A.J., Berger, B., 2019. Positive-unlabeled convolutional neural networks for particle picking in cryo-electron micrographs. Nat. Methods 16, 1153–1160. https://doi.org/10.1038/s41592-019-0575-8

Biyani, N., Righetto, R.D., McLeod, R., Caujolle-Bert, D., Castano-Diez, D., Goldie, K.N., Stahlberg, H., 2017. Focus: The interface between data collection and data processing in cryo-EM. J. Struct. Biol. 198, 124–133. https://doi.org/10.1016/j.jsb.2017.03.007

Blatt, P., Wong-Deyrup, S.W., McCarthy, A., Breznak, S., Hurton, M.D., Upadhyay, M., Bennink, B., Camacho, J., Lee, M.T., Rangan, P., 2021. RNA degradation is required for the germ-cell to maternal transition in Drosophila. Curr. Biol. 31, 2984-2994.e7. https://doi.org/10.1016/j.cub.2021.04.052

Bonneau, F., Basquin, J., Ebert, J., Lorentzen, E., Conti, E., 2009. The yeast exosome functions as a macromolecular cage to channel RNA substrates for degradation - PubMed [WWW Document]. URL https://pubmed.ncbi.nlm.nih.gov/19879841/ (accessed 5.2.23).

Büttner, K., Nehring, S., Hopfner, K.-P., 2007. Structural basis for DNA duplex separation by a superfamily-2 helicase. Nat. Struct. Mol. Biol. 14, 647–652. https://doi.org/10.1038/nsmb1246

Cabrera-Quio, L.E., Schleiffer, A., Mechtler, K., Pauli, A., 2021. Zebrafish Ski7 tunes RNA levels during the oocyte-to-embryo transition. PLoS Genet. 17, e1009390. https://doi.org/10.1371/journal.pgen.1009390

Chlebowski, A., Lubas, M., Jensen, T.H., Dziembowski, A., 2013. RNA decay machines: The exosome. Biochim. Biophys. Acta BBA - Gene Regul. Mech., RNA Decay Mechanisms 1829, 552–560. https://doi.org/10.1016/j.bbagrm.2013.01.006

Dziembowski, A., Lorentzen, E., Conti, E., Séraphin, B., 2007. A single subunit, Dis3, is essentially responsible for yeast exosome core activity. Nat. Struct. Mol. Biol. 14, 15–22. https://doi.org/10.1038/nsmb1184

Emsley, P., Lohkamp, B., Scott, W.G., Cowtan, K., 2010. Features and development of Coot. Acta Crystallogr. Sect. D 66, 486–501. https://doi.org/10.1107/S0907444910007493

Falk, S., Bonneau, F., Ebert, J., Kögel, A., Conti, E., 2017. Mpp6 Incorporation in the Nuclear Exosome Contributes to RNA Channeling through the Mtr4 Helicase. Cell Rep. 20, 2279–2286. https://doi.org/10.1016/j.celrep.2017.08.033

Fasken, M.B., Morton, D.J., Kuiper, E.G., Jones, S.K., Leung, S.W., Corbett, A.H., 2020. The RNA Exosome and Human Disease, in: LaCava, J., Vaňáčová, Š. (Eds.), The Eukaryotic RNA Exosome: Methods and

Protocols, Methods in Molecular Biology. Springer, New York, NY, pp. 3–33. https://doi.org/10.1007/978-1-4939-9822-7_1

Gerlach, P., Schuller, J.M., Bonneau, F., Basquin, J., Reichelt, P., Falk, S., Conti, E., 2018. Distinct and evolutionary conserved structural features of the human nuclear exosome complex - PubMed [WWW Document]. URL https://pubmed.ncbi.nlm.nih.gov/30047866/ (accessed 5.2.23).

Goddard, T.D., Huang, C.C., Meng, E.C., Pettersen, E.F., Couch, G.S., Morris, J.H., Ferrin, T.E., 2018. UCSF ChimeraX: Meeting modern challenges in visualization and analysis. Protein Sci. 27, 14–25. https://doi.org/10.1002/pro.3235

Halbach, F., Reichelt, P., Rode, M., Conti, E., 2013. The yeast ski complex: crystal structure and RNA channeling to the exosome complex. Cell 154, 814–826. https://doi.org/10.1016/j.cell.2013.07.017

Halbach, F., Rode, M., Conti, E., 2012. The crystal structure of S. cerevisiae Ski2, a DExH helicase associated with the cytoplasmic functions of the exosome. RNA N. Y. N 18, 124–134. https://doi.org/10.1261/rna.029553.111

Johnson, A.W., Kolodner, R.D., 1995. Synthetic lethality of sep1 (xrn1) ski2 and sep1 (xrn1) ski3 mutants of Saccharomyces cerevisiae is independent of killer virus and suggests a general role for these genes in translation control. Mol. Cell. Biol. 15, 2719–2727. https://doi.org/10.1128/MCB.15.5.2719

Jumper, J., Evans, R., Pritzel, A., Green, T., Figurnov, M., Ronneberger, O., Tunyasuvunakool, K., Bates, R., Žídek, A., Potapenko, A., Bridgland, A., Meyer, C., Kohl, S.A.A., Ballard, A.J., Cowie, A., Romera-Paredes, B., Nikolov, S., Jain, R., Adler, J., Back, T., Petersen, S., Reiman, D., Clancy, E., Zielinski, M., Steinegger, M., Pacholska, M., Berghammer, T., Bodenstein, S., Silver, D., Vinyals, O., Senior, A.W., Kavukcuoglu, K., Kohli, P., Hassabis, D., 2021. Highly accurate protein structure prediction with AlphaFold. Nature 596, 583–589. https://doi.org/10.1038/s41586-021-03819-2

Kalisiak, K., Kuliński, T.M., Tomecki, R., Cysewski, D., Pietras, Z., Chlebowski, A., Kowalska, K., Dziembowski, A., 2017. A short splicing isoform of HBS1L links the cytoplasmic exosome and SKI complexes in humans. Nucleic Acids Res. 45, 2068–2080. https://doi.org/10.1093/nar/gkw862

Keidel, A., Conti, E., Falk, S., 2020. Purification and Reconstitution of the S. cerevisiae TRAMP and Ski Complexes for Biochemical and Structural Studies, in: LaCava, J., Vaňáčová, Š. (Eds.), The Eukaryotic RNA Exosome: Methods and Protocols, Methods in Molecular Biology. Springer, New York, NY, pp. 491–513. https://doi.org/10.1007/978-1-4939-9822-7_24

Koegel, A., Keidel, A., Bonneau, F., Schäfer, I.B., Conti, E., 2022. The human SKI complex regulates channeling of ribosome-bound RNA to the exosome via an intrinsic gatekeeping mechanism. Mol. Cell 82, 756-769.e8. https://doi.org/10.1016/j.molcel.2022.01.009

Kowalinski, E., Koegel, A., Ebert, J., Reichelt, P., Stegmann, E., Habermann, B., Conti, E., 2016. Structure of a Cytoplasmic 11-Subunit RNA Exosome Complex - ScienceDirect [WWW Document]. URL https://www.sciencedirect.com/science/article/pii/S1097276516301915?via%3Dihub (accessed 5.2.23).

Kowalinski, E., Schuller, A., Green, R., Conti, E., 2015. Saccharomyces cerevisiae Ski7 Is a GTP-Binding Protein Adopting the Characteristic Conformation of Active Translational GTPases - PubMed [WWW Document]. URL https://pubmed.ncbi.nlm.nih.gov/26051716/ (accessed 5.2.23).

Larimer, F.W., Stevens, A., 1990. Disruption of the gene XRN1, coding for a 5'----3' exoribonuclease, restricts yeast cell growth. Gene 95, 85–90. https://doi.org/10.1016/0378-1119(90)90417-p

Lingaraju, M., Schuller, J.M., Falk, S., Gerlach, P., Bonneau, F., Basquin, J., Benda, C., Conti, E., 2019. To Process or to Decay: A Mechanistic View of the Nuclear RNA Exosome. Cold Spring Harb. Symp. Quant. Biol. 84, 155–163. https://doi.org/10.1101/sqb.2019.84.040295

Makino, Debora Lika, Baumgärtner, M., Conti, E., 2013. Crystal structure of an RNA-bound 11-subunit eukaryotic exosome complex. Nature 495, 70–75. https://doi.org/10.1038/nature11870

Makino, Debora L., Halbach, F., Conti, E., 2013. The RNA exosome and proteasome: common principles of degradation control. Nat. Rev. Mol. Cell Biol. 14, 654–660. https://doi.org/10.1038/nrm3657

Malet, H., Topf, M., Clare, D.K., Ebert, J., Bonneau, F., Basquin, J., Drazkowska, K., Tomecki, R., Dziembowski, A., Conti, E., Saibil, H.R., Lorentzen, E., 2010. RNA channelling by the eukaryotic exosome - PubMed [WWW Document]. URL https://pubmed.ncbi.nlm.nih.gov/21072061/ (accessed 5.2.23).

Marshall, A.N., Montealegre, M.C., Jiménez-López, C., Lorenz, M.C., van Hoof, A., 2013. Alternative splicing and subfunctionalization generates functional diversity in fungal proteomes. PLoS Genet. 9, e1003376. https://doi.org/10.1371/journal.pgen.1003376

Mitchell, P., Petfalski, E., Shevchenko, A., Mann, M., Tollervey, D., 1997. The exosome: a conserved eukaryotic RNA processing complex containing multiple 3'-->5' exoribonucleases. Cell 91, 457–466. https://doi.org/10.1016/s0092-8674(00)80432-8

Mitchell, P., Tollervey, D., 2003. An NMD Pathway in Yeast Involving Accelerated Deadenylation and Exosome-Mediated 3'→5' Degradation. Mol. Cell 11, 1405–1413. https://doi.org/10.1016/S1097-2765(03)00190-4

Olsen, K.J., Johnson, S.J., 2021. Mtr4 RNA helicase structures and interactions. Biol. Chem. 402, 605–616. https://doi.org/10.1515/hsz-2020-0329

Sanchez-Garcia, R., Gomez-Blanco, J., Cuervo, A., Carazo, J.M., Sorzano, C.O.S., Vargas, J., 2021. DeepEMhancer: a deep learning solution for cryo-EM volume post-processing. Commun. Biol. 4, 1–8. https://doi.org/10.1038/s42003-021-02399-1

Schmid, M., Jensen, T.H., 2019. The Nuclear RNA Exosome and Its Cofactors, in: Oeffinger, M., Zenklusen, D. (Eds.), The Biology of MRNA: Structure and Function, Advances in Experimental Medicine and Biology. Springer International Publishing, Cham, pp. 113–132. https://doi.org/10.1007/978-3-030-31434-7_4

Schmidt, C., Kowalinski, E., Shanmuganathan, V., Defenouillère, Q., Braunger, K., Heuer, A., Pech, M., Namane, A., Berninghausen, O., Fromont-Racine, M., Jacquier, A., Conti, E., Becker, T., Beckmann, R., 2016. The cryo-EM structure of a ribosome-Ski2-Ski3-Ski8 helicase complex. Science 354, 1431–1433. https://doi.org/10.1126/science.aaf7520

Schuch, B., Feigenbutz, M., Makino, D.L., Falk, S., Basquin, C., Mitchell, P., Conti, E., 2014. The exosome-binding factors Rrp6 and Rrp47 form a composite surface for recruiting the Mtr4 helicase. EMBO J. 33, 2829–2846. https://doi.org/10.15252/embj.201488757

Schuller, J.M., Falk, S., Fromm, L., Hurt, E., Conti, E., 2018. Structure of the nuclear exosome captured on a maturing preribosome. Science 360, 219–222. https://doi.org/10.1126/science.aar5428

Takahashi, T.T., Austin, R.J., Roberts, R.W., 2003. mRNA display: ligand discovery, interaction analysis and beyond. Trends Biochem. Sci. 28, 159–165. https://doi.org/10.1016/S0968-0004(03)00036-7

Toh-E, A., Guerry, P., Wickner, R.B., 1978. Chromosomal superkiller mutants of Saccharomyces cerevisiae [WWW Document]. https://doi.org/10.1128/jb.136.3.1002-1007.1978

Tuck, A., A, R., Ab, A., La, L., D, H., V, I., V, C.-S., D, G., M, B., 2020. Mammalian RNA Decay Pathways Are Highly Specialized and Widely Linked to Translation. Mol. Cell 77. https://doi.org/10.1016/j.molcel.2020.01.007

van Hoof, A., Frischmeyer, P.A., Dietz, H.C., Parker, R., 2002. Exosome-mediated recognition and degradation of mRNAs lacking a termination codon. Science 295, 2262–2264. https://doi.org/10.1126/science.1067272

Vodkin, M., Katterman, F., Fink, G.R., 1974. Yeast Killer Mutants with Altered Double-Stranded Ribonucleic Acid [WWW Document]. https://doi.org/10.1128/jb.117.2.681-686.1974

Wasmuth, E.V., Zinder, J.C., Zattas, D., Das, M., Lima, C.D., 2017. Structure and reconstitution of yeast Mpp6-nuclear exosome complexes reveals that Mpp6 stimulates RNA decay and recruits the Mtr4 helicase. eLife 6, e29062. https://doi.org/10.7554/eLife.29062

Weick, E.-M., Lima, C.D., 2021. RNA helicases are hubs that orchestrate exosome-dependent 3'–5' decay. Curr. Opin. Struct. Biol., Theory and Simulation/Computational Methods ● Macromolecular Assemblies 67, 86–94. https://doi.org/10.1016/j.sbi.2020.09.010

Weick, E.-M., Puno, M.R., Januszyk, K., Zinder, J.C., DiMattia, M.A., Lima, C.D., 2018. Helicase-Dependent RNA Decay Illuminated by a Cryo-EM Structure of a Human Nuclear RNA Exosome-MTR4 Complex. Cell 173, 1663-1677.e21. https://doi.org/10.1016/j.cell.2018.05.041

Zakeri, B., Fierer, J.O., Celik, E., Chittock, E.C., Schwarz-Linek, U., Moy, V.T., Howarth, M., 2012. Peptide tag forming a rapid covalent bond to a protein, through engineering a bacterial adhesin. Proc. Natl. Acad. Sci. U. S. A. 109, E690-697. https://doi.org/10.1073/pnas.1115485109

Zheng, S.Q., Palovcak, E., Armache, J.-P., Verba, K.A., Cheng, Y., Agard, D.A., 2017. MotionCor2: anisotropic correction of beam-induced motion for improved cryo-electron microscopy. Nat. Methods 14, 331–332. https://doi.org/10.1038/nmeth.4193

Zinder, J.C., Lima, C.D., 2017. Targeting RNA for processing or destruction by the eukaryotic RNA exosome and its cofactors. Genes Dev. 31, 88–100. https://doi.org/10.1101/gad.294769.116

Zinoviev, A., Ayupov, R.K., Abaeva, I.S., Hellen, C.U.T., Pestova, T.V., 2020. Extraction of mRNA from Stalled Ribosomes by the Ski Complex. Mol. Cell 77, 1340-1349.e6. https://doi.org/10.1016/j.molcel.2020.01.011

4.3 Publication 3:

Purification and Reconstitution of the S. cerevisiae TRAMP and Ski Complexes for Biochemical and structural studies

Achim Keidel, Elena Conti and Sebastian Falk

This article was published as part of the Methods in Molecular Biology book series (MIMB, volume 2062) on the 26th of November 2019. It summarizes the current literature on the purification and reconstitution of two exosome adaptor complexes from *S. cerevisiae*, the nuclear TRAMP complex and the cytoplasmic Ski238 complex. The article contains detailed step-by-step protocols to obtain highly pure protein samples that can be used for further experiments. The protocols go beyond the standard materials and methods section in the available literature and aim to improve the reproducibility of existing results for other scientists.

Chapter 24

Purification and Reconstitution of the *S. cerevisiae* TRAMP and Ski Complexes for Biochemical and Structural Studies

Achim Keidel, Elena Conti, and Sebastian Falk

Abstract

The RNA exosome is a macromolecular machine that degrades a large variety of RNAs from their 3′-end. It comprises the major 3′-to-5′ exonuclease in the cell, completely degrades erroneous and overly abundant RNAs, and is also involved in the precise processing of RNAs. To degrade transcripts both specifically and efficiently the exosome functions together with compartment-specific cofactors. In the yeast *S. cerevisiae*, the exosome associates with the Ski complex in the cytoplasm and with Mtr4 alone or with Mtr4 as part of the TRAMP complex in the nucleus. Here we describe how to produce, purify, and assemble the Ski and TRAMP complexes from *S. cerevisiae*.

Key words Exosome, Mtr4, Trf4, Air2, TRAMP, Ski2, Ski3, Ski8, Ski complex

1 Introduction

The RNA exosome is an evolutionary conserved multisubunit protein complex that degrades a large variety of RNAs from their 3′-end (reviewed in [1, 2]). The exosome is formed by a 10-subunit core complex (Exo-10) that is present in both the nuclear and cytoplasmic compartments and degrades RNAs in a processive manner [3]. Exosome-mediated RNA degradation leads to the complete elimination of nuclear and cytoplasmic transcripts in turnover and quality control pathways, and to the partial trimming of RNA precursors in nuclear biogenesis pathways [2, 4]. How the exosome combines versatility and specificity to either completely eliminate or precisely process RNAs is not well understood. One way to regulate the activity is achieved through the interaction of the exosome with cofactors (*see* Chapter 11), which are involved in both substrate recognition and activity modulation. In *S. cerevisiae* the exosome associates in the cytoplasm with the Ski

The original version of this chapter was revised. The correction to this chapter is available at https://doi.org/10.1007/978-1-4939-9822-7_25

John LaCava and Štěpánka Vaňáčová (eds.), *The Eukaryotic RNA Exosome: Methods and Protocols*, Methods in Molecular Biology, vol. 2062, https://doi.org/10.1007/978-1-4939-9822-7_24, © Springer Science+Business Media, LLC, part of Springer Nature 2020

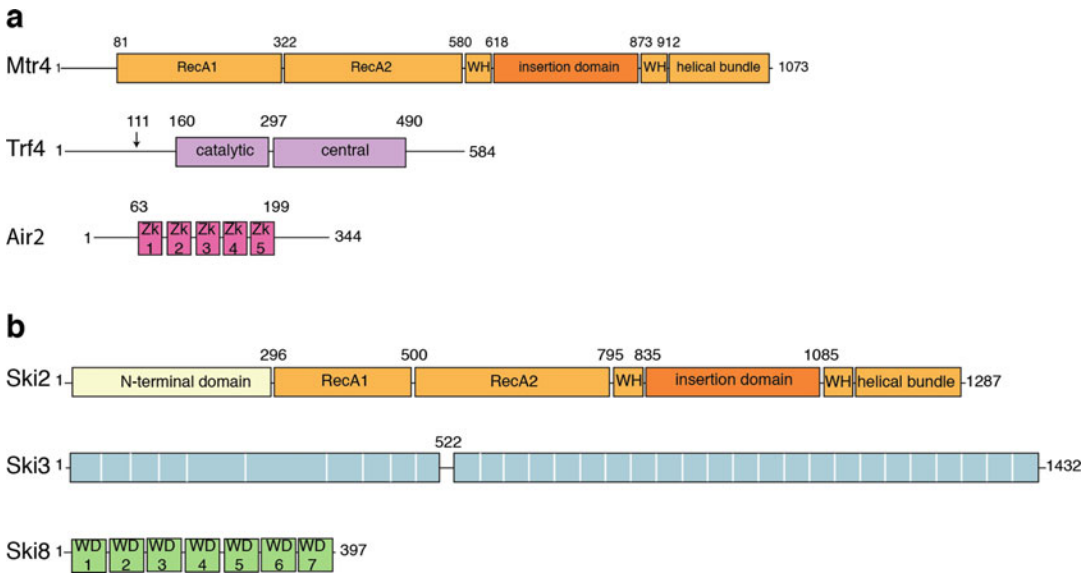

Fig. 1 Overview of the domain organization of the proteins forming the TRAMP (**a**) and the Ski complex (**b**)

complex and in the nucleus with the helicase Mtr4 alone or within the context of the TRAMP complex (*see* Chapter 12), of which Mtr4 is a constituent [1, 2]. In both compartments, the cofactor complexes are centered around ATP-dependent RNA helicases, Ski2 in the cytoplasm and Mtr4 in the nucleus [5]. The exosome-associated helicases contain a unique insertion domain, the so-called arch, which is embedded in the helicase core, formed by two RecA, a winged-helix (WH) and a helical bundle domain [5–8] (Fig. 1). The insertion domains of Ski2 [8] and Mtr4 [6] both possess RNA binding properties and for Mtr4 has been additionally shown to be a binding site for ribosome biogenesis factors [9, 10]. Whether other proteins bind to the insertion domain of Ski2 is not yet known. Another characteristic feature of Ski2 and Mtr4 is that, N-terminal to the helicase core domain, they both possess extensions that mediate the interaction with other factors.

The TRAMP complex is a heterotrimeric assembly consisting of the RNA helicase Mtr4 and the poly(A) polymerase subcomplex formed by the non-canonical poly(A) polymerase Trf4 (aka. Pap2) and the RNA binding protein Air2 [11–13]. Trf4 contains a catalytic and a central domain, which together form the active poly (A) polymerase core that is flanked by unstructured regions at the N- and C-terminus. Air2 contains five zinc knuckles (Zk), which are flanked up- and downstream by low complexity regions. The binding of Air2 to Trf4 is mediated by zinc knuckles: specifically Zk4, Zk5, and the hydrophobic linker connecting them [14, 15]. Air2 is believed to provide RNA binding capacity [16, 17] and Zk2-4 were shown to be directly involved in the binding of RNA substrates [18]. Both Air2 and Trf4 use their intrinsically disordered

N-terminal regions upstream of folded core domains to bind cooperatively to the helicase core of Mtr4 [19].

The Ski complex consists of the proteins Ski2, Ski3, and Ski8 and forms a heterotetrameric assembly with a 1:1:2 stoichiometry (Ski2-3-8_2) [20–22]. The helicase Ski2 is 146 kDa protein and contains at the N-terminus a region that mediates the binding to Ski3 followed by the C-terminal helicase core domain [8, 23]. The Ski2-insertion domain is embedded into the helicase core and consists of a helical stalk and a β-barrel domain [8]. The Ski3 subunit is a 168 kDa protein that consists of twenty-four tetratricopeptide repeats (TPR). It serves as a scaffold protein and anchors the N-terminus of Ski2 through extensive hydrophobic interactions [23]. Finally, Ski8 is a 44 kDa protein that has a β-propeller shape formed by seven WD40 repeats [23].

Here we provide a detailed protocol enabling the production and purification of the Ski and TRAMP complexes, respectively, for biochemical and structural studies.

2 Materials

2.1 General Equipment (Hardware)

1. Orbital shaker fitted with holders (for bacterial and insect cell cultivation).
2. Centrifuge (e.g., Beckman Coulter Avanti J-26XPI) with different rotors.
   (a) JLA-8.100 to harvest cells.
   (b) JA-25.50 to clear lysates.
3. Sonifier Sonopuls HD 3200 together with a VS-70 T probe (Bandelin).
4. Peristaltic pump.
5. Protein Purification system that measure absorption in the UV range and has a gradient mixer (e.g., ÄKTAprime plus, ÄKTA Pure or Bio-Rad NGC).
6. Equipment to run SDS-PAGE gels and Coomassie brilliant blue staining.
7. UV spectrophotometer.
8. Cell counter (e.g., Vi-Cell™ XR (Beckman Coulter)).

2.2 Chromatography Columns

1. HisTrap™ FF 5 mL (GE Healthcare).
2. HiTrap™ Heparin HP 5 mL (GE Healthcare).
3. HiTrap™ Q HP 5 mL (GE Healthcare).
4. Superdex™ 200 increase 10/300 GL (GE Healthcare).
5. HiLoad™ S200 pg 16/600 (GE Healthcare).
6. Superdex™ 75 increase 10/300 GL (GE Healthcare).
7. HiLoad™ S75 pg 16/600 (GE Healthcare).

2.3 Consumables

1. 5 µm Nitrocellulose membrane filter to clear lysate supernatant (MF-Millipore).
2. Ultrafiltration devices (Centrifugal filters).

   Amicon® Ultra-4 or Ultra-15 with molecular weight cut-off (MWCO): 10k, 30k, 50k and 100k (Merck). Amicon® Ultra-4 or Ultra-15 differ in the volume that can be applied for concentration.
3. Culture growth containers and flasks.
   (a) 250 mL glass Erlenmeyer flash for bacterial cell culture.
   (b) TUNAIR™ 2,5 L shake flasks (IBI Scientific) for bacterial cell culture.
   (c) Falcon® 6-well Clear Flat Bottom TC-treated multiwell cell culture plate, with lid, individually wrapped, sterile (Corning) for insect cell culture.
   (d) 125 mL polycarbonate Erlenmeyer (Corning) for insect cell culture.
   (e) 2 L polycarbonate Fernbach flasks (Corning) for insect cell culture.

2.4 Materials for Protein Production

1. Bacterial strains.
   (a) BL21 Star™(DE3) Competent Cells (Thermo Fisher Scientific).
   (b) BL21-Gold (DE3) pLysS (Agilent).
   (c) DH10EMBacY (Geneva Biotech).
2. Insect cell strains.
   (a) Sf21 cells (Thermo scientific).
   (b) High Five cells (Thermo scientific).
3. Bacterial growth media and antibiotics.
   (a) Lysogeny broth (LB).
   (b) LB-Agar plates.
   (c) Terrific broth (TB).
   (d) Kanamycin (30 mg/mL) (1000× Stock, use 1×).
   (e) Streptomycin (25 mg/mL) (1000× Stock, use 1×).
   (f) Chloramphenicol (34 mg/mL) in ethanol (1000× Stock, use 1×).
4. Insect cell growth medium: Sf-900™ II SFM medium (Thermo Fisher Scientific).
5. FuGENE® HD Transfection Reagent (Promega) for insect cell culture.
6. Plasmids for the expression of Mtr4, Trf4, and the Ski2-insertion domain are derived from the pBR322 backbone and

contain a kanamycin resistance gene and a T7 promoter that allows induction of protein expression with IPTG. Purification tags are always located at the N-terminus (*see* **Note 1**). Mtr4 constructs are fused to His_6-GST followed by a 3C protease cleave site; Trf4 to a His_6-tag followed by a TEV cleavage site; and the Ski2-insertion domain His_6-tag followed by a 3C cleavage site. Air2 constructs are cloned without tag into a pCDF vector, which carries streptomycin resistance gene and a T7 promoter that allows induction of protein expression with IPTG.

2.5 Materials for Protein Purification

1. Phenylmethylsulfonyl fluoride (PMSF), Stock 100 mM (in isopropanol).
2. Complete EDTA-free protease inhibitor cocktail (Roche).
3. DNase I from bovine pancreas lyophilized, Stock: 1 mg/mL.
4. Lysozyme from chicken egg white lyophilized, Stock: 10 mg/mL.
5. His-tagged 3C protease (recombinant, in house production), Stock 1 mg/mL.
6. His-tagged TEV protease (recombinant, in house production), Stock 1 mg/mL.

2.6 Buffers for Mtr4, Trf4-Air2, and TRAMP Complex Purification

1. IMAC-lysis buffer: 50 mM Hepes–NaOH pH 7.5, 500 mM NaCl, 20 mM imidazole, 10% (v/v) glycerol, 5 mM 2-mercaptoethanol (β-ME). Supplemented with 1 mM PMSF and 5 μg/mL DNase I (*see* Subheading 2.5).
2. IMAC-high salt wash buffer: 20 mM Hepes–NaOH pH 7.5, 1 M NaCl, 20 mM imidazole, 10% (v/v) glycerol, 5 mM β-ME.
3. IMAC-chaperone wash buffer: 20 mM Hepes–NaOH pH 7.5, 50 mM KCl, 10 mM $MgCl_2$, 2 mM ATP, 20 mM imidazole, 10% (v/v) glycerol, 5 mM β-ME.
4. IMAC-elution buffer: 20 mM Hepes–NaOH pH 7.5, 150 mM NaCl, 500 mM Imidazole, 10% (v/v) glycerol, 5 mM β-ME.
5. Dialysis and Heparin buffer A: 20 mM Hepes–NaOH pH 7.5, 150 mM NaCl, 10% (v/v) glycerol, 5 mM β-ME.
6. Heparin buffer B: 20 mM Hepes–NaOH pH 7.5, 1 M NaCl, 10% (v/v) glycerol, 5 mM β-ME.
7. TRAMP Gel filtration buffer: 20 mM Hepes–NaOH pH 7.5, 150 mM NaCl, 2 mM DTT.
8. Glycerol stock buffer: 20 mM Hepes–NaOH pH 7.5, 150 mM NaCl, 2 mM DTT, 50% (v/v) glycerol.

2.7 Buffers for Ski Complex and Ski2 Purification

1. Lysis buffer Ski: 20 mM Tris–HCl pH 7.4, 150 mM NaCl, 2 mM $MgCl_2$, 25 mM imidazole, 1 mM 2-mercaptoethanol (β-ME).

2. Wash buffer Ski: 20 mM Tris–HCl pH 7.4, 1000 mM NaCl, 2 mM $MgCl_2$, 25 mM imidazole, 1 mM β-ME.
3. Elution buffer Ski: 20 mM Tris–HCl pH 7.4, 150 mM NaCl, 2 mM $MgCl_2$, 300 mM imidazole, 1 mM β-ME.
4. Q buffer Ski A: 20 mM Tris–HCl pH 7.4, 150 mM NaCl, 1 mM β-ME.
5. Q buffer Ski B: 20 mM Tris–HCl pH 7.4, 1 M NaCl, 1 mM β-ME.
6. Dialysis buffer Ski: 20 mM Tris–HCl pH 7.4, 150 mM NaCl, 2 mM $MgCl_2$, 1 mM β-ME.
7. Gel filtration buffer Ski: 20 mM Hepes–NaOH pH 7.4, 150 mM NaCl, 2 mM $MgCl_2$, 1 mM β-ME.

2.8 Buffers for Ski2-Insertion Domain Purification

1. Lysis buffer Ski2-insertion: 20 mM Tris–HCl pH 7.4, 500 mM NaCl, 25 mM imidazole, 1 mM β-ME.
2. Elution buffer Ski2-insertion: 20 mM Tris–HCl pH 7.4, 500 mM NaCl, 300 mM imidazole, 1 mM β-ME.
3. Dialysis buffer Ski2-insertion: 20 mM Tris–HCl pH 7.4, 150 mM NaCl, 1 mM β-ME.
4. Gel filtration buffer Ski2-insertion: 20 mM Hepes–NaOH pH 7.4, 200 mM NaCl, 1 mM β-ME.

3 Methods

3.1 Purification of Yeast Mtr4 and Trf4-Air2 and Reconstitution of the TRAMP Complex

The *S. cerevisiae* TRAMP complex is a heterotrimeric complex and consists of the helicase Mtr4 and the poly(A) polymerase module Trf4-Air2 [11–13]. To reconstitute the TRAMP complex, Mtr4 and the Trf4-Air2 subcomplex are purified separately and then combined to form the TRAMP complex [6, 19]. This modular approach allows the analysis of different combinations of mutants and truncated constructs. For a detailed overview of successfully used constructs refer to Table 1. All proteins can be produced in *E. coli* and the purification protocols for Mtr4 and Trf4-Air2 are essentially identical. After cell lysis the proteins are purified in a three-step procedure, including Ni-affinity (IMAC), heparin-affinity, and finally size-exclusion chromatography (Fig. 2). All buffers and all protein containing solutions should be kept at 4 °C. All steps should be carried out on ice or in a temperature-controlled room at 4 °C.

3.1.1 Production and Purification of Recombinant Yeast Mtr4 and Trf4-Air2

1. Transform BL21 Star (DE3) cells with the plasmid encoding the desired Mtr4 construct. For Trf4-Air2 cotransform both plasmids encoding Trf4 and Air2 into BL21 Star (DE3) cells. In both cases select transformants on LB-Agar plates with the respective antibiotics (*see* **Note 2**).

Table 1
List of constructs, which have been successfully used to study the *S. cerevisiae* Ski and the TRAMP complexes. The production host is indicated. Structures determined by X-ray crystallography (X-ray), Cryo-electron microscopy (EM) or small angle X-ray scattering (SAXS) that have been obtained with the respective protein constructs are listed

Protein	Start	End	Purpose	Comment	Production host	Structures (PDB codes)
Mtr4						
Mtr4 FL	1	1073	Biochemistry, X-ray, EM		*E. coli*	X-ray: 4QU4, EM: 6FSZ
Mtr4ΔN	81	1073	Biochemistry, X-ray, SAXS	Lacks N-terminal exosome binding region. Forms TRAMP	*E. coli*	X-ray: 2XGJ, 4U4C, 5OOQ
Mtr4ΔInsertion	1	1073	Biochemistry	Lacks the insertion domain: 618-873 replaced by GSGS linker. Forms TRAMP	*E. coli*	
Mtr4ΔNΔInsertion	81	1073	Biochemistry, SAXS	Lacks the N-terminus and the insertion domain: residues 618-873 replaced by GSGS linker. Forms TRAMP	*E. coli*	TRAMP SAXS model
Mtr4-insertion	613	874	Biochemistry	Does not bind Trf4-Air2	*E. coli*	
Trf4-Air2						
Trf4 FL Air2 FL	1 1	584 344	Biochemistry		*E. coli*[b]	
Trf4 Air2	161 118	481 198	Biochemistry, X-ray	Poly(A)polymerase core, does not contain Mtr4 binding sites	*E. coli*[b]	X-ray: 3NYB
Trf4 Air2	111 1	490 199	Biochemistry, SAXS	Contains Mtr4 binding sites	*E. coli*[b]	TRAMP SAXS model
Fusion:Air2^{N}-Trf4^{N}	Air2(1-62)-Trf4 (111-160)		Biochemistry, X-ray	Synthetic fusion of the Mtr4 bindings sites from Air2 and Trf4.	*E. coli*	X-ray: 4U4C

(continued)

Table 1
(continued)

Protein	Start	End	Purpose	Comment	Production host	Structures (PDB codes)
Ski2						
Ski2 FL	1	1287	Biochemistry, EM		Insect cells[a]	EM: 5MC6
Ski2ΔN	296	1287	Biochemistry, X-ray	Does not contain N-terminus that is required for Ski complex formation	Insect cells	X-ray|: 4A4Z
Ski2-insertion	835	1085	Biochemistry, X-ray	Consists of helical stalk and ß-barrel	*E. coli*	X-ray: 4A4K
Ski2Δinsertion	1	1287	Biochemistry, X-ray	Does not contain the insertion domain: 836-1084 replaced by GSRG linker. Forms Ski complex.	Insect cells[a]	X-ray: 4BUJ
Ski3						
Ski3	1	1432	Biochemistry, X-ray, EM		Insect cells[a]	X-ray: 4BUJ, EM: 5MC6
Ski3ΔN	522	1432	Biochemistry	Does not contain the flexible N-terminus. Forms Ski complex	Insect cells[a]	
Ski8						
Ski8 FL	1	397	Biochemistry, X-ray, EM		Insect cells[a]	X-ray: 4BUJ, 1S4U and 1SQ9 EM: 5MC6

[a]Should be coexpressed with the other components of the Ski complex
[b]Trf4 and Air2 should be coexpressed together
References to the PDB codes: 4QU4 [7], 6FSZ [28], 2XGJ [6], 5OOQ [10], 3NYB [14], 4U4C and TRAMP SAXS model [19], 5MC6 [29], 4A4Z and 4A4K [8], 4BUJ [23], 1S4U [30], 1SQ9 [31]

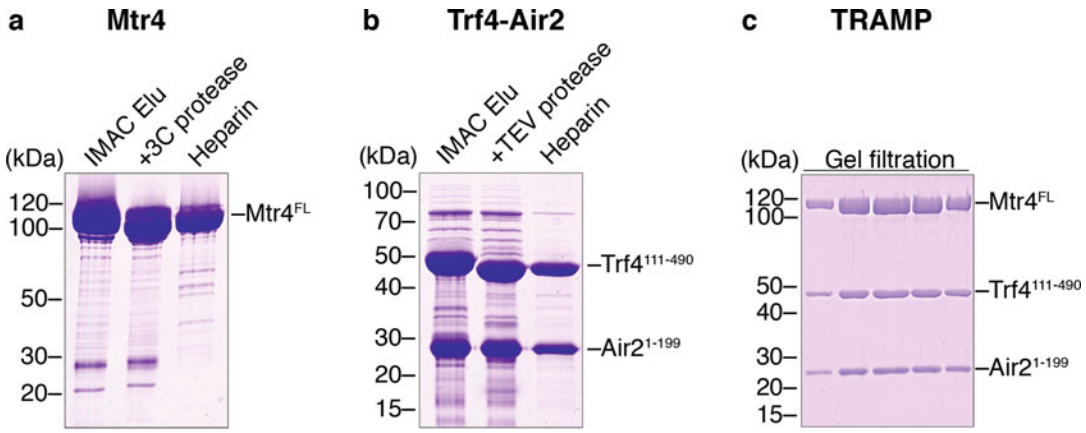

Fig. 2 Representative analysis of the Mtr4 (**a**) and Trf4-Air2 (**b**) purification progress and the TRAMP reconstitution (**c**) by SDS-PAGE and CBB staining. *IMAC Elu* Elution fraction from Ni-affinity column. *Heparin* Elution fraction from Heparin-affinity column

(a) The day before you grow the large main culture (**step 2**), grow an overnight preculture in 50 mL LB medium (37 °C, 220 rpm).

2. Protein production.

   Prepare 3 L of TB medium in TUNAIR culture flasks (1 L per flask).

   (a) Add the respective antibiotics.

   (b) Inoculate with 30 mL (1:100 dilution) of the preculture (*see* **step 1**).

   (c) Grow at 37 °C shaking at 185 rpm.

   (d) When the cells reach an OD_{600} of ~1.5–2.0, lower the temperature to 18 °C.

   (e) After approximately 2 h, when the medium reaches a temperature below 25 °C, add 0.4 mM IPTG and cultivate the cells for 12–16 h (*see* **Note 3**).

3. Harvest the cell pellet by centrifugation at 8900 RCF for 10 min at 4 °C.

   (a) Option 1: Directly proceed with the protein purification (*see* **step 4**).

   (b) Option 2: Freeze the cell pellet in liquid nitrogen and store it in the freezer. The cell pellet may be stored at −20 °C for a short time; for longer periods (more than 1 year), store at −80 °C.

4. Resuspend the cells.

   (a) Transfer the cell pellet corresponding to 3 L of culture (*see* **step 3**) into a glass beaker with a magnetic stir bar.

(b) Add 2 mL of IMAC-lysis buffer per gram of cell pellet wet weight.

(c) Once the cells are resuspended, add DNase I (final concentration 5 μg/mL) and PMSF (final concentration 1 mM) (*see* **Note 4)**.

5. Lyse the cells by sonication.

(a) Place the glass beaker containing the resuspended cells in an ice water bath.

(b) Disrupt the cells by sonication using a Bandelin Sonopuls HD 3200 together with a VS-70 T probe. Typical settings are: Amplitude 40%, pulse 1 s, pause 1 s. Sonicate twice for 10 min and resuspend the lysate in between the two sonication steps (*see* **Note 5**).

6. Centrifuge the crude extract at 75,600 RCF in JA-25.50 rotor for 30 min at 4 °C.

(a) Decant the supernatant from the cell debris.

(b) Filter the cleared lysate through a 5 μm membrane to remove larger particles.

7. Affinity chromatography (IMAC).

(a) Attach one 5 mL His-Trap™ column to a peristaltic pump.

(b) Equilibrate the column with 10 column volumes (CV) of IMAC-Lysis buffer (flow rate: 2.5 mL/min).

(c) Load the lysate (**step 6**) onto the His-Trap™ column (flow rate: 2.5 mL/min).

(d) To remove non-specifically bound proteins and nucleic acid contaminations wash the columns with 10 column volumes (CV) of IMAC-lysis, 10 CV IMAC-chaperone wash, and 10 CV IMAC-high salt wash buffers.

(e) Elute the protein in 10 CV IMAC-elution buffer, collecting five fractions corresponding to 2 CV each.

(f) Analyze the wash and elution fractions by SDS-PAGE and Coomassie brilliant blue (CBB) staining to monitor the progress of the purification (*see* **Note 6**).

(g) Pool all the elution fractions that contain Mtr4 or Trf4-Air2 and have the desired purity.

8. Remove the affinity tag by protease cleavage (*see* **Note 7**).

(a) Add His-tagged 3C protease to remove the affinity tag from Mtr4 constructs (5 μg of 3C protease per 1 mg of Mtr4).

(b) Add His-tagged TEV protease to remove the affinity tag from Trf4 (10 μg of TEV protease per 1 mg of Mtr4).

9. Dialyze overnight against 2 L of dialysis buffer.
10. Recover the protein solution from the dialysis bag and centrifuge the sample at 3200 RCF for 15 min at 4 °C to the remove aggregates (*see* **Note 8**).
11. Load the supernatant with a peristaltic pump onto a 5 mL HisTrap™ FF (flow rate: 2.5 mL/min) to remove uncleaved fusion-protein, the His-GST-tag and the His-tagged protease (*see* **step 7**). The Mtr4 and Trf4-Air2 that do not harbour a tag anymore should be present in the flow-through.
12. Heparin-Affinity chromatography.
    (a) Connected one HiTrap™ Heparin HP 5 mL column to a peristaltic pump.
    (b) Equilibrate the column with 10 CV of Heparin buffer A (flow rate: 2 mL/min).
    (c) Load the flow-through from the reverse IMAC-step (from **step 11**) containing Mtr4 or Trf4-Air2 onto the column (flow rate: 2 mL/min).
    (d) Connect the column to an ÄKTAprime plus (or other chromatography system) to monitor UV absorption at 280 nm (*see* **Note 9**).
    (e) Apply a step gradient with 5 CV of each 0%, 10%, 50% and 100% Heparin buffer B. Both Mtr4 and Trf4-Air2 will elute at the 50% B step. The 100% B wash is used to regenerate the column.
    (f) Analyze the peak fractions by SDS-PAGE and CBB staining to monitor the purity of the preparation (Fig. 2a, b).
    (g) Pool the protein-containing fractions with desired purity.
13. Concentrate the sample by ultrafiltration with an Amicon® Ultra Centrifugal Filter to a final volume of ~2 mL (*see* **Note 10**).
    (a) For Mtr4 use a MWCO of 50k.
    (b) For Trf4-Air2 a MWCO of 30k.
14. After concentrating the sample, centrifuge the sample at 15,000 RCF for at least 10 min at 4 °C to remove aggregates.
15. Size-exclusion chromatography on a Superdex 200 increase 16/600 GL column.
    (a) Equilibrate the column in TRAMP gel filtration buffer (flow rate: 1 mL/min).
    (b) Apply the concentrated sample (**step 14**) and develop the column with 1.5 CV of TRAMP gel filtration buffer.

(c) Analyze the peak fractions of the chromatogram by SDS-PAGE and CBB staining to monitor the purity of the sample.

(d) Pool fractions that contain Mtr4 or Trf4-Air2.

16. Concentrate the protein-containing fractions as in **step 13**.
17. Centrifuge the sample at 15,000 RCF for at least 10 min at 4 °C to remove aggregates.
    (a) Option 1: Use Mtr4 or Trf4-Air2 to directly perform structural characterization, biochemical assays or for the reconstitution of the TRAMP complex (*see* **step 18**).
    (b) Option 2: Freeze the samples until further use. Before freezing, dilute the protein sample with glycerol stock buffer, so that the final concentration of glycerol is 10% (v/v). Divide the sample into small aliquots (max. 50 µL) and snap-freeze them in liquid nitrogen and store at −80 °C.

3.1.2 Reconstitution of the TRAMP Complex

1. Determine the concentration of Mtr4 and the Trf4-Air2 complex by UV spectroscopy.
   (a) Mix Mtr4 and Trf-Air2 in a 1.0:1.2 molar ratio and incubate them for 30 min on ice (*see* **Note 11**).
   (b) Purify the TRAMP complex by size-exclusion chromatography as in (*see* Subheading 3.1.1, **step 15**) and analyze the peak fractions by SDS-PAGE and CBB staining and pool the fractions containing TRAMP (Fig. 2c).
2. Concentrate the TRAMP complex by ultrafiltration with an Amicon® Ultra Centrifugal Filter (MWCO 100k).
3. Centrifuge the sample at 15,000 RCF for at least 10 min at 4 °C to remove aggregates.
   (a) Option 1: Use TRAMP to directly perform structural characterization or biochemical assays.
   (b) Option 2: Freeze the samples until further use. Before freezing, dilute the protein sample with glycerol stock buffer, so that the final concentration of glycerol is 10% (v/v). Divide the sample into small aliquots (max. 50 µL) and snap-freeze them in liquid nitrogen and store at −80 °C.

3.2 Purification Ski2 and the Ski Complex

The *S. cerevisiae* Ski complex is a heterotetrameric complex that consists of one copy of the helicase Ski2, one copy of the scaffolding protein Ski3, and two copies of the β-propeller protein Ski8. In the complex, the N-terminus of Ski2 is buried within the tetratricopeptide repeat (TPR) of Ski3 forming an extensive hydrophobic interaction network. Therefore, Ski2, Ski3, and Ski8 must be

coexpressed. To accomplish this, we use High Five (Hi5) insect cells as the expression system for the Ski complex and cotransfect two different Bacmids: one containing Ski3 in combination with Ski8 and one containing Ski2. If the helicase Ski2 is to be analyzed on its own, that is, in the absence of Ski3 and Ski8, a Ski2 construct that does not contain the N-terminus can be produced in insect cells analogous to the described Ski complex expression procedure. Additionally, the insertion domain of Ski2 can be produced in *E.coli* BL21-Gold (DE3) pLysS. For a detailed overview of successfully used constructs refer to Table 1.

After cell lysis the Ski complex or Ski2 are purified in a three-step procedure, including Ni-affinity (IMAC) chromatography, ion-exchange chromatography (IEC), and finally size-exclusion chromatography (Fig. 3). As above, all buffers and protein-containing solutions should be kept at 4 °C, with all steps carried out on ice or in a temperature-controlled room at 4 °C. All work that involves insect cell culture should be performed in a temperature-controlled room at 27 °C and in a sterile laminar flow hood.

3.2.1 Production of the Ski Complex and Ski2 in Insect Cells

1. Bacmid preparation: Bacmids for protein expression in insect cells are generated using the MultiBac™ System [24, 25]. For troubleshooting and more detailed information refer to the MultiBac™ manual from Geneva Biotech [26].
   (a) Clone the genes encoding Ski2 and Ski3 into a pAECBac1 acceptor vector and the gene encoding Ski8 into pIDC donor vector. Introduce a His_6-tag followed by a 3C cleavage site at the N-terminus of Ski3 (*see* **Note 1**).
   (b) After successfully cloning all components into the vectors individually, generate a bicistronic vector containing Ski3 and Ski8 using Cre-LoxP recombination.
   (c) Select for positive clones by multiantibiotic resistance based on the combination of acceptor and donor vectors (*see* [26]).
   (d) Transform the final vectors into *E.coli* DH10EMBacY cells. Select for positive clones using a blue–white screening (positive clones are white) and isolate Bacmids from the positive clones. For a more detailed description refer to MultiBac™ manual from Geneva Biotech [26].
2. P1 Baculovirus production.
   (a) Incubate 2 mL of freshly diluted Sf21 cells at a density of 0.8×10^6 cells/mL in SF-900™ II SFM medium (hereafter referred to as SFM-medium) for 20 min at 27 °C in a Falcon® 6-well cell culture plate.
   (b) Add a solution containing 1 µg of bacmid DNA and 5 µL FuGene Transfection reagent in 200 µL SFM-medium.

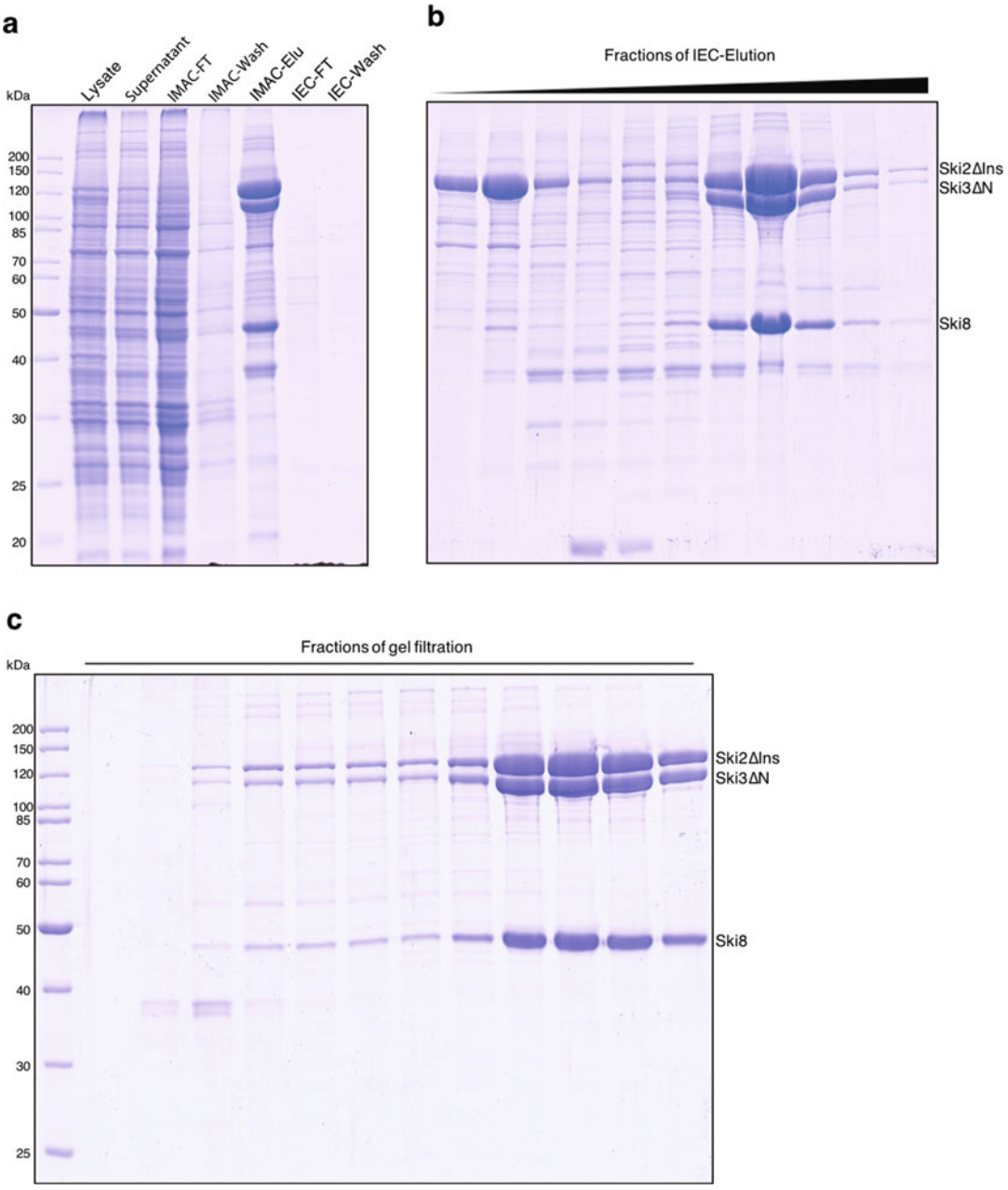

Fig. 3 Representative SDS-PAGE analysis of IMAC (**a**), IEC (**b**) and gel filtration (**c**) steps to monitor the purification progress of the Ski2Δinsert-Ski3ΔN-Ski8 complex from High Five insect cells. *FT* flow-through, *Elu* Elution

(c) Incubate for 4 days at 27 °C at 85 rpm.

(d) Harvest the P1 virus by transferring the medium from the individual wells of the cell culture plate into a 15 mL Falcon tubes and centrifuge for 5 min at 500 RCF.

Transfer the supernatant containing the P1 virus to a new Falcon tube and store at 4 °C (*see* **Note 12**).

3. P2 Baculovirus production.
   (a) Place 25 mL of freshly diluted cells Sf21 (0.5×10^6 cells/mL) in SFM-medium in a 125 mL Erlenmeyer flask.
   (b) Add 1 mL of P1 virus (from **step 2**).
   (c) Incubate at 27 °C for 48 h at 85 rpm.
   (d) Count cells and split them so that the final cell density is below 1.0×10^6 cells/mL.
   (e) Incubate at 27 °C for 48 h at 85 rpm.
   (f) Centrifuge the cells for 10 min at 2000 RCF to remove cells and cell debris and transfer the supernatant containing the P2 virus into a fresh tube and store at 4 °C (*see* **Note 12**).
4. P3 Baculovirus production.
   (a) Place 250 mL of freshly diluted cells Sf21 (0.5×10^6 cells/mL) in SFM-medium in a 125 mL polycarbonate Erlenmeyer flask.
   (b) Add 0.25 mL (0.1% (v/v) of P2 virus (from **step 3**).
   (c) Incubate at 27 °C for 48–72 h 85 rpm.
   (d) Centrifuge the cells for 10 min at 2000 RCF to remove cells and cell debris and transfer the supernatant containing the P3 virus into a fresh tube and store at 4 °C (*see* **Note 12**).
5. Protein production in Hi5 insect cells.
   (a) Place 500 mL of Hi5 insect cells at 1.0×10^6 cells/mL in SFM-medium in a 2 L Fernbach flask.
   (b) Infect the cells by adding 0.5 mL (0.1% (v/v)) of the P3 virus from **step 4.**
   (c) Incubate the cell suspensions for 3 days at 27 °C while shaking at 85 rpm.
6. Harvest the cells by centrifugation at 800 RCF for 10 min at 4 °C.
   (a) Option 1: directly proceed with the protein purification (*see* Subheading 3.2.2).
   (b) Option 2: freeze the cell pellet in liquid nitrogen and store it at −80 °C.

3.2.2 Purification of the Ski Complex or Ski2 from Hi5 Insect Cells

1. Resuspend cells.
   (a) Transfer the cell pellet corresponding to 3 L of Hi5 insect cell expression into a 500 mL glass beaker with a magnetic stir bar.

(b) Add 300 mL Lysis buffer Ski, 3 mL PMSF stock (final concentration 1 mM) and 300 µL DNase stock (final concentration 1 µg/mL).

(c) Place the glass beaker on a magnetic stirrer in the cold room and wait until the cell pellet is completely dissolved.

2. Lyse cells by sonication.

(a) Place the glass beaker with the resuspended cells in an ice water bath.

(b) Disrupt the cells by sonication using a Bandelin Sonopuls HD 3200 together with a VS-70 T probe. Typical settings are Amplitude 35%, pulse 5 s, and pause 10 s. Sonicate twice for 10 min and resuspend the lysate in between the two sonication steps (*see* **Note 5**).

3. Remove insoluble material and cell debris by centrifugation of the crude extract at 75,000 × *g* in a JA-25.50 rotor for 60 min at 4 °C.

(a) Filter the cleared lysate through a membrane with 5 µm pore size.

(b) Supplement the lysate with one cOmplete EDTA-free protease inhibitor cocktail tablet.

4. Affinity chromatography (IMAC-affinity).

(a) Attach two interconnected 5 mL His-Trap™ columns to a peristaltic pump.

(b) Equilibrate the columns with 10 column volumes (CV) of Lysis buffer Ski.

(c) Load the lysate onto the His-Trap™ columns for at least 3 h or overnight by circulating the lysate several times over the columns.

(d) To remove non-specifically bound proteins and nucleic acid contaminations wash the columns with 10 CV Lysis buffer Ski and 10 CV Wash buffer Ski.

(e) Elute proteins from the columns with 10 CV Elution buffer Ski.

5. Analyze the wash and elution fractions by SDS-PAGE and CBB staining to monitor the progress of the purification (Fig. 3a) (*see* **Note 6**).

(a) Pool all the elution fractions that contain the Ski complex and have the desired purity.

6. Anion-exchange chromatography.

(a) Attach one HiTrap™ 5 mL Q HP column to a peristaltic pump.

(b) Equilibrate the column with 10 CV of Q buffer Ski A (flow rate: 2 mL/min).

(c) Load the combined fractions from the IMAC eluate onto the Q-column (flow rate: 1 mL/min).

(d) Attach the column to ÄKTAprime plus (or other chromatography system) (*see* **Note 9**).

(e) Wash column with 10–15 CV Q buffer Ski A (flow: 1 mL/min) until the UV absorption reaches baseline level.

(f) Elute the Ski complex with a linear gradient of Q buffer Ski B against Q buffer Ski A (50% Q buffer Ski B in 45 mL, flow rate 1 mL/min, fraction size 2 mL).

(g) Analyze the peak fractions of the chromatogram by SDS-PAGE and CBB staining to monitor the purity of the preparation (Fig. 3b).

(h) Pool fractions that contain the Ski complex and have the desired purity.

7. Dialyze the protein solution against Dialysis buffer Ski overnight.

   (a) Option 1: Keep the His_6-tag affinity tag.

   (b) Option 2: Remove His_6-tag by adding His-tagged 3C protease (5 μg of 3C protease per 1 mg of Ski complex) to the protein solution prior to dialysis (*see* **Note 13**).

8. Recover the protein solution from the dialysis bag and centrifuge at 3200 RCF for 15 min at 4 °C to the remove aggregates.

9. Concentrate the sample by ultrafiltration with an Amicon® Ultra Centrifugal Filters (MWCO 100k) to a volume of ~2 mL.

10. Centrifuge the sample at 15,000 RCF for at least 10 min at 4 °C to remove aggregates.

11. Size-exclusion chromatography on a Superdex 200 increase 16/600 GL (*see* **Note 14**).

    (a) Equilibrate the gel filtration column in Gel filtration buffer Ski (flow rate: 1 mL/min).

    (b) Apply the concentrated sample (**step 10**) and develop the column with 1.5 CV of Gel filtration buffer Ski.

    (c) Analyze the peak fractions of the chromatogram by SDS-PAGE and CBB staining to monitor the purity of the preparation (Fig. 3c).

    (d) Pool fractions that contain soluble Ski complex.

12. Concentrate the sample by Ultrafiltration with an Amicon® Ultra Centrifugal Filter (MWCO 100k) to the desired concentration.

13. Centrifuge the sample at 15,000 RCF for at least 10 min at 4 °C to remove aggregates.
    (a) Option 1: Perform crystallization trials or biochemical assays.
    (b) Option 2: Freeze the sample. Supplement the protein sample with glycerol, so that the final concentration of glycerol is 10% (v/v). Divide the sample into small aliquots (max. 50 µL) and snap-freeze them in liquid nitrogen and store at −80 °C.

3.2.3 Production and Purification of the Ski2-Insertion Domain

1. Transformation, protein production and cell harvesting are carried out according to the protocol of the TRAMP complex with the only exception that the *E. coli* strain BL21-Gold (DE3) pLysS is used (*see* Subheading 3.1.1, **steps 1–3**).
2. Cell resuspension.
   (a) Transfer the cell pellet corresponding to 3 L of *E.coli* expression into a 500 mL glass beaker with a magnetic stir bar.
   (b) Add 300 mL Lysis buffer Ski2-insertion, 3 mL PMSF stock (final concentration 1 mM) and 300 µL DNase stock (final concentration 1 µg/mL).
   (c) Place the glass beaker on a magnetic stirrer in the cold room and wait until the cell pellet is completely dissolved.
3. Lyse cells by sonication.
   (a) Place the glass beaker with the resuspended cells in an ice water bath.
   (b) Disrupt the cells by sonication using a Bandelin Sonopuls HD 3200 together with a VS-70 T probe. Typical settings are Amplitude 35%, pulse 5 s, and pause 10 s. Sonicate twice for 10 min and resuspend the lysate in between the two sonication steps (*see* **Note 5**).
4. Remove insoluble material and cell debris by centrifugation of the crude extract at 75,000 × *g* in a JA-25.50 rotor for 60 min at 4 °C.
   (a) Filter the cleared lysate through a membrane with 5 µm pore size.
5. Affinity chromatography (IMAC-affinity).
   (a) Attach two connected 5 mL His-Trap™ columns to a peristaltic pump.
   (b) Equilibrate the columns with 10 CV of Lysis buffer Ski2-insertion.
   (c) Load the lysate (**step 4**) onto the His-Trap™ columns (flow rate 2.5 mL/min).

(d) To remove nonspecifically bound proteins and nucleic acid contaminations wash the columns with 10 CV Lysis buffer Ski2-insertion.

(e) Elute proteins with 10 CV of Elution buffer Ski2-insertion.

6. Analyze the wash and elution fractions by SDS-PAGE and CBB staining to monitor the progress of the purification (*see* **Note 6**).
   (a) Pool all the elution fractions that contain the Ski2-insertion domain and have the desired purity.
7. Dialyze protein solution against dialysis buffer Ski2-insertion overnight to decrease the NaCl concentration in the sample solution.
   (a) Option 1: Keep the His_6-tag on Ski2.
   (b) Option 2: Remove His_6-tag by adding His-tagged 3C protease to the protein solution prior to dialysis5 μg of 3C protease per 1 mg of Ski2- insertion domain) (*see* **Note 13**).
8. Anion-exchange chromatography (*see* **Note 15**).
   (a) Attach one HiTrap™ 5 mL Q HP column to a peristaltic pump.
   (b) Equilibrate the column with 10 CV of Q buffer Ski A (flow rate: 2 mL/min).
   (c) Load the combined fractions from the IMAC eluate onto the Q-column (flow rate: 1 mL/min).
   (d) Connect column to ÄKTAprime plus (or other chromatography system).
   (e) Wash column with 10–15 CV LS buffer Ski (flow: 1 mL/min) until the UV absorption reaches baseline level.
   (f) Elute the Ski2-insertion with a linear gradient of Q buffer Ski2-insertion B against Q buffer Ski2-insertion A (60% Q buffer Ski2-insertion B in 60 mL, flow rate 1 mL/min, fraction size 2 mL).
   (g) Analyze the peak fractions of the chromatogram by SDS-PAGE and CBB staining to monitor the purity of the preparation.
   (h) Pool fractions that contain the Ski2-insertion domain.
9. Concentrate the sample by ultrafiltration with an Amicon® Ultra Centrifugal Filters (MWCO 10k) to a volume of ~2 mL.
10. Size-exclusion chromatography on a Superdex 75 increase 16/600 GL.

(a) Equilibrate the gel filtration column in gel filtration Ski2-insertion buffer (flow rate: 1 mL/min).

(b) Apply the concentrated sample (from **step 8**) and develop the column with 1.5 CV of gel filtration Ski2-insertion buffer.

(c) Analyze the peak fractions of the chromatogram by SDS-PAGE and CBB staining to monitor the purity of the preparation.

(d) Pool fractions that contain Ski2-insertion domain.

11. Concentrate the sample by Ultrafiltration with an Amicon® Ultra Centrifugal Filter (MWCO 100k) to the desired concentration.
12. Centrifuge the sample at 15,000 RCF for at least 10 min at 4 °C to remove aggregates.

(a) Option 1: Perform crystallization trials or biochemical assays.

(b) Option 2: Freeze the sample. Supplement the protein sample with glycerol, so that the final concentration of glycerol is 10% (v/v). Divide the sample into small aliquots (max. 50 µL) and snap-freeze them in liquid nitrogen and store at −80 °C.

4 Notes

1. The C-terminus of Mtr4 is highly conserved and folded back on the helicase core domain. Although it is possible to tag Mtr4 on the C-terminus, we do not recommend to do this. The N-terminus of Mtr4 also contains a conserved short linear motif, which mediates binding to the exosome cofactors Rrp6-Rrp47 but tagging does not interfere with this interaction [19, 27]. The same applies to Ski2, where the C-terminus is highly conserved and folded back on the helicase core [8]. The N-terminus of Ski2 forms an intricate interaction with the TPRs of Ski3 [23]. In the case of the Ski complex, we therefore recommend tagging Ski3 at the N-terminus. Trf4 and Air2 form a very stable sub-complex and Air2 forms inclusion bodies, when expressed alone [18]. Therefore, Trf4 and Air2 should always be coexpressed.
2. After spreading, the agar plates can be used for up to 1 week to inoculate a preculture. Afterward the cells should be freshly transformed with plasmid.
3. Check the temperature of your *E. coli* cultures carefully. The temperature that is displayed by the temperature-controlled

orbital shaker does often not match the temperature of the growth medium, especially during the cooling process.

4. In the case that full length Mtr4 or Trf4-Air2 are purified, add one tablet of cOmplete EDTA-free protease inhibitor cocktail per 100 mL of lysate in addition to PMSF.
5. The duration of sonication depends on the volume of the resuspended cells. During sonication, the sample heats up. This can lead to protein denaturation and aggregation. Therefore, it is recommended to sonicate in several small time intervals, to control the temperature and mix the lysate in between.
6. We recommend to take samples at every step of the purification, especially at the beginning. This allows to document the purification progress and to identify potential technical problems.
7. If you want to keep the affinity tag, for example, for GST-pulldowns, do not add 3C or TEV protease. In this case you can omit dialysis and proceed directly to the heparin-affinity chromatography step.
8. Protein aggregates are not always visible by eye. Removing the aggregates by centrifugation decreases the risk to clog the column and increases their lifetime.
9. If the system allows multiple wavelengths to be detected simultaneously, we recommend recording at 260 and 280 nm. This allows the parallel detection of proteins and nucleic acids.
10. If the sample can only be concentrated slowly, this may be due to aggregates clogging the membrane. In this case, centrifuge the protein sample to remove aggregates and use a new concentrator.
11. TRAMP does not stably form at NaCl concentrations higher than 500 mM.
12. Since the Baculoviruses decay over time, we recommend storing the P1 virus at −80 °C since this improves virus stability. Furthermore, we recommend to immediately use the P1 and P2 viruses for amplification and the final P3 Virus for protein production. From our experience, it is better to store the insect cell pellets after production rather than the viruses.
13. If His-tagged 3C protease is added prior to dialysis, it is advised to include an additional IMAC-affinity step to remove His-tagged 3C protease and the cleaved tag before the final SEC. The protein of interest (Ski complex, Ski2 or the Ski2-insertion domain) will be present in the flow-through of the IMAC-affinity.

14. The protein expression levels in Hi5 insect cells can vary between different batches. This can be for example due to the virus quality, the passage number of insect cells or medium quality. If the IEC step only yields small amounts of protein it is advised to use a smaller gel filtration column (e.g., a S200 10/300 GL column) instead of the HiLoad S200 16/600 in the size-exclusion chromatography step.
15. The Ski2 helicase that either lacks the N-terminus or both the N-terminus and the Insertion domain, can also be produced and purified alone from Hi5 insect cells. For constructs containing the insertion domain of Ski2, one can use a HiTrap™ Heparin HP 5 mL instead of a HiTrap™ HP Q-column.

References

1. Zinder JC, Lima CD (2017) Targeting RNA for processing or destruction by the eukaryotic RNA exosome and its cofactors. Genes Dev 31:88–100
2. Chlebowski A, Lubas M, Jensen TH, Dziembowski A (2013) RNA decay machines: the exosome. Biochim Biophys Acta 1829:552–560
3. Makino DL, Schuch B, Stegmann E et al (2015) RNA degradation paths in a 12-subunit nuclear exosome complex. Nature 524:54–58
4. Kilchert C, Wittmann S, Vasiljeva L (2016) The regulation and functions of the nuclear RNA exosome complex. Nat Rev Mol Cell Biol 17:227–239
5. Johnson SJ, Jackson RN (2013) Ski2-like RNA helicase structures common themes and complex assemblies. RNA Biol 10:33–43
6. Weir JR, Bonneau F, Hentschel J, Conti E (2010) Structural analysis reveals the characteristic features of Mtr4, a DExH helicase involved in nuclear RNA processing and surveillance. Proc Natl Acad Sci U S A 107:12139–12144
7. Jackson RN, Klauer AA, Hintze BJ et al (2010) The crystal structure of Mtr4 reveals a novel arch domain required for rRNA processing. EMBO J 29:2205–2216
8. Halbach F, Rode M, Conti E (2012) The crystal structure of S. cerevisiae Ski2, a DExH helicase associated with the cytoplasmic functions of the exosome. RNA 18:124–134
9. Thoms M, Thomson E, Bassler J et al (2015) The exosome is recruited to RNA substrates through specific adaptor proteins. Cell 162:1029–1038
10. Falk S, Tants J-N, Basquin J et al (2017) Structural insights into the interaction of the nuclear exosome helicase Mtr4 with the preribosomal protein Nop53. RNA 23:1780–1787
11. Wyers F, Rougemaille M, Badis G et al (2005) Cryptic pol II transcripts are degraded by a nuclear quality control pathway involving a new poly(a) polymerase. Cell 121:725–737
12. Vaňáčová Š, Wolf J, Martin G et al (2005) A new yeast poly(a) polymerase complex involved in RNA quality control. PLoS Biol 3:e189
13. LaCava J, Houseley J, Saveanu C et al (2005) RNA degradation by the exosome is promoted by a nuclear polyadenylation complex. Cell 121:713–724
14. Hamill S, Wolin SL, Reinisch KM (2010) Structure and function of the polymerase core of TRAMP, a RNA surveillance complex. Proc Natl Acad Sci 107:15045–15050
15. Fasken MB, Leung SW, Banerjee A et al (2011) Air1 zinc knuckles 4 and 5 and a conserved IWRXY motif are critical for the function and integrity of the Trf4/5-Air1/2-Mtr4 polyadenylation (TRAMP) RNA quality control complex. J Biol Chem 286:37429–37445
16. Schmidt K, Butler JS (2013) Nuclear RNA surveillance: role of TRAMP in controlling exosome specificity. WIREs RNA 4:217–231
17. Schmidt K, Xu Z, Mathews DH, Butler JS (2012) Air proteins control differential TRAMP substrate specificity for nuclear RNA surveillance. RNA 18:1934–1945
18. Holub P, Lalakova J, Cerna H et al (2012) Air2p is critical for the assembly and RNA-binding of the TRAMP complex and the KOW domain of Mtr4p is crucial for exosome activation. Nucleic Acids Res 40:5679–5693

19. Falk S, Weir JR, Hentschel J et al (2014) The molecular architecture of the TRAMP complex reveals the organization and interplay of its two catalytic activities. Mol Cell 55:856–867
20. Anderson JS, Parker RP (1998) The 3′ to 5′ degradation of yeast mRNAs is a general mechanism for mRNA turnover that requires the SKI2 DEVH box protein and 3″ to 5″ exonucleases of the exosome complex. EMBO J 17:1497–1506
21. Brown JT, Bai X, Johnson AW (2000) The yeast antiviral proteins Ski2p, Ski3p, and Ski8p exist as a complex in vivo. RNA 6:449–457
22. Synowsky SA, Heck AJR (2008) The yeast Ski complex is a hetero-tetramer. Protein Sci 17:119–125
23. Halbach F, Reichelt P, Rode M, Conti E (2013) The yeast Ski complex: crystal structure and RNA channeling to the exosome complex. Cell 154:814–826
24. Berger I, Fitzgerald DJ, Richmond TJ (2004) Baculovirus expression system for heterologous multiprotein complexes. Nat Biotechnol 22:1583–1587
25. Bieniossek C, Imasaki T, Takagi Y, Berger I (2012) MultiBac: expanding the research toolbox for multiprotein complexes. Trends Biochem Sci 37:49–57
26. Geneva Biotech (2018) Multibac™ User Manual 6.1. https://geneva-biotech.com/wp-content/uploads/2018/01/MultiBac%20Manual%20v6.1.pdf. Accessed 3 Aug 2018
27. Schuch B, Feigenbutz M, Makino DL et al (2014) The exosome-binding factors Rrp6 and Rrp47 form a composite surface for recruiting the Mtr4 helicase. EMBO J 33:2829–2846
28. Schuller JM, Falk S, Fromm L et al (2018) Structure of the nuclear exosome captured on a maturing preribosome. Science 360:219–222
29. Schmidt C, Kowalinski E, Shanmuganathan V et al (2016) The cryo-EM structure of a ribosome-Ski2-Ski3-Ski8 helicase complex. Science 354:1431–1433
30. Cheng Z, Liu Y, Wang C et al (2004) Crystal structure of Ski8p, a WD-repeat protein with dual roles in mRNA metabolism and meiotic recombination. Protein Sci 13:2673–2684
31. Madrona AY, Wilson DK (2004) The structure of Ski8p, a protein regulating mRNA degradation: implications for WD protein structure. Protein Sci 13:1557–1565

4.4 Biochemical characterization of the Ska1 protein and its interaction with the Ski238 complex

In *S. cerevisiae*, the Ska1 protein is associated with the cytoplasmic Ski238 complex targeting a variety of mRNAs that are mainly depleted of ribosomes. Ska1 is likely to regulate the substrate recognition and activity of the Ski238 complex and therefore is a potential new cytoplasmic cofactor of the RNA exosome.

Ska1 is a ~32 kDa protein that is predicted to be mainly unstructured (alphafold databse: AF-P36103-F1). We cloned the full ORF of Ska1, obtained from the *S. cerevisiae* W303 strain, into a bacterial expression vector that contains an N-terminal 10xHis tagged followed by a Thioredoxin domain and a 3C cleavage site. Initial purification trials suggested that Ska1 is prone to degradation (data not shown). We therefore, engineered a StrepII tag on the C-terminus to counteract C-terminal degradation and to enable separation of full-length Ska1 from eventual degradation products (Figure10 A). In brief, the purification involved an initial Ni^{2+} affinity purification step, via the N-terminal His-tag, followed by a StrepII affinity purification step, via the C-terminal strep tag. This strategy allowed us to mostly enrich for intact Ska1 proteins. To further remove impurities in the sample, the proteins were bound to a heparin column and eluted with a salt gradient. The resulting protein was obtained in sufficient amounts and purity. However, some remaining impurities, most likely degradation byproducts could not be separated from the full-length product. The sample was then used to further characterize a potential interaction between Ska1 and the Ski238 complex.

In parallel to the purification trials, we screened for a predicted complex between Ska1 and Ski238 using the Alphafold2 protein structure prediction tool (Jumper et al., 2021). We performed predictions of Ska1 with the individual protein components of the Ski238 complex. Predictions of Ska1 with Ski3 resulted in a few hits where the N-terminus of Ska1 forms a short helix that interacts with Ski3-N (Figure 10 B). Despite the low confidence score of the prediction, we set out to explore this interaction using size exclusion chromatography (SEC) and co-precipitation experiments (Figure 10). At first, we reconstituted a complex of Ska1 and full-length Ski238 on a SEC column(Figure 10 C).

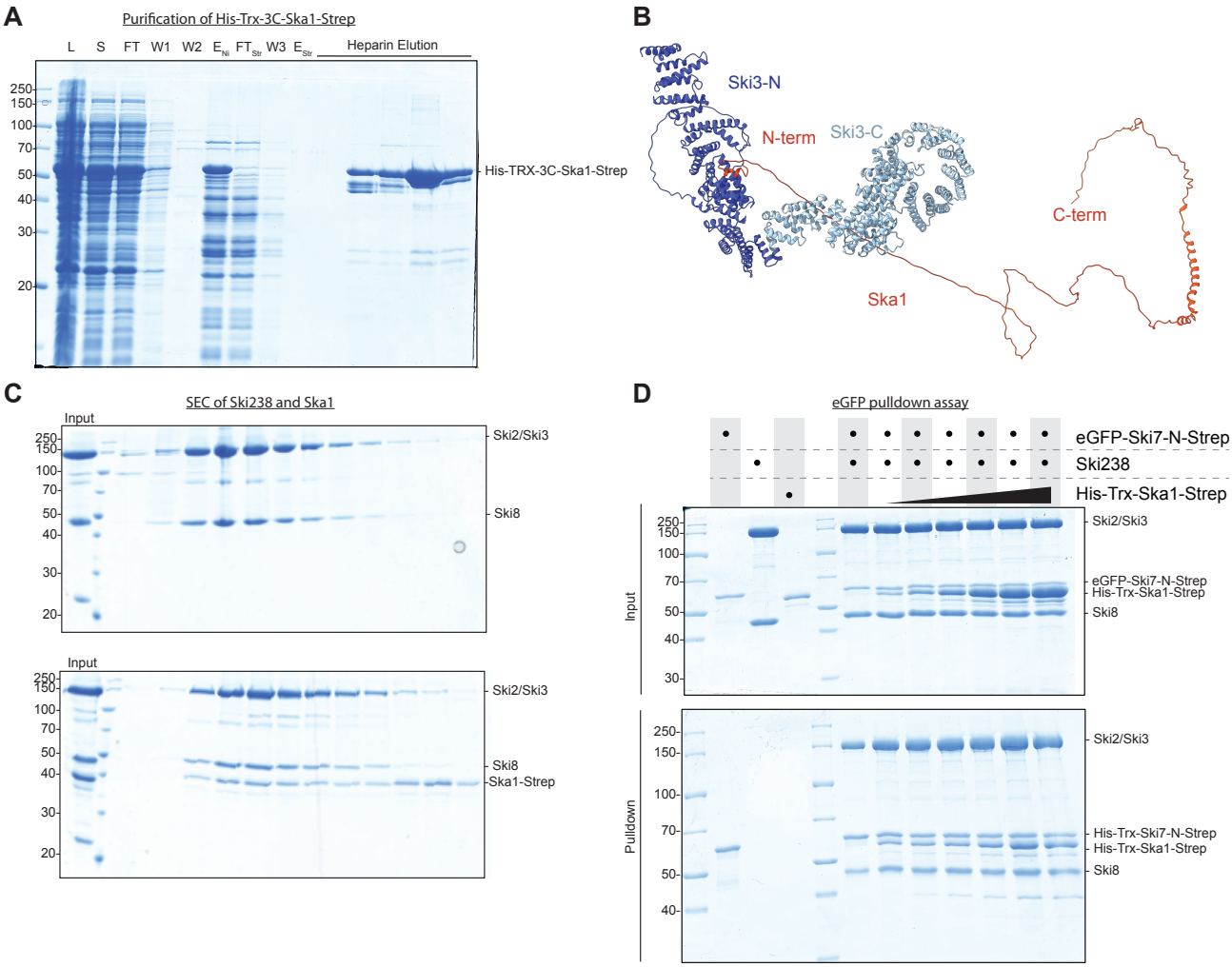

Figure 10: Purification of the Ska1 protein and biochemical characterization of its interaction with the Ski238 complex. **A**: SDS-PAGE analysis of the purification progress of His-Trx-Ska1-Strep from bacteria. L = lysate, S = supernatant, FT = flow through Ni-column, W1 = wash 1, W2 = wash 2, E_{Ni}= elution Ni-column, FT_{Str} = flow through Strep-column, W3 = wash Strep-column, E_{Str} = elution strep- column. The molecular weight of marker bands in kDa is indicated on the left. **B**: Alphafold2 predictions of Ski3 together with Ska1. Ski3-N is shown in dark blue, and Ski3-C is shown in light blue. Ska1 is shown in orange with its C- and N-terminus highlighted by labels. **C:** SDS-PAGE analysis of SEC runs with Ski238 (upper panel) and Ski238 + Ska1 (lower panel). **D**: eGFP pulldown assay with eGFP tagged Ski7-N. Each sample contains Ski238 and Ska1 is added in increasing concentrations indicated by the black triangle. The upper gel shows the input and the lower gel the proteins retrieved after the pulldown.

The experiments indicated comigration of Ska1 together with Ski23 suggesting that they form a stable complex. Notably, the unstructured nature of Ska1 did not allow us to run it over SEC in the absence of Ski238, as it did not elute from the column. Based on this behavior we decided to perform pulldown experiments instead speculating that these would be less time-consuming and more robust. After initial buffer optimization (data not shown) we set out to test if Ska1 affects Ski238 binding to Ski7 (Figure 10 D). We therefore performed co-

precipitation assays with full-length Ski238 and eGFP tagged Ski7-N, purifying via the eGFP tag of Ski7. The titration of Ska1 did not impair the binding of Ski238-Ski7-N and all proteins eluted as a complex. The experiments suggest, that Ska1 and Ski7-N can both interact with the Ski238 complex at the same time, probably through different binding sites.

Based on the Alphafold2 prediction, we further investigated the hypothesis that Ska1 binds to Ski3-N. Since Ski3-N can directly interact with Ski2-Arch (see Chapter 4.1), we also wanted to probe the interaction of this domain with Ska1. The individual proteins were purified according to published protocols and used for pulldown experiments (see Chapter 4.3 and Halbach et al., 2013, 2012). This time, we used Strep-tagged Ska1 as a bait and purified via a Strep-resin (Figure 11). Consistent with the experiments in which Ski7 was the bait, Ska1 effectively copurifies with the Ski238 complex (lane 5). Notably, Ski238 showed unspecific binding to the beads but the intensity for Ski238 proteins in the pulldown experiment significantly increased (compare lanes 2 and 5). In the case of Ski2-Arch, no interaction with Ska1 could be observed (lane 6). For Ski3-N, we observed a band of similar intensity to the bait protein, indicating a strong interaction and the formation of a stoichiometric complex. This suggests that the Ska1 binding site on Ski238 is indeed within Ski3-N, as predicted by Alphafold2. To cross validate our finding we performed the same experiments this time with individual Ski238 complexes that lack either the Ski2-Arch domain (Ski2Arch38) or Ski3-N (Ski23ΔN8) (Figure 11 B). In the case of Ski2ΔArch38, Ska1 effectively pulled down the complex (lane 6). In the case of Ski23ΔN8, we could observe a strong decrease in the intensity of the band for Ski2ΔArch, Ski3 and Ski8 (lane 7). In the control, Ski2ΔArch38 shows unspecific binding to the beads (lane 4), but we cannot exclude that Ska1 still binds this complex. Nevertheless, the interaction of Ska1 towards Ski2ΔArch38 is significantly weaker compared to Ski238 and Ski23ΔN8 (compare lane 7 with lanes 5 and 6). This result is in accordance with the previous pulldown experiment (Figure 11 A) showing that Ska1 binds to the Ski238 complex via Ski3-N.

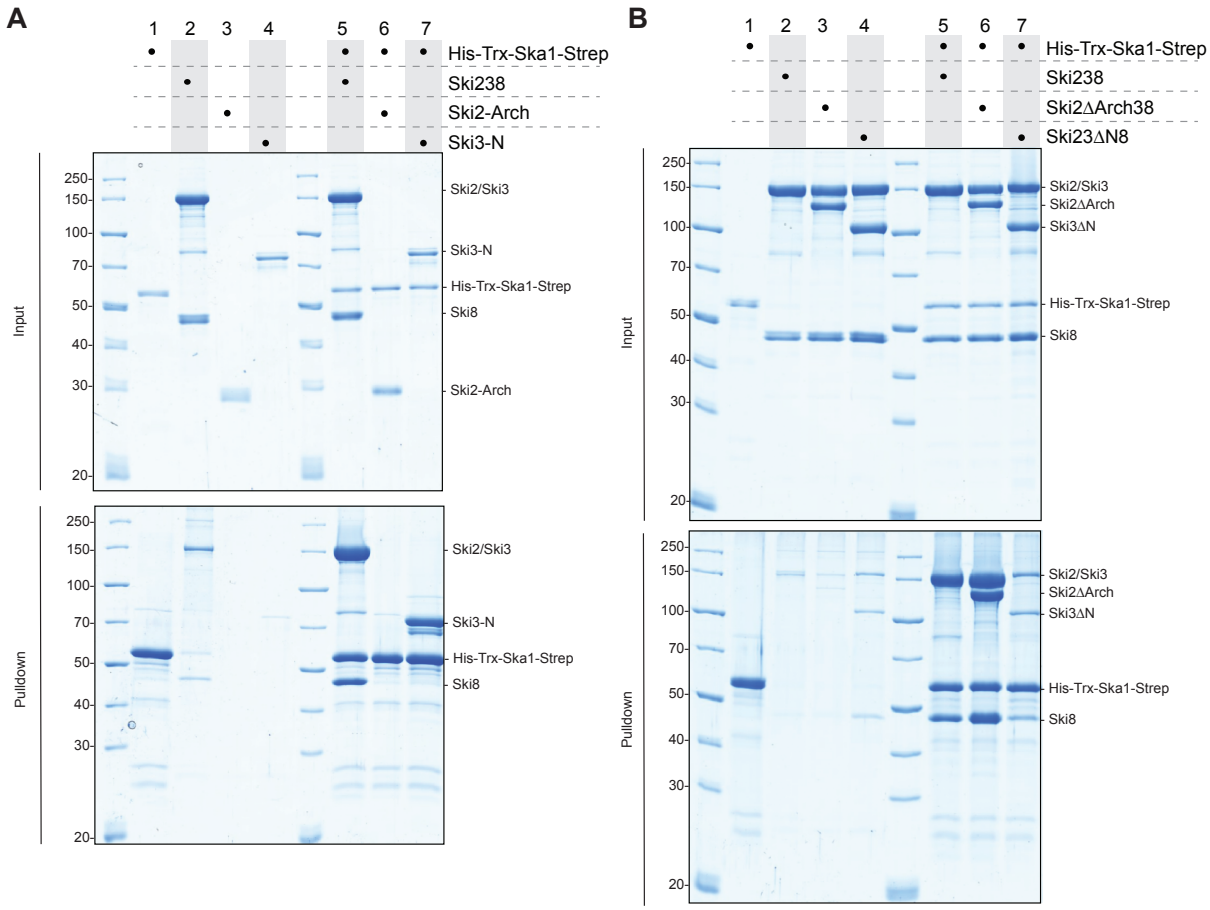

Figure 11: Pulldown assays of Ska1 with different domains of Ski238 (**A**) and different Ski238 complexes (**B**). The upper gel shows the input and the lower gel the proteins retrieved after the pulldown. Molecular weights are indicated on the left side in kDa and proteins are labeled on the right side.

Taken together, we provide a purification strategy for full-length Ska1 from bacteria that yield sufficient amounts of protein for biochemical experiments. Furthermore, we were able to show that Ska1 and Ski238 can form a stable complex *in vitro*. The binding of Ska1 does not interfere with binding to Ski7, suggesting that the exosome could be recruited to Ski238 complexes that are bound by Ska1. This hypothesis is also supported by the current literature (Zhang et al., 2019). At last, the pulldown experiments provide the first insights into the Ska1 binding site on the Ski238 complex. The data indicate that Ska1 directly interacts with Ski3-N although it can be possible that further binding sites exist.

5. Discussion

5.1 Comparison of structure and function of the Ski238 complex in yeast and human

The first results presented in this thesis focus on the structural and biochemical characterization of the human Ski238 complex (Chapter 4.1). CryoEM SPA revealed that the complex can undergo large structural rearrangements in which the helicase Ski2 can detach from the base of the complex while remaining tethered to Ski3-C via Ski2-N (Figure 12). These conformational states are directly connected to the activity of the Ski2 helicase and provide a gatekeeping mechanism that regulates the helicase processivity. Hence, we partitioned the complex into two distinct modules: the helicase module and the gatekeeping module. The helicase module encompasses the helicase core consisting of Ski2-Cat and the Ski2-Arch domain, which provide the RNA binding and unwinding activity. The gatekeeping module comprises Ski3-C, Ski2-N and two copies of Ski8, serving as a foundation of the complex and safeguarding the RNA exit site on the helicase. Interestingly, these conformational states were also observed for the yeast Ski238 complex pointing towards a conserved mode of operation between the species.

In addition, this thesis reports the first structure of the RNA-bound yeast full-length Ski238 complex (Chapter 4.2). The model of the yeast Ski238 complex bound to RNA obtained from cryoEM SPA resembles the previously reported crystal structure of the Ski2ΔArch38 complex (Halbach et al., 2013a) (Figure 12 A). We were able to visualize the Ski2-Arch domain which bends down from Ski2-Cat and forms extensive interactions with Ski3-N. This conformation is different from previously reported crystal structures where it was proposed that Ski2-Arch is in close proximity to the RNA entry site of Ski2-Cat (Halbach et al., 2012a). It also varies from the conformation of Ski2 on the ribosome where Ski2-Arch forms extensive interactions with the 40S subunit (Schmidt et al., 2016a). In addition, Ski8-OUT also contacts the 40S subunit via extensive interactions. Interestingly, both Ski2-Arch and Ski3-N have been shown to regulate the activity of the Ski2 helicase. Removal of either of these domains strongly increases the ATP-hydrolysis rate compared to the full-length complex (Halbach et al., 2013a). The molecular basis of this auto-inhibition mediated by these auxiliary domains was proposed to regulate access of the RNA substrate to the helicase core but our model suggests that it rather

regulates the activity of the Ski2 helicase itself. This is supported by the fact that RNA is bound to Ski2-Cat and that the Ski2-Arch domain does not interfere with the RNA entry site.

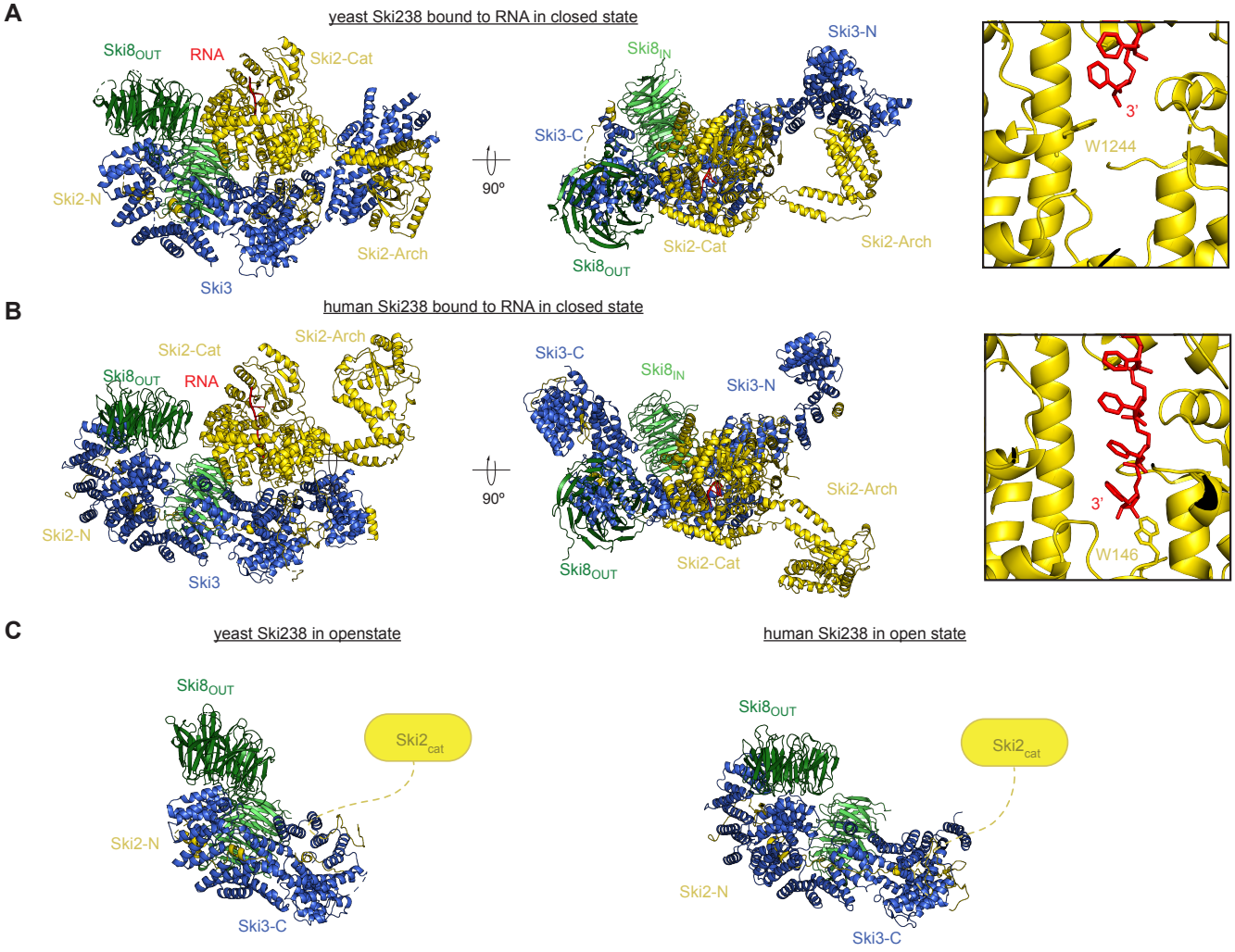

Figure 12: Atomic models of Ski238 from yeast and humans in different conformational states, obtained from cryoEM SPA. Ski2 is in yellow, Ski3 in blue, Ski8IN in green, Ski8OUT in dark green and RNA in red. Ski2 is divided in Ski2-N, Ski2-Cat and Ski2-Arch. Ski3 is divided into Ski3-N and Ski3-C. Model is shown in cartoon representation. All proteins are highlighted with labels. **A** The model of yeast Ski238 bound to RNA in the closed state is shown in two orientations related by a 90˚ rotation around a horizontal axis. (panel on the right) Close up on the RNA bound within Ski2-Cat. The RNA 3' end directly contacts a Tryptophan (W1244) which blocks the RNA path. **B** Model of human ski238 bound to RNA in the closed state shown in two orientations related by a 90˚ rotation around a horizontal axis. (panel on the right) Close up on the RNA bound within Ski2-Cat. The RNA 3' end directly contacts a Tryptophan (W146) which blocks the RNA path. **C** Model of yeast and human ski238 in the open state. The connection to the detached helicase module is indicated by a dotted line.

We hypothesize that the interaction of Ski2-Arch with Ski3-N anchors the helicase module on the gatekeeping module and thereby stabilizes the complex in a closed state. The anchoring would prevent the release of the helicase module leaving the complex in an inactive, substrate-bound state that would require additional factors for activation of the helicase. In conclusion, the self-anchoring mechanism between Ski2-Arch and Ski3-N could prevent the helicase from being active in the absence of the cytoplasmic RNA exosome to ensure that RNA unwinding is coupled to degradation.

The core of the human Ski238 complex revealed an overall similar architecture to that of the yeast complex (Figure 12 B). But in contrast to yeast, human Ski3 contains an additional C-terminal domain that consists of multiple TPR repeats. This additional domain further extends the protein scaffold of human Ski3 and provides a potential binding interface for other species specific factors. In addition, the human Ski2-Arch domain remained rather flexible and was only poorly resolved in the cryoEM reconstruction. We did not observe a direct interaction with Ski3-N as shown for the yeast complex. Nevertheless, ATP hydrolysis assays also showed that the removal of Ski2-Arch slightly increases the activity of the Ski2 helicase although the effect was significantly weaker compared to the yeast system (Chapter 4.1 Figure 4). This suggests that the regulation of Ski2 in the human system is different from yeast and does not necessarily depend on an autoinhibitory mechanism that involves Ski2-Arch and Ski3-N. In contrast to yeast, the structure of the human Ski238 complex bound to 80S ribosomes is exclusively mediated by the Ski2-Arch domain which contacts the 40S subunit. Moreover, there are no further contact sites between the other components of Ski238 with the ribosome resulting in a rather flexible assembly. Comparison of the substrate-bound structures from human and yeast Ski238 complexes in the closed state reveal differences in the positioning within the helicase core of Ski2-Cat (Figure 12 A and B). In the yeast structure, we were able to identify four nucleotides that are bound in the RNA channel with the 3’ end contacting a tryptophan residue (W1244) that seems to block the RNA. Interestingly, this residue is not conserved in higher eukaryotes and other yeast (e.g. *Shizosaccharomyces pombe*). In the human case, we were able to identify six nucleotides in Ski2-Cat that extend further toward the RNA exit site of the helicase. In this case, the 3’ end directly contacts a tryptophan residue (W146) within the wedge/RG-loop of Ski2-N. The wedge/RG-loop is a short segment within Ski2-N that is sandwiched between Ski3-C and Ski2-Cat in the closed

conformation. Despite any secondary structure elements, it adopts a well-structured conformation and shields the bottom of the RNA channel of Ski2-Cat. In the open state reconstructions of yeast and human Ski238, the wedge/RG-loop is unfolded and remains flexibly attached to the complex (Figure 12 C). Initially, we thought that a direct contact between the RNA 3' end and this segment could be involved in the transition from the inactive closed state to the active open state, but ATP hydrolysis rates of Ski2Δwedge38 are similar compared to the wild type (Chapter 4.1 Figure 4). The observed differences between the positioning of RNA in the yeast and human structure suggest, that the wedge/RG-loop is not involved in the regulation of Ski238 activity in yeast. We further hypothesize that it could be crucial for the transition from an open state back to the closed state which would be needed after substrate unwinding. This is supported by the fact that the removal of wedge/RG-loop in human Ski238 shifts the complex towards the open state (Chapter 4.1 Figure S4).

Taken together, Ski238 complexes from yeast and humans share an overall similar architecture. In both species, the activity of the helicase is linked by a transition from a closed state to an open state. While this mode of operation is conserved between the species, the regulation of this conformational change seems to be different. The structural basis of the autoinhibition by the auxiliary domains Ski2-Arch and Ski3-N, could only be observed in the yeast complex and shows that a direct interaction between these domains can stabilize the closed state conformation. In addition, the biochemical assays show that their effect on the ATPase activity of Ski2 is greatly enhanced in the yeast complex and only has a weak effect in the case of the human complex. This suggests that the role of Ski2-Arch in the human complex is different from the yeast system and might require additional factors to regulate the conformational changes and thereby, the activity of the Ski238 complex.

5.2 Recruitment of the Ski238 complex to the eukaryotic RNA exosome by Ski7 and Hbs1L3

The second manuscript presented in this thesis focuses on the characterization of the yeast Ski238 complex bound to the adaptor protein Ski7 (Chapter 4.2). The results provide the first structural insights on how the helicase Ski2 is recruited to the RNA exosome to deliver the RNA substrate for degradation (Chapter 4.2). Despite the ability of Ski7 to bind to the full-length Ski238 complex in pulldown and SEC experiments, we were not able to observe this interaction in cryoEM SPA (Chapter 4.2 Figure 1). Previous RNA protection assays showed that the formation of a continuous RNA channel between Ski238, Ski7 and the exosome is greatly enhanced if the autoinhibition, mediated by Ski2-Arch and Ski3-N, is obstructed (Halbach et al., 2013a). We therefore used a Ski238 complex that lacks the Ski2-Arch domain and reconstituted a complex with Ski7-N, which was subjected to cryoEM SPA. The resulting 3D reconstructions revealed a direct interaction of Ski3-C with three helices of Ski7-N (Chapter 4.2 Figure 3). We were able to link the association of Ski7-N with Ski3-C to the different conformational states of the Ski238 complex (Chapter 4.2 Figure 2). In the closed state, only two helices of Ski7 were observed and the low local resolution of the cryoEM map at the interaction site pointed towards a rather transient interaction. In the open state, the signal significantly improved and we observed three helices of Ski7-N (Figure 13A). The binding interface was validated by point mutations *in vitro* and *in vivo* showing the importance of this interaction. The results suggest that the recruitment of Ski7 to Ski3-C correlates with the transition of the Ski238 complex from a closed to an open state conformation.

In the human system, Hbs1L3 has an analogous role to Ski7 in yeast, by bridging the interaction between the exosome and the Ski238 complex (Chapter 4.1 Figure 6). Hbs1L3 is crucial for the formation of a Ski238-Hbs1L3-exosome complex in SEC experiments and it is also required for the formation of a continuous RNA channel between the two subcomplexes. We continued to compare the binding interface of Ski7-N on Ski3-C, with the structure of the human complex in the open state to identify potential equivalent binding regions in human Ski3 and Hbs1L3 (Figure 13 A). Despite the structural similarities of the complex between the two species, multiple sequence alignments revealed, that the residues in Ski3-C that are involved in the interaction in yeast are within regions that are only poorly conserved (Figure 13 B). Notably, most residues that we identify to participate in the interaction surface are only present in

yeast and absent in higher eukaryotes. We further analyzed the hydrophobicity and the electrostatic potential of the binding site on Ski3-C (Figure 13 C). In the yeast structure, Ski7-N mainly interacts via hydrophobic interactions, especially through two hydrophobic patches in Ski3-C that bind Ski7-N helix1 and Ski7-N helix3. The hydrophobicity plot revealed that these patches are not present in the human complex suggesting that the interaction is unlikely to depend on the same chemical properties observed. The electrostatic potential also differs between the species, showing a negatively charged surface in the yeast structure with a prominent patch that forms the binding site for Ski7-N helix2. In the case of the human Ski238 complex, these sites show a different charge distribution with no obvious similarities to the yeast structure.

Taken together, the binding sites of Ski7-N on Ski3-C are not conserved in higher eukaryotes and the overall chemical properties of the interaction surface are different. This suggests that the interaction of the human Ski238 complex with Hbs1L3 differs from the yeast system and likely requires a different binding interface. In addition, identification of the human Ski238 interacting domains within Hbs1L3 remains challenging because of the above mentioned lack of sequence conservation.

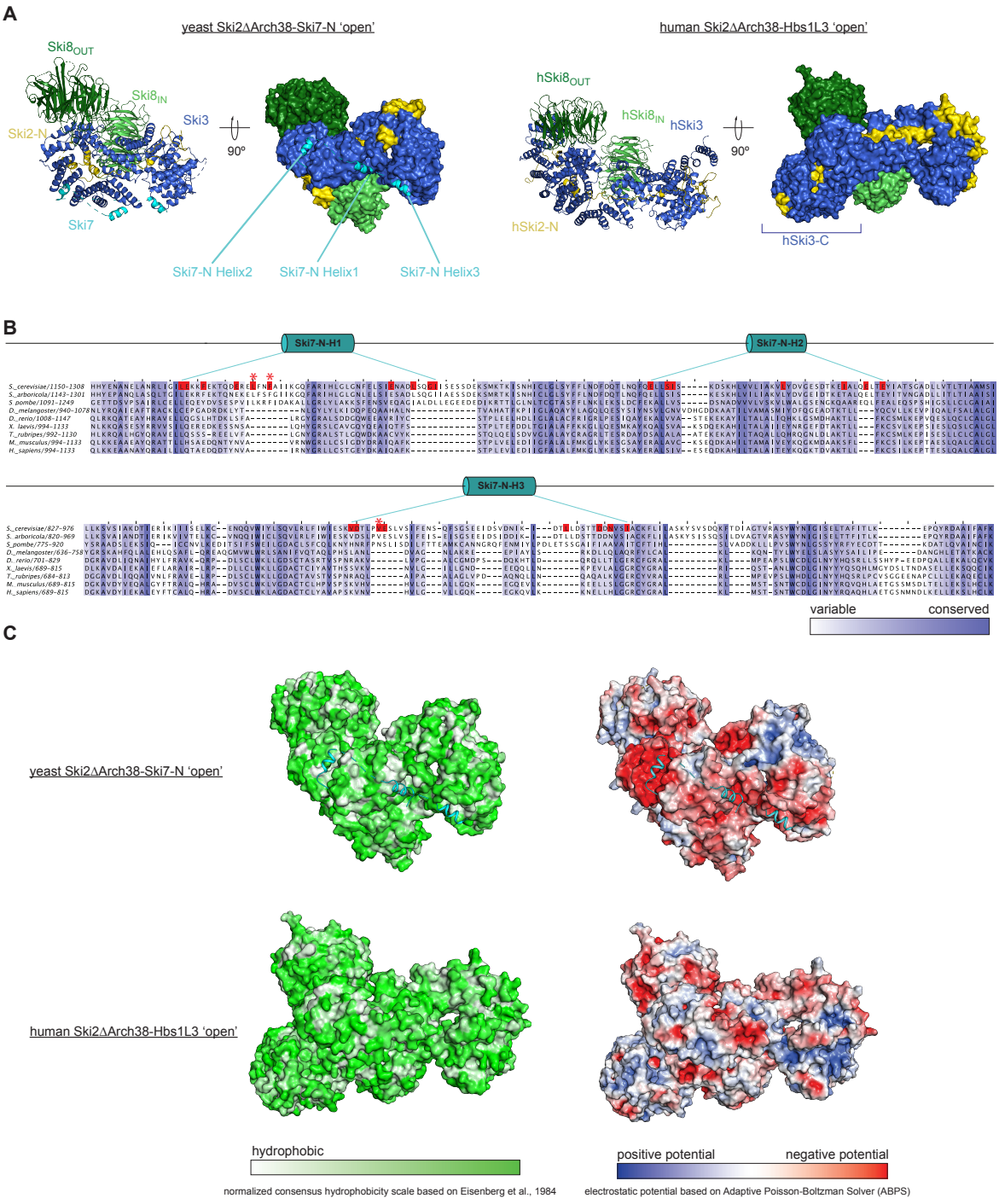

Figure 13: Comparison of yeast Ski2ΔArch38 bound to Ski7-N with human Ski238 in the open state. **A** Model of yeast Ski2ΔArch38 bound to Ski7-N (left panel) and human Ski238 (right panel) in the open state. Each model is shown in two different orientations related by a 90˚ rotation around a vertical axis. Colors are analog to Figure 12 and Ski7-N is shown in cyan. Models are shown in cartoon representation (left) or surface representation (right). **B** Multiple sequence alignments (msa) of Ski3 from different organisms show a lack of conservation of Ski7-N binding sites. (Organism with uniport identifier; *S. cerevisiae*: P17883, *S. pombe*: O94474, *S. arboricola* J8PXS5, *S. pombe*: O94474, *D. melanogaster*: Q6NNB2, *D. rerio*: A0A8M1RLS7, *X. laevis*: Q6DFB8 *T. rubripes*:

H2RXP3, *M. musculus*: F8VPK0 and *H. sapiens*: Q6PGP7). Alignments were performed using Clustal Omega and visualized with Jalview. Sequence conservation is shown by color from variable (white) to conserved (blue). Ski7-N binding sites are indicated by cylinders above the msa. Residues involved in protein-protein interactions are highlighted in red and residues that abolish interaction upon mutation are highlighted with an asterisk. **C** Hydrophobicity (left) and electrostatic potential (right) of yeast (upper) and human (lower) Ski238 complexes. Models are shown in surface representation in the same orientation as shown in A. Ski7 is shown in cartoon representation in cyan for easier comparison. Hydrophobicity is shown in white (hydrophobic) to green (non-hydrophobic). The electrostatic potential is shown from positive (blue) over neutral (white) to negative (red).

5.3 RNA channeling from Ski2-Cat to the exosome is conserved

The second manuscript presented in this thesis also reports the first structure of an active cytoplasmic exosome that actively degrades RNA (Chapter 4.2). The structure reveals for the first time how the helicase module of the yeast Ski238 complex can directly interact with the exosome cap proteins and threads the RNA substrate into the exosome core towards the nuclease Rrp44 for degradation (Chapter 4.2 Figure 4 and Figure 14 A). In the closed structure of the yeast Ski238 complex, the exosome-interaction sites on Ski2 are buried within the gatekeeping module. The transition of the Ski238 complex to its active open state is required to expose the interaction surface thus enabling the interaction with the exosome. This is in accordance with the preferred binding of Ski7-N to the open state Ski238 complex, which relates the recruitment of Ski7-N to the Ski238 complex with its transition to the open state. The Ski238-Ski7-exosome structure reveals remarkable conservation with the nuclear exosome in complex with Mtr4 showing that the positioning of Ski2 in the cytoplasm and Mtr4 in the nucleus is almost identical within these complexes (Chapter 4.2 Figure 5). This points towards a similar mode of helicase recruitment to the exosome in the two compartments, despite the differences in cofactor composition. Analysis of the structural data in combination with multiple sequence alignments also revealed that the interaction sites on the exosome are to a large extent overlapping with the sites observed on the nuclear exosome (Chapter 4.2 Figure S6). This is not only true for yeast, but also translates to metazoan including humans (Weick et al., 2018a). In addition, residues of Ski2 interacting with the exosome are conserved in metazoan, suggesting that a similar assembly between the exosome and Ski2 also exists in the case of the human cytoplasmic exosome.

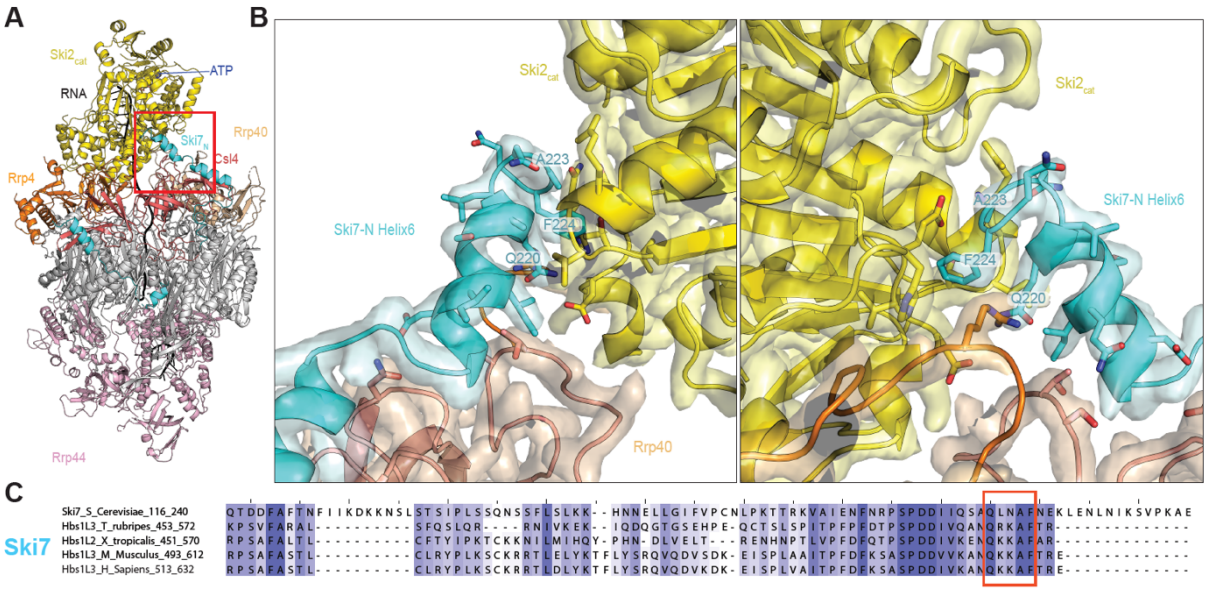

Figure 14: Conservation analysis of Ski7-N residues that interact with the Ski2 helicase core. **A**: Structure of Ski238-Ski7-N-Exo10 bound to RNA, obtained from cryoEM SPA shown in cartoon representation (upper left). Ski2 in yellow, Cap proteins Rrp4 in orange, Csl4 in salmon and Rrp40 in wheat. The exosome barrel is colored in grey and Rrp44 in pink. RNA in black. **B** Close up on the Ski7-N – Ski2 interaction side shown in two orientations. Colors are analog to A. In addition, a transparent cryoEM map is shown. Residues that are crucial for the interaction are shown in stick representation and residue numbers are highlighted for Ski7-N. **C** Multiple sequence alignments (msa) of Ski7/Hbs1L3 from different organisms shows the conservation of Ski7-N residues involved in the interaction with Ski2. The interaction site is indicated by a red box. (Organism with uniport identifier; *S. cerevisiae*: Q08491, *X. tropicalis*: B3DLY5 *T. rubripes*:, *M. musculus*: L7N209 and *H. sapiens*: Q9Y450). Alignments were performed using Clustal Omega and visualized with Jalview. Sequence conservation is shown by color from variable (white) to conserved (blue).

In addition to the Ski2 interaction with the exosome cap proteins, we observed an interaction with the C-terminal end of Ski7-N helix6 (Figure 14 B). This helix binds to the cap protein Rrp40 and extends towards the RNA entry site on the exosome. Interestingly, this positioning of Ski7-N helix6 had already been reported in a crystal structure of the yeast exosome bound to Ski7-N containing a C-terminal T4 Lysozyme domain which directly contacted parts of the exosome cap and was thought to influence the positioning of Ski7-N helix6 (Kowalinski et al., 2016a). However, in our cryoEM dataset, we could identify a population of exosome particles that were bound to Ski7-N, but not by Ski2 and we could observe the same positioning of this helix. So far it remains unclear whether this interaction is required for exosome functions *in vivo* and if it affects the activity of Ski2. Nevertheless, it provides an additional binding

interface that anchors the Ski2 helicase on top of the exosome. Upon closer inspection, we were able to identify three residues within Ski7-N helix6 (Q220, A223 and F224) that contact one of the RecA domains of Ski2. Multiple sequence alignments of Ski7 with different homologs from higher eukaryotes revealed remarkable conservation of this helix (previously reported in Kowalinski et al., 2016, Figure 14 C). The conservation further promotes the idea that the direct interaction of Ski2 and the exosome cap also exist in higher eukaryotes. The Ski7 binding site on Ski2 shows only low conservation with Mtr4. On the exosome, Ski7 occupies almost the same interaction site as the nuclear cofactor Rrp6. However, Rrp6 does not have the extended helix, that in the case of Ski7 contacts Ski2 (Schuller et al., 2018a; Weick et al., 2018a). But another nuclear cofactor, Mpp6, binds to a similar region on Mtr4, indicating that the different exosome assemblies, cytosolic and nuclear, share similarities in the mode of helicase recruitment (Chapter 4.2 Figure S6).

5.4 Ska1 as a potential regulator of Ski238 helicase activity

The final results section of this thesis (Chapter 4.4) presents the initial characterization of the Ska1 protein from yeast, which is a potential cytoplasmic cofactor of the RNA exosome capable of interacting with the Ski238 complex. The activity of the Ski2 helicase is regulated by an autoinhibitory mechanism involving two flexible domains: Ski2-Arch and Ski3-N. Our findings demonstrate that when the RNA substrate binds, the Ski2-Arch directly interacts with Ski3-N, effectively anchoring the helicase module to the gatekeeping module and rendering the complex inactive. By removing this autoinhibition, we observed destabilization of the closed conformation, leading to the detachment of the helicase module and consequently enhancing the complex's activity (Chapter 4.2, Chapter 5.1 ,Halbach et al., 2013). In the presented manuscript (Chapter 4.2), we successfully overcame the autoinhibitory mechanism by deleting the Ski2-Arch domain. However, it remains unclear what triggers this event in an *in vivo* scenario. Alphafold2 predictions suggest that Ska1 can bind to Ski3-N via a short N-terminal helix (Figure 10 B). Through our biochemical characterization utilizing pulldown assays and SEC experiments (Figures 11 and 12), we confirmed this interaction. Upon closer examination of the binding interface, we observed its proximity to the Ski2-Arch interaction site on Ski3-N. Based on these findings, we propose that Ska1 could potentially influence the autoinhibition within the Ski238 complex by binding to Ski3-N, either releasing Ski2-Arch or preventing its binding altogether. Unfortunately, Alphafold2 predictions including the

Ski2-Arch domain did not yield any results. In addition, the unstructured nature of Ska1 makes it a challenging protein for complex reconstitution and it needs to be researched further in the future.

6. Outlook

The results presented in this thesis provide a significant contributions to our understanding of the cytoplasmic RNA exosome and its cofactors in both yeast and human systems, offering valuable biochemical and structural insights. Notably, this research has revealed novel information regarding the conformational states of the Ski238 complex, which have been found to correlate with the activity of the Ski2 helicase. Furthermore, the thesis elucidates the structural basis of the Ski238-Ski7 interaction, shedding light on the intricate molecular interactions within this complex. This allowed us to reveal the mechanisms involved in RNA transfer from Ski2 to the exosome within the Ski238-Ski7-exosome assembly. These discoveries not only expand our current knowledge but also lay a solid groundwork for future investigations.

In the yeast system, the mechanisms regulating the autoinhibition by Ski2-Arch remain elusive. It is evident that the positioning of the Arch domain influences the helicase activity, but the factors triggering these conformational changes remain unknown. The Ska1 protein emerges as a promising candidate involved in this regulation (Zhang et al., 2019.). Therefore, further dissection of the interaction between Ska1 and the Ski238 complex and testing its impact on helicase activity would offer a suitable starting point in future studies. However, it is important to note that Ska1 is reported to function primarily on specific RNA substrates, such as untranslated transcripts or ribosome-free transcripts. This suggests the existence of other factors that could regulate Ski238 activity, especially in the event of co-translational degradation of a transcript. The Ski238 complex exhibits a preference for substrates with a short 3' RNA overhang. In the case of mRNA surveillance, this necessitates endonucleolytic cleavage of the mRNA before degradation. In non-stop decay, the leading ribosome stalls on the poly(A) tail, resulting in a 5' fragment that likely possesses a long 3' poly(A) tail, possibly covered by PABPs. It remains unclear how the RNA end is shortened and how the ribosome is recycled from the message in this particular case. In yeast, it has been shown that the C-terminal GTP binding domain of Ski7 is required for the degradation of these aberrant transcripts, and it has yet to be shown whether Ski7 can directly interact with the ribosome in such a scenario.

In the human Ski238-Hbs1L3-exosome complex, the role of Ski2-Arch appears to differ, and it is unclear whether it regulates the activity of the Ski238 complex in an analogous manner.

Recent studies have shown that human Ski238 is mainly involved in mRNA surveillance pathways and plays only a minor role in mRNA turnover (A. Tuck et al., 2020). Investigating whether the human Ski2-Arch has evolved to modulate Ski238 activity differently, potentially through the recruitment of additional factors is an interesting question for future studies. In this context two proteins, Aven and Focad, are of special interest. Both have been shown to interact with the human Ski238 complex during mRNA surveillance (A. Tuck et al., 2020).

Future research should also address the role of the human Ski7 ortholog, Hbs1L3, in bridging the helicase activity of the Ski238 complex and the nuclease activity of the exosome. While we have demonstrated the coordination of Ski7 in associating these complexes in yeast, there is limited knowledge regarding the binding mechanism of Hbs1L3 to the human exosome and its recruitment of the Ski238 complex. Fortunately, the exosome binding site has already been identified, providing a promising starting point for the structural characterization of the exosome-Hbs1L3 complex. Besides the exosome binding site, Hbs1L3 and Ski7 share only low sequence homology suggesting that the interaction with the Ski238 complex differs from the yeast system. Consequently, the binding site of Hbs1L3 for Ski238 remains unknown. These functional and structural differences in the behavior of human versus yeast Ski238 complexes remain yet unknown and require further investigation on a molecular scale.

At last, the structural data presented results from recombinantly expressed protein complexes that are reconstituted in vitro. Therefore a crucial question remains unanswered: Do the exosome and the Ski238 complex come together as a stable assembly *in vivo*? Recent advantages in *in-situ* cryoEM tomography presents an exciting opportunity to try to visualize a Ski238-Ski7-exosome assembly within the dynamic environment of a living cell.

7. References

Allmang, C., Kufel, J., Chanfreau, G., Mitchell, P., Petfalski, E., Tollervey, D., 1999. Functions of the exosome in rRNA, snoRNA and snRNA synthesis. EMBO J. 18, 5399–5410. https://doi.org/10.1093/emboj/18.19.5399

Allmang, Christine, Petfalski, E., Podtelejnikov, A., Mann, M., Tollervey, D., Mitchell, P., 1999. The yeast exosome and human PM–Scl are related complexes of 3′ → 5′ exonucleases. Genes Dev. 13, 2148–2158.

Anderson, J.S., Parker, R.P., 1998. The 3′ to 5′ degradation of yeast mRNAs is a general mechanism for mRNA turnover that requires the SKI2 DEVH box protein and 3′ to 5′ exonucleases of the exosome complex. EMBO J. 17, 1497–1506. https://doi.org/10.1093/emboj/17.5.1497

Anderson, J.T., Wang, X., 2009. Nuclear RNA surveillance: no sign of substrates tailing off. Crit. Rev. Biochem. Mol. Biol. 44, 16–24. https://doi.org/10.1080/10409230802640218

Araki, Yasuhiro, Takahashi, S., Kobayashi, T., Kajiho, H., Hoshino, S., Katada, T., 2001. Ski7p G protein interacts with the exosome and the Ski complex for 3′-to-5′ mRNA decay in yeast. EMBO J. 20, 4684–4693. https://doi.org/10.1093/emboj/20.17.4684

Arora, C., Kee, K., Maleki, S., Keeney, S., 2004. Antiviral Protein Ski8 Is a Direct Partner of Spo11 in Meiotic DNA Break Formation, Independent of Its Cytoplasmic Role in RNA Metabolism. Mol. Cell 13, 549–559. https://doi.org/10.1016/S1097-2765(04)00063-2

Beaulieu, Y.B., Kleinman, C.L., Landry-Voyer, A.-M., Majewski, J., Bachand, F., 2012. Polyadenylation-dependent control of long noncoding RNA expression by the poly(A)-binding protein nuclear 1. PLoS Genet. 8, e1003078. https://doi.org/10.1371/journal.pgen.1003078

Benard, L., Carroll, K., Valle, R.C., Masison, D.C., Wickner, R.B., 1999. The ski7 antiviral protein is an EF1-alpha homolog that blocks expression of non-Poly(A) mRNA in Saccharomyces cerevisiae. J. Virol. 73, 2893–2900. https://doi.org/10.1128/JVI.73.4.2893-2900.1999

Benard, L., Carroll, K., Valle, R.C.P., Wickner, R.B., 1998. Ski6p Is a Homolog of RNA-Processing Enzymes That Affects Translation of Non-Poly(A) mRNAs and 60S Ribosomal Subunit Biogenesis. Mol. Cell. Biol. 18, 2688–2696. https://doi.org/10.1128/MCB.18.5.2688

Bresson, S., Tuck, A., Staneva, D., Tollervey, D., 2017. Nuclear RNA Decay Pathways Aid Rapid Remodeling of Gene Expression in Yeast. Mol. Cell 65, 787-800.e5. https://doi.org/10.1016/j.molcel.2017.01.005

Bresson, S.M., Conrad, N.K., 2013. The human nuclear poly(a)-binding protein promotes RNA hyperadenylation and decay. PLoS Genet. 9, e1003893. https://doi.org/10.1371/journal.pgen.1003893

Buschauer, R., Matsuo, Y., Sugiyama, T., Chen, Y.-H., Alhusaini, N., Sweet, T., Ikeuchi, K., Cheng, J., Matsuki, Y., Nobuta, R., Gilmozzi, A., Berninghausen, O., Tesina, P., Becker, T., Coller, J., Inada, T., Beckmann, R., 2020. The Ccr4-Not complex monitors the translating ribosome for codon optimality. Science 368, eaay6912. https://doi.org/10.1126/science.aay6912

Büttner, K., Wenig, K., Hopfner, K.-P., 2005. Structural framework for the mechanism of archaeal exosomes in RNA processing. Mol. Cell 20, 461–471. https://doi.org/10.1016/j.molcel.2005.10.018

Chekanova, J.A., Gregory, B.D., Reverdatto, S.V., Chen, H., Kumar, R., Hooker, T., Yazaki, J., Li, P., Skiba, N., Peng, Q., Alonso, J., Brukhin, V., Grossniklaus, U., Ecker, J.R., Belostotsky, D.A., 2007. Genome-wide high-resolution mapping of exosome substrates reveals hidden features in the Arabidopsis transcriptome. Cell 131, 1340–1353. https://doi.org/10.1016/j.cell.2007.10.056

Chen, C.Y., Gherzi, R., Ong, S.E., Chan, E.L., Raijmakers, R., Pruijn, G.J., Stoecklin, G., Moroni, C., Mann, M., Karin, M., 2001. AU binding proteins recruit the exosome to degrade ARE-containing mRNAs. Cell 107, 451–464. https://doi.org/10.1016/s0092-8674(01)00578-5

Chlebowski, A., Lubas, M., Jensen, T.H., Dziembowski, A., 2013b. RNA decay machines: The exosome. RNA Decay Mech. 1829, 552–560. https://doi.org/10.1016/j.bbagrm.2013.01.006

Claeys Bouuaert, C., Tischfield, S.E., Pu, S., Mimitou, E.P., Arias-Palomo, E., Berger, J.M., Keeney, S., 2021. Structural and functional characterization of the Spo11 core complex. Nat. Struct. Mol. Biol. 28, 92–102. https://doi.org/10.1038/s41594-020-00534-w

Cristea, I.M., Chait, B.T., 2011. Conjugation of Magnetic Beads for Immunopurification of Protein Complexes. Cold Spring Harb. Protoc. 2011, pdb.prot5610. https://doi.org/10.1101/pdb.prot5610

Decker, C.J., Parker, R., 1993. A turnover pathway for both stable and unstable mRNAs in yeast: evidence for a requirement for deadenylation. Genes Dev. 7, 1632–1643. https://doi.org/10.1101/gad.7.8.1632

Doma, M.K., Parker, R., 2006. Endonucleolytic cleavage of eukaryotic mRNAs with stalls in translation elongation. Nature 440, 561–564. https://doi.org/10.1038/nature04530

Domanski, M., Molloy, K., Jiang, H., Chait, B.T., Rout, M.P., Jensen, T.H., LaCava, J., 2012. Improved methodology for the affinity isolation of human protein complexes expressed at near endogenous levels. BioTechniques 0, 1–6. https://doi.org/10.2144/000113864

D'Orazio, K.N., Wu, C.C.-C., Sinha, N., Loll-Krippleber, R., Brown, G.W., Green, R., 2019. The endonuclease Cue2 cleaves mRNAs at stalled ribosomes during No Go Decay. eLife 8, e49117. https://doi.org/10.7554/eLife.49117

Dziembowski, A., Lorentzen, E., Conti, E., Séraphin, B., 2007b. A single subunit, Dis3, is essentially responsible for yeast exosome core activity. Nat. Struct. Mol. Biol. 14, 15–22. https://doi.org/10.1038/nsmb1184

Eckmann, C.R., Rammelt, C., Wahle, E., 2011. Control of poly(A) tail length. Wiley Interdiscip. Rev. RNA 2, 348–361. https://doi.org/10.1002/wrna.56

Fabre, A., Martinez-Vinson, C., Goulet, O., Badens, C., 2013. Syndromic diarrhea/Tricho-hepato-enteric syndrome. Orphanet J. Rare Dis. 8, 5. https://doi.org/10.1186/1750-1172-8-5

Falk, S., Bonneau, F., Ebert, J., Kögel, A., Conti, E., 2017b. Mpp6 Incorporation in the Nuclear Exosome Contributes to RNA Channeling through the Mtr4 Helicase. Cell Rep. 20, 2279–2286. https://doi.org/10.1016/j.celrep.2017.08.033

Ford, Lance P., Bagga, P.S., Wilusz, J., 1997. The Poly(A) Tail Inhibits the Assembly of a 3'-to-5' Exonuclease in an In Vitro RNA Stability System. Mol. Cell. Biol. 17, 398–406. https://doi.org/10.1128/MCB.17.1.398

Frischmeyer, P.A., van Hoof, A., O'Donnell, K., Guerrerio, A.L., Parker, R., Dietz, H.C., 2002. An mRNA surveillance mechanism that eliminates transcripts lacking termination codons. Science 295, 2258–2261. https://doi.org/10.1126/science.1067338

Fromm, L., Falk, S., Flemming, D., Schuller, J.M., Thoms, M., Conti, E., Hurt, E., 2017b. Reconstitution of the complete pathway of ITS2 processing at the pre-ribosome. Nat. Commun. 8, 1787. https://doi.org/10.1038/s41467-017-01786-9

Garneau, N.L., Wilusz, J., Wilusz, C.J., 2007. The highways and byways of mRNA decay. Nat. Rev. Mol. Cell Biol. 8, 113–126. https://doi.org/10.1038/nrm2104

Gerlach, P., Garland, W., Lingaraju, M., Salerno-Kochan, A., Bonneau, F., Basquin, J., Jensen, T.H., Conti, E., 2022a. Structure and regulation of the nuclear exosome targeting complex guides RNA substrates to the exosome. Mol. Cell 82, 2505-2518.e7. https://doi.org/10.1016/j.molcel.2022.04.011

Gerlach, P., Schuller, J.M., Bonneau, F., Basquin, J., Reichelt, P., Falk, S., Conti, E., 2018b. Distinct and evolutionary conserved structural features of the human nuclear exosome complex. eLife 7, e38686. https://doi.org/10.7554/eLife.38686

Glover, M.L., Burroughs, A.Max., Monem, P.C., Egelhofer, T.A., Pule, M.N., Aravind, L., Arribere, J.A., 2020. NONU-1 Encodes a Conserved Endonuclease Required for mRNA Translation Surveillance. Cell Rep. 30, 4321-4331.e4. https://doi.org/10.1016/j.celrep.2020.03.023

Gudipati, R.K., Villa, T., Boulay, J., Libri, D., 2008. Phosphorylation of the RNA polymerase II C-terminal domain dictates transcription termination choice. Nat. Struct. Mol. Biol. 15, 786–794. https://doi.org/10.1038/nsmb.1460

Gudipati, R.K., Xu, Z., Lebreton, A., Séraphin, B., Steinmetz, L.M., Jacquier, A., Libri, D., 2012. Extensive Degradation of RNA Precursors by the Exosome in Wild-Type Cells. Mol. Cell 48, 409–421. https://doi.org/10.1016/j.molcel.2012.08.018

Guydosh, N.R., Green, R., 2017. Translation of poly(A) tails leads to precise mRNA cleavage. RNA N. Y. N 23, 749–761. https://doi.org/10.1261/rna.060418.116

Halbach, F., Reichelt, P., Rode, M., Conti, E., 2013b. The Yeast Ski Complex: Crystal Structure and RNA Channeling to the Exosome Complex. Cell 154, 814–826. https://doi.org/10.1016/j.cell.2013.07.017

Halbach, F., Rode, M., Conti, E., 2012b. The crystal structure of S. cerevisiae Ski2, a DExH helicase associated with the cytoplasmic functions of the exosome. RNA 18, 124–134. https://doi.org/10.1261/rna.029553.111

Ito-Harashima, S., Kuroha, K., Tatematsu, T., Inada, T., 2007. Translation of the poly(A) tail plays crucial roles in nonstop mRNA surveillance via translation repression and protein destabilization by proteasome in yeast. Genes Dev. 21, 519–524. https://doi.org/10.1101/gad.1490207

Jackson, R.J., Hellen, C.U.T., Pestova, T.V., 2010. The mechanism of eukaryotic translation initiation and principles of its regulation. Nat. Rev. Mol. Cell Biol. 11, 113–127. https://doi.org/10.1038/nrm2838

Jalkanen, A.L., Coleman, S.J., Wilusz, J., 2014. Determinants and implications of mRNA poly(A) tail size--does this protein make my tail look big? Semin. Cell Dev. Biol. 34, 24–32. https://doi.org/10.1016/j.semcdb.2014.05.018

Jinek, M., Coyle, S.M., Doudna, J.A., 2011. Coupled 5' nucleotide recognition and processivity in Xrn1-mediated mRNA decay. Mol. Cell 41, 600–608. https://doi.org/10.1016/j.molcel.2011.02.004

Johnson, A.W., Kolodner, R.D., 1995b. Synthetic lethality of sep1 (xrn1) ski2 and sep1 (xrn1) ski3 mutants of Saccharomyces cerevisiae is independent of killer virus and suggests a general role for these genes in translation control. Mol. Cell. Biol. 15, 2719–2727. https://doi.org/10.1128/MCB.15.5.2719

Johnson, S.J., Jackson, R.N., 2013. Ski2-like RNA helicase structures. RNA Biol. 10, 33–43. https://doi.org/10.4161/rna.22101

Kadaba, S., WANG, X., ANDERSON, J.T., 2006. Nuclear RNA surveillance in Saccharomyces cerevisiae: Trf4p-dependent polyadenylation of nascent hypomethylated tRNA and an aberrant form of 5S rRNA. RNA 12, 508–521. https://doi.org/10.1261/rna.2305406

Kalisiak, K., Kuliński, T.M., Tomecki, R., Cysewski, D., Pietras, Z., Chlebowski, A., Kowalska, K., Dziembowski, A., 2017b. A short splicing isoform of HBS1L links the cytoplasmic exosome and SKI complexes in humans. Nucleic Acids Res. 45, 2068–2080. https://doi.org/10.1093/nar/gkw862

Karousis, E.D., Mühlemann, O., 2019. Nonsense-Mediated mRNA Decay Begins Where Translation Ends. Cold Spring Harb. Perspect. Biol. 11. https://doi.org/10.1101/cshperspect.a032862

Kim, M., Vasiljeva, L., Rando, O.J., Zhelkovsky, A., Moore, C., Buratowski, S., 2006. Distinct pathways for snoRNA and mRNA termination. Mol. Cell 24, 723–734. https://doi.org/10.1016/j.molcel.2006.11.011

Kowalinski, E., Kögel, A., Ebert, J., Reichelt, P., Stegmann, E., Habermann, B., Conti, E., 2016b. Structure of a Cytoplasmic 11-Subunit RNA Exosome Complex. Mol. Cell 63, 125–134. https://doi.org/10.1016/j.molcel.2016.05.028

Kurosaki, T., Popp, M.W., Maquat, L.E., 2019b. Quality and quantity control of gene expression by nonsense-mediated mRNA decay. Nat. Rev. Mol. Cell Biol. 20, 406–420. https://doi.org/10.1038/s41580-019-0126-2

Larimer, F.W., Stevens, A., 1990b. Disruption of the gene XRN1, coding for a 5'----3' exoribonuclease, restricts yeast cell growth. Gene 95, 85–90. https://doi.org/10.1016/0378-1119(90)90417-p

Le Hir, H., Gatfield, D., Izaurralde, E., Moore, M.J., 2001. The exon–exon junction complex provides a binding platform for factors involved in mRNA export and nonsense-mediated mRNA decay. EMBO J. 20, 4987–4997. https://doi.org/10.1093/emboj/20.17.4987

Liu, Q., Greimann, J.C., Lima, C.D., 2006. Reconstitution, Activities, and Structure of the Eukaryotic RNA Exosome. Cell 127, 1223–1237. https://doi.org/10.1016/j.cell.2006.10.037

Lorentzen, E., Dziembowski, A., Lindner, D., Seraphin, B., Conti, E., 2007. RNA channelling by the archaeal exosome. EMBO Rep. 8, 470–476. https://doi.org/10.1038/sj.embor.7400945

Lorentzen, E., Walter, P., Fribourg, S., Evguenieva-Hackenberg, E., Klug, G., Conti, E., 2005. The archaeal exosome core is a hexameric ring structure with three catalytic subunits. Nat. Struct. Mol. Biol. 12, 575–581. https://doi.org/10.1038/nsmb952

Lubas, M., Andersen, P.R., Schein, A., Dziembowski, A., Kudla, G., Jensen, T.H., 2015. The human nuclear exosome targeting complex is loaded onto newly synthesized RNA to direct early ribonucleolysis. Cell Rep. 10, 178–192. https://doi.org/10.1016/j.celrep.2014.12.026

Lubas, M., Christensen, M.S., Kristiansen, M.S., Domanski, M., Falkenby, L.G., Lykke-Andersen, S., Andersen, J.S., Dziembowski, A., Jensen, T.H., 2011. Interaction profiling identifies the human nuclear exosome targeting complex. Mol. Cell 43, 624–637. https://doi.org/10.1016/j.molcel.2011.06.028

Lykke-Andersen, S., Brodersen, D.E., Jensen, T.H., 2009. Origins and activities of the eukaryotic exosome. J. Cell Sci. 122, 1487–1494. https://doi.org/10.1242/jcs.047399

Makino, D.L., Schuch, B., Stegmann, E., Baumgärtner, M., Basquin, C., Conti, E., 2015. RNA degradation paths in a 12-subunit nuclear exosome complex. Nature 524, 54–58. https://doi.org/10.1038/nature14865

Maquat, L.E., 2001. Evidence that selenium deficiency results in the cytoplasmic decay of GPx1 mRNA dependent on pre-mRNA splicing proteins bound to the mRNA exon-exon junction. BioFactors Oxf. Engl. 14, 37–42. https://doi.org/10.1002/biof.5520140106

Matsumoto, Y., Sarkar, G., Sommer, S.S., Wickner, R.B., 1993. A yeast antiviral protein, SKI8, shares a repeated amino acid sequence pattern with beta-subunits of G proteins and several other proteins. Yeast Chichester Engl. 9, 43–51. https://doi.org/10.1002/yea.320090106

Meola, N., Domanski, M., Karadoulama, E., Chen, Y., Gentil, C., Pultz, D., Vitting-Seerup, K., Lykke-Andersen, S., Andersen, J.S., Sandelin, A., Jensen, T.H., 2016. Identification of a Nuclear Exosome Decay Pathway for Processed Transcripts. Mol. Cell 64, 520–533. https://doi.org/10.1016/j.molcel.2016.09.025

Meola, N., Jensen, T.H., 2017. Targeting the nuclear RNA exosome: Poly(A) binding proteins enter the stage. RNA Biol. 14, 820–826. https://doi.org/10.1080/15476286.2017.1312227

Mitchell, P., Petfalski, E., Shevchenko, A., Mann, M., Tollervey, D., 1997b. The exosome: a conserved eukaryotic RNA processing complex containing multiple 3'-->5' exoribonucleases. Cell 91, 457–466. https://doi.org/10.1016/s0092-8674(00)80432-8

Mitchell, P., Tollervey, D., 2003b. An NMD pathway in yeast involving accelerated deadenylation and exosome-mediated 3'-->5' degradation. Mol. Cell 11, 1405–1413. https://doi.org/10.1016/s1097-2765(03)00190-4

Muhlrad, D., Parker, R., 1994. Premature translational termination triggers mRNA decapping. Nature 370, 578–581. https://doi.org/10.1038/370578a0

Orban, T.I., Izaurralde, E., 2005. Decay of mRNAs targeted by RISC requires XRN1, the Ski complex, and the exosome. RNA N. Y. N 11, 459–469. https://doi.org/10.1261/rna.7231505

Pefanis, E., Wang, J., Rothschild, G., Lim, J., Chao, J., Rabadan, R., Economides, A.N., Basu, U., 2014. Noncoding RNA transcription targets AID to divergently transcribed loci in B cells. Nature 514, 389–393. https://doi.org/10.1038/nature13580

Puno, M.R., Lima, C.D., 2022. Structural basis for RNA surveillance by the human nuclear exosome targeting (NEXT) complex. Cell 185, 2132-2147.e26. https://doi.org/10.1016/j.cell.2022.04.016

Puno, M.R., Lima, C.D., 2018. Structural basis for MTR4–ZCCHC8 interactions that stimulate the MTR4 helicase in the nuclear exosome-targeting complex. Proc. Natl. Acad. Sci. 115, E5506–E5515. https://doi.org/10.1073/pnas.1803530115

Puno, M.R., Weick, E.-M., Das, M., Lima, C.D., 2019. SnapShot: The RNA Exosome. Cell 179, 282-282.e1. https://doi.org/10.1016/j.cell.2019.09.005

Rhee, S.-K., Icho, T., Wickner, R.B., 1989b. Structure and nuclear localization signal of the SK13 antiviral protein of Saccharomyces cerevisiae. Yeast 5, 149–158. https://doi.org/10.1002/yea.320050304

Rogalska, M.E., Vivori, C., Valcárcel, J., 2023. Regulation of pre-mRNA splicing: roles in physiology and disease, and therapeutic prospects. Nat. Rev. Genet. 24, 251–269. https://doi.org/10.1038/s41576-022-00556-8

Safaee, N., Kozlov, G., Noronha, A.M., Xie, J., Wilds, C.J., Gehring, K., 2012b. Interdomain Allostery Promotes Assembly of the Poly(A) mRNA Complex with PABP and eIF4G. Mol. Cell 48, 375–386. https://doi.org/10.1016/j.molcel.2012.09.001

Schaeffer, D., Tsanova, B., Barbas, A., Reis, F.P., Dastidar, E.G., Sanchez-Rotunno, M., Arraiano, C.M., van Hoof, A., 2009. The exosome contains domains with specific endoribonuclease, exoribonuclease and cytoplasmic mRNA decay activities. Nat. Struct. Mol. Biol. 16, 56–62. https://doi.org/10.1038/nsmb.1528

Schmid, M., Jensen, T.H., 2019c. The Nuclear RNA Exosome and Its Cofactors. Adv. Exp. Med. Biol. 1203, 113–132. https://doi.org/10.1007/978-3-030-31434-7_4

Schmidt, C., Kowalinski, E., Shanmuganathan, V., Defenouillère, Q., Braunger, K., Heuer, A., Pech, M., Namane, A., Berninghausen, O., Fromont-Racine, M., Jacquier, A., Conti, E., Becker, T., Beckmann, R., 2016b. The cryo-EM structure of a ribosome-Ski2-Ski3-Ski8 helicase complex. Science 354, 1431–1433. https://doi.org/10.1126/science.aaf7520

Schmidt, K., Butler, J.S., 2013a. Nuclear RNA surveillance: role of TRAMP in controlling exosome specificity. WIREs RNA 4, 217–231. https://doi.org/10.1002/wrna.1155

Schneider, C., Leung, E., Brown, J., Tollervey, D., 2009. The N-terminal PIN domain of the exosome subunit Rrp44 harbors endonuclease activity and tethers Rrp44 to the yeast core exosome. Nucleic Acids Res. 37, 1127–1140. https://doi.org/10.1093/nar/gkn1020

Schneider, C., Tollervey, D., 2013. Threading the barrel of the RNA exosome. Trends Biochem. Sci. 38, 485–493. https://doi.org/10.1016/j.tibs.2013.06.013

Schuch, B., Feigenbutz, M., Makino, D.L., Falk, S., Basquin, C., Mitchell, P., Conti, E., 2014b. The exosome-binding factors Rrp6 and Rrp47 form a composite surface for recruiting the Mtr4 helicase. EMBO J. 33, 2829–2846. https://doi.org/10.15252/embj.201488757

Schuller, J.M., Falk, S., Fromm, L., Hurt, E., Conti, E., 2018b. Structure of the nuclear exosome captured on a maturing preribosome. Science 360, 219–222. https://doi.org/10.1126/science.aar5428

Shatkin, A.J., Manley, J.L., 2000. The ends of the affair: capping and polyadenylation. Nat. Struct. Biol. 7, 838–842. https://doi.org/10.1038/79583

Shoemaker, C.J., Green, R., 2012. Translation drives mRNA quality control. Nat. Struct. Mol. Biol. 19, 594–601. https://doi.org/10.1038/nsmb.2301

Sloan, K.E., Schneider, C., Watkins, N.J., 2012. Comparison of the yeast and human nuclear exosome complexes. Biochem. Soc. Trans. 40, 850–855. https://doi.org/10.1042/BST20120061

Stoecklin, G., Mühlemann, O., 2013. RNA decay mechanisms: specificity through diversity. Biochim. Biophys. Acta 1829, 487–490. https://doi.org/10.1016/j.bbagrm.2013.04.002

Tesina, P., Heckel, E., Cheng, J., Fromont-Racine, M., Buschauer, R., Kater, L., Beatrix, B., Berninghausen, O., Jacquier, A., Becker, T., Beckmann, R., 2019. Structure of the 80S ribosome–Xrn1 nuclease complex. Nat. Struct. Mol. Biol. 26, 275–280. https://doi.org/10.1038/s41594-019-0202-5

Toh-E A, Guerry P, Wickner R B, 1978. Chromosomal superkiller mutants of Saccharomyces cerevisiae. J. Bacteriol. 136, 1002–1007. https://doi.org/10.1128/jb.136.3.1002-1007.1978

Tomecki, R., Dziembowski, A., 2010. Novel endoribonucleases as central players in various pathways of eukaryotic RNA metabolism. RNA N. Y. N 16, 1692–1724. https://doi.org/10.1261/rna.2237610

Tuck, A.C., Rankova, A., Arpat, A.B., Liechti, L.A., Hess, D., Iesmantavicius, V., Castelo-Szekely, V., Gatfield, D., Bühler, M., 2020. Mammalian RNA Decay Pathways Are Highly Specialized and Widely Linked to Translation. Mol. Cell 77, 1222-1236.e13. https://doi.org/10.1016/j.molcel.2020.01.007

Tucker, M., Valencia-Sanchez, M.A., Staples, R.R., Chen, J., Denis, C.L., Parker, R., 2001b. The Transcription Factor Associated Ccr4 and Caf1 Proteins Are Components of the Major Cytoplasmic mRNA Deadenylase in Saccharomyces cerevisiae. Cell 104, 377–386. https://doi.org/10.1016/S0092-8674(01)00225-2

van Hoof, A., Frischmeyer, P.A., Dietz, H.C., Parker, R., 2002b. Exosome-mediated recognition and degradation of mRNAs lacking a termination codon. Science 295, 2262–2264. https://doi.org/10.1126/science.1067272

van Hoof, A., Staples, R.R., Baker, R.E., Parker, R., 2000. Function of the Ski4p (Csl4p) and Ski7p Proteins in 3'-to-5' Degradation of mRNA. Mol. Cell. Biol. 20, 8230–8243.

Vorländer, M.K., Pacheco-Fiallos, B., Plaschka, C., 2022. Structural basis of mRNA maturation: Time to put it together. Curr. Opin. Struct. Biol. 75, 102431. https://doi.org/10.1016/j.sbi.2022.102431

Weick, E.-M., Lima, C.D., 2021b. RNA helicases are hubs that orchestrate exosome-dependent 3'-5' decay. Curr. Opin. Struct. Biol. 67, 86–94. https://doi.org/10.1016/j.sbi.2020.09.010

Weick, E.-M., Puno, M.R., Januszyk, K., Zinder, J.C., DiMattia, M.A., Lima, C.D., 2018b. Helicase-Dependent RNA Decay Illuminated by a Cryo-EM Structure of a Human Nuclear RNA Exosome-MTR4 Complex. Cell 173, 1663-1677.e21. https://doi.org/10.1016/j.cell.2018.05.041

Weir, J.R., Bonneau, F., Hentschel, J., Conti, E., 2010. Structural analysis reveals the characteristic features of Mtr4, a DExH helicase involved in nuclear RNA processing and surveillance. Proc. Natl. Acad. Sci. 107, 12139–12144. https://doi.org/10.1073/pnas.1004953107

Widner, W.R., Wickner, R.B., 1993. Evidence that the SKI Antiviral System of Saccharomyces cerevisiae Acts by Blocking Expression of Viral mRNA. Mol. Cell. Biol. 13, 4331–4341. https://doi.org/10.1128/mcb.13.7.4331-4341.1993

Wiederhold, K., Passmore, L.A., 2010. Cytoplasmic deadenylation: regulation of mRNA fate. Biochem. Soc. Trans. 38, 1531–1536. https://doi.org/10.1042/BST0381531

Wilusz, C.J., Wang, W., Peltz, S.W., 2001. Curbing the nonsense: the activation and regulation of mRNA surveillance. Genes Dev. 15, 2781–2785. https://doi.org/10.1101/gad.943701

Zhang, E., Khanna, V., Dacheux, E., Namane, A., Doyen, A., Gomard, M., Turcotte, B., Jacquier, A., Fromont-Racine, M., 2019. A specialised SKI complex assists the cytoplasmic RNA exosome in the absence of direct association with ribosomes. EMBO J. 38, e100640.

Zinder, J.C., Lima, C.D., 2017b. Targeting RNA for processing or destruction by the eukaryotic RNA exosome and its cofactors. Genes Dev. 31, 88–100. https://doi.org/10.1101/gad.294769.116

Zinoviev, A., Ayupov, R.K., Abaeva, I.S., Hellen, C.U.T., Pestova, T.V., 2020b. Extraction of mRNA from Stalled Ribosomes by the Ski Complex. Mol. Cell 77, 1340-1349.e6. https://doi.org/10.1016/j.molcel.2020.01.011

Zuo, Y., Deutscher, M.P., 2001. Exoribonuclease superfamilies: structural analysis and phylogenetic distribution. Nucleic Acids Res. 29, 1017–1026.

8. Acknowledgements

I would like to express my gratitude to my supervisor, Prof. Elena Conti, for her unwavering trust and limitless support throughout my Ph.D. journey. The working environment in our lab is truly exceptional, and I take great pride in being a part of it.

I am immensely grateful to Ingmar for serving as both a mentor and a friend during this period. Your support, both professionally and personally, has been invaluable throughout these past years.

I also want to express my sincere appreciation to my predecessor, Eva, for consistently offering support and assistance during this time. Despite her own lab responsibilities, she has always made herself available for guidance and discussions.

I also want to thank all the lab members, both past and present, for creating an exceptional working environment in the lab, but also in the outside world. Yair, Sebastian, Jana, Michaela, Lisa, Lukas, Felix, Sofia, Marcela, Christian, Marc, Steffi, Dirk, Guilia, Julian, Mahesh, Timo, Daniel, Judith, Claire, Nicole, Matina, Ariane, Steffen and Walter without you, it would not have been the same! My special thanks go to Fabien, for his inexhaustible discussion modus and all the provided protocols and infrastructure which I used on a daily basis. Alex, for all discussions and input on the project. Petra and Tatjana, for being the master of clones. Marc and Lisa, for helping with purifications. Jérôme and Ingmar, for being part of the after 4 pm balcony club. Peter, for being the “Äkta-whisperer”, you are a true Rockstar! Courtney, for helping me overcome my antipathy towards writing and all the help.
At the MPIB, I want to express my gratitude to Rajan and Christian for their dedicated care of our computing infrastructure. This continuous support has been invaluable not only to me but also to the entire lab. I also want to thank Daniel and Tilman for their unwavering commitment to keeping the microscopes running and for always being there to offer help and advice.

I want to thank the boys, Robert, Peter, Matthias, Stephan and Matt. I already miss the CFL. Thanks for being part of this journey! I’m truly grateful to have you guys as friends! Thank you

Isabel! Without you, I would still be trying to pass the AC exam. Thank you Henri, without you, I would not have started this journey in the first place and our time in Ulm was indispensable!

Finally, I want to say thank you to my entire family, friends, and Nadine for their unwavering support throughout this journey. Despite not fully understanding what I do, you have never hesitated to provide unconditional support and love. Dad, thank you for always encouraging me and giving me the freedom to pursue my passions. Without your support, I would not have been able to achieve all that I have. Mum, I want to thank you for everything. You have been the biggest influence in my life, and your kindness, positivity, and love have shown me that there is always a bright side to life.